



HAL
open science

Global Climate

Robert Dunn, John Miller, Kate Willett, Nadine Gobron, Melanie Ades,
Robert Adler, Mihai Alexe, Richard Allan, John Anderson, Orlane Anneville,
et al.

► **To cite this version:**

Robert Dunn, John Miller, Kate Willett, Nadine Gobron, Melanie Ades, et al.. Global Climate. Bulletin of the American Meteorological Society, 2023, 104 (9), pp.S11-S145. 10.1175/BAMS-D-23-0090.1 . hal-04846861

HAL Id: hal-04846861

<https://hal.science/hal-04846861v1>

Submitted on 5 Jan 2025

HAL is a multi-disciplinary open access archive for the deposit and dissemination of scientific research documents, whether they are published or not. The documents may come from teaching and research institutions in France or abroad, or from public or private research centers.

L'archive ouverte pluridisciplinaire **HAL**, est destinée au dépôt et à la diffusion de documents scientifiques de niveau recherche, publiés ou non, émanant des établissements d'enseignement et de recherche français ou étrangers, des laboratoires publics ou privés.



Distributed under a Creative Commons Attribution 4.0 International License

STATE OF THE CLIMATE IN 2022

GLOBAL CLIMATE

R. J. H. Dunn, J. B. Miller, K. M. Willett, and N. Gobron, Eds.



Special Online Supplement to the *Bulletin of the American Meteorological Society* Vol. 104, No. 9, September, 2023

<https://doi.org/10.1175/BAMS-D-23-0090.1>

Corresponding author: Robert Dunn / robert.dunn@metoffice.gov.uk

©2023 American Meteorological Society

For information regarding reuse of this content and general copyright information, consult the [AMS Copyright Policy](#).

STATE OF THE CLIMATE IN 2022

Global Climate

Editors

Ellen Bartow-Gillies
Jessica Blunden
Tim Boyer

Chapter Editors

Peter Bissolli
Kyle R. Clem
Howard J. Diamond
Matthew L. Druckenmiller
Robert J. H. Dunn
Catherine Ganter
Nadine Gobron
Gregory C. Johnson
Rick Lumpkin
Ademe Mekonnen
John B. Miller
Twila A. Moon
Marilyn N. Raphael
Ahira Sánchez-Lugo
Carl J. Schreck III
Richard L. Thoman
Kate M. Willett
Zhiwei Zhu

Technical Editor

Lukas Noguchi

BAMS Special Editor for Climate

Michael A. Alexander

American Meteorological Society

Cover Credit:

Photo by Taaniela Kula, Tongan Geological Services (TGS).

Eruption at Hunga Tonga–Hunga Ha’apai, witnessed by TGS observer team, a 5-kilometer wide plume rises over 18 kilometers above sea level, 14 January 2022, 5:14 pm local time.

How to cite this document:

Global Climate is one chapter from the *State of the Climate in 2022* annual report and is available from <https://doi.org/10.1175/BAMS-D-23-0090.1>. Compiled by NOAA’s National Centers for Environmental Information, *State of the Climate in 2022* is based on contributions from scientists from around the world. It provides a detailed update on global climate indicators, notable weather events, and other data collected by environmental monitoring stations and instruments located on land, water, ice, and in space. The full report is available from <https://doi.org/10.1175/2023BAMSStateoftheClimate.1>.

Citing the complete report:

Blunden, J., T. Boyer, and E. Bartow-Gillies, Eds., 2023: “State of the Climate in 2022”. *Bull. Amer. Meteor. Soc.*, 104 (9), S1–S501 <https://doi.org/10.1175/2023BAMSStateoftheClimate.1>.

Citing this chapter:

Dunn, R. J. H., J. B. Miller, K. M. Willett, and N. Gobron, Eds., 2023: Global Climate [in “State of the Climate in 2022”]. *Bull. Amer. Meteor. Soc.*, 104 (9), S11–S145, <https://doi.org/10.1175/BAMS-D-23-0090.1>.

Citing a section (example):

Füllekrug, M., E. Williams, C. Price, S. Goodman, R. Holzworth, K. Virts, D. Buechler, T. Lang, and Y. Liu, 2023: Lightning [in “State of the Climate in 2022”]. *Bull. Amer. Meteor. Soc.*, 104 (9), S76–S78, <https://doi.org/10.1175/BAMS-D-23-0090.1>.

Editor and Author Affiliations (alphabetical by name)

- Ades, Melanie**, European Centre for Medium-Range Weather Forecasts, Reading, United Kingdom
- Adler, Robert**, CMNS-Earth System Science Interdisciplinary Center, University of Maryland, College Park, Maryland
- Alexe, Mihai**, European Centre for Medium-Range Weather Forecasts, Bonn, Germany
- Allan, Richard P.**, Department of Meteorology and National Centre for Earth Observation, University of Reading, Reading, United Kingdom
- Anderson, John**, Hampton University, Hampton, Virginia
- Anneville, Orlane**, National Research Institute for Agriculture, Food and Environment (INRAE), CARRTEL, Université Savoie Mont Blanc, Chambéry, France
- Aono, Yasuyuki**, Graduate School of Agriculture, Osaka Metropolitan University, Sakai, Japan
- Arguez, Anthony**, NOAA/NESDIS National Centers for Environmental Information, Asheville, North Carolina
- Arosio, Carlo**, University of Bremen, Bremen, Germany
- Augustine, John A.**, NOAA Global Monitoring Laboratory, Boulder, Colorado
- Azorin-Molina, Cesar**, Centro de Investigaciones sobre Desertificación – Spanish National Research Council (CSIC-UV-GVA), Valencia, Spain
- Barichivich, Jonathan**, Instituto de Geografía, Pontificia Universidad Católica de Valparaíso, Valparaíso, Chile; Laboratoire des Sciences du Climat et de l'Environnement (LSCE), LSCE/IPSL, CEA-CNRS-UVSQ, Gif-sur-Yvette, France
- Barnes, John E.**, retired, NOAA Global Monitoring Laboratory, Boulder, Colorado
- Beck, Hylke E.**, Physical Science and Engineering Division, King Abdullah University of Science and Technology, Thuwal, Saudi Arabia
- Bellouin, Nicolas**, University of Reading, Reading, United Kingdom
- Benedetti, Angela**, European Centre for Medium-Range Weather Forecasts, Reading, United Kingdom
- Blagrove, Kevin**, Department of Biology, York University, Toronto, Canada
- Blenkinsop, Stephen**, School of Engineering, Newcastle University, Newcastle-upon-Tyne, United Kingdom
- Bock, Olivier**, Université Paris Cité, Institut de Physique du Globe de Paris, CNRS, IGN, F-75005 Paris, France; ENSG-Géomatique, IGN, F-77455 Marne-la-Vallée, France
- Bodin, Xavier**, Laboratoire EDYTEM, CNRS/Université Savoie Mont-Blanc, Chambéry, France
- Bosilovich, Michael**, Global Modeling and Assimilation Office, NASA Goddard Space Flight Center, Greenbelt, Maryland
- Boucher, Olivier**, Sorbonne Université, Paris, France
- Buechler, Dennis**, University of Alabama in Huntsville, Huntsville, Alabama
- Buehler, Stefan A.**, Universität Hamburg, Hamburg, Germany
- Campos, Diego**, Dirección Meteorológica de Chile (DMC), Santiago, Chile
- Carrea, Laura**, Department of Meteorology, University of Reading, Reading, United Kingdom
- Chang, Kai-Lan**, Cooperative Institute for Research in Environmental Sciences, University of Colorado Boulder, Boulder, Colorado; NOAA Chemical Sciences Laboratory, Boulder, Colorado
- Christiansen, Hanne H.**, Geophysics Department, University Centre in Svalbard, Longyearbyen, Norway
- Christy, John R.**, University of Alabama in Huntsville, Huntsville, Alabama
- Chung, Eui-Seok**, Korea Polar Research Institute, Incheon, South Korea
- Ciasto, Laura M.**, NOAA/NWS National Centers for Environmental Prediction Climate Prediction Center, College Park, Maryland
- Clingan, Scott**, Cooperative Institute for Research in the Earth Sciences, NOAA Global Monitoring Laboratory, Boulder, Colorado
- Coldewey-Egbers, Melanie**, DLR (German Aerospace Center) Oberpfaffenhofen, Germany
- Cooper, Owen R.**, Cooperative Institute for Research in Environmental Sciences, University of Colorado Boulder, Boulder, Colorado; NOAA Chemical Sciences Laboratory, Boulder, Colorado
- Cornes, Richard C.**, National Oceanography Centre, Southampton, United Kingdom
- Covey, Curt**, Lawrence Livermore National Laboratory, Livermore, California
- Créatux, Jean-François**, LEGOS (CNES/CNRS/IRD/UPS), University of Toulouse, Toulouse, France
- Crimmins, Theresa**, USA National Phenology Network, School of Natural Resources and the Environment, University of Arizona, Tucson, Arizona
- Cropper, Thomas**, National Oceanography Centre, Southampton, United Kingdom
- Crotwell, Molly**, Cooperative Institute for Research in the Earth Sciences, NOAA Global Monitoring Laboratory, Boulder, Colorado
- Culpepper, Joshua**, Department of Biology, York University, Toronto, Canada
- Cusicanqui, Diego**, Université Grenoble Alpes, Institut de Géosciences de l'Environnement (IGE), Grenoble, France
- Davis, Sean M.**, NOAA Chemical Sciences Laboratory, Boulder, Colorado
- de Jeu, Richard A. M.**, Planet Labs, Haarlem, The Netherlands
- Degenstein, Doug**, University of Saskatchewan, Saskatoon, Canada
- Delaloye, Reynald**, Department of Geosciences, University of Fribourg, Fribourg, Switzerland
- Dokulil, Martin T.**, Research Institute for Limnology, University of Innsbruck, Mondsee, Austria
- Donat, Markus G.**, Barcelona Supercomputing Centre, Barcelona, Spain; Catalan Institution for Research and Advanced Studies (ICREA), Barcelona, Spain
- Dorigo, Wouter A.**, TU Wien, Department of Geodesy and Geoinformation, Vienna, Austria
- Dugan, Hilary A.**, Center for Limnology, University of Wisconsin-Madison, Madison, Wisconsin
- Dunn, Robert J. H.**, Met Office Hadley Centre, Exeter, United Kingdom
- Durre, Imke**, NOAA/NESDIS National Centers for Environmental Information, Asheville, North Carolina
- Dutton, Geoff**, Cooperative Institute for Research in the Earth Sciences, NOAA Global Monitoring Laboratory, Boulder, Colorado
- Duveiller, Gregory**, Max Planck Institute for Biogeochemistry, Jena, Germany
- Estilow, Thomas W.**, Rutgers University, Piscataway, New Jersey
- Estrella, Nicole**, Ecoclimatology, Department of Life Science Systems, TUM School of Life Sciences, Technical University of Munich, Freising, Germany
- Fereday, David**, Met Office Hadley Centre, Exeter, United Kingdom
- Fioletov, Vitali E.**, Environment and Climate Change Canada, Toronto, Canada
- Flemming, Johannes**, European Centre for Medium-Range Weather Forecasts, Reading, United Kingdom
- Foster, Michael J.**, Cooperative Institute for Meteorological Satellite Studies, Space Science and Engineering Center, University of Wisconsin-Madison, Madison, Wisconsin
- Franz, Bryan**, NASA Goddard Space Flight Center, Greenbelt, Maryland
- Frith, Stacey M.**, Science Systems and Applications, Inc, Lanham, Maryland; NASA Goddard Space Flight Center, Greenbelt, Maryland
- Froidevaux, Lucien**, Jet Propulsion Laboratory, California Institute of Technology, Pasadena, California
- Füllekrug, Martin**, University of Bath, Bath, United Kingdom
- Garforth, Judith**, Woodland Trust, Grantham, United Kingdom
- Garg, Jay**, Science Systems and Applications, Inc. (SSAI), Hampton, Virginia
- Gibbes, Badin**, School of Civil Engineering, The University of Queensland, Brisbane, Australia
- Gobron, Nadine**, European Commission Joint Research Centre, Ispra, Italy
- Goodman, Steven**, Thunderbolt Global Analytics, Huntsville, Alabama
- Goto, Atsushi**, World Meteorological Organization, Geneva, Switzerland

Editor and Author Affiliations (continued)

- Gruber, Alexander**, TU Wien, Department of Geodesy and Geoinformation, Vienna, Austria
- Gu, Guojun**, CMNS-Earth System Science Interdisciplinary Center, University of Maryland, College Park, Maryland
- Hahn, Sebastian**, TU Wien, Department of Geodesy and Geoinformation, Vienna, Austria
- Haimberger, Leopold**, University of Vienna, Vienna, Austria
- Hall, Bradley D.**, NOAA Global Monitoring Laboratory, Boulder, Colorado
- Harris, Ian**, National Centre for Atmospheric Science (NCAS), University of East Anglia, Norwich, United Kingdom; Climatic Research Unit, School of Environmental Sciences, University of East Anglia, Norwich, United Kingdom
- Hemming, Deborah L.**, Met Office Hadley Centre, Exeter, United Kingdom; Birmingham Institute of Forest Research, Birmingham University, Birmingham, United Kingdom
- Hirschi, Martin**, ETH Zurich, Department of Environmental Systems Science, Zürich, Switzerland
- Ho, Shu-peng (Ben)**, Center for Satellite Applications and Research, NOAA, College Park, Maryland; Remote Sensing Systems, Santa Rosa, California
- Holzworth, Robert**, University of Washington, Seattle, Washington
- Hrbáček, Filip**, Department of Geography, Masaryk University, Brno, Czech Republic
- Hu, Guojie**, Cryosphere Research Station on Qinghai-Tibet Plateau, Northwestern Institute of Eco-Environment and Resources, CAS, Beijing, China
- Hurst, Dale F.**, Cooperative Institute for Research in Environmental Sciences, University of Colorado Boulder, Boulder, Colorado; NOAA Global Monitoring Laboratory, Boulder, Colorado
- Inness, Antje**, European Centre for Medium-Range Weather Forecasts, Reading, United Kingdom
- Isaksen, Ketil**, Norwegian Meteorological Institute, Oslo, Norway
- John, Viju O.**, EUMETSAT, Darmstadt, Germany
- Jones, Philip D.**, Climatic Research Unit, School of Environmental Sciences, University of East Anglia, Norwich, United Kingdom
- Junod, Robert**, Earth System Science Center (ESSC), University of Alabama in Huntsville, Huntsville, Alabama
- Kääb, Andreas**, Department of Geosciences, University of Oslo, Norway
- Kaiser, Johannes W.**, SatFire Kaiser, Hofheim am Taunus, Germany
- Kaufmann, Viktor**, Institute of Geodesy, Working Group Remote Sensing and Photogrammetry, Graz University of Technology, Graz, Austria
- Kellerer-Pirklbauer, Andreas**, Institute of Geography and Regional Science, Cascade – The Mountain Processes and Mountain Hazards Group, University of Graz, Graz, Austria
- Kent, Elizabeth C.**, National Oceanography Centre, Southampton, United Kingdom
- Kidd, Richard**, EODC GmbH, Vienna, Austria
- Kipling, Zak**, European Centre for Medium-Range Weather Forecasts, Reading, United Kingdom
- Koppa, Akash**, Hydro-Climate Extremes Lab (H-CEL), Ghent University, Ghent, Belgium
- Kraemer, Benjamin M.**, University of Konstanz, Konstanz, Germany
- Kramarova, Natalya**, NASA Goddard Space Flight Center, Greenbelt, Maryland
- Kruger, Andries**, Climate Service, South African Weather Service, Pretoria, South Africa
- La Fuente, Sofia**, Dundalk Institute of Technology, Dundalk, Ireland
- Laas, Alo**, Estonian University of Life Sciences, Tartumaa, Estonia
- Lan, Xin**, CIRES, University of Colorado Boulder & NOAA Global Monitoring Laboratory, Boulder, Colorado
- Lang, Timothy**, NASA Marshall Space Flight Center, Huntsville, Alabama
- Lantz, Kathleen O.**, NOAA Global Monitoring Laboratory, Boulder, Colorado
- Lavers, David A.**, European Centre for Medium-Range Weather Forecasts, Reading, United Kingdom
- Leblanc, Thierry**, Jet Propulsion Laboratory, California Institute of Technology, Wrightwood, California
- Leibensperger, Eric M.**, Department of Physics and Astronomy, Ithaca College, Ithaca, New York
- Lennard, Chris**, Department of Environmental and Geographical Science, University of Cape Town, Cape Town, South Africa
- Liu, Yakun**, Massachusetts Institute of Technology, Cambridge, Massachusetts
- Loeb, Norman G.**, NASA Langley Research Center, Hampton, Virginia
- Loyola, Diego**, DLR (German Aerospace Center) Oberpfaffenhofen, Germany
- Maberly, Stephen C.**, UK Centre for Ecology & Hydrology, Lancaster, United Kingdom
- Madelon, Remi**, CESBIO, Université de Toulouse, CNES/CNRS/INRAe/IRD/UPS, Toulouse, France
- Magnin, Florence**, Laboratoire EDYTEM, CNRS/Université Savoie Mont-Blanc, Chambéry, France
- Matsuzaki, Shin-Ichiro**, National Institute for Environmental Studies, Tsukuba, Japan
- May, Linda**, UK Centre for Ecology & Hydrology, Edinburgh, United Kingdom
- Mayer, Michael**, University of Vienna, Vienna, Austria; European Centre for Medium-Range Weather Forecasts, Reading, United Kingdom
- McCabe, Matthew F.**, Climate and Livability Initiative, Division of Biological and Environmental Sciences and Engineering, King Abdullah University of Science and Technology, Thuwal, Saudi Arabia
- McVicar, Tim R.**, CSIRO Environment, Canberra, Australia; Australian Research Council Centre of Excellence for Climate Extremes, Sydney, Australia
- Mears, Carl A.**, Remote Sensing Systems, Santa Rosa, California
- Menzel, Annette**, Ecoclimatology, Department of Life Science Systems, TUM School of Life Sciences, Technical University of Munich, Freising, Germany; Institute for Advanced Study, Technical University of Munich, Garching, Germany
- Merchant, Christopher J.**, Department of Meteorology, University of Reading, Reading, United Kingdom
- Meyer, Michael F.**, United States Geological Survey, Madison, Wisconsin
- Miller, John B.**, NOAA Global Monitoring Laboratory, Boulder, Colorado
- Miralles, Diego G.**, Hydro-Climate Extremes Lab (H-CEL), Ghent University, Ghent, Belgium
- Moesinger, Leander**, TU Wien, Vienna, Austria
- Monet, Ghislaine**, Université Savoie Mont Blanc, INRAE, CARRTEL, Chambéry, France
- Montzka, Stephan A.**, NOAA Global Monitoring Laboratory, Boulder, Colorado
- Morice, Colin**, Met Office Hadley Centre, Exeter, United Kingdom
- Mrekaj, Ivan**, Technical University in Zvolen, Zvolen, Slovakia
- Mühle, Jens**, AGAGE, Scripps Institution of Oceanography, University of California, San Diego, La Jolla, California
- Nance, David**, Cooperative Institute for Research in the Earth Sciences, NOAA Global Monitoring Laboratory, Boulder, Colorado
- Nicolas, Julien P.**, European Centre for Medium-Range Weather Forecasts, Bonn, Germany
- Noetzli, Jeannette**, WSL Institute for Snow and Avalanche Research SLF, Davos-Dorf, Switzerland; Climate Change, Extremes and Natural Hazards in Alpine Regions Research Center CERC, Davos Dorf, Switzerland
- Noll, Ben**, National Institute of Water and Atmospheric Research, Auckland, New Zealand
- O'Keefe, John**, The Harvard Forest, Harvard University, Petersham, Massachusetts
- Osborn, Timothy J.**, Climatic Research Unit, School of Environmental Sciences, University of East Anglia, Norwich, United Kingdom
- Park, Taejin**, NASA Ames Research Center, Mountain View, California; Bay Area Environmental Research Institute, Mountain View, California

Editor and Author Affiliations (continued)

- Parrington, Mark**, European Centre for Medium-Range Weather Forecasts, Bonn, Germany
- Pellet, Cécile**, Department of Geosciences, University of Fribourg, Fribourg, Switzerland
- Pelto, Mauri S.**, Nichols College, Dudley, Massachusetts
- Petersen, Kyle**, Cooperative Institute for Research in the Earth Sciences, NOAA Global Monitoring Laboratory, Boulder, Colorado
- Phillips, Coda**, Cooperative Institute for Meteorological Satellite Studies, Space Science and Engineering Center, University of Wisconsin-Madison, Madison, Wisconsin
- Pierson, Don**, Department of Ecology and Genetics, Uppsala University, Uppsala, Sweden
- Pinto, Izidine**, Royal Netherlands Meteorological Institute (KNMI), De Bilt, The Netherlands
- Po-Chedley, Stephen**, Lawrence Livermore National Laboratory, Livermore, California
- Pogliotti, Paolo**, Environmental Protection Agency of Valle d'Aosta, Saint-Christophe, Italy
- Polvani, Lorenzo**, Columbia University, New York, New York
- Preimesberger, Wolfgang**, TU Wien, Department of Geodesy and Geoinformation, Vienna, Austria
- Price, Colin**, Tel Aviv University, Tel Aviv, Israel
- Pulkkanen, Merja**, Finnish Environment Institute (SYKE), Jyväskylä, Finland
- Randel, William J.**, National Center for Atmospheric Research, Boulder, Colorado
- Rémy, Samuel**, HYGEOS, Lille, France
- Ricciardulli, Lucrezia**, Remote Sensing Systems, Santa Rosa, California
- Richardson, Andrew D.**, School of Informatics, Computing, and Cyber Systems, Flagstaff, Arizona; Center for Ecosystem Science and Society, Northern Arizona University, Flagstaff, Arizona
- Robinson, David A.**, Rutgers University, Piscataway, New Jersey
- Rocha, Willy**, Servicio Nacional de Meteorología e Hidrología, Bolivia
- Rodell, Matthew**, Earth Sciences Division, NASA Goddard Space Flight Center, Greenbelt, Maryland
- Rodriguez-Fernandez, Nemesio**, CESBIO, Université de Toulouse, CNES/CNRS/INRAe/IRD/UPS, Toulouse, France
- Rosenlof, Karen H.**, NOAA Chemical Sciences Laboratory, Boulder, Colorado
- Rozanov, Alexei**, University of Bremen, Bremen, Germany
- Rozkošný, Jozef**, Slovak Hydrometeorological Institute, Bratislava, Slovakia
- Rusanovskaya, Olga O.**, Irkutsk State University, Institute of Biology, Irkutsk, Russia
- Rutishauser, This**, Swiss Academy of Sciences (SCNAT), Bern, Switzerland
- Sabeerali, C. T.**, India Meteorological Department, Ministry of Earth Sciences, Pune, India
- Sánchez-Lugo, Ahira**, NOAA/NESDIS National Centers for Environmental Information, Asheville, North Carolina
- Sawaengphokhai, Parnchai**, Science Systems and Applications, Inc. (SSAI), Hampton, Virginia
- Schenzinger, Verena**, Medical University of Innsbruck, Innsbruck, Austria
- Schlegel, Robert W.**, Laboratoire d'Océanographie de Villefranche, Sorbonne Université, CNRS, Villefranche-sur-mer, France
- Schmid, Martin**, Eawag, Swiss Federal Institute of Aquatic Science and Technology, Surface Waters - Research and Management, Kastanienbaum, Switzerland
- Schneider, Udo**, Global Precipitation Climatology Centre, Deutscher Wetterdienst, Offenbach, Germany
- Sezaki, Fumi**, Japan Meteorological Agency, Tokyo, Japan
- Sharma, Sapna**, Department of Biology, York University, Toronto, Canada
- Shi, Lei**, NOAA/NESDIS National Centers for Environmental Information, Asheville, North Carolina
- Shimaraeva, Svetlana V.**, Irkutsk State University, Institute of Biology, Irkutsk, Russia
- Silow, Eugene A.**, Irkutsk State University, Institute of Biology, Irkutsk, Russia
- Simmons, Adrian J.**, European Centre for Medium-Range Weather Forecasts, Reading, United Kingdom
- Smith, Sharon L.**, Geological Survey of Canada, Natural Resources Canada, Ottawa, Canada
- Soden, Brian J.**, University of Miami, Miami, Florida
- Sofieva, Viktoria**, FMI (Finnish Meteorological Institute), Helsinki, Finland
- Sparks, Tim H.**, Poznań University of Life Sciences, Poznań, Poland
- Sreejith, O.P.**, India Meteorological Department, Ministry of Earth Sciences, Pune, India
- Stackhouse, Jr., Paul W.**, NASA Langley Research Center, Hampton, Virginia
- Stauffer, Ryan**, NASA Goddard Space Flight Center, Greenbelt, Maryland
- Steinbrecht, Wolfgang**, DWD (German Weather Service), Hohenpeissenberg, Germany
- Steiner, Andrea K.**, Wegener Center for Climate and Global Change, University of Graz, Graz, Austria
- Stradiotti, Pietro**, TU Wien, Department of Geodesy and Geoinformation, Vienna, Austria
- Streletskiy, Dmitry A.**, George Washington University, Washington DC
- Surendran, Divya E.**, India Meteorological Department, Ministry of Earth Sciences, Pune, India
- Thackeray, Stephen J.**, UK Centre for Ecology and Hydrology, Lancaster, United Kingdom
- Thibert, Emmanuel**, Université Grenoble Alpes, INRAE, CNRS, IRD, Grenoble INP, IGE, Grenoble, France.
- Timofeyev, Maxim A.**, Irkutsk State University, Institute of Biology, Irkutsk, Russia
- Tourpali, Kleareti**, Aristotle University, Thessaloniki, Greece
- Tye, Mari R.**, National Center for Atmospheric Research, Boulder, Colorado
- van der A, Ronald**, Royal Netherlands Meteorological Institute (KNMI), De Bilt, The Netherlands
- van der Schalie, Robin**, Planet Labs, Haarlem, The Netherlands
- van der Schrier, Gerard**, Royal Netherlands Meteorological Institute (KNMI), De Bilt, The Netherlands
- van Vliet, Arnold J.H.**, Environmental Systems Analysis Group, Wageningen University and Research, The Netherlands
- Verborg, Piet**, National Institute of Water and Atmospheric Research, Wellington, New Zealand
- Vernier, Jean-Paul**, NASA Langley Research Center, Hampton, Virginia
- Vimont, Isaac J.**, NOAA Global Monitoring Laboratory, Boulder, Colorado
- Virts, Katrina**, University of Alabama in Huntsville, Huntsville, Alabama
- Vivero, Sebastián**, Department of Geosciences, University of Fribourg, Fribourg, Switzerland
- Vömel, Holger**, Earth Observing Laboratory, National Center for Atmospheric Research, Boulder, Colorado
- Vose, Russell S.**, NOAA/NESDIS National Centers for Environmental Information, Asheville, North Carolina
- Wang, Ray H. J.**, Georgia Institute of Technology, Atlanta, Georgia
- Wang, Xinyue**, National Center for Atmospheric Research, Boulder, Colorado
- Warnock, Taran**, University of Saskatchewan, Saskatoon, Canada
- Weber, Mark**, University of Bremen, Bremen, Germany
- Wiese, David N.**, Jet Propulsion Laboratory, California Institute of Technology, Pasadena, California
- Wild, Jeannette D.**, ESSIC/University of Maryland, College Park, Maryland; NOAA NESDIS/STAR, College Park, Maryland
- Willett, Kate M.**, Met Office Hadley Centre, Exeter, United Kingdom

Editor and Author Affiliations (continued)

Williams, Earle, Massachusetts Institute of Technology, Cambridge, Massachusetts

Wong, Takmeng, NASA Langley Research Center, Hampton, Virginia

Woolway, Richard Iestyn, School of Ocean Sciences, Bangor University, Menai Bridge, Anglesey, Wales

Yin, Xungang, NOAA/NESDIS National Centers for Environmental Information, Asheville, North Carolina

Zeng, Zhenzhong, School of Environmental Science and Engineering, Southern University of Science and Technology, Shenzhen, China

Zhao, Lin, School of Geographical Sciences, Nanjing University of Information Science and Technology, Nanjing, China

Zhou, Xinjia, Center for Satellite Applications and Research, NOAA, College Park, Maryland

Ziemke, Jerry R., Goddard Earth Sciences Technology and Research, Morgan State University, Baltimore, Maryland; NASA Goddard Space Flight Center, Greenbelt, Maryland

Ziese, Markus, Global Precipitation Climatology Centre, Deutscher Wetterdienst, Offenbach, Germany

Zotta, Ruxandra M., TU Wien, Vienna, Austria

Zou, Cheng-Zhi, NOAA/NESDIS Center for Satellite Applications and Research, College Park, Maryland

Editorial and Production Team

Allen, Jessica, Graphics Support, Cooperative Institute for Satellite Earth System Studies, North Carolina State University, Asheville, North Carolina

Camper, Amy V., Graphics Support, Innovative Consulting and Management Services, LLC, NOAA/NESDIS National Centers for Environmental Information, Asheville, North Carolina

Haley, Bridgette O., Graphics Support, NOAA/NESDIS National Centers for Environmental Information, Asheville, North Carolina

Hammer, Gregory, Content Team Lead, Communications and Outreach, NOAA/NESDIS National Centers for Environmental Information, Asheville, North Carolina

Love-Brotak, S. Elizabeth, Lead Graphics Production, NOAA/NESDIS National Centers for Environmental Information, Asheville, North Carolina

Ohlmann, Laura, Technical Editor, Innovative Consulting and Management Services, LLC, NOAA/NESDIS National Centers for Environmental Information, Asheville, North Carolina

Noguchi, Lukas, Technical Editor, Innovative Consulting and Management Services, LLC, NOAA/NESDIS National Centers for Environmental Information, Asheville, North Carolina

Riddle, Deborah B., Graphics Support, NOAA/NESDIS National Centers for Environmental Information, Asheville, North Carolina

Veasey, Sara W., Visual Communications Team Lead, Communications and Outreach, NOAA/NESDIS National Centers for Environmental Information, Asheville, North Carolina

2. Table of Contents

List of authors and affiliations	S14
a. Overview	S20
b. Temperature	S27
1. Global surface temperature.....	S27
2. Lake surface water temperature.....	S28
3. Night marine air temperature.....	S31
4. Surface temperature extremes.....	S33
5. Tropospheric temperature.....	S36
6. Stratospheric temperature.....	S38
c. Cryosphere	S39
1. Permafrost temperature and active layer thickness.....	S39
2. Rock glacier velocity.....	S41
3. Alpine glaciers.....	S43
4. Lake ice.....	S45
5. Northern Hemisphere continental snow-cover extent.....	S47
d. Hydrological cycle	S49
1. Surface humidity.....	S49
Sidebar 2.1: Assessing humid heat extremes over land.....	S51
2. Total column water vapor.....	S54
3. Upper-tropospheric humidity.....	S55
4. Precipitation.....	S57
5. Land surface precipitation extremes.....	S58
6. Cloudiness.....	S60
7. Lake water levels.....	S61
8. Groundwater and terrestrial water storage.....	S63
9. Soil moisture.....	S65
10. Monitoring global drought using the self-calibrating Palmer Drought Severity Index.....	S66
11. Land evaporation.....	S68
e. Atmospheric circulation	S69
1. Mean sea-level pressure and related modes of variability.....	S69
2. Land and ocean surface winds.....	S72
3. Upper air winds.....	S74
4. Lightning.....	S76
f. Earth radiation budget	S79
1. Earth radiation budget at top-of-atmosphere.....	S79
2. Mauna Loa apparent transmission record.....	S81

2. Table of Contents

Sidebar 2.2: Hunga Tonga–Hunga Ha’apai eruption.....	S82
g. Atmospheric composition.....	S85
1. Long-lived greenhouse gases.....	S85
2. Ozone-depleting substances and their substitutes.....	S87
3. Aerosols.....	S91
4. Stratospheric ozone.....	S94
5. Stratospheric water vapor.....	S96
6. Tropospheric ozone.....	S98
7. Carbon monoxide.....	S101
h. Land surface properties.....	S102
1. Terrestrial surface albedo dynamics.....	S102
2. Terrestrial vegetation dynamics.....	S103
3. Biomass burning.....	S105
4. Phenology of primary producers.....	S107
5. Vegetation optical depth.....	S110
Acknowledgments.....	S113
Appendix 1: Chapter 2 – Acronyms.....	S118
Appendix 2: Chapter 2 – Supplemental Material.....	S122
References.....	S130

Please refer to Chapter 8 (Relevant Datasets and Sources) for a list of all climate variables and datasets used in this chapter for analyses, along with their websites for more information and access to the data.

2. GLOBAL CLIMATE

R. J. H. Dunn, J. B. Miller, K. M. Willett, and N. Gobron, Eds.

a. Overview

—R. J. H. Dunn, J. B. Miller, K. M. Willett, and N. Gobron

Throughout 2022, the “triple-dip” La Niña (three consecutive years) showed its hand in a large number of the essential climate variables and metrics that are covered in this chapter. La Niña conditions tend to have a cooling effect on global temperatures in comparison to neutral or El Niño years and impact precipitation patterns around the globe. Upper-level wind patterns at 200 hPa across the globe for 2020–22 showed a striking similarity with the last triple-dip La Niña that occurred in 1998–2000.

Yet, despite the cooling effect of the ongoing La Niña, 2022 was still among the six warmest years since global records began in the mid-to-late 1880s, according to six datasets of global surface temperatures. It was also the warmest La Niña year on record, surpassing 2021.

Exceptional heatwaves occurred across the globe in 2022, boosted by above-average temperatures that continue their relentless long-term rise. In Europe, the “unweather”—an Old English term for weather so severe that it appears to come from a different climate or world—shattered records across the continent during the summer months, while rivers and reservoirs fell to critically low levels. Meanwhile China experienced its hottest summer on record and at Wuhan, the Yangtze River reached record-low values.

The extreme high summer temperatures over Europe resulted in unprecedented melting of glaciers in the Alps, with over 6% of their volume lost in Switzerland this year alone, a record loss. Globally, 2022 was the 35th consecutive year of glacier mass loss and the 14th consecutive year of exceptional loss (more than 500 mm water equivalent). Ice cover on lakes was almost nine days shorter than average, the fourth shortest since 1980; the five shortest ice seasons have all occurred since 2016. The average temperature anomaly for more than 1950 lakes across the Northern Hemisphere was the second highest since the beginning of the record in 1995.

Drought conditions were pervasive, occurring across Europe (linked to the extreme summer temperatures), as well as the American West, China, and most of Southern Hemisphere South America. Globally, record-high areas of land experiencing extreme drought (6.2%) were reached in August 2022; overall, 29% of land experienced moderate or worse categories of drought. Low values of terrestrial water storage also occurred in Europe and parts of China (linked to the heatwaves), but La Niña influenced high values in southeastern Australia. Extreme rainfall was observed in southeastern and eastern Australia as well as in Pakistan, which received around three times its normal August monsoon rainfall. However, precipitation amounts for the globe as a whole and over the ocean was much lower than normal, but close to normal over land. Total column water vapor and surface humidity were close to normal over the ocean. Despite ‘normal’ rainfall amounts over land and lower terrestrial water storage, 2022 saw continued above-average soil moisture values, which are approaching the level of the previous global record in 2011. Lake water levels were higher than normal overall, but cloudiness was below normal. Overall, 2022 was a mixed year for the hydrological variables presented in this chapter.

In addition to the ongoing La Niña, other climate modes of variability in 2022 included a negative Indian Ocean dipole, a positive winter North Atlantic Oscillation (NAO), and the second highest summer NAO on record. The Southern Annular Mode was positive for a record-equaling

76% of days in 2022; it was the sixth time 60% of days has been exceeded since 2015, compared to only 10 years between 1979 and 2014 where high positive rates of >60% of days occurred.

The most significant long-term changes in atmospheric composition continue to be record levels of long-lived greenhouse gases (LLGHGs). Globally averaged carbon dioxide, methane, and nitrous oxide levels in 2022 continued to increase rapidly by 2.2 ppm, 14.4 ppb, and 1.3 ppb to 417.1 ppm, 1911.8 ppb, and 335.7 ppb, respectively. Collectively, all LLGHGs contributed 3.4 W m^{-2} of all radiative forcing, with the main three LLGHGs accounting for 98% of the increase in the last five years. As measured by equivalent effective stratospheric chlorine, the gases that destroy stratospheric ozone continue to decline nearly linearly. Since the 2018 discovery of post-2011 renewed trichlorofluoromethane (CFC-11) emissions, in violation of the Montreal Protocol, illegal emissions have mostly disappeared.

Considering short-lived atmospheric components, global mean aerosol optical depth in 2022 was the lowest on record, as was carbon monoxide, reflecting fewer fires in 2022 on top of a long-term decreasing trend likely reflecting global improvements in fossil fuel combustion efficiency. Tropospheric ozone has continued to trend upwards with an 8% increase since 2004. The most remarkable impact on short-lived species in 2022 resulted from the Hunga Tonga–Hunga Haʻapai underwater volcanic eruption (HTHH) in January 2022, discussed in Sidebar 2.2. Stratospheric aerosols registered their largest perturbation since the Mt. Pinatubo eruption of 1991. The HTHH eruption injected ~50 Tg–150 Tg of water vapor into the stratosphere, an amount unprecedented in the satellite record which represents more than 10% of the entire stratospheric water vapor burden, an anomaly that will persist for several years.

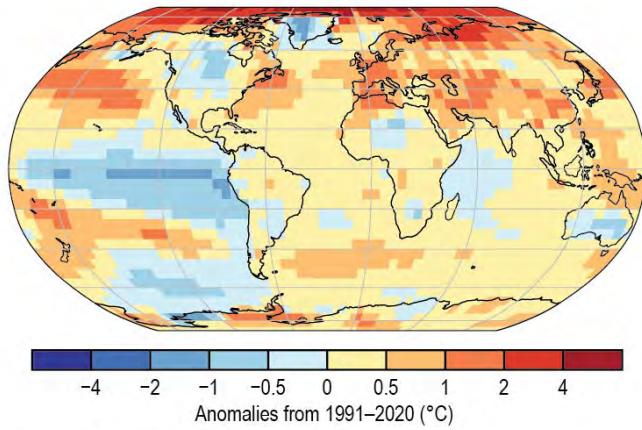
Low amounts of early summer snow cover in the Northern Hemisphere, along with increased plant growth and associated greening resulting from La Niña-induced rainfall decreased the global albedo in 2022. Carbon emissions from biomass burning during 2022 were 22% below the long-term average, making it the lowest fire year on record. However, considerable fire activity was still observed in boreal North America, parts of Europe, and central South America.

This year, a new measure of humid heat events is introduced in Sidebar 2.1, using equivalent heat indices based on the wet bulb temperature rather than air temperature. Humid heat extremes have increased in both magnitude and frequency since 1973, and 2022 was above average for both.

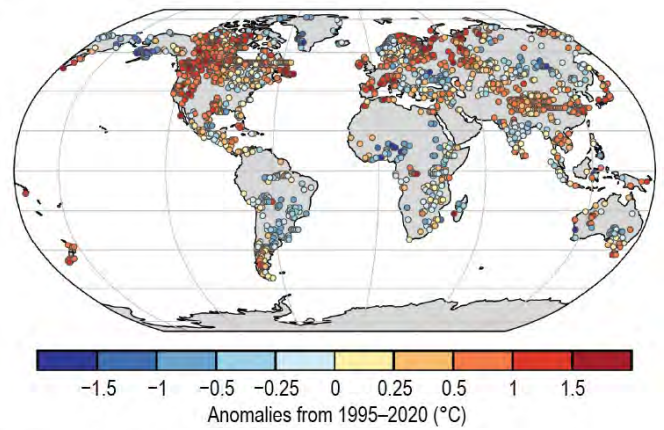
Time series and anomaly maps for 2022 from many of the variables described in this chapter can be found in Plates 1.1 (Chapter 1) and 2.1. Most sections now use the 1991–2020 climatological reference period, in line with World Meteorological Organization recommendations. This was not possible for all datasets depending on their length of record or legacy processing methods at the time of writing and is noted accordingly.

Finally, already looking towards the next reports, we welcome expressions of interest from those who wish to propose new sections for this chapter or wish to bring their expertise to existing author teams.

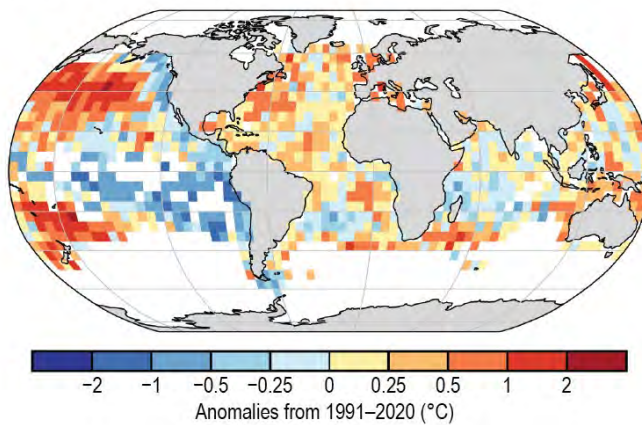
(a) Surface Temperature



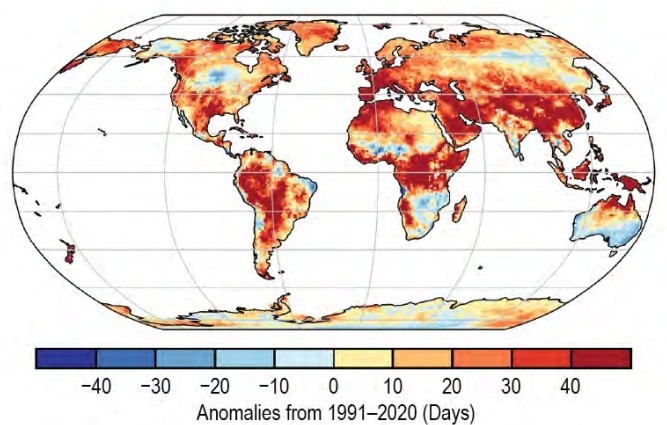
(b) Lake Temperature



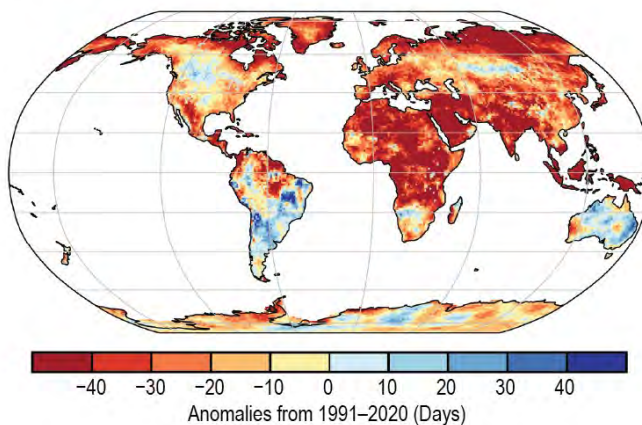
(c) Night Marine Air Temperature



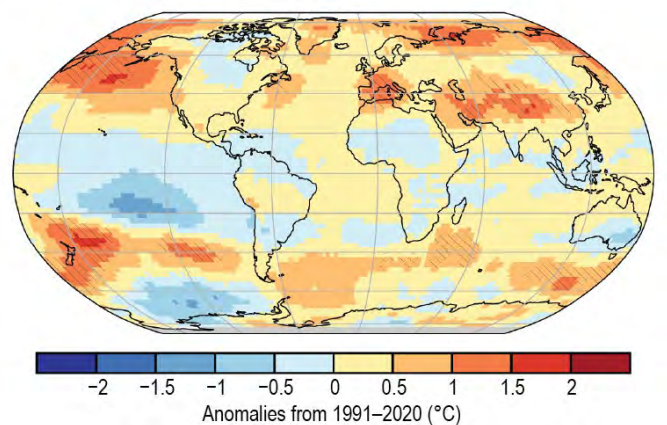
(d) Warm Days



(e) Cool Nights



(f) Lower Tropospheric Temperature



(g) Surface Specific Humidity

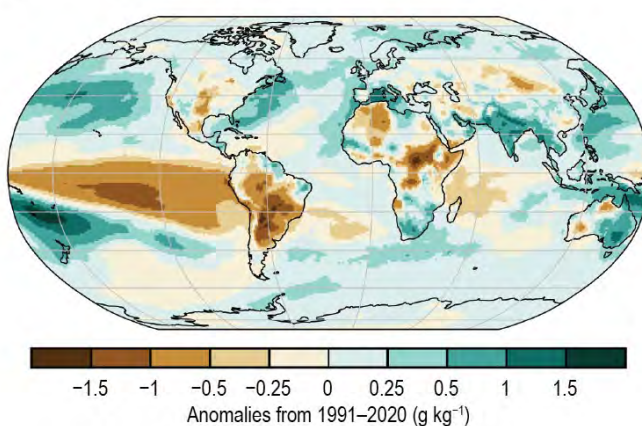
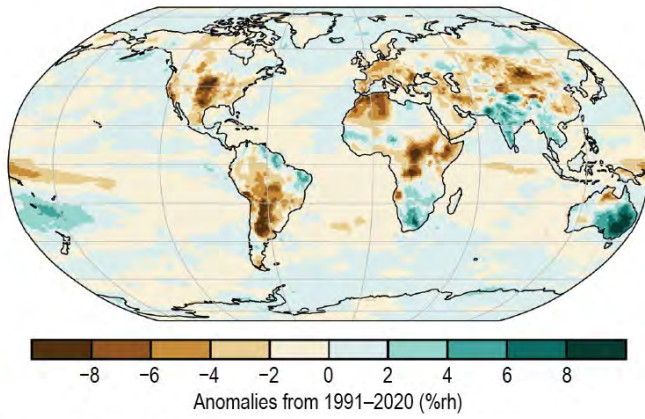
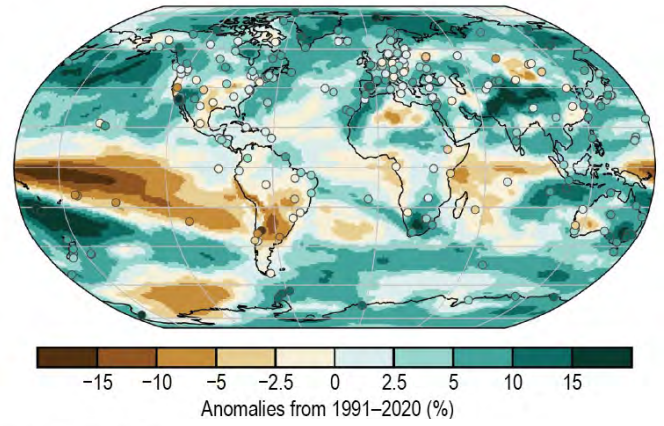


Plate 2.1. (a) NOAA NCEI Global land and ocean surface annual temperature anomalies (°C); (b) Satellite-derived lake surface water temperature anomalies, from ESA CCI LAKES/Copernicus C3S (°C); (c) CLASSmat night marine air temperature annual average anomalies (°C); (d) ERA5 warm day threshold exceedance (TX90p); (e) ERA5 cool night threshold exceedance (TN10p); (f) Average of RSS and UAH lower-tropospheric temperature anomalies (°C). Hatching denotes regions in which 2022 was the warmest year on record; (g) ERA5 surface specific humidity anomalies (g kg⁻¹);

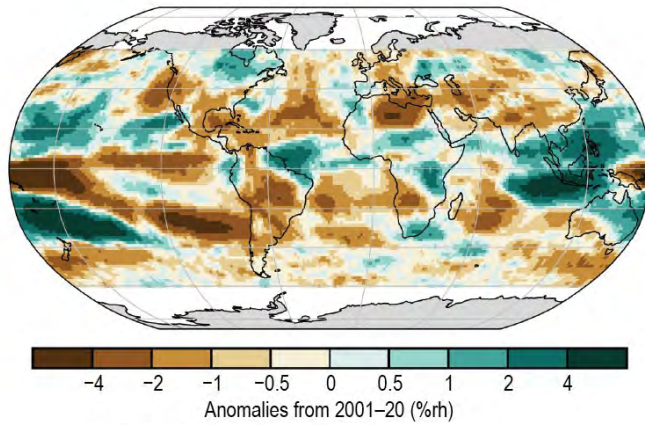
(h) Surface Relative Humidity



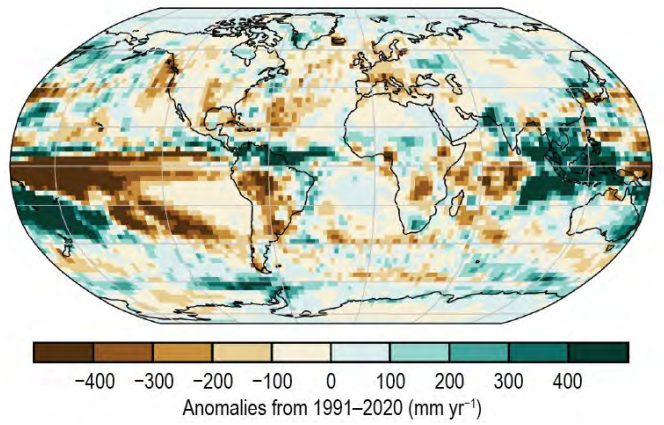
(i) Total Column Water Vapor



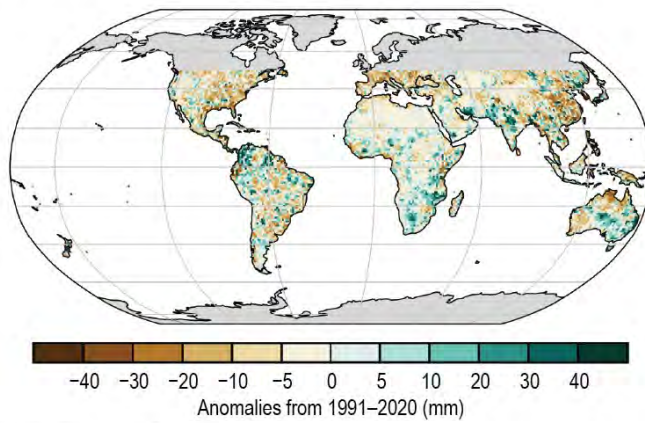
(j) Upper Tropospheric Humidity



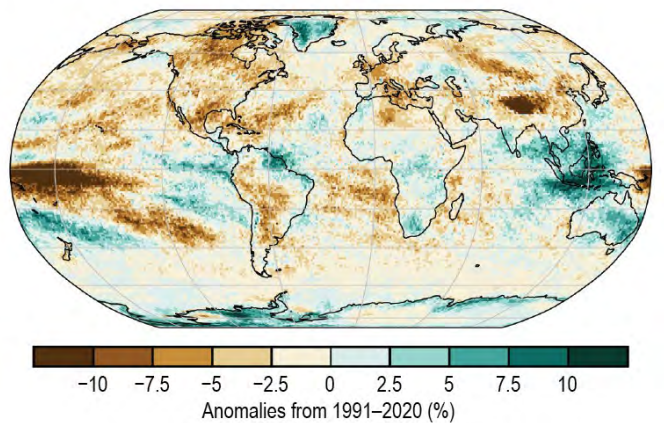
(k) Precipitation



(l) Maximum 1 Day Precipitation Amount



(m) Cloudiness



(n) Lake Water Level

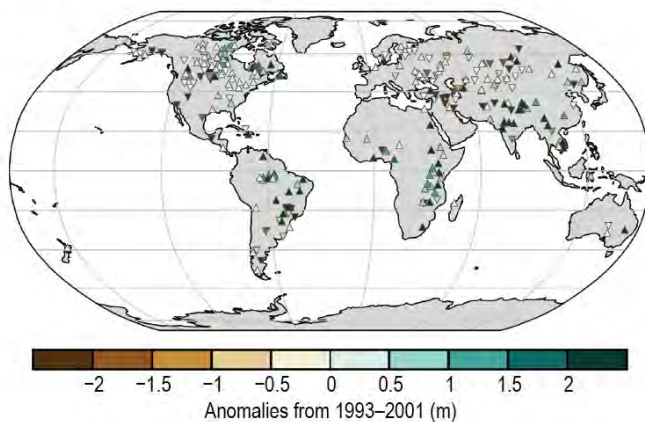
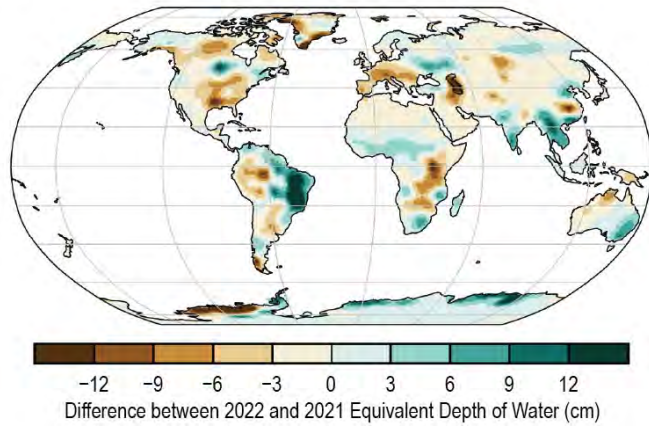
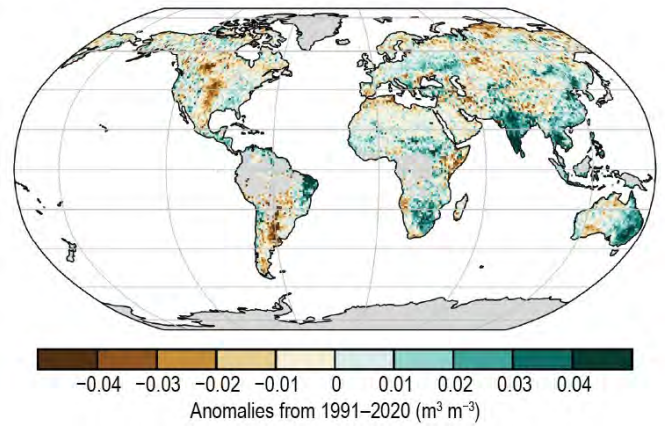


Plate 2.1 (cont.) (h) ERA5 surface relative humidity anomalies (%rh); (i) ERA5 TCWV anomalies (%). Data from GNSS stations are plotted as filled circles; (j) Annual microwave-based UTH anomalies (%rh); (k) GPCP v2.3 annual mean precipitation anomalies (mm yr⁻¹); (l) CHIRPS maximum 1-day (Rx1day) annual precipitation anomalies (mm); (m) PATMOS-x 6.0 cloud fraction annual anomalies (%); (n) G_REALM lake water level anomalies. Triangles pointing upward indicate positive anomalies, and triangles pointing down indicate negative anomalies;

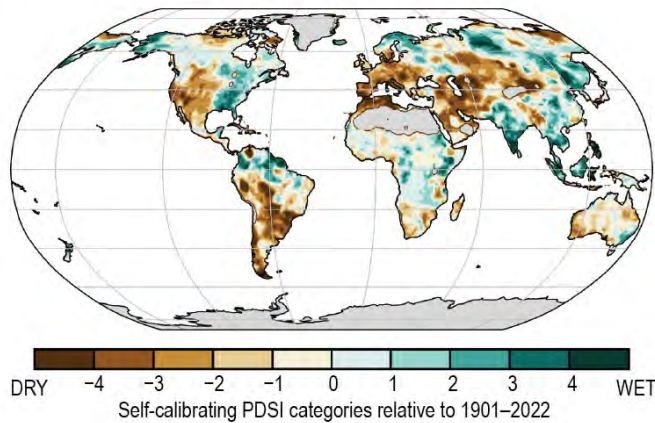
(o) Terrestrial Water Storage



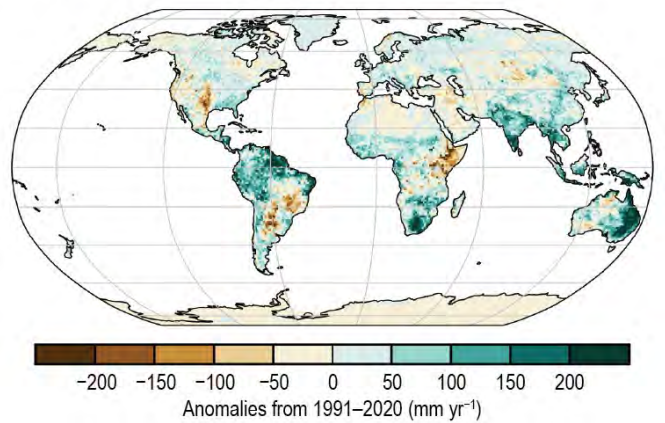
(p) Soil Moisture



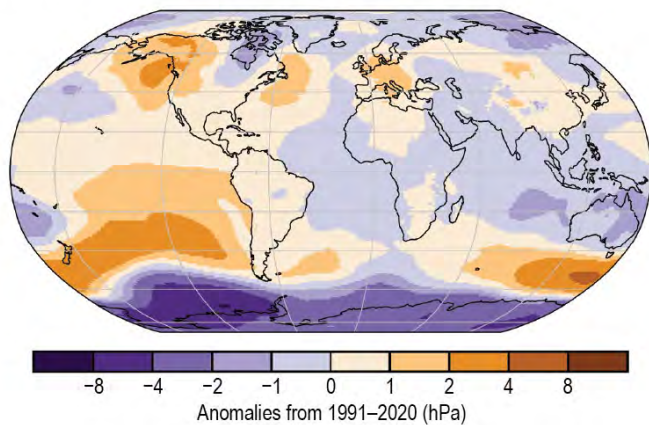
(q) Drought



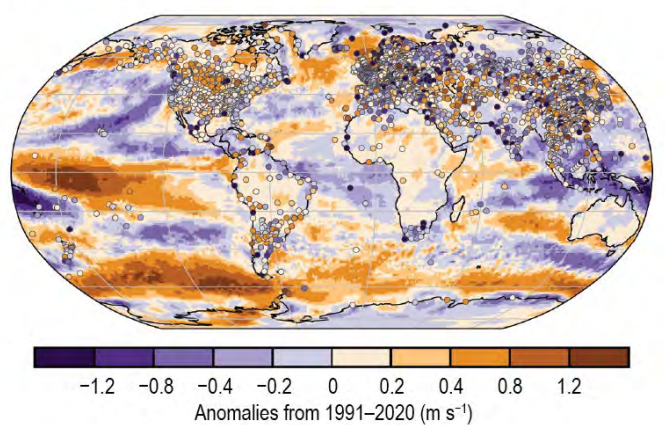
(r) Land Evaporation



(s) Sea Level Pressure



(t) Surface Winds



(u) Upper Air (850-hPa) Eastward Winds

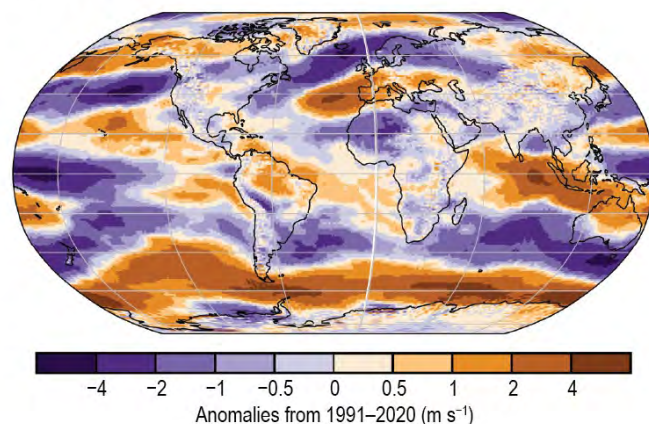
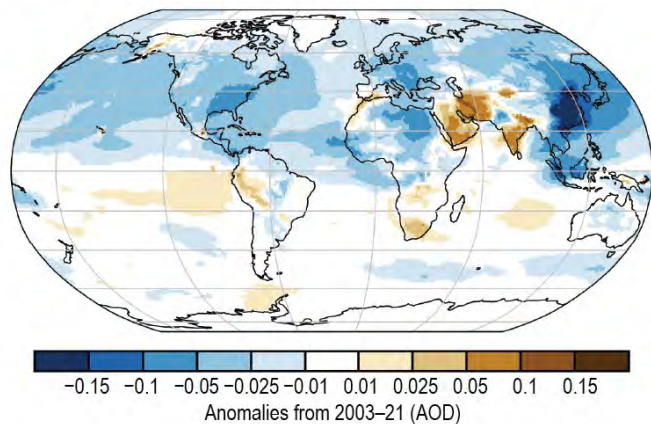
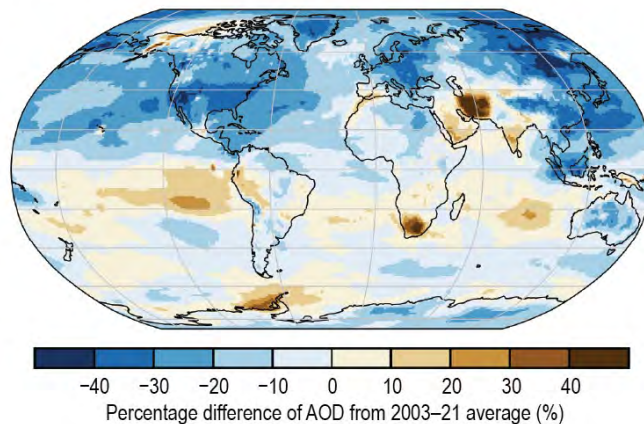


Plate 2.1 (cont.) (o) GRACE and GRACE-FO difference in annual-mean terrestrial water storage between 2020 and 2021 (cm); (p) C3S average surface soil moisture anomalies ($\text{m}^3 \text{m}^{-3}$). Data are masked where no retrieval is possible or where the quality is not assured and flagged, for example due to dense vegetation, frozen soil, or radio frequency interference; (q) Mean scPDSI for 2021. Droughts are indicated by negative values (brown), wet episodes by positive values (green); (r) GLEAM land evaporation anomalies (mm yr^{-1}); (s) ERA5 mean sea-level pressure anomalies (hPa); (t) Surface wind speed anomalies (m s^{-1}) from the observational HadISD3 dataset (land, circles), the ERA5 reanalysis output (land, shaded areas), and RSS satellite observations (ocean, shaded areas); (u) ERA5 850-hPa eastward wind speed anomalies (m s^{-1});

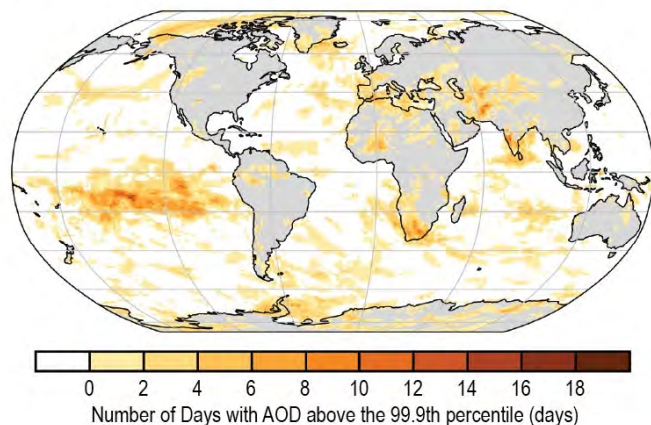
(v) Total Aerosol



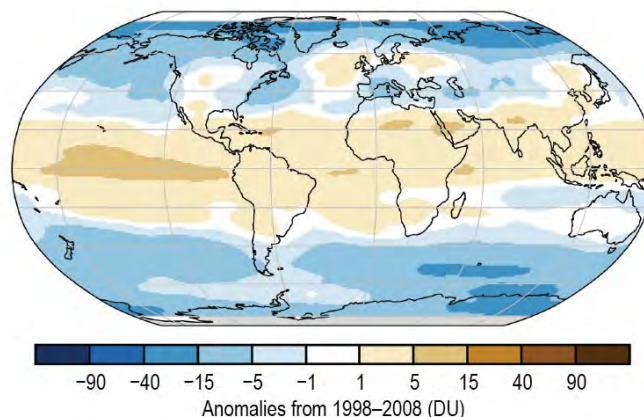
(w) AOD Percentage Anomaly



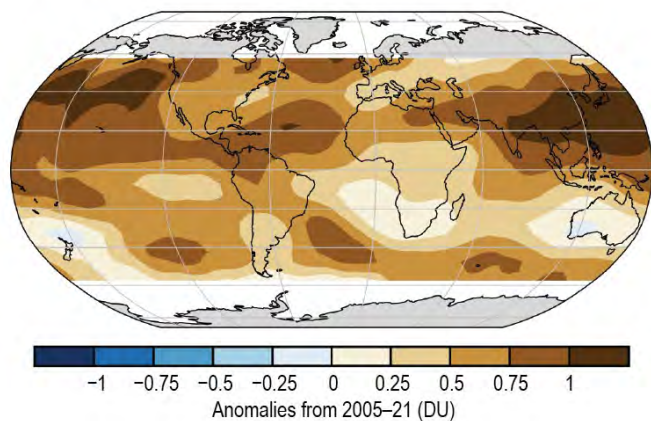
(x) Extreme Aerosol Days



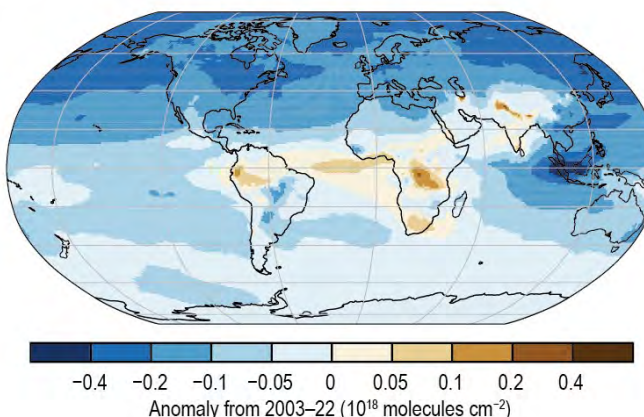
(y) Stratospheric (Total Column) Ozone



(z) OMI/MLS Tropospheric Column Ozone



(aa) Carbon Monoxide



(ab) Land Surface Albedo in the Visible

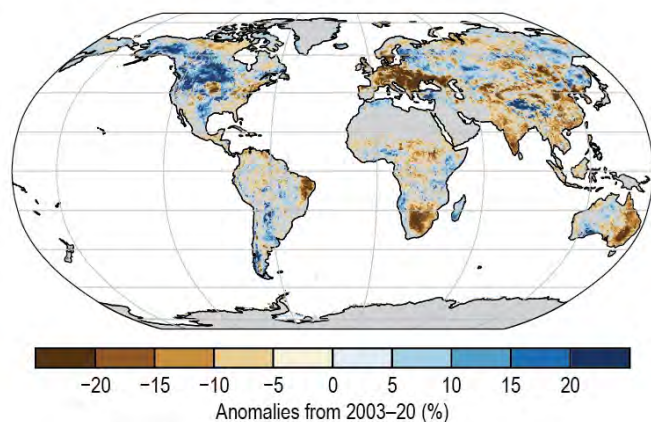
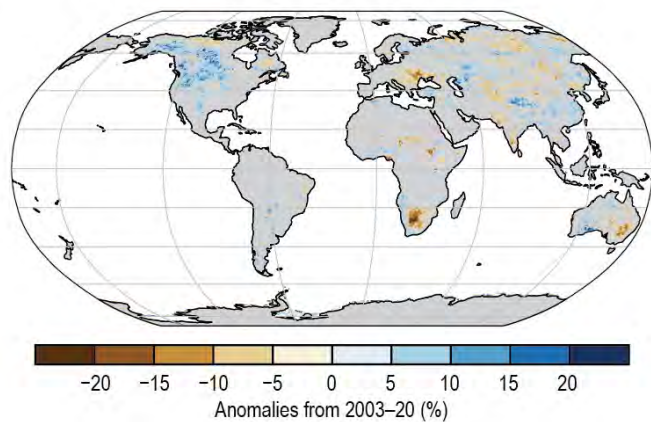
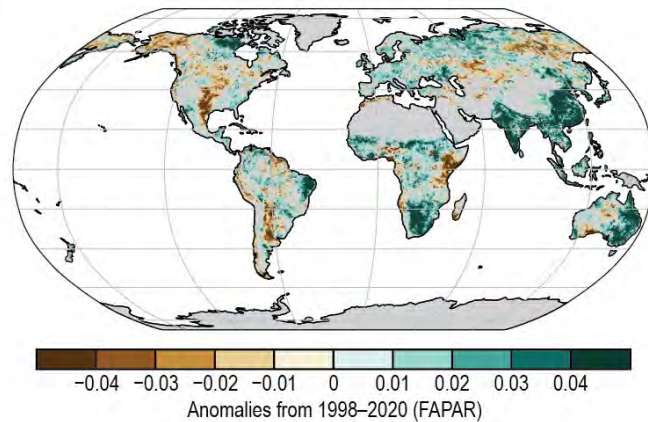


Plate 2.1 (cont.) (v) Total aerosol optical depth (AOD) anomalies at 550 nm; (w) Percent difference of total AOD at 550 nm in 2022 relative to 2003–21; (x) Number of days with AOD above the 99.9th percentile. Areas with zero days appear as the white/gray background; (y) TROPOMI aboard Sentinel-5 Precursor (S5P) measurements of total column ozone anomalies relative to the 1998–2008 mean from GSG merged dataset (DU); (z) OMI /MLS tropospheric ozone column anomalies for 60°S–60°N (DU); (aa) CAMS reanalysis total column CO anomalies ($\times 10^{18}$ molecules cm^{-2}); (ab) Land surface visible broadband albedo anomalies (%);

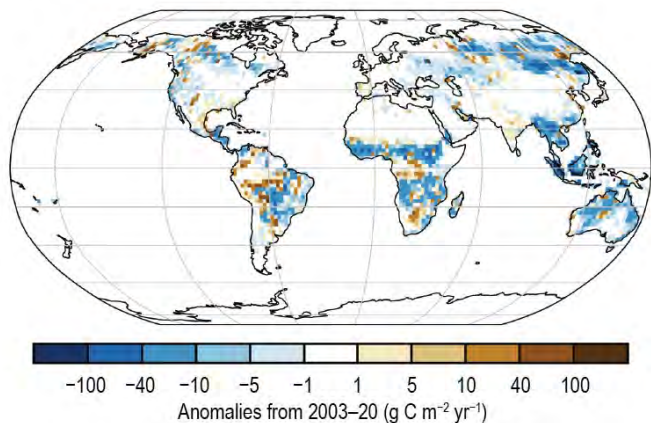
(ac) Land Surface Albedo in the Near-Infrared



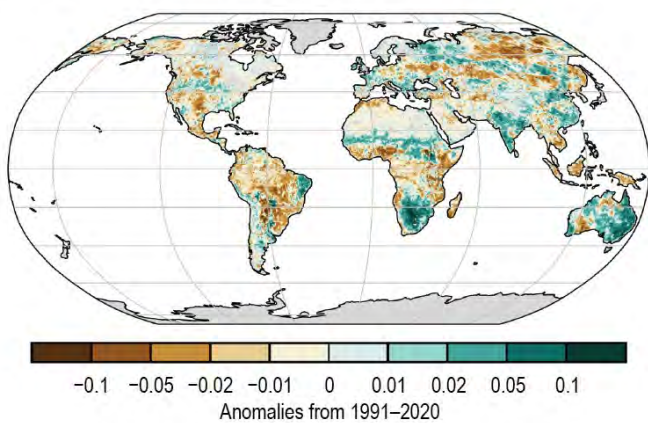
(ad) Fraction of Absorbed Photosynthetically Active Radiation



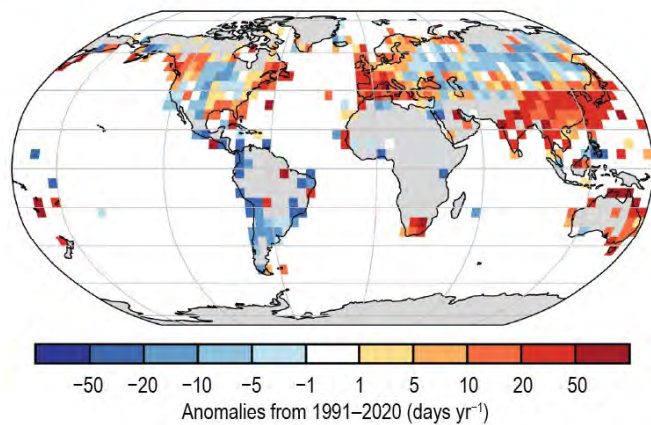
(ae) Carbon Emissions from Biomass Burning



(af) Vegetation Optical Depth



(ag) Humid-heat days (TwX90p)



(ah) Maximum T_{wet}

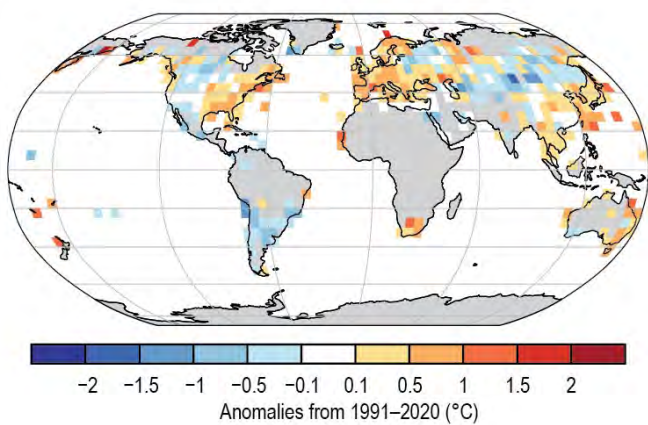


Plate 2.1 (cont.) (ac) Land surface near-infrared albedo anomalies (%); (ad) FAPAR anomalies; (ae) GFASv1.4 carbonaceous emission anomalies ($\text{g C m}^{-2} \text{ yr}^{-1}$) from biomass burning; (af) VODCA Ku-band VOD anomalies; (ag) HadISDH extremes daily maximum wet bulb temperature 90th percentile exceedances (days yr^{-1}); (ah) HadISDH extremes annual mean anomaly in daily maximum wet bulb of the month ($^{\circ}\text{C}$).

b. Temperature

1. GLOBAL SURFACE TEMPERATURE

—A. Sánchez-Lugo, C. Morice, J. P. Nicolas, A. Arguez, F. Sezaki, A. Goto, and W. Rocha

The year 2022 secured its place as one of the 10 warmest years since global records began (in the mid-1800s to mid-1900s, with the length of record depending on the dataset), with a global surface temperature between 0.25° and 0.30°C above the 1991–2020 average, according to six global temperature datasets (Table 2.1). Depending on the dataset, 2022 was either the fifth-warmest (equal with 2015 in some datasets) or sixth-warmest year on record. Despite these minor differences in anomalies and ranks between datasets, all six datasets agree that the last eight years (2015–22) were the eight warmest years on record (Fig. 2.1), and the global trends at the short- (1980–2022) and long-term (1880–2022) periods for each dataset are consistent with each other. The annual global average surface temperature has increased at an average rate of 0.08°C decade⁻¹ to 0.09°C decade⁻¹ since 1880 and at a rate more than twice that since 1980 (0.19°C decade⁻¹ to 0.20°C decade⁻¹). The datasets consist of four global in situ surface temperature analyses (NASA GISS Surface Temperature Analysis version 4 [NASA-GISSTEMP v4], Lenssen et al. 2019; Hadley Centre/Climatic Research Unit Temperature version 5 [HadCRUT5], Morice et al. 2021; NOAA Merged Land Ocean Global Surface Temperature Analysis version 5.1.0 [NOAAGlobalTemp v5.1.0], Vose et al. 2021; Berkeley Earth, Rhode and Hausfather 2020) and two global atmospheric reanalyses (European Centre for Medium-Range Weather Forecasts Reanalysis version 5 [ERA5], Hersbach et al. 2020, Bell et al. 2021; Japanese 55-year Reanalysis [JRA-55], Kobayashi et al. 2015).

Even though 2022 ranked as one of the six warmest years on record, the presence of

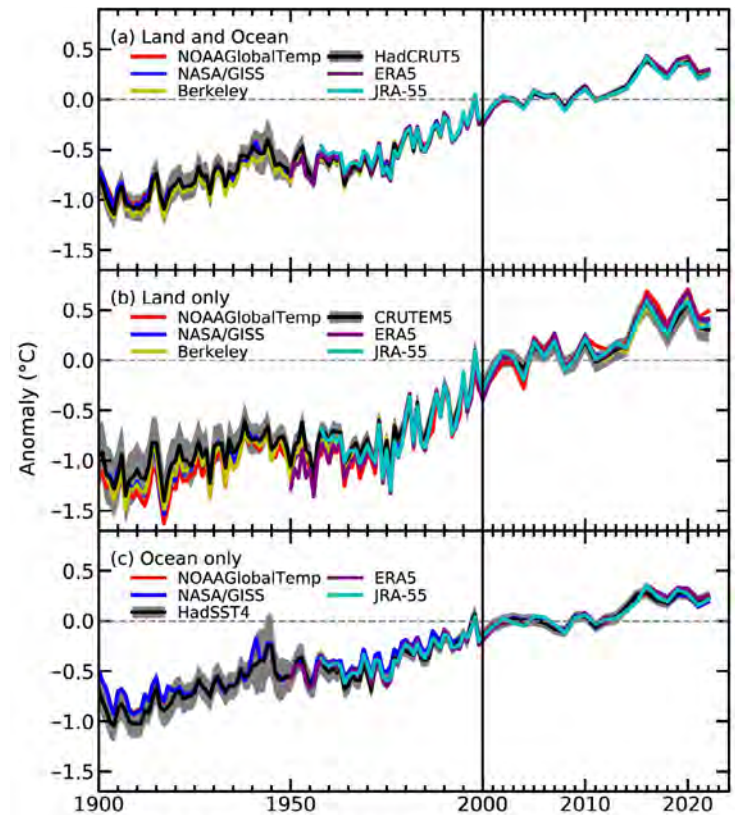


Fig. 2.1. Global average surface air temperature anomalies (°C; 1991–2020 base period) for (a) land and ocean, (b) land only, and (c) ocean only. In situ estimates are shown from the datasets NOAA GlobalTemp (Vose et al. 2021), NASA-GISS (Lenssen et al. 2019), HadCRUT5 (Morice et al. 2021), CRUTEM5 (Osborn et al. 2021), HadSST4 (Kennedy et al. 2019), and Berkeley (Rhode and Hausfather 2020). The 95% confidence ranges are also shown for HadCRUT5, CRUTEM5, and HadSST4. Reanalyses estimates are shown from the datasets ERA5 (Hersbach et al. 2020) and JRA-55 (Kobayashi et al. 2015).

Table 2.1. Temperature anomalies (°C; 1991–2020 base period) for 2022. Note that for the HadCRUT5 column, land values were computed using the CRUTEM.5.0.1.0 dataset (Osborn et al. 2021), ocean values were computed using the HadSST.4.0.1.0 dataset (Kennedy et al. 2019), and global land and ocean values used the HadCRUT.5.0.1.0 dataset (Morice et al. 2021).

Global	NASA-GISS	HadCRUT5	NOAA GlobalTemp	Berkeley Earth	ERA5	JRA-55
Land	+0.40	+0.30	+0.49	+0.34	+0.41	+0.34
Ocean	+0.19	+0.23	+0.19	–	+0.26	+0.22
Land and Ocean	+0.28	+0.26	+0.28	+0.27	+0.30	+0.25

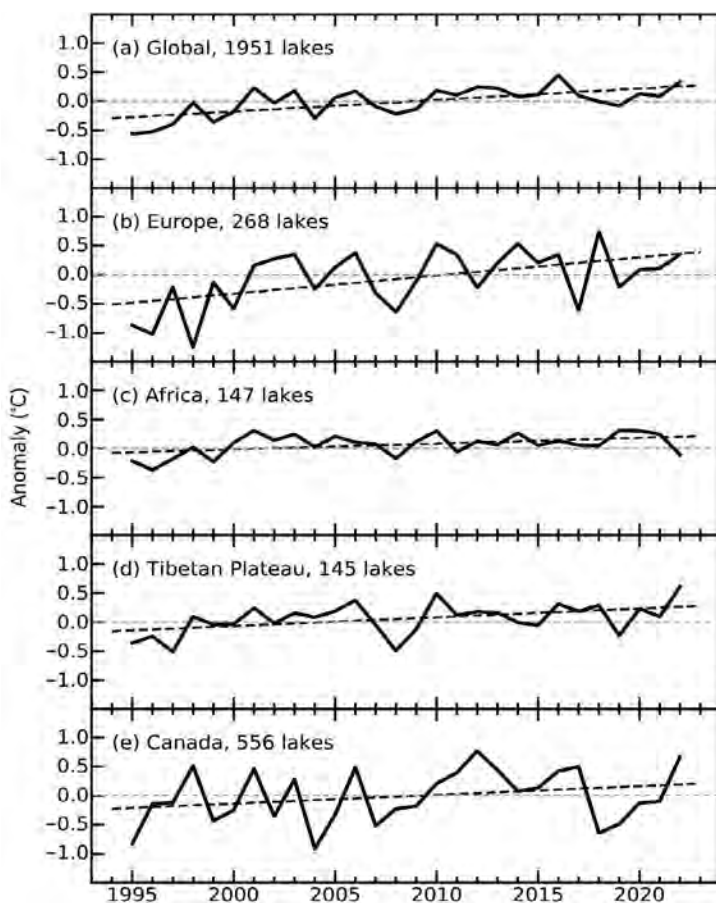
La Niña—the cool phase of the El Niño–Southern Oscillation (ENSO)—in the Pacific Ocean had a dampening effect on the global temperatures, in comparison to years characterized by El Niño or ENSO-neutral conditions. The year began with La Niña conditions, which first developed in August 2020 and persisted throughout most of 2021 and all of 2022 (see section 4b for details). 2022 was also the warmest La Niña year on record, surpassing the previous record set in 2021.

While it is common, and arguably expected, for each newly completed year to rank as a top 10 warmest year (see Arguez et al. 2020), the global annual temperature for 2022 was lower than we would expect due to the secular warming trend alone, with trend-adjusted anomalies registering between the 20th and 40th percentiles (depending on the dataset) following the Arguez et al. (2020) approach. Trend-adjusted anomalies for 2022 are consistent with the typical slight cooling influence of La Niña and similar to the trend-adjusted anomalies recorded over the relatively cool years from 2011 to 2014, as well as 2021, years that also predominantly exhibited cooler-than-normal ENSO index values.

Above-normal temperatures were observed across much of the world’s land and ocean surfaces during 2022 (Plate 2.1a; Appendix Figs. A2.1–A2.4). Notably, record-high annual temperatures were present across Europe, northern Africa, and parts of the Middle East, central Asia, and China, as well as the northern and southwestern Pacific, Atlantic, and Southern Oceans. Below-normal annual temperatures were present across parts of northern North America, South America, Africa, Australia, and the southeastern, central, and eastern tropical Pacific Ocean. The global land-only surface temperature was 0.30°C–0.49°C above normal, the fifth to seventh highest on record, depending on the dataset. The annual global sea-surface temperature was also fifth or sixth highest on record, at 0.19°C–0.26°C above normal.

2. LAKE SURFACE WATER TEMPERATURE

—L. Carrea, C. J. Merchant, J.-F. Creatux, T. M. Dokulil, H. A. Dugan, B. Gibbes, A. Laas, E. M. Leibensperger, S. Maberly, L. May, S.-I. Matsuzaki, G. Monet, D. Pierson, M. Pulkkanen, O. O. Rusanovskaya, S. V. Shimaraeva, E. A. Silow, M. Schmid, M. A. Timofeyev, P. Verburg, and R. I. Woolway



In 2022, the worldwide averaged satellite-derived lake surface water temperature (LSWT) warm-season anomaly was +0.33°C with respect to the 1995–2020 baseline, the second highest since the record began in 1995. The mean LSWT trend between 1995 and 2022 was $0.20 \pm 0.01^\circ\text{C decade}^{-1}$, broadly consistent with previous analyses (e.g., Carrea et al. 2020, 2021, 2022a; Fig. 2.2a). Warm-season anomalies for each lake are shown in Plate 2.1b. The lake-mean temperature anomalies were positive for 70% and negative for 30% of the 1951 globally distributed lakes. For about 30 other lakes, no anomalies could be computed since no water was found in 2022.

Large regions of coherently high LSWT anomalies were identified in 2022, with 40% of the observed lakes experiencing LSWT

Fig. 2.2. Annual time series of satellite-derived warm-season lake surface water temperature anomalies (°C; 1995–2020 base period) from 1995 to 2022 for lakes distributed (a) globally, and regionally in (b) Europe, (c) Africa, (d) the Tibetan Plateau, and (e) Canada.

anomalies in excess of +0.5°C (Plate 2.1b). The highest anomalies were for lakes situated in the northwestern contiguous United States and Canada. Negative LSWT anomalies were consistently observed throughout most of South America (except Patagonia), parts of Africa, and in Alaska and Greenland.

Four regions of interest were studied in more detail: Canada (number of lakes, $n = 556$, Figs. 2.2e, 2.3c), Europe ($n = 268$, Figs. 2.2b, 2.3a), Tibet ($n = 145$, Figs. 2.2d, 2.3d), and Africa ($n = 147$, Figs. 2.2c, 2.3b). In these regions, the warm season LSWT anomalies are consistent with the corresponding 2-m air temperature anomalies, as measured by NASA GISS (Hansen et al. 2010; GISS Surface Temperature Analysis [GISTEMP] Team 2022) and show an average warming trend of $+0.31 \pm 0.03^\circ\text{C decade}^{-1}$ in Europe (Fig. 2.2b) and $+0.15 \pm 0.03^\circ\text{C decade}^{-1}$ in Canada (Fig. 2.2e). In Africa, long-term change in LSWT is comparatively smaller at $+0.10 \pm 0.01^\circ\text{C decade}^{-1}$ (Fig. 2.2c), while in Tibet the warming tendency has increased relative to previous reports with the largest positive anomaly in 2022. The warming rate of LSWT in Tibet from 1995 to 2022 was $+0.15 \pm 0.02^\circ\text{C decade}^{-1}$ (Fig. 2.2d). Moreover, in Tibet, all the observed lakes, except one, experienced positive LSWT anomalies in 2022 with an average of $+0.6^\circ\text{C}$, which is more than double the standard deviation of mean anomalies from 1995 to 2022 and confirmed by high anomalies for the air temperature (Fig. 2.3d). In Europe, below-normal LSWT in northern Europe (80 lakes) was less prevalent than above-normal LSWT (188 lakes), resulting in an average of $+0.35^\circ\text{C}$. In Africa, 60% of the 147 lakes experienced negative LSWT anomalies, and the average anomaly in 2022 was -0.11°C . In Canada, 91% of the observed lakes experienced positive anomalies, with only 9% experiencing negative anomalies for an average of $+0.67^\circ\text{C}$ in 2022.

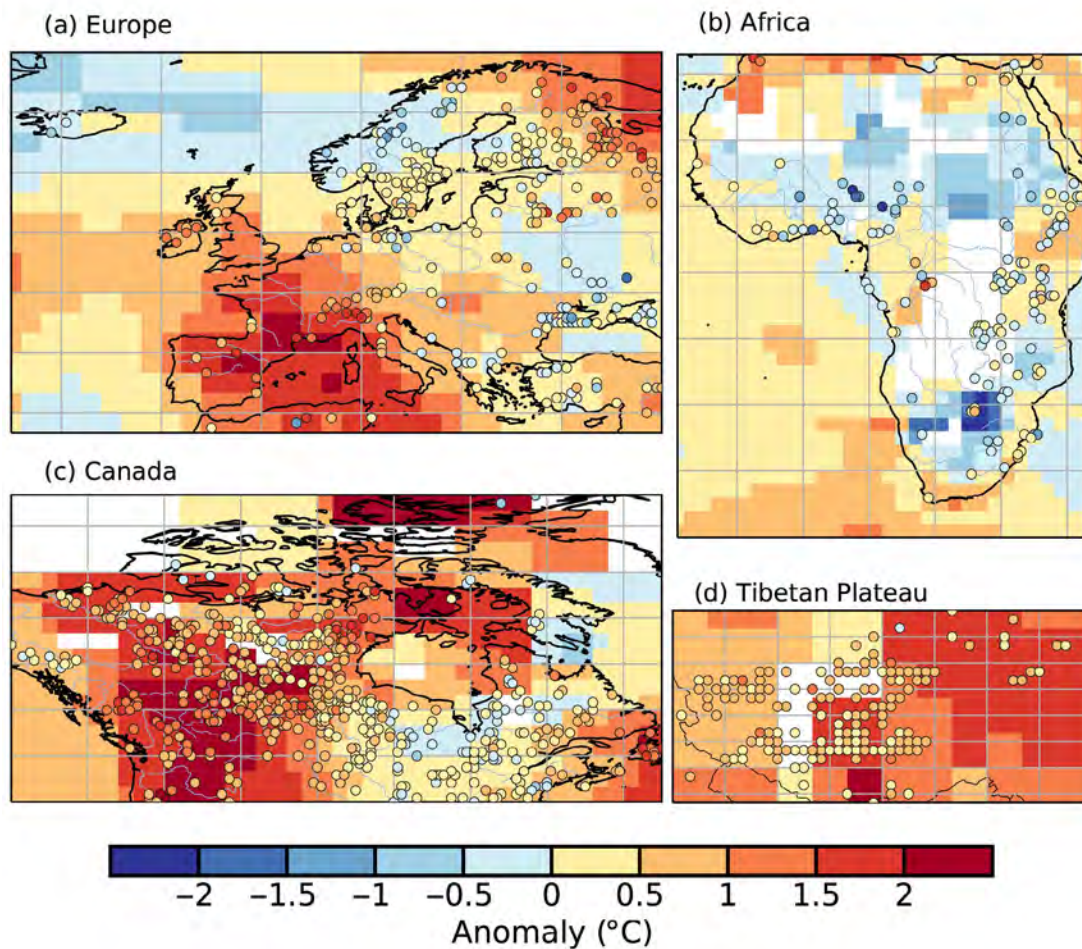


Fig. 2.3. Lake temperature anomalies ($^\circ\text{C}$, colored dots) and 2-m air temperature anomalies ($^\circ\text{C}$) in 2022 for lakes in (a) Europe, (b) Africa, (c) Canada, and (d) the Tibetan Plateau. These values were calculated for the warm season (Jul–Sep in the extratropical Northern Hemisphere; Jan–Mar in the extratropical Southern Hemisphere; Jan–Dec in the tropics) with reference to the 1995–2020 base period.

In situ observations of warm season LSWT anomalies from the 1995–2020 mean for 40 lakes, 18 of which have measurements for the year 2022, are shown in Fig. 2.4 with an average anomaly of -0.03°C . Fourteen lakes experienced positive anomalies (average: $+0.70^{\circ}\text{C}$) and four lakes negative anomalies (average: -2.60°C) in 2022. At the in situ measurement site on Lake Baikal in Siberia, a temperature anomaly of -6.9°C was recorded, which is very different from the satellite lake-mean anomaly of -0.47°C , suggesting a within-lake variation of the LSWT anomalies (see Carrea et al. 2022a; Toffolon et al. 2020) on Lake Baikal. At the in situ site, such a large negative anomaly suggests a potential intrusion of colder water resembling upwellings in ocean waters; this has been recorded on the lake for more than 20 years at different depths. Overall, the time series of the 18 lakes show clearly that lakes are warming, especially after the year 2000.

In North America, the anomalies recorded from the in situ data for Lakes Superior, Erie, Michigan, and Huron are -2.98°C , $+0.67^{\circ}\text{C}$, $+0.69^{\circ}\text{C}$, and $+0.55^{\circ}\text{C}$, respectively, which are noticeably larger (in absolute terms) than those estimated from satellite measurements (-0.61°C , $+0.20^{\circ}\text{C}$, $+0.28^{\circ}\text{C}$, and $+0.18^{\circ}\text{C}$, respectively). The difference is largely because in situ data are point measurements whereas satellite data represent lake-wide averages, suggesting spatial patterns of the LSWT anomalies (see Carrea et al. 2022a; Toffolon et al. 2020). In Europe, all the lakes with in situ data had positive anomalies, except Lake Balaton (Hungary) which was 0.36°C below its 1995–2020 average (-0.01°C with satellite). Mondsee (Austria) was 1.51°C warmer than average in 2022 and the highest recorded value for the in situ data. In New Zealand, Lake Taupō had a slight negative anomaly of -0.15°C ($+0.98^{\circ}\text{C}$ from satellites) while Rotorua had a positive anomaly of $+0.51^{\circ}\text{C}$ (with reference period 2011–2020) compared to the anomaly from satellite of $+0.6^{\circ}\text{C}$ (with reference period 1995–2020).

The LSWT warm-season averages for midlatitude lakes are computed for summers (July–September in the Northern Hemisphere and January–March in the Southern Hemisphere), and whole-year averages are presented for tropical lakes (within 23.5° of the equator).

LSWT time series were derived from the European Space Agency Climate Change Initiative LAKES/Copernicus C3S climate data record (Carrea et al. 2022b, 2023). For 2022, satellite observation from the Sea and Land Surface Temperature Radiometer on Sentinel3B and MODIS on *Terra* were used. The retrieval method of MacCallum and Merchant (2012) was applied on image pixels filled with water according to both the inland water dataset of Carrea et al. (2015) and a reflectance-based water detection scheme (Carrea et al. 2023).

The satellite-derived LSWT data are spatial averages for each of a total of 1951 lakes. The satellite-derived LSWT data were validated with in situ measurements with an average satellite-minus-in situ temperature difference of less than 0.5°C (Carrea et al. 2023). Lake-wide average surface temperatures have been shown to give a more representative picture of LSWT responses to climate change than single-point measurements (Woolway and Merchant 2018).

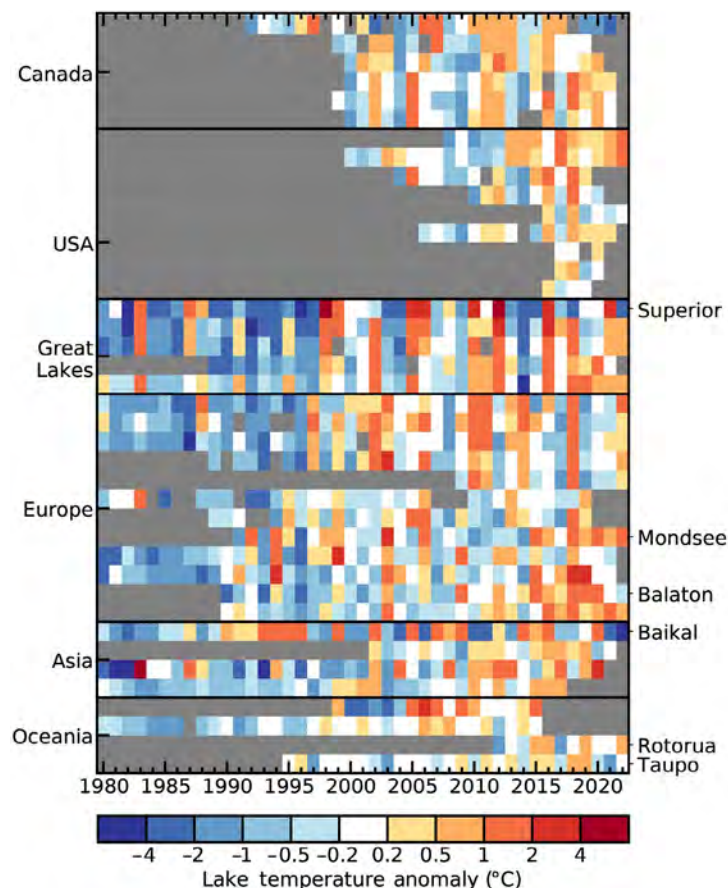


Fig. 2.4. In situ lake surface water temperature (LSWT) observations from 40 globally distributed lakes (the name is reported for the lakes mentioned in the text), showing the annually averaged warm season (Jul–Sep in the Northern Hemisphere; Jan–Mar in the Southern Hemisphere) anomalies ($^{\circ}\text{C}$; 1995–2020 base period).

3. NIGHT MARINE AIR TEMPERATURE

—R. C. Cornes, T. Cropper, R. Junod, and E. C. Kent

Air temperature measurements have been made onboard ships for centuries and continue to be collected today thanks to the Voluntary Observing Ship initiative (<https://www.ocean-ops.org/reportcard2022/>). Gridded datasets of marine air temperature (MAT) are constructed from the individual measurements, and two such datasets that are routinely updated are used in this section: University of Alabama in Huntsville night-time MAT (UAHNMAT; Junod and Christy 2020) and Climate Linked Atlantic Sector Science night MAT (CLASSnmat; Cornes et al. 2020). Since daytime MAT observations are biased warm due to heating from the ship superstructure, only night-time values are currently used in these datasets and, hence, they are referred to as night marine air temperature (NMAT). These NMAT datasets provide comparison against the more widely used sea-surface temperature (SST) datasets. In keeping with this theme, we also include SST statistics from The Met Office Hadley Centre's sea-surface temperature dataset (HadSST4; Kennedy et al. 2019) in this section. Note, however, that the large-scale average values from HadSST4 presented in this section (Fig. 2.5 and Table 2.2) may differ slightly from other estimates from the dataset presented in this report because the data have been masked such that the spatial coverage is the same across the three datasets in order to ensure a fair comparison.

Evidence from the NMAT datasets and HadSST4 indicates that across global ocean regions, 2022 was the fifth-warmest year since 1900 (Table 2.2). As with the global estimates of temperature discussed in section 2b1, the “triple-dip” La Niña conditions (see Sidebar 3.1 for details) suppressed

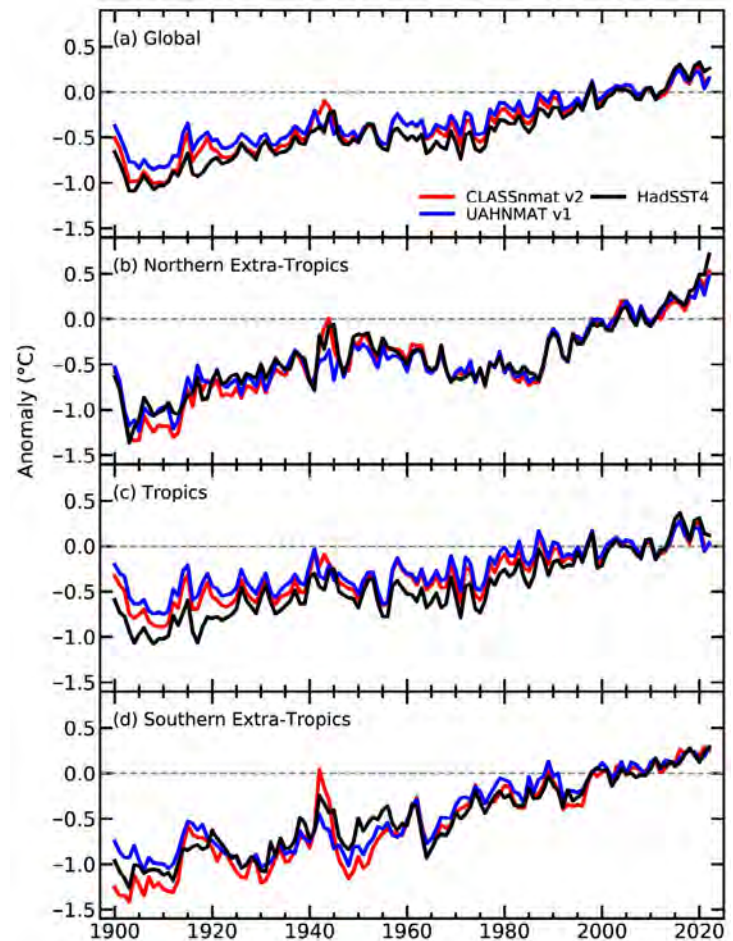


Fig. 2.5. Annual mean night marine air and sea-surface temperature anomalies (°C; 1991–2020 base period) calculated from the CLASSnmat, UAHNMAT, and HadSST4 datasets averaged over the (a) globe, (b) northern extra-tropics, (c) tropics, and (d) southern extra-tropics. The tropics is defined as the latitude range 30°S–30°N and the northern (southern) extra-tropics as >30°N (<30°S). The averages only include values that are common to all three datasets for a given year and since UAHNMAT starts in 1900, only values for the period 1900–2022 are plotted.

Table 2.2. Average anomalies (°C; 1991–2020 base period) for 2022 calculated from two NMAT datasets (CLASSnmat and UAHNMAT) and HadSST4. The regions are defined as in Fig. 2.5. The values in parentheses indicate the ranking of 2022 values within the period 1900–2022.

Dataset	Global	Northern Extra-Tropics	Tropics	Southern Extra-Tropics
CLASSnmat	0.16 (5)	0.52 (1)	0.03 (16)	0.25 (3)
UAHNMAT	0.15 (5)	0.47 (1)	0.03 (20)	0.28 (1)
HadSST4	0.26 (5)	0.71 (1)	0.12 (8)	0.29 (1)

the global average NMAT values during the year. This feature is apparent in the maps of temperature anomalies (Fig. 2.6) and is reflected in the average anomalies for the tropics, where 2022 ranked as only the 16th- or 20th-warmest year on record (Table 2.2).

Across the northern extra-tropics (north of 30°N), 2022 was the warmest year in the 123-year record according to all three datasets. Monthly anomalies were more than 0.3°C above the 1991–2020 average throughout all months of the year, with particularly large anomalies greater than +0.7°C recorded from August to November. The annual average anomaly was greatest in HadSST4 (+0.7°C) compared to the NMAT datasets where it was approximately +0.5°C. The highest positive temperature anomalies in this region were recorded across the northern Pacific Ocean (Fig. 2.6). Across all datasets, relatively high anomalies were also recorded in the north-east Atlantic Ocean, particularly in the seas around western Europe and the Mediterranean, and across the western boundary current region of the North Atlantic.

Across the southern extra-tropics, NMAT anomalies were also high in 2022, with relatively high anomalies recorded in the western South Pacific/Coral Sea region. For CLASSnmat, the year ranked as third warmest for the region whereas both UAHNMAT and HadSST4 ranked 2022 as the warmest year in the series. Due to the incorporation of drifting buoy data in HadSST4, the spatial coverage is generally better than for the NMAT datasets, which only use ship-based measurements of air temperature, and this is most apparent across the Southern Ocean. This sparser coverage results in a greater uncertainty in the NMAT datasets in this region.

In previous *State of the Climate* reports (e.g., Cornes et al. 2022), the discrepancy in trends between the NMAT and SST datasets has been discussed. While the global average trend between 1900 and 2022 is slightly higher in HadSST4 compared to the NMAT datasets (c.f. 0.09°C decade⁻¹ in UAHNMAT and 0.11°C decade⁻¹ in CLASSnmat compared to 0.16°C decade⁻¹ in HadSST4) there is a much larger discrepancy in temperature trends between SST and NMAT after around 1990. This is particularly the case in the tropics where temperature increased at a rate of 0.05°C decade⁻¹ or 0.07°C decade⁻¹ in NMAT compared to 0.13°C decade⁻¹ in HadSST4. The reason for this discrepancy remains unclear and a wider discussion of this feature of the data, which also considers trends in Coupled Model Intercomparison Project (CMIP) simulations, is provided by Cross-chapter box 2.3 in Gulev et al. (2021).

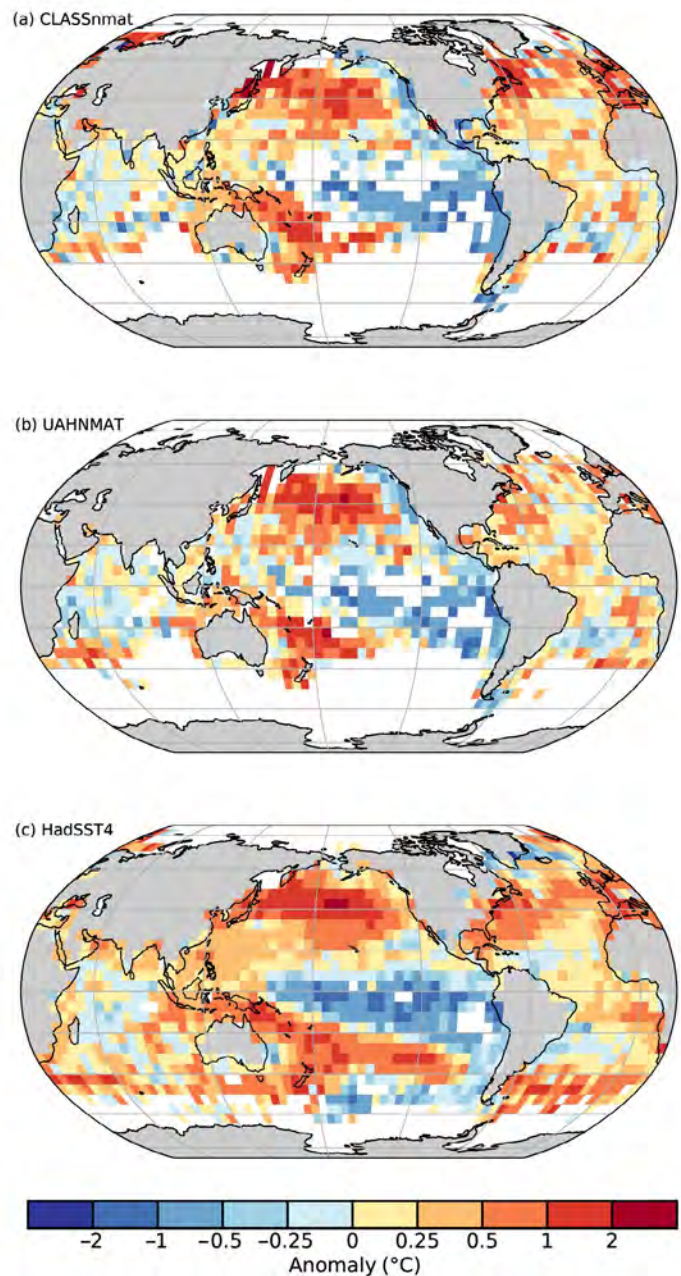


Fig. 2.6. Average annual night marine air and sea-surface anomalies (°C; 1991–2020 base period) for 2022 in the (a) CLASSnmat, (b) UAHNMAT, and (c) HadSST4 datasets. Averages were calculated for a grid-cell where more than six months of data are present. This calculation has been done separately for each dataset and results in a different spatial coverage in the three datasets.

4. SURFACE TEMPERATURE EXTREMES

—M. G. Donat, R. J. H. Dunn, R. W. Schlegel, and A. Kruger

In 2022, the globally averaged frequency of warm days (TX90p; see Table 2.3 for the definition) in reanalyses products was about 49 (ERA5, Hersbach et al. 2020), 40 (MERRA-2, Gelaro et al. 2017) and 44 (JRA-55, Kobayashi et al. 2015), and 66 based on observational data from the Global Historical Climatology Network Index (GHCNDEX; which has more limited spatial coverage and uses a different reference period; Donat et al. 2013), slightly lower than in the previous year (Fig. 2.7). While the global average warm-day frequency in 2022 cannot be regarded as extraordinary compared to previous years, the frequencies are substantially above the average value of 36 days per year (Fig 2.7).

Large areas of the globe were affected by strong, and in some places record-breaking hot extremes in 2022. In particular, large parts of Europe, Asia, and South America were affected by anomalously frequent warm days (in many areas, more than double the average frequency; Plate 2.1d). The frequency of warm days was highest on record in large parts of China and Western and southwestern Europe (and northwestern Africa, for ERA5; Fig. 2.8; Supp. Fig. A2.5b). This high frequency of warm days was accompanied by heat events of record-breaking intensity. Large parts of China, Central Asia, and Central and Western Europe show the highest TXx values (annual maximum of daily maximum temperatures) in the GHCNDEX record (Supp. Fig. A2.5a). These extreme

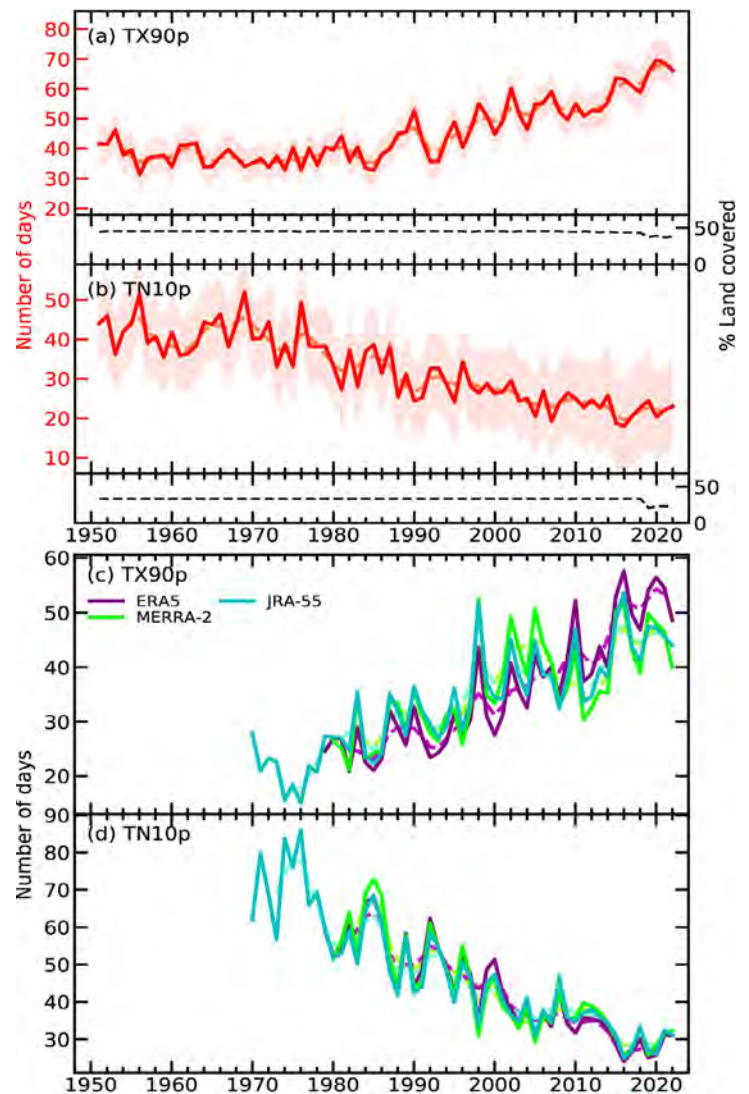


Fig. 2.7. Time series of the annual number of (a),(c) warm days and (b),(d) cool nights averaged over global land regions based on gridded station data from the GHCNDEX dataset (a),(b) and three atmospheric reanalyses (ERA5, MERRA-2, JRA-55; (c),(d)). The spatial coverage in GHCNDEX is limited; the black dotted lines show the percentage of land area covered (right y-axis in (a),(b)), and the coverage uncertainty ($2\text{-}\sigma$, following Brohan et al. 2006, Dunn et al. 2020) is shown as the light red bands in (a),(b).

Table 2.3. Definitions of temperature extremes indices, along with 2022 value and ranks from the four datasets. Reference period for GHCNDEX (1961–90) is different to that used for the reanalyses products (1991–2020).

Index	Name	Definition	GHCNDEX (1951–2022) Value, Rank	ERA5 (1979–2022) Value, Rank	MERRA-2 (1980–2022) Value, Rank	JRA-55 (1970–2022) Value, Rank
TX90p	Warm days	The annual count of days when the daily maximum temperature exceeds the 90th percentile	66.2 days, 3rd highest	48.6 days, 8th highest	40.0 days, 14th highest	44.0 days, 10th highest
TN10p	Cool nights	The annual count of nights when the daily minimum temperature falls below the 10th percentile	23.0 days, 11th lowest	31.1 days, 8th lowest	32.3 days, 9th lowest	31.2 days, 6th lowest
TXx	Hottest Day	Annual highest value of daily maximum temperature	–	–	–	–

temperature values include the first-ever occurrence of temperatures exceeding 40°C in the United Kingdom and other parts of northwestern Europe (see section 7f for more details). In contrast, likely due to the persisting La Niña conditions, southeastern Australia recorded its lowest TXx values in 2022 in the ERA5 and GHCNDEX records (Fig. 2.8a and Supp. Fig. A2.6a, respectively).

The frequency of cool nights (TN10p; see definition in Table 2.3) was the eighth lowest on record for ERA5 and 16th lowest based on the GHCNDEX global average. Regions affected by an above-average frequency of cool nights, reflecting relatively low temperatures in general, include parts of Australia, South America, and northwestern North America (Plate 2.1e). Parts of South America had minimum night-time temperatures that were among the lowest on record based on ERA5 (Fig. 2.8c). In contrast, most other land regions showed below-average frequency of cold extremes (Plate 2.1e).

Analysis of NOAA Optimum Interpolation Sea Surface Temperature (NOAA OISST v2.1; Huang et al. 2021) showed that, in 2022, 58% of the ocean surface experienced at least one marine heatwave (MHW; Hobday et al. 2016; Figs. 2.9a,b), and 25% experienced at least one marine cold spell (MCS; Figs. 2.9c,d). Category 2 Strong MHWs (Hobday et al. 2018) were the most common (26%) warm events for the ninth consecutive year, whereas Category 1 Moderate MCSs have remained the most common (20%) cool events in all years since 1985. The ocean experienced a global average of 57 MHW days (18 MCS days) in 2022, which is greater than the 2021 average of 48 days (13 days), but less than the 2016 record of 61 days (1982 record of 27 days; Figs. 2.9a,c). This daily average equates to 16% (5%) of the surface of the ocean experiencing a MHW (MCS) on any given day (Figs. 2.9a,c).

Land surface temperature extremes are characterized by indices developed by the former World Meteorological Organization Expert Team in Climate Change Detection and Indices (Zhang et al. 2011). The observations-based GHCNDEX (Donat et al. 2013) uses daily maximum and minimum temperatures from the GHCND dataset (Menne et al. 2012) to calculate these indices for each station, which are then interpolated onto a regular 2.5° grid. Spatial coverage for 2022 is, as in previous years, limited to primarily the Northern

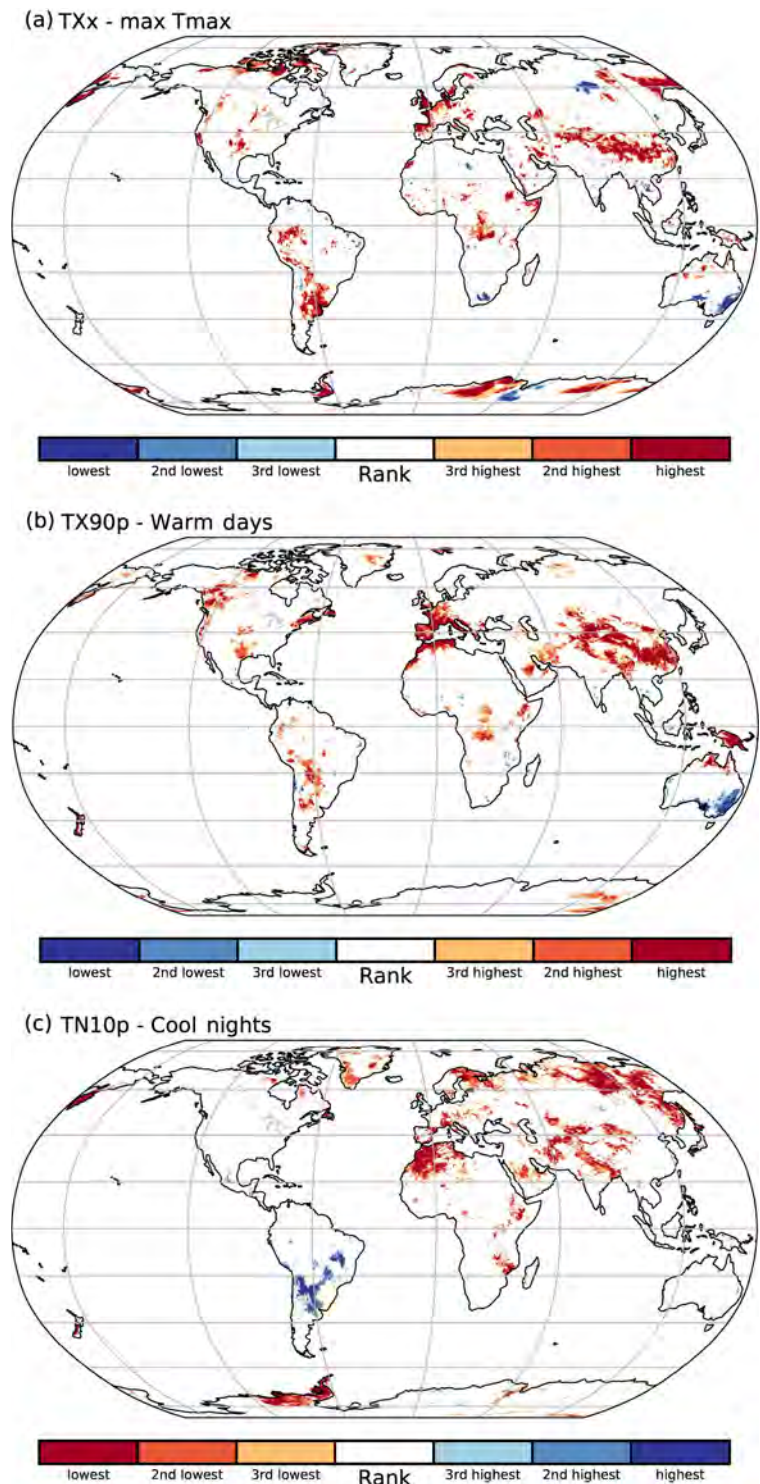


Fig. 2.8. Maps indicating grid cells where the temperature indices for 2022 ranked in the three highest or three lowest values based on ERA5 since 1979: (a) hottest day of the year (TXx), (b) annual number of warm days (TX90p), and (c) annual number of cool nights (TN10p).

Hemisphere extra-tropics and Australia, with very little coverage in Africa and South America (Fig. A2.5). We use the ERA5 reanalysis (Hersbach et al. 2020) to provide globally complete fields of these indices covering 1979–2022, which performed well in a recent intercomparison between observation and reanalyses datasets (Dunn et al. 2022). The indices quantifying exceedances of percentile-based thresholds use a fixed reference period, and intercomparison between these is complex in a strongly warming climate (Dunn et al. 2020; Yosef et al. 2021; Dunn and Morice 2022). The percentile period in GHCNDEX is 1961–90, whereas for the index calculations with ERA5 the percentiles are calculated for the 1991–2020 period.

An MHW is detected when five or more consecutive days of temperature are above a 90th percentile daily climatology (Hobday et al. 2016). MHWs are categorized as moderate when the greatest temperature anomaly during the event is less than double the 90th percentile for the seasonal anomaly. When this value is more than double, triple, or quadruple the distance, the MHW is categorized as strong, severe, or extreme, respectively (Hobday et al. 2018). The direct inverse is used to detect and categorize MCSs (i.e., days below the 10th percentile). The baseline period used to detect events in this report is 1982–2011, because 1982 is the first full year of the NOAA OISST product.

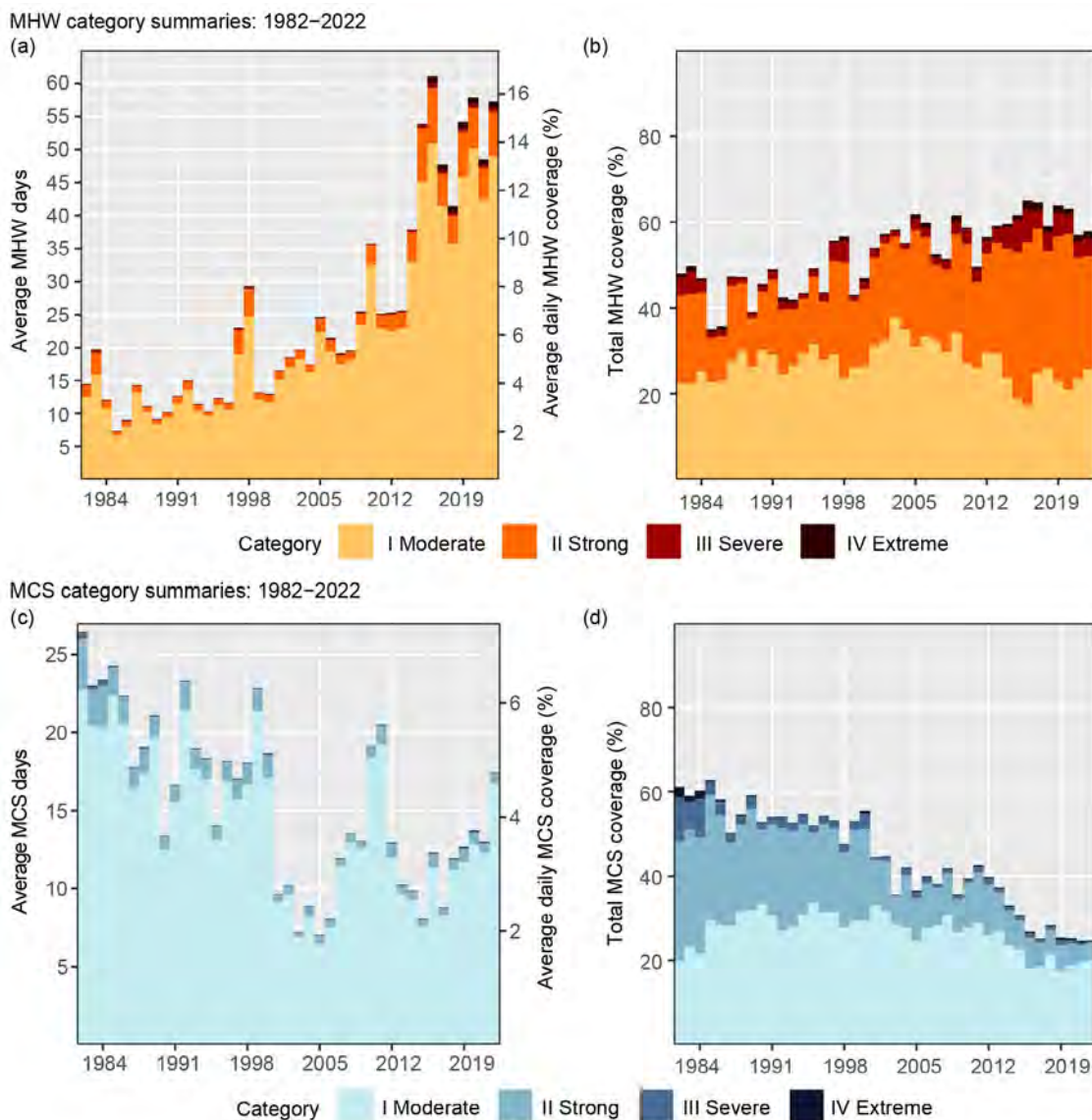


Fig. 2.9. (a),(c) Average annual number of global marine heatwave (MHW) and marine cold-spell (MCS) days experienced over the surface of the ocean each year (left y-axis), also expressed as the percent of the surface of the ocean experiencing an MHW/MCS on any given day (right y-axis) of that year. (b),(d) Total percent of the surface area of the ocean that experienced an MHW/MCS at some point during the year. The values shown are for the highest category of MHW/MCS experienced at any point. The base period is 1982–2011. (Source: NOAA OISST v2.1.)

5. TROPOSPHERIC TEMPERATURE

—S. Po-Chedley, J. R. Christy, C.-Z. Zou, C. A. Mears, and L. Haimberger

The 2022 globally averaged lower-tropospheric temperature (LTT) anomaly was 0.26°C (0.17°C to 0.37°C) above the 1991–2020 average, ranking among the nine warmest years on record (fourth to ninth warmest, depending on the dataset). Long-term warming of the troposphere is consistent with our understanding of greenhouse warming. Other factors, such as volcanic eruptions, decadal variability, and solar activity also modulate the long-term warming trend (Christy and McNider 2017; Po-Chedley et al. 2022). Interannual variations in global LTT are dominated by the El Niño–Southern Oscillation, which has largely been in a La Niña state since August 2020 (see section 4b and Sidebar 3.1 for details; Figs. 2.10a,b). As with the year 2021, the depression of atmospheric temperature due to La Niña combined with the background warming trend (Table 2.4) produced a year that was warmer than average, but not record breaking.

La Niña events are accompanied by a distinct pattern of tropospheric temperature anomalies, which are evident in the annual average departures in both 2022 (Plate 2.1f) and 2021 (see Plate 2.1f

Table 2.4. Temperature trends (units of °C decade⁻¹) for global lower-tropospheric temperature (LTT) and tropical tropospheric temperature (TTT) over the periods 1958–2022 and 1979–2022. NASA MERRA-2 data begins in 1980 and NOAA STAR v5.0 TLT begins in 1981. UW does not produce an LTT product.

Method	Source	LTT (90°S–90°N) 1958–2022	LTT (90°S–90°N) 1979–2022	TTT (20°S–20°N) 1958–2022	TTT (20°S–20°N) 1979–2022
Radiosonde	NOAA RATPAC vA2 (Free et al. 2005)	0.18	0.22	0.17	0.18
Radiosonde	RAOBCORE v1.9 (Haimberger et al. 2012)	0.16	0.17	0.13	0.15
Radiosonde	RICH v1.9 (Haimberger et al. 2012)	0.18	0.20	0.18	0.19
Satellite	UAH v6.0 (Spencer et al. 2017)	–	0.13 ^[1]	–	0.12
Satellite	RSS v4.0 (Mears and Wentz, 2016)	–	0.21	–	0.16
Satellite	UW v1.0 (Po-Chedley et al. 2015)	–	–	–	0.16
Satellite	NOAA STAR v5.0 (Zou et al. 2023)	–	0.13 ^[1]	–	0.10
Reanalysis	ERA5 (Hersbach et al. 2020)	–	0.18	–	0.15
Reanalysis	JRA-55 (Kobayashi et al. 2015)	0.17	0.18	0.16	0.14
Reanalysis	NASA MERRA-2 (Gelaro et al. 2017)	–	0.19	–	0.17
Median	Calculated from previous values	0.17	0.18	0.16	0.15

^[1]The vertical sampling in UAH and NOAA STAR LTT is slightly different from other datasets and results in temperature trends that are approximately 0.01°C decade⁻¹ smaller than other datasets.

in Blunden and Boyer 2022). La Niña conditions over late 2021 through 2022 contributed to record-breaking LTT values over the North and South Pacific Ocean, China, and parts of South Asia. Persistent summertime heatwaves during June to August contributed to record-breaking tropospheric temperatures over Europe in 2022. Large positive total column water vapor anomalies were collocated with the anomalous tropospheric warmth (Plate 2.1i; section 2d2). Overall, the global LTT was above average across 70% of the globe, with 6% of Earth experiencing the highest temperatures since the start of the record in 1979 (Plate 2.1f; Fig. 2.10c). In contrast, 1% of Earth experienced its coldest year on record.

Atmospheric temperature data are derived from balloon-borne radiosonde measurements, satellite-based microwave soundings, and atmospheric reanalyses (Table 2.4). Each dataset employs different strategies to remove biases and drifts from sources of atmospheric temperature data. Across datasets and measurement techniques, there is good agreement on interannual timescales (Fig. 2.10a; Supp. Fig. A2.7), but structural uncertainty leads to non-negligible difference in long-term warming trends (Table 2.4).

One issue in the construction of tropospheric temperature microwave records is that short-term trends from overlapping satellites do not always agree after estimated biases are removed. For example, tropospheric warming inferred from the Microwave Sounding Unit (MSU) onboard the NOAA-14 satellite exceeds that from Advanced MSU (AMSU) data from NOAA-15. Reliance on data from NOAA-14 (NOAA-15) results in larger (smaller) estimates of tropospheric warming (Mears and Wentz 2016; Santer et al. 2021). A new version of the NOAA STAR dataset treats data from the latest microwave sounding instruments (AMSU and the Advanced Technology Microwave Sounder) as a reference with which to calibrate earlier data from earlier MSU instruments (Zou et al. 2021, 2023). This decision has the effect of substantially reducing global tropical tropospheric temperature (TTT) warming over 1979 to 2021 (from $0.23^{\circ}\text{C decade}^{-1}$ to $0.14^{\circ}\text{C decade}^{-1}$; Zou et al. 2023). Changes in the estimated rate of warming of a few hundredths of a degree per decade are common when tropospheric temperature datasets are updated. These changes illustrate the challenges and pronounced structural uncertainty in constructing records of tropospheric warming.

General circulation models (GCMs) tend to simulate greater tropospheric warming than satellite observations over 1979 to present, particularly in the tropics (McKittrick and Christy 2020; Po-Chedley et al. 2021; Zou et al. 2023). Observed tropical sea-surface warming, which is closely coupled to tropospheric warming, is also smaller than the average warming in GCMs (Eyring et al. 2021). Two factors likely contribute to faster-than-observed model warming: biases in

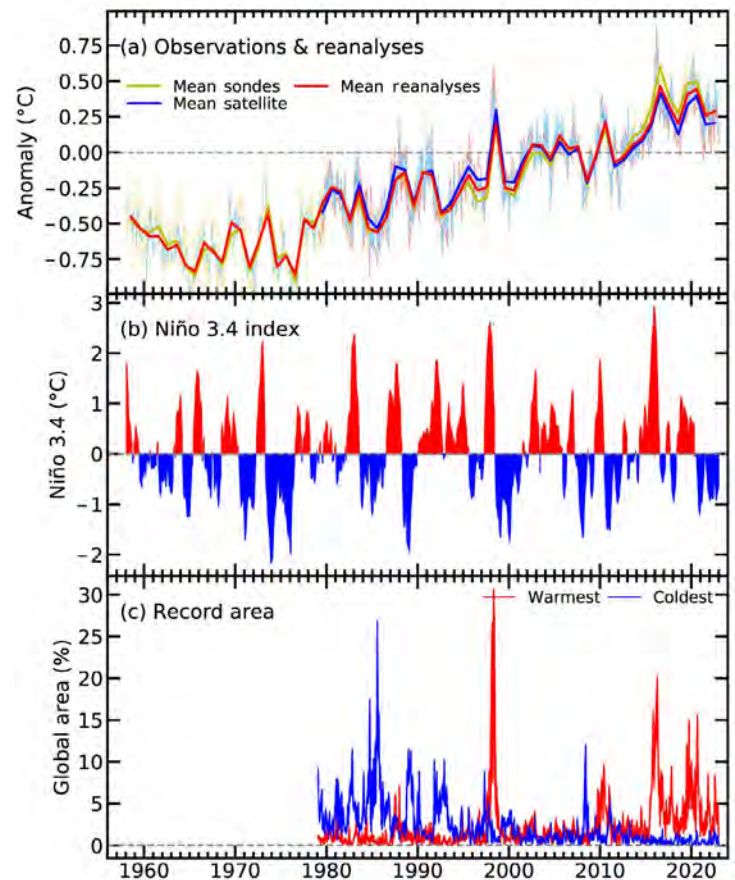


Fig. 2.10. Time series of (a) global average lower-tropospheric temperature (LTT; $^{\circ}\text{C}$) anomalies, (b) central Pacific (Niño-3.4 region) sea-surface temperature anomalies ($^{\circ}\text{C}$), and (c) percentage of Earth experiencing record-high (red) and low (blue) LTT values, according to RSS and UAH LTT datasets for the period 1979–2022. Bold lines in (a) represent the annual average values (across datasets) for sondes (yellow), reanalysis (red), and satellite (blue) data. Monthly values for individual datasets are also plotted with thinner and lighter lines for context. The climatological base period for (a) and (b) is 1991–2020. Niño-3.4 anomalies are calculated using the HadISST1 dataset (Rayner et al. 2003). STAR data are not included in the satellite LTT time series because the time series begins in 1981 (versus 1979 for RSS and UAH data).

the prescribed model forcing and biases in the GCM response to greenhouse gas forcing. For example, Fasullo et al. (2022) shows that a discontinuity in the biomass-burning aerosol forcing prescribed to models in Phase 6 of the Coupled Model Intercomparison Project (CMIP6) results in inflated warming in version 2 of the Community Earth System Model—an issue that may affect other CMIP6 GCMs. Several GCMs also exceed the likely range of estimates of climate sensitivity (Forster et al. 2021)—the global surface warming response to a doubling of atmospheric carbon dioxide—which in turn contributes to overestimates of historical warming (Scafetta 2023). Multidecadal internal variability has also reduced observed warming since 1979 (Po-Chedley et al. 2022), which contributes to the difference between observed and simulated warming. Aside from these factors, it is also possible that observational biases may affect observed tropospheric warming (Santer et al. 2021).

6. STRATOSPHERIC TEMPERATURE

—W. J. Randel, C. Covey, L. Polvani, and A. K. Steiner

Global mean temperatures in the lower, middle, and upper stratosphere were anomalously low during 2022, a result of the large volcanic eruption of Hunga Tonga–Hunga Ha‘apai (HTHH) in January 2022 (Sidebar 2.2). These cold anomalies were primarily observed in the Southern Hemisphere (SH), and these volcanic effects accentuated the multi-decadal global-scale cooling of the stratosphere due to increases of anthropogenic carbon dioxide concentrations in the atmosphere. The Antarctic polar vortex was strong and persistent in 2022, while the Arctic polar vortex was disturbed by a major stratospheric warming in March. The stratospheric quasi-biennial oscillation (QBO) progressed normally, with equatorial westerly winds and positive temperature anomalies descending from the middle stratosphere to the lower stratosphere during the year.

The HTHH eruption (~20°S, 175°W) on 15 January 2022 injected extreme amounts of water vapor (H₂O) and a moderate amount of the aerosol precursor sulfur dioxide into the stratosphere. The amount of stratospheric H₂O injected from HTHH is unprecedented in the continuous satellite record beginning in the middle 1980s (Davis et al. 2016; Milan et al. 2022; Vömel et al. 2022). The H₂O and aerosol perturbations persisted throughout 2022 (e.g., Schoeberl et al. 2022; Mishra et al. 2022), and the radiative effects of enhanced H₂O resulted in large-scale cooling of the SH stratosphere, in contrast to aerosol-induced warming of the stratosphere observed from past large volcanic eruptions (e.g., Labitzke and McCormick 1992). Additional H₂O cools the stratosphere because of enhanced longwave emission to space (e.g., Forster and Shine 1999). Observations show low temperatures in 2022 that are well outside the range of previous variability (Fig. 2.11a), with corresponding anomalies in stratospheric winds and circulation in balance

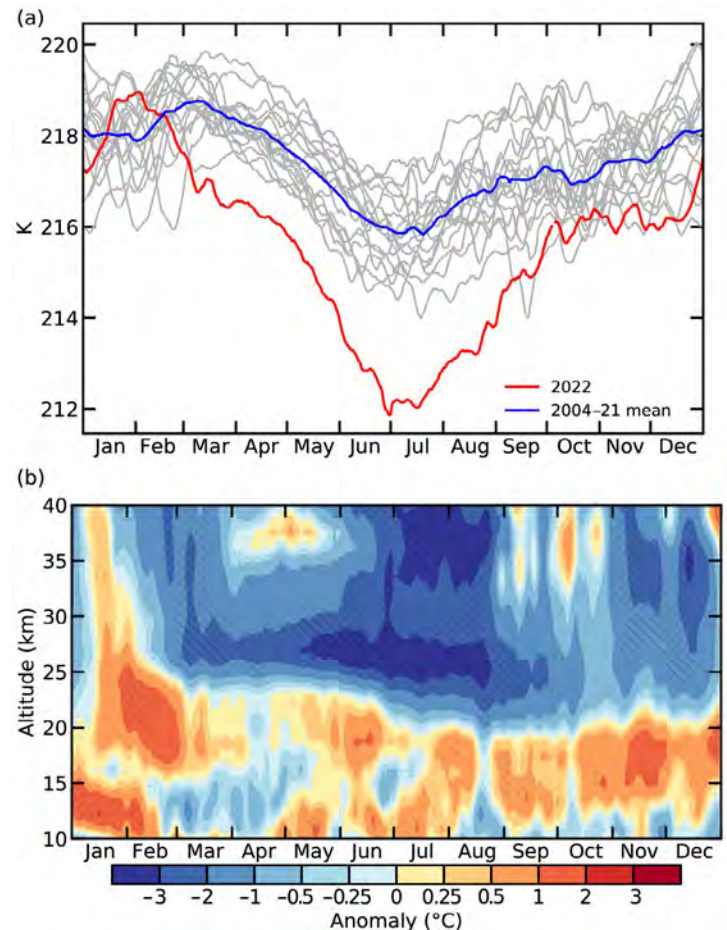


Fig. 2.11. Evolution of Southern Hemisphere midlatitude (10°S–50°S) stratospheric temperature anomalies (°C) in 2022 from Aura MLS measurements (<https://aura.gsfc.nasa.gov/>). (a) Time series of temperatures at 25 km for each individual year, highlighting anomalously cold temperatures in 2022 (red) compared to previous years 2004–21. (b) Height–time evolution of temperature anomalies in 2022 (2022 minus 2004–21 average). Hatching denotes 2022 anomalies that are outside of all previous variability during 2004–21.

with the anomalous temperatures (Coy et al. 2022; Wang et al. 2022). Low anomalies were largest during SH winter (Fig. 2.11b), with a corresponding equatorward shift of the Antarctic polar vortex and circulation-induced midlatitude ozone losses (Wang et al. 2022). While the HTHH H₂O plume is slowly dispersing throughout the global stratosphere, it is expected to persist for a number of years as H₂O is chemically inert, and the main loss processes are due to transport in the slow overturning stratospheric circulation. Hence the HTHH H₂O anomalies will continue to influence stratospheric temperatures beyond 2022.

The Antarctic polar vortex was strong and characterized by anomalously low temperatures during spring 2022, persisting through December (see section 6b for details). Springtime polar temperatures and vortex persistence are closely linked with springtime polar ozone amounts, due to ozone radiative forcing after the sun returns in October. Springtime polar ozone was also relatively low in 2022 (section 2g4), likely contributing to the observed low temperatures.

The Arctic polar vortex was stable and relatively cold during winter but was disturbed by a major stratospheric warming event in March (Vargin et al. 2022), with polar temperature increases over a few days of about 30K. The vortex did not recover, and this event thus corresponded to the ‘final warming’ for that winter. The stratospheric QBO in 2022 continued its usual regular progression (as observed since the 1950s) in contrast to the anomalous disruption events of 2016 and 2020 (section 2e3).

c. Cryosphere

1. PERMAFROST TEMPERATURE AND ACTIVE LAYER THICKNESS

—J. Noetzli, H. H. Christiansen, F. Hrbáček, G. Hu, K. Isaksen, F. Magnin, P. Pogliotti, S. L. Smith, L. Zhao, and D. A. Streletskiy

Permafrost is a subsurface phenomenon in polar and high mountain regions and defined as ground with a maximum temperature of 0°C throughout the year. Permafrost temperatures close to the depth where annual fluctuations become minimal (the depth of zero annual amplitude) increased across all permafrost regions in the past decades with rates ranging from below 0.3°C decade⁻¹ in warm permafrost (with temperatures close to 0 °C) to above 0.8°C decade⁻¹ in cold permafrost (Biskaborn et al. 2019; Smith et al. 2022; Etzelmüller et al. 2020; Zhao et al. 2020; Fig. 2.12; see also section 5i). The thickness of the active layer (ALT), the layer above the permafrost that thaws during summer, increased in the Arctic by a few centimeters per decade in cold continuous permafrost and by more than 10 cm decade⁻¹ in discontinuous permafrost. ALT increased by 19.6 cm decade⁻¹ over the past 40 years in the Qinghai-Tibet Plateau (Fig. 2.13) and has increased by a few meters in the past 20 years at several sites in the European Alps.

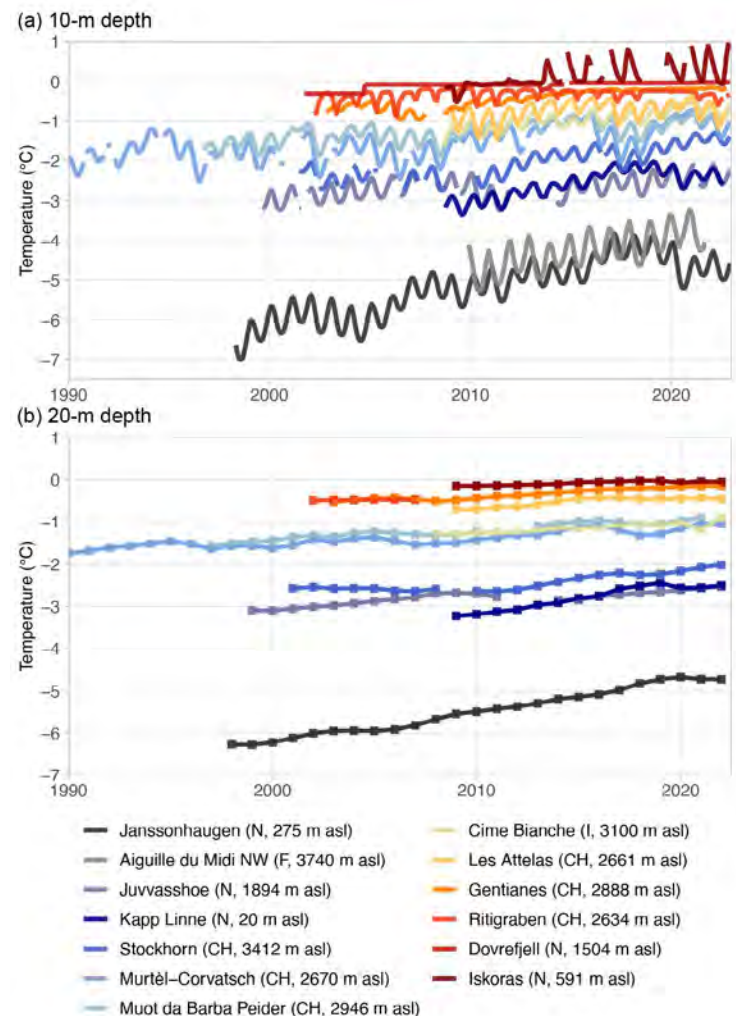


Fig. 2.12. Permafrost temperatures (°C) measured in boreholes in the European Alps and the Nordic countries at a depth of (a) ~10 m (monthly means) and (b) 20 m (annual means). (Sources: Switzerland: Swiss Permafrost Monitoring Network; Norway: Norwegian Meteorological Institute and the Norwegian Permafrost Database; France: updated from Magnin et al. 2015; Italy: updated from Pogliotti et al. 2015.)

Permafrost temperatures in 2022 were the highest on record at 11 of the 25 sites monitored in the Arctic (section 5i), while they were lower than in 2021 in northern Alaska, the northern Mackenzie region in northwestern Canada, and the Canadian high Arctic. This is partly associated with lower air temperatures in those regions over the past two to three years. ALT in Arctic Alaska was one of the lowest since 1995 where most of the sites were established. ALT was lower than 2021 but above the long-term averages in Interior Alaska, northwestern Canada, Greenland, and northern European Russia. ALT in West Siberia was on average 5 cm higher in 2022 than in 2021, while in Central Siberia it was 6 cm lower, but 13 cm higher than average. In East Siberia and Chukotka, ALT was 2 cm–3 cm higher than in 2021, but close to the long-term mean. In high-Arctic Svalbard, permafrost temperatures were the fourth highest on record. ALT was not at maximum due to lower air temperatures in April and early May, and despite record air temperatures in summer 2022 in western and northern Svalbard.

Several countries in Europe recorded extremely dry and warm conditions in summer 2022 (see section 7f; sections 2b4, 2d11; Copernicus 2023). In northern Norway, the permafrost degradation continued, with permafrost thaw down to 20-m depth at Iskoras, and in southern Norway the permafrost temperature was the highest on record at Juvvasshøe (Fig. 2.12). Nearby, on Dovrefjell, since 2021 the active layer has not completely frozen down to the underlying permafrost during winter, resulting in a talik (unfrozen zone; Isaksen et al. 2022). In the European Alps, mean annual ground surface temperature increased in 2022 by more than 1°C compared to 2021 at the majority of the 30 Swiss sites due to higher air temperatures and early snow melt (section 2c5; MeteoSwiss 2023; Pielmeier et al. 2023). The active layer was the thickest on record at most monitoring sites in the Swiss, French, and Italian Alps. In contrast, permafrost temperatures at 10-m depth decreased in 2022 at many sites (update from the Swiss Permafrost Monitoring Network [PERMOS] 2022; Pogliotti et al. 2015; Magnin et al. 2015; Fig. 2.12) reflecting the colder conditions of 2021 (Noetzli et al. 2022). Permafrost temperatures at 20-m depth—where they react to longer-term trends—continued to increase in 2022 at most sites and were close to record levels.

Permafrost temperatures in the Qinghai-Tibet Plateau continued to increase from 2005 to 2021 at 10- and 20-m depth at six sites, with stronger warming in colder permafrost. At the 10 ALT sites along the Qinghai-Tibet Highway (Kunlun mountain pass), ALT increased from the start of the measurements in 1981 to a new maximum of 250 cm in 2021 (the latest value available; Fig. 2.12).

On James Ross Island in the northern Antarctic Peninsula, 2022 was the warmest of the instrumental records since 2004. The mean annual near-surface temperature (−3.2°C) was 2.2°C above the 2011–20 mean (reference site AWS-JGM), leading to a mean annual temperature at the permafrost table (i.e., the top of permafrost) 1.6°C above average. The ALT was 71 cm in 2022 and 22 cm above the mean during 2011–20 (Kaplan-Pastirikova et al. 2023). ALT has been increasing at all Antarctic Peninsula monitoring sites since 2015, whereas it has remained stable in the other regions of Antarctica.

International field data of ALT, permafrost temperatures, and rock glacier velocity (Streletskiy et al. 2021; section 2c2) are collected by the Global Terrestrial Network for Permafrost (GTN-P). Permafrost temperatures are manually recorded or continuously logged in boreholes with a

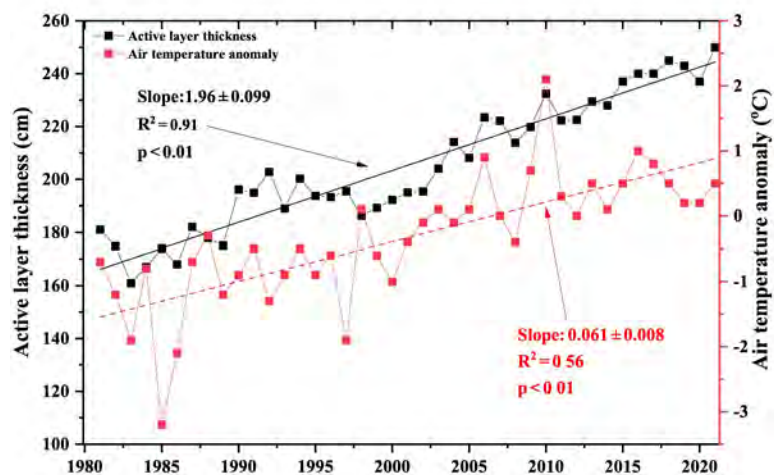


Fig. 2.13. Active layer thickness (cm) and air temperature anomaly (°C; 1991–2020 base period) in the permafrost zone along the Qinghai-Tibet Highway for the period 1981–2021. (Source: Cryosphere Research Station on Qinghai-Xizang Plateau, CAS.)

measurement accuracy of $\sim 0.1^\circ\text{C}$ (Biskaborn et al. 2019; Noetzli et al. 2021; Streletskiy et al. 2021). ALT is either determined by mechanical probing (with an accuracy of ~ 1 cm) or interpolated from borehole temperature measurements. The global coverage of permafrost monitoring sites is sparse and biased to the Northern Hemisphere. Permafrost data are particularly limited in regions such as Siberia, central Canada, Antarctica, and the Himalayan and Andes Mountains.

2. ROCK GLACIER VELOCITY

—C. Pellet, X. Bodin, D. Cusicanqui, R. Delaloye, A. Kääh, V. Kaufmann, J. Noetzli, E. Thibert, S. Vivero, and A. Kellerer-Pirklbauer

Rock glaciers are debris landforms generated by the creep of frozen ground (permafrost) whose velocity changes are indicative of changes in the thermal state of permafrost (RGIK 2022a,b). Rock glacier velocities (RGV) observed in different mountain ranges worldwide have been increasing since the 1950s, with large regional and inter-annual variability. In 2022, RGVs in the European Alps decreased at all monitoring sites. For some rock glaciers this was the second consecutive year of decreasing velocities. These changes are consistent with the evolution of permafrost temperatures (section 2c1) to which rock glacier surface velocities respond synchronously (e.g., Kenner et al. 2017; Staub et al. 2016).

Although summer was marked by exceptionally high air temperatures (Fig. 2.14a; section 2b4), RGVs in the European Alps decreased at all sites in 2022, which contrasts with the general

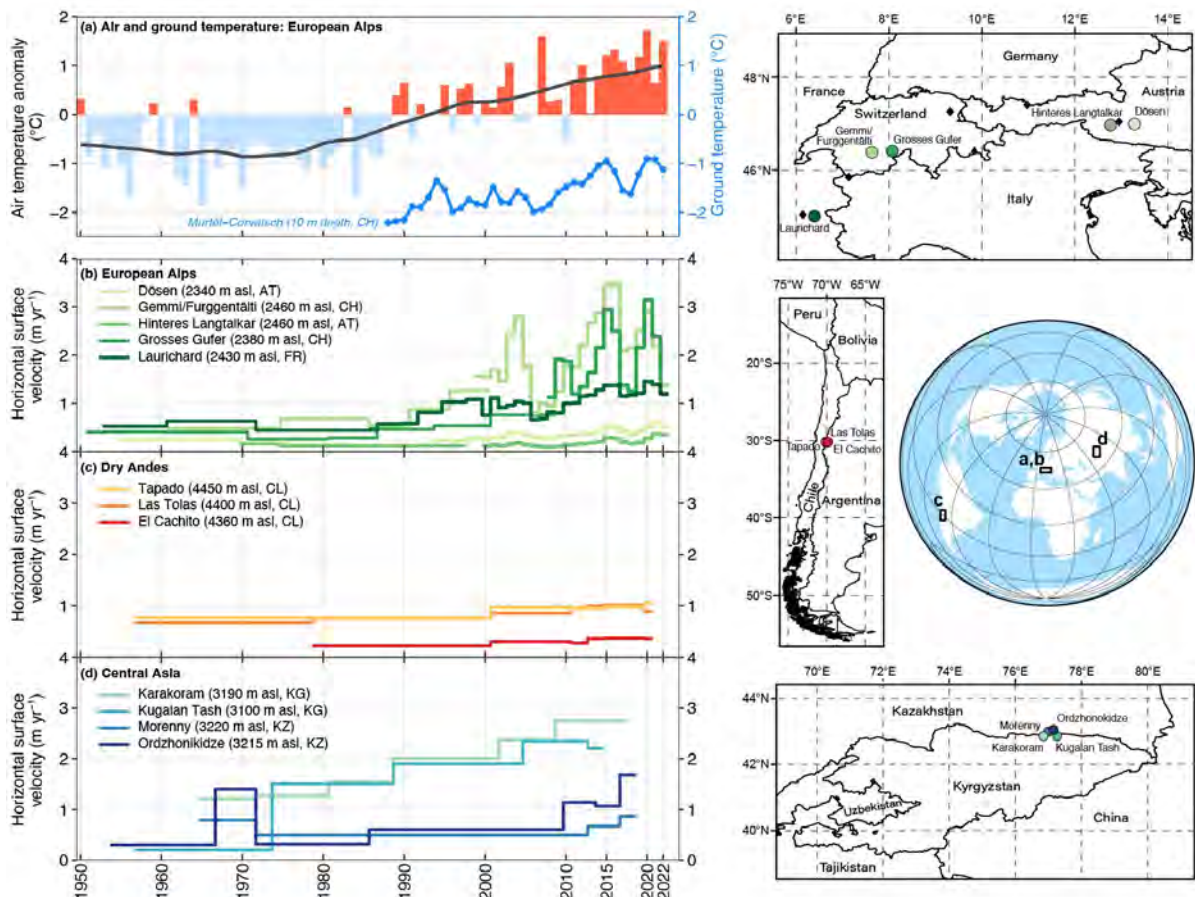


Fig. 2.14. (a) Air and ground temperatures ($^\circ\text{C}$) in the European Alps, (b) rock glacier velocities (m yr^{-1}) at selected sites in the European Alps, (c) the Dry Andes (adapted from Vivero et al. 2021), and (d) Central Asia (adapted from Kääh et al. 2021). Rock glacier velocities are based on in situ geodetic surveys or photogrammetry in the context of long-term monitoring. In situ hydrological mean annual permafrost temperature measured at 10-m depth (blue line) at Murtèl Corvatsch (black triangle on Europe map) and air temperature: composite anomaly to the 1981–2010 average (bars) and composite 20-yr running mean (solid line) at Besse (FR), Grand Saint-Bernard (CH), Saentis (CH), Sonnblick (AT), and Zugspitze (D, black diamonds on Europe map). (Sources: Météo France, Deutscher Wetterdienst, MeteoSwiss, GeoSphere Austria, Swiss Permafrost Monitoring Network, University of Fribourg, University of Graz, Graz University of Technology, Université Grenoble Alpes, University of Oslo.)

acceleration trend observed since the 1950s (Pellet et al. 2022; PERMOS 2022). Maximum velocity decrease compared to 2021 was observed in the Swiss Alps (e.g., Grosses Gufer: -49% and Gemmi/Furggentälti: -37%), whereas a smaller decrease was reported in the French (e.g., Laurichard: -14%) and Austrian (e.g., Dösen: -15% and Hinteres Langtalkar: -5%) Alps (Fig. 2.14b). The velocity decrease is consistent with a decrease in permafrost temperatures observed at 10-m depth (section 2c1), which reflects the comparatively cold year of 2021. The relatively dry winter of 2021/22 and dry and warm spring and summer of 2022 affected the geohydrological conditions at all sites (i.e., reduced the amount of water available in the terrain) and also contributed to velocity decrease (i.e., reduced shearing due to reduced pore water pressure; see Cicoira et al. 2019)

There are only a few long-term in situ RGV measurements outside of the European Alps. However, RGVs have been increasingly observed and reconstructed using (archival) aerial photographs and high-resolution satellite data (e.g., Cusicanqui et al. 2021; Eriksen et al. 2018). In the Dry Andes, RGVs reconstructed on three rock glaciers show low velocities from 1950 to 2000, followed by a steady acceleration since the 2000s (Fig. 2.14c), consistent with the climatic conditions in the region (Vivero et al. 2021).

RGVs observed in Central Asia have increased overall since the first available measurements in the 1950s, although their inter-annual evolution differs (Fig. 2.14d; Kääb et al. 2021). This general trend is consistent with increasing air temperatures in the region and with the acceleration reported in the European Alps and Dry Andes.

RGVs are mostly related to the evolution of ground temperature and liquid water content between the upper surface of permafrost (i.e., permafrost table) and the layer at depth where most of the deformation occurs (the so-called shear horizon; Cicoira et al. 2019; Frauenfelder et al. 2003; Kenner et al. 2017; Staub et al. 2016). Despite variable size, morphology, topographical and geological settings, and velocity ranges, consistent regional RGV evolutions have been highlighted in several studies (e.g., Delaloye et al. 2010; Kääb et al. 2021; Kellerer-Pirklbauer et al. 2018). Given the global occurrence of rock glaciers and the sensitivity of their surface velocity to ground temperatures and, by extension, to climate change, RGV was adopted in 2021 as a new associated product to the essential climate variable permafrost by the Global Climate Observing System (GCOS 2022a,b) and the GTN-P (Streletskiy et al. 2021). Multi-annual long-term RGV time series are reconstructed using repeated aerial or optical satellite images. Horizontal displacements are computed based on cross-correlation feature tracking on multi-temporal ortho-images or digital elevation model matching (Kääb et al. 2021; Vivero et al. 2021). The resulting accuracy strongly depends on the spatial resolution of the images and on the image quality (i.e., snow-free and shadows). Surface displacements are averaged for a cluster of points/pixels selected within areas representative of the downslope movement of the rock glacier (RGIK 2022a). Annual rock glacier velocities are measured using terrestrial geodetic surveys performed each year at the same time (usually at the end of summer). The positions of selected boulders (10–100 per landform) are measured with an average accuracy in the range of mm to cm (Delaloye et al. 2008; Kellerer-Pirklbauer and Kaufmann. 2012; PERMOS 2022; Thibert and Bodin 2022).

3. ALPINE GLACIERS

—M. S. Pelto

In 2022 heat events in the European Alps, Svalbard, High Mountain Asia, and the central Andes of Argentina and Chile resulted in a global mean annual mass balance of -1433 mm w.e. (water equivalent) for all 108 reporting alpine (mountain-region) glaciers, with data reported from 20 nations on five continents. In the hydrological year 2021/22, the preliminary regionally averaged annual mass balance based on the World Glacier Monitoring Service (WGMS 2021) reference glaciers was -1179 mm w.e. compared to the 1970–2020 average of -490 mm w.e. This makes 2022 the 35th consecutive year with a global alpine mass balance loss and the 14th consecutive year with a mean global mass balance below -500 mm w.e. (Fig. 2.15). This acceleration in mass loss from global alpine glaciers in the twenty-first century matches the findings of Huguenot et al. (2021). Since the start of the record in 1970, 9 of the 10 most negative mass balances have occurred since 2013.

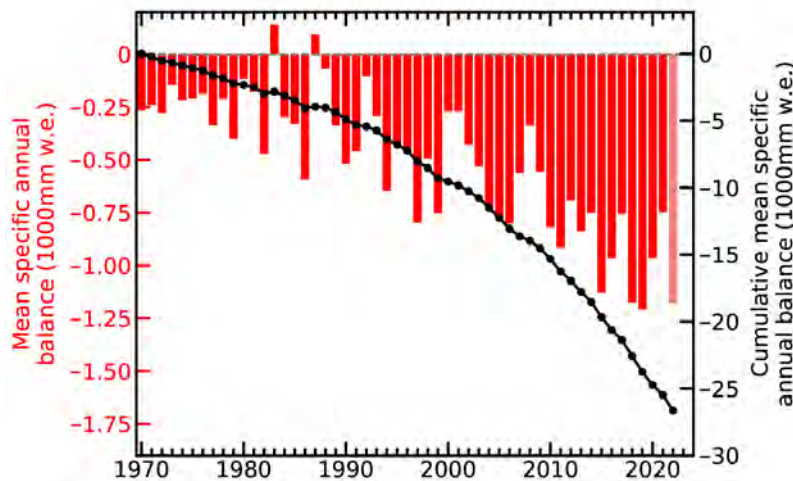


Fig. 2.15. Global average annual (left axis, red bars) and cumulative (right axis, black line) mass balance (1000 mm w.e.) of alpine glaciers for the period 1970–2022. (Source: WGMS regionally averaged reference glacier network.)

In 2022, a negative annual mass balance was reported from 34 of the 37 reference glaciers reported to WGMS. The mean annual mass balance of the 37 reference glaciers was -1547 mm w.e. Reference glaciers each with at least 30 continuous years of observation are used to generate regional averages. Global values are calculated using a single value (averaged) for each of 19 mountain regions in order to avoid a bias toward well-observed regions.

More frequent and intense heatwaves impacting glaciated ranges continued to take a toll on alpine glaciers in 2022. Heatwaves reduce snow cover extent earlier in the melt season, exposing ice surfaces earlier and enhancing surface darkening, both of which cause higher melt rates on alpine glaciers (Shaw et al. 2021; Pelto et al. 2022; Cremona et al. 2023).

All 32 reporting glaciers in the Alps, Pyrenees, and Caucasus Mountains had a negative mass balance averaging -3100 mm w.e. in 2022. In the European Alps, the combination of low winter snowpack and several summer heatwaves generated unprecedented mass loss (sections 2b4, 7f3). In Switzerland, the 25 days of heatwaves in 2022 are estimated to have melted 1.27 ± 0.10 km³ w.e., equivalent to 35% of the overall glacier mass loss that occurred during the summer, a period that led to a 6.2% overall glacier volume loss (Cremona et al. 2023).

In Norway and Sweden, the average balance of 11 reporting glaciers was -443 mm w.e., with three glaciers in Norway having a positive balance. Iceland completed surveys of nine glaciers; five had a positive balance and four a negative balance, with a mean mass balance of -7 mm w.e., close to equilibrium.

On Svalbard, the mean loss of the four reporting glaciers was -1102 mm w.e. The negative mass balances were due to several summer heat events (see section 5b, Sidebar 5.1), which led to many glaciers and ice caps losing all or most of their snow cover, further accelerating mass loss (Fig. 2.16).

In Alberta and British Columbia, Canada, and in Alaska and Washington, United States, 19 glaciers had a negative mass balance, averaging -965 mm w.e. The Alberta, British Columbia, and Washington regions experienced several prolonged heatwaves as they did in 2021. Daily glacier ablation in this region was noted as increasing by 30%–40% during heatwave periods (Pelto et al. 2022).

In South America, mass balance data, reported from five Andean glaciers in Ecuador, Argentina, and Chile were negative, with a mean of -1465 mm w.e. The combination of drought and heat events left many central Andean glaciers snow free by mid-summer in early 2022. Shaw et al. (2021) noted a significant decline in surface albedo (section 2h1) due to decreased fractional snow cover that further enhances melt.

In High Mountain Asia, mass balance measurements were completed on glaciers in China, Kazakhstan, Kyrgyzstan, Russia, and Tajikistan. All 20 glaciers reported negative balances, with an average of -1040 mm w.e. The negative balances were driven by above-average melting during the May–July period.

In New Zealand, the mass balance assessed on Brewster and Rolleston Glaciers were strongly negative at -1125 mm and -1065 mm w.e., respectively. The end of year snowline observations on 50 glaciers was one of the five highest of the last 45 years.

Annual mass balance is reported in mm water equivalent (w.e.). A value of -1000 m w.e. per year represents a mass loss of 1000 kg m^{-2} of ice, or an annual glacier-wide thickness loss of about 1100 mm yr^{-1} .

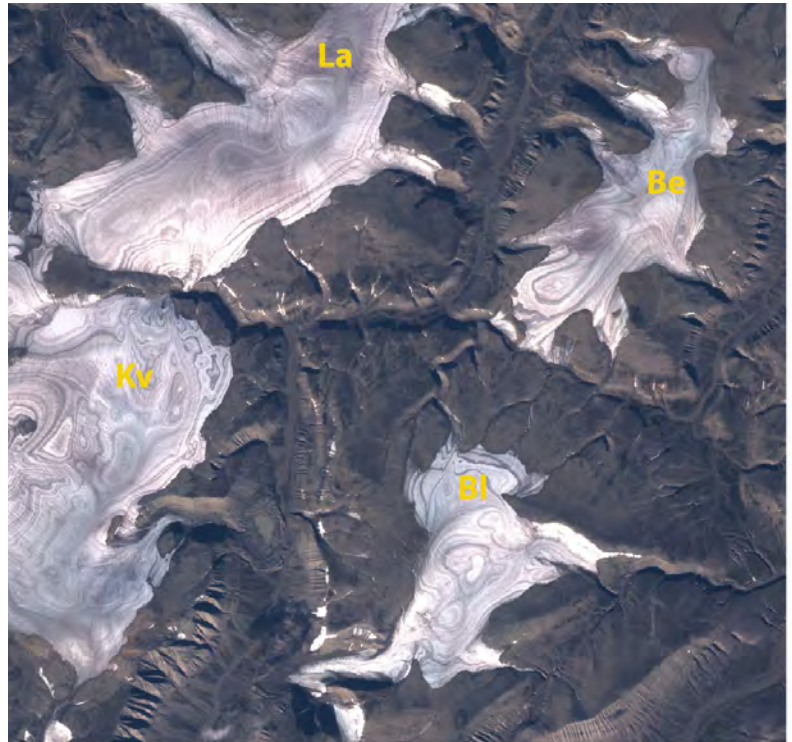


Fig. 2.16. Langjokulen (La), Kvitisen (Kv), Bergfonna (Be), and Blaisen (Bl) ice caps on the northeastern island of Edgeøya, Svalbard, in Copernicus Sentinel-2 MSI image (RGB) on 20 Aug 2022 illustrating the lack of snow cover, limited firn areas, and numerous annual layers. This pattern of annual layers due to glaciers being stripped of snow cover is becoming increasingly frequent.

4. LAKE ICE

—S. Sharma, R. I. Woolway, J. Culpepper, and K. Blagrave

In winter 2021/22, many, but not all lakes across the Northern Hemisphere (NH) had later ice-on dates, earlier ice-off dates, and shorter seasonal ice cover, thus continuing the pattern observed in recent decades (Sharma and Woolway 2021; Sharma et al. 2022).

NH lakes froze on average 5.6 days later and thawed 3.2 days earlier, with 8.9 days shorter ice duration relative to the 1991–2020 base period based on ERA5 reanalysis data (Figs. 2.17, 2.18). The duration of lake ice cover was the fourth shortest since the start of the record in 1980 (Fig. 2.18c). The regional variations in ice duration were consistent with NH winter air temperature anomalies. Some regions in North America, such as western Canada and Alaska, experienced below-average air temperatures, which resulted in longer-than-average ice duration. Conversely, many regions in Eurasia, in particular Siberia, experienced warmer-than-average conditions that resulted in shorter-than-average ice duration (Fig. 2.17).

In situ ice records from 118 lakes distributed across North America, Europe, and Asia revealed mixed patterns for the 2021/22 winter relative to 1991–2020. On average, across this set of 118 lakes,

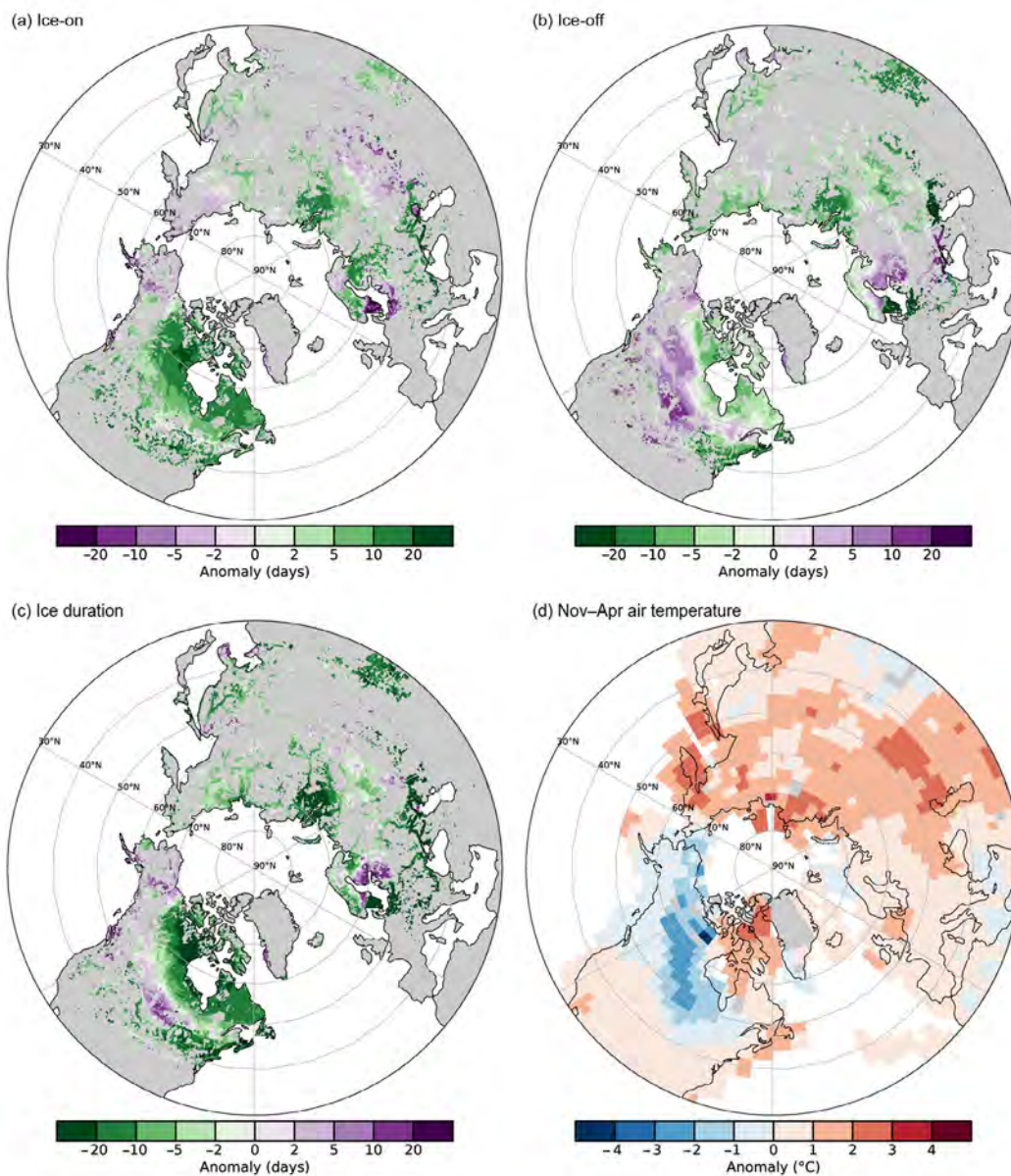


Fig. 2.17. Anomalies (days) in 2022 for (a) ice-on, (b) ice-off, and (c) ice duration for lakes across the Northern Hemisphere (NH), and (d) surface air temperature anomalies (°C) for the NH cold season (Nov–Apr average), the time of year in which lakes typically freeze. The base period is 1991–2020. In (a)–(c), green colors represent higher ice loss (i.e., later ice-on, earlier ice-off, and shorter ice duration), and purple colors represent higher ice coverage (i.e., earlier ice-on, later ice-off, and shorter ice duration). (Sources: ERA5, GISTEMP.)

ice-on was 0.5 days later, ice-off was 3.5 days later, and ice duration was 3.7 days longer (Fig. 2.18). For North American lakes on average, ice duration was 1 day longer, whereas for European lakes, ice-on was 7.1 days longer in 2021/22 relative to 1991–2020. In Asia, Lake Suwa in Japan froze on 7 January 2022. This lake has frozen two years in a row, an event that has not occurred in a decade, though historically the lake froze most years (Sharma et al. 2016, 2021).

We further collated in situ records from 18 mountain lakes (>1000 m a.s.l.) as Pepin et al. (2015) suggests that high-elevation regions will experience more rapid warming than lower elevations.

On average, these mountain lakes froze 11 days later and thawed 5.3 days earlier than the 1991–2020 baseline period (Fig. 2.18). Lake Lunz in Austria showed particularly strong reductions in ice cover as it only froze for 1 day in January and 2 days in February, freezing 41.3 days later, thawing 21.1 days earlier, and losing 58.2 days of duration. This lake also showed multiple freeze and breakup events during the last two years, which had not occurred previously in its continuous 102-year record (Kainz et al. 2017).

The Laurentian Great Lakes had 10.9% more maximal ice coverage, relative to the winters of 1991–2020. Lake Superior was the most anomalous with 25% more ice coverage in 2022, followed by Lake Ontario which had 17.8% more ice coverage (Fig. 2.19). Ice formation was quite late in the Great Lakes owing to warmer autumn water temperatures in late 2021.

We used ice simulations from the European Centre for Medium-Range Weather Forecasts (ECMWF) Reanalysis version 5 (ERA5) reanalysis product (Hersbach et al. 2020) to calculate ice-on and ice-off dates, in addition to ice duration dates across NH lakes following the methodology of Grant et al. (2021). We obtained in situ data for 118 lakes: Canada (4), United States (74), Estonia (1), Finland (27), Norway (10), Sweden (1), and Japan (1). We also obtained in situ data for mountain lakes for the United States (8) and Europe (10; Benson et al. 2000, updated 2022). Furthermore, we acquired annual maximum ice cover (%) data for each of the Laurentian Great Lakes from 1973–2022 (<https://www.glerl.noaa.gov/data/ice/>). Surface air temperature data for the NH cold season (November–April average) were downloaded from the NASA GISS surface temperature analysis (GISTEMP Team 2023). Anomalies for each of our ice metrics were calculated for the 2021/22 winter relative to the 1991–2020 normal base period.

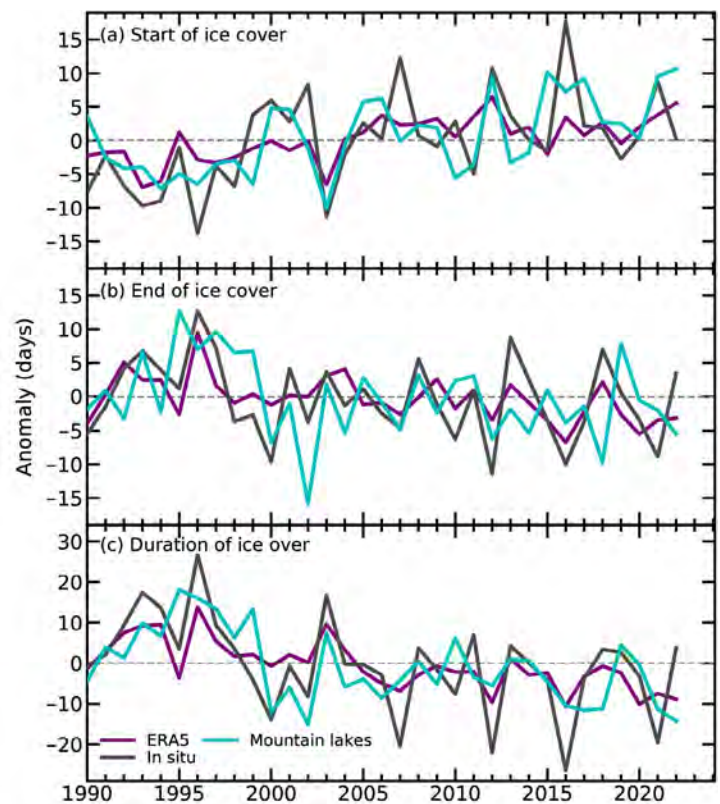


Fig. 2.18. Lake (a) ice-on, (b) ice-off, and (c) ice duration anomalies (days) from 1980 to 2022, relative to the 1991–2020 base period, derived from ERA5 reanalysis, in situ observations, and mountain lakes. Positive values for ice-on suggest later freezing, whereas negative values for ice-off and ice-duration indicate earlier ice-thaw and shorter ice duration.

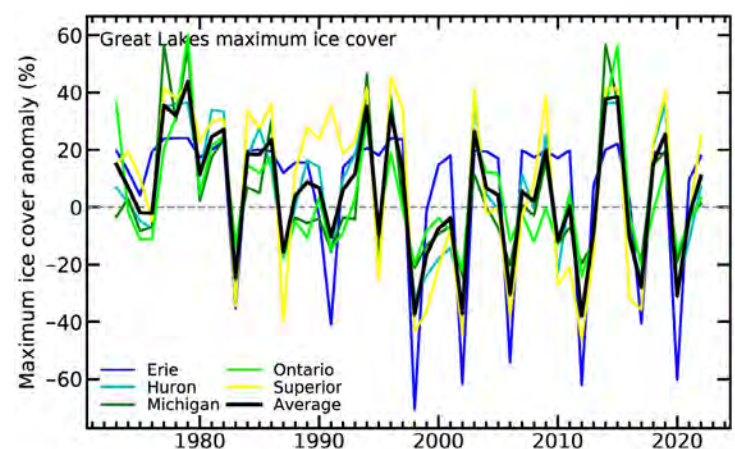


Fig. 2.19. Anomalies in Great Lakes maximum ice cover extent (%) for the period 1973–2022, relative to the 1991–2020 base period. The black line shows the average anomaly for all of the Great Lakes, whereas the lines in color show individual lakes (Erie, Michigan, Superior, Ontario, and Huron).

5. NORTHERN HEMISPHERE CONTINENTAL SNOW-COVER EXTENT

—D. A. Robinson and T.W. Estilow

Annual snow-cover extent (SCE) over NH lands averaged 24.9 million km² in 2022. This is 0.04 million km² less than the 1991–2020 mean and 0.23 million km² below the full period of record (1967–2022) mean (Fig.2.20; Table 2.5). This ranks 2022 as having the 24th least-extensive cover (33rd most) on record. Monthly SCE in 2022 ranged from 47.3 million km² in January to 2.4 million km² in August (Fig. 2.21).

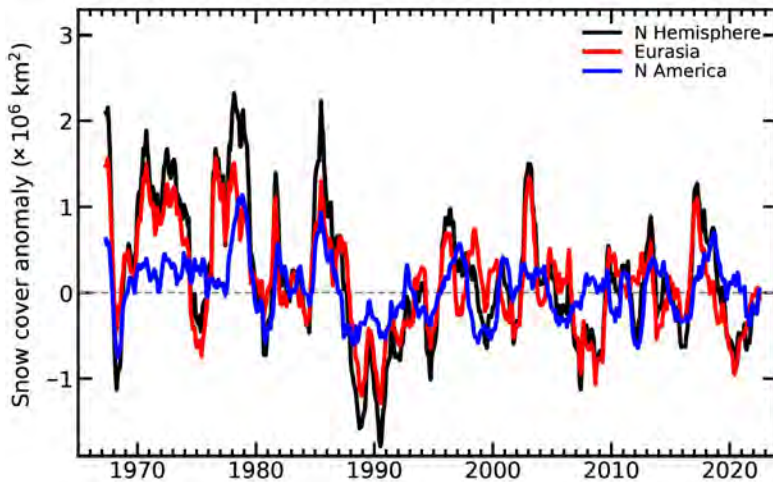


Fig. 2.20. Twelve-month running anomalies of monthly snow-cover extent (SCE; $\times 10^6$ km²) over Northern Hemisphere (NH) lands as a whole and Europe (EUR) and North America (NA) separately plotted on the seventh month using values from Nov 1966 to Dec 2022. Anomalies from the 1991–2020 mean are calculated from NOAA snow maps. Mean NH SCE is 25.1×10^6 km² for the full period of record. Monthly means for the period of record are used for nine missing months during 1968, 1969, and 1971 to create a continuous series of running means. The missing months fall between Jun and Oct.

Table 2.5. Monthly and annual climatological information on Northern Hemisphere (NH), Eurasian (EUR), and North American (NA) snow cover extent (SCE) between Nov 1966 and Dec 2022. Included are the numbers of years with data used in the calculations, NH means, standard deviations (std. dev.), 2022 values, and rankings. Areas are in millions of square kilometers (km²). The years 1968, 1969, and 1971 have 1, 5, and 3 missing months respectively, thus are not included in the annual (Ann) calculations. NA includes Greenland. Ranks are from most (1) to least extensive.

Month	Yrs	NH Mean	Std. Dev.	2022	2022 NH rank	2022 EUR rank	2022 NA rank
Jan	56	47.1	1.5	47.3	26	24	32
Feb	56	46.0	1.8	45.8	27	22	37
Mar	56	40.4	1.8	40.0	31	33	32
Apr	56	30.5	1.7	30.9	23	32	13
May	56	19.1	2.0	18.0	40	44	23
Jun	55	9.3	2.5	5.5	53	54	51
Jul	53	3.9	1.2	2.7	45	51	43
Aug	54	3.0	0.7	2.4	43	45	38
Sep	54	5.4	0.9	5.9	14	6	45
Oct	55	18.6	2.6	18.7	25	22	34
Nov	57	34.3	2.1	37.7	4	11	3
Dec	57	43.7	1.8	43.6	37	48	13
Annual Calculations	53	25.1	0.8	24.9	33	34	30

The first four months of 2022 saw NH SCE rank in the middle tercile of the 56-year record. This dropped to the lower tercile in May, and June was the third least extensive on record (Fig. 2.22a). When snowfall resumed in September the SCE over Eurasia (EUR) quickly climbed to sixth most extensive, while North America (NA) SCE grew more slowly. NH October SCE was in the middle tercile before both continents experienced above-normal November SCE (NA ranking third most extensive and EUR 11th; Fig. 2.22b). However, the pace of seasonally advancing SCE slowed considerably across EUR in December (10th least extensive on record), while NA continued to see above-normal SCE (13th most extensive).

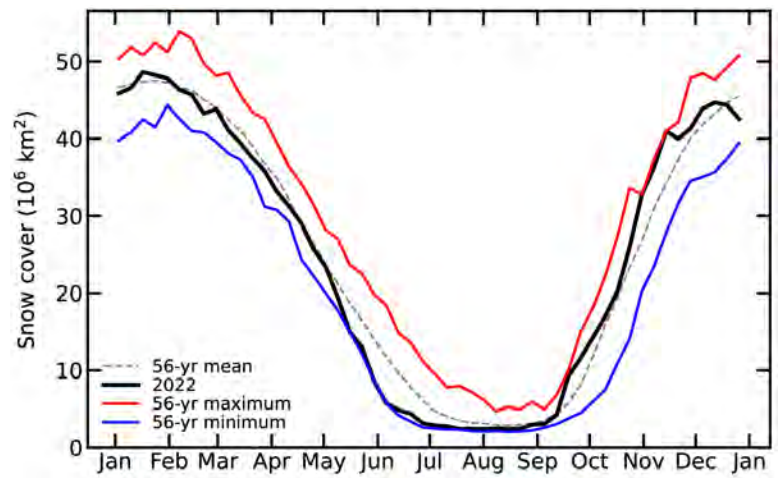


Fig. 2.21. Weekly Northern Hemisphere snow-cover extent (SCE; $\times 10^6 \text{ km}^2$) for 2022 (black) plotted with the mean (gray dashed line), maximum (red), and minimum (blue) SCE for each week. Mean weekly SCE and extremes are calculated using the 56-yr record from Jan 1967 to Dec 2022. Weekly data granules represent SCE for each seven-day period ending on Monday.

Compared to normal, monthly SCE over the contiguous United States varied considerably in 2022. Rankings were in the middle tercile in January, the lowest tercile in February, and was the seventh least extensive on record in March. Melt slowed considerably in April, with the 19th most extensive cover occurring, followed by a middle tercile ranking in May. End-of-year SCE for the United States was above normal, ranking 11th, 6th, and 14th most extensive in October, November, and December, respectively.

SCE is calculated at the Rutgers Global Snow Lab (GSL) from daily SCE maps produced by meteorologists at the U.S. National Ice Center, who rely primarily on visible satellite imagery to construct the maps (Estilow et al. 2015). Maps depicting daily, weekly, and monthly conditions, anomalies, and climatologies may be viewed at the GSL website (<https://snowcover.org>).

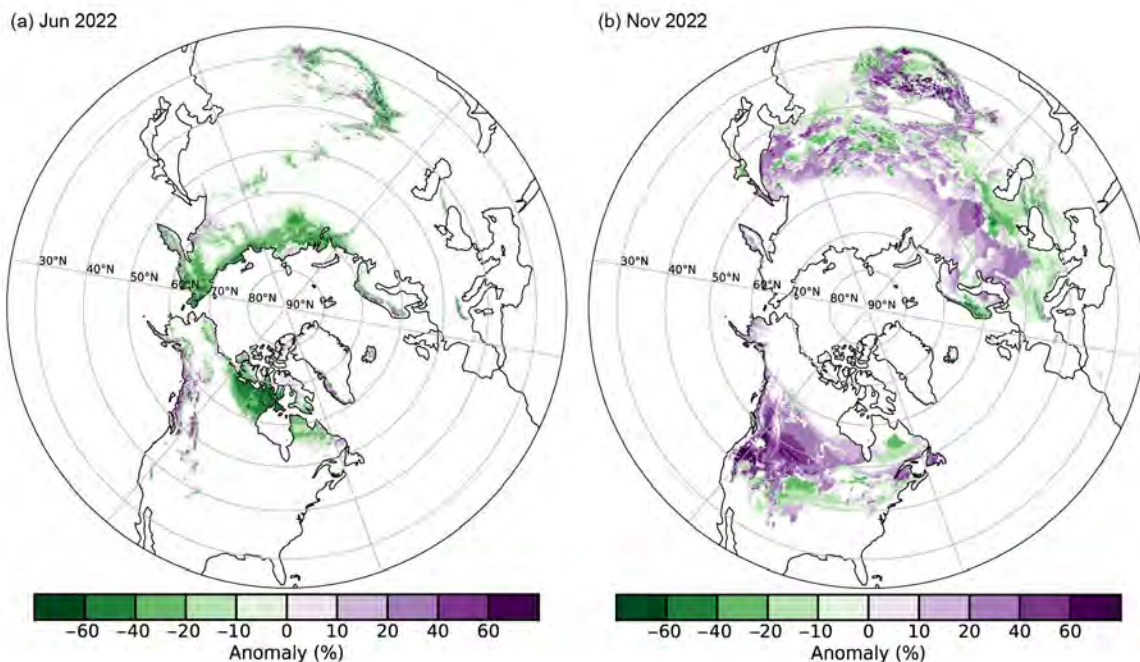


Fig. 2.22. Monthly snow-cover extent (SCE) departure (%; 1991–2020 base period) maps showing (a) Jun 2022 and (b) Nov 2022. The monthly percent anomaly for a grid cell is based on the percent of days that cell was snow covered in that month compared to the long-term climatological average of snow cover days. Jun exhibited the lowest SCE anomaly ($-3.91 \text{ million km}^2$) during 2022, while Nov was the highest above normal ($+3.79 \text{ million km}^2$). Negative departures indicate less SCE than normal (green) with positive departures (purple) showing areas of SCE above the 30-year mean.

d. Hydrological cycle

1. SURFACE HUMIDITY

—K. M. Willett, A. J. Simmons, M. Bosilovich, and D. A. Lavers

In 2022, surface humidity exhibited similar levels of water vapor to 2021, as measured by specific humidity (q). Saturation levels, as measured by relative humidity (RH), were slightly higher than in 2021 over land, yet remained drier than the 1991–2020 average (Figs. 2.23e,f). This finding is common to all products shown here, which comprise the in situ Hadley Centre Integrated Surface Database Humidity (HadISDH [v4.5.1.2022f]) and the European Centre for Medium-Range Weather Forecasts (ECMWF) Reanalysis version 5 (ERA5), Modern-Era Retrospective Analysis for Research and Applications version 2 (MERRA-2), and Japanese 55-year Reanalysis (JRA-55) reanalysis products. It is consistent with the similarity of global near-surface temperatures to those in 2021 and the continuing La Niña conditions that were mostly present throughout both years. Relative humidity over oceans remained highly uncertain, as represented by the spread across the two reanalysis estimates (ERA5 and JRA-55; Figs. 2.23h). Note that this year HadISDH.marine is not included while a discrepancy linked to reduced data coverage in the updated version is investigated.

Despite overall agreement between products for much of the more-than-40-year record, 2022 saw a continued widening of the divergence in anomaly estimates apparent from around 2019. HadISDH showed 2022 as having a slightly higher water vapor content compared to 2021 with the specific humidity anomaly over land (q_{land}) remaining wetter than the 1991–2020 average at 0.13 (0.09 to 0.17 2-sigma uncertainty range) g kg^{-1} . ERA5 placed q_{land} much lower at -0.01 g kg^{-1} , identical to its estimate in 2021. ERA5 q_{ocean} was slightly drier than 2021 at 0.03 g kg^{-1} . MERRA-2 and

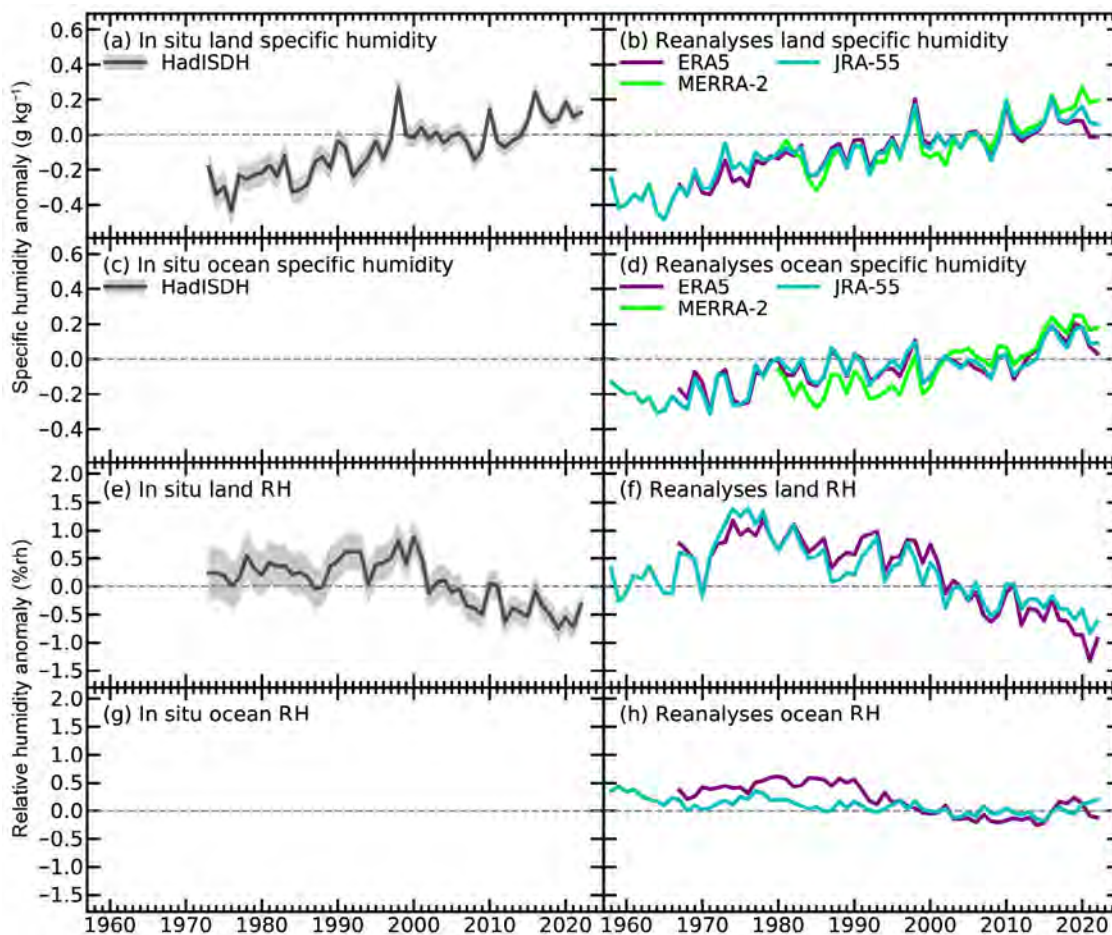


Fig. 2.23. Global average surface humidity annual anomalies (1991–2020 base period). For the in situ datasets 2-m surface humidity is used over land and ~10 m over the oceans. For the reanalysis, 2-m humidity is used over the whole globe. For ERA5 ocean series-only points over open sea are selected. 2- σ uncertainty is shown for the HadISDH dataset capturing the observation, gridbox sampling, and spatial coverage uncertainty. (Sources: HadISDH [Willett et al. 2013, 2014]; ERA5 [Hersbach et al. 2020]; JRA-55 [Kobayashi et al. 2015]; MERRA-2 [Gelaro et al. 2017].)

JRA-55 remained wetter-than-average over land and ocean, with MERRA-2 anomalies reaching the highest at 0.19 g kg^{-1} and 0.18 g kg^{-1} for q_{land} and q_{ocean} , respectively.

In terms of saturation, all products show that RH_{land} remained drier-than-average but was more humid than in 2021. Anomalies ranged from -0.93 \%rh for ERA5 to -0.33 (-0.53 to -0.13 2-sigma uncertainty range) \%rh for HadISDH. ERA5 has consistently presented drier RH_{land} anomalies than HadISDH since 2019. Over ocean, ERA5 and JRA-55 had RH_{ocean} anomalies drier than average at -0.12 \%rh and more humid than average at 0.21 \%rh , respectively.

Interestingly, the divergence in products is also apparent in the global land average for total column water vapor (TCWV; section 2d2; Fig. 2.23c). ERA5 and GPS radio occultation (GPS-RO) estimates show TCWV close to average for 2022 whereas MERRA-2, JRA-55, and the more spatially limited ground-based global navigation satellite system (GNSS) record place 2022 much wetter at levels comparable with the previous five years.

At least part of the reason behind the ERA5-HadISDH land divergence is driven by spatial coverage differences. Plates 2.1g,h and Fig. 2.24 show that central South America and western and central Africa are regions of dry anomalies in ERA5 but mostly missing gridboxes in HadISDH. Over Africa, MERRA-2 shows mostly wet anomalies, contributing to its wetter q_{land} anomaly for 2022 which appears more comparable with HadISDH. This is similar to 2021, where La Niña was also present, with near-identical spatial patterns of anomalies. Plate 2.1g (using ERA5) shows expansive dry q anomalies spreading across the central Pacific, surrounded by expansive strong wet anomalies. These are characteristic of La Niña and are respectively drier and wetter in 2022 compared to 2021. Over land, wet anomalies over India extended farther west over Pakistan in 2022 (when Pakistan had severe flooding, section 2d5) compared to 2021, and they were also more expansive over eastern Australia and southern Africa in 2022. Dry anomalies over the northern midlatitudes were similar but located farther east compared to 2021. The

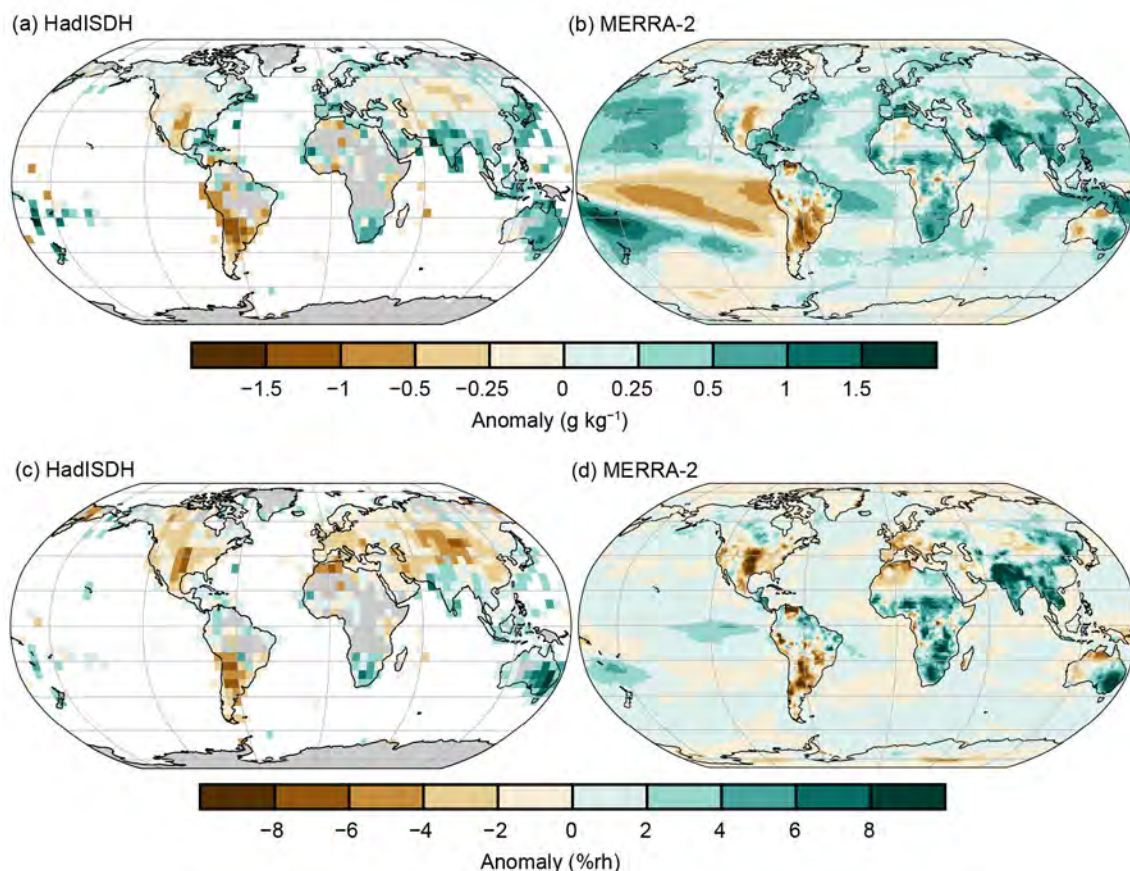


Fig. 2.24. Annual average surface humidity anomalies from the 1991–2020 average for (a),(b) specific humidity (g kg^{-1}) and (c),(d) relative humidity (\%rh). Maps for (a) and (c) are from the HadISDH in situ product that uses weather station observations. Maps for (b) and (d) are from the MERRA-2 reanalysis product.

south-central United States and subtropical South America experienced very dry anomalies in 2022. These were also regions suffering from drought.

Li et al. (2020) and Freychet et al. (2020) demonstrate a possible dry bias in ERA5 (and HadISDH.land [Willett 2023a,b]) over China from the early 2000s onward when manual wet bulb thermometers were replaced with automated RH sensors nationwide. All products contain some degree of uncertainty. For HadISDH, this is dominated by incomplete coverage and remaining inhomogeneity from changes to the observing system over time, despite considerable efforts to homogenize the data (Willett et al. 2013, 2014). For reanalyses, observation sparseness and quality and the drop in/out of data platforms over time are all sources of uncertainty. These do not undermine the conclusion of generally increasing water vapor alongside decreasing saturation levels.

Sidebar 2.1: Assessing humid heat extremes over land

— K. M. WILLETT

Extremes of heat based solely on temperature have been routinely monitored for some time using a wide range of Climpact indices (which includes those from the World Meteorological Organization Expert Team on Climate Change Detection and Indices; section 2b4; <https://climpact-sci.org/>). Although temperature is likely the dominant factor for heat-related mortality (Armstrong et al. 2019; Lo et al. 2023), humidity can also play an important role. In fact, even at more moderate temperatures, high humidity increases the overall ‘heat’ loading on the body and can therefore lead to negative impacts on health. Physical and even mental tasks can become more difficult to complete, slowing the rate at which people function and increasing the amount of rest required. The resulting decreased productivity can have a negative economic impact in addition to health and wellbeing impacts (Parsons et al. 2022).

Relative humidity is the level of water vapor saturation in the atmosphere. As this depends both on the water vapor content and the temperature of the air, knowing the relative humidity alone is not a useful measure in terms of heat stress. The wet bulb temperature, T_w , was until recently a commonly observed meteorological variable and can be relatively easily calculated from standard meteorological variables in most conditions. The lower the level of saturation, the lower the T_w will be compared to the air temperature. If the air is completely saturated (relative humidity [RH]=100%rh), then the T_w will

equal the air temperature. This becomes important for human health when the T_w approaches skin temperature, which is on average about 35°C. At this point the air closest to the skin is then saturated, meaning that sweat can no longer evaporate from the body and therefore it is no longer an effective cooling mechanism. This is then a theoretical critical threshold above which humans cannot survive, as we have no other biophysical cooling mechanisms available and so would overheat rapidly even if inactive. In practice, the critical level of T_w for the human body to function is below 32°C (Vecellio et al. 2022).

With this in mind, quantifying the current exposure to high T_w and monitoring change over time is important, as is looking at future potential changes given further warming. Building on the existing surface-humidity monitoring product HadISDH.land (Willett et al. 2013, 2014), a new dataset of gridded, monthly, wet bulb and air temperature extremes indices from 1973 to present has been developed: HadISDH.extremes (v1.0.0.2022f, Willett 2023a,b). By utilizing the existing framework of the Climpact indices we can assess the different exposures to dry versus humid heat, exploring the concept of ‘stealth heat events’, where the temperature may not be considered extreme but the humidity is high. Such events may not be sufficient to cause fatalities but could still impact productivity and health. Table SB2.1 describes the core indices used here; more indices are available from the HadISDH.extremes.

Table SB2.1. Heat extreme indices for wet bulb temperature (T_w). A bigger range of indices are available at HadISDH.extremes dataset pages on HadOBS and CEDA (HadOBSID: www.metoffice.gov.uk/hadobs/hadisdh CEDA: <https://catalogue.ceda.ac.uk/uuid/2d1613955e1b4cd1b156e5f3edbd7e66>).

Index	Long name	Description
T_wX	Maximum wet bulb temperature	Gridbox mean of station month maxima of daily maximum T_w
T_wX90p	90th percentile maximum wet bulb temperature exceedance	Gridbox mean of station percentages of days where the daily maximum T_w exceeds the climatological 90th percentile of daily maxima for the month
T_wX29	29°C maximum wet bulb temperature exceedance	Gridbox mean of station percentages of days where the daily maximum $T_w \geq 29^\circ\text{C}$

HadISDH.extremes uses hourly weather station observations of wet bulb temperature that have been quality controlled from the HadISD dataset (Dunn et al. 2012, 2014, 2016; Dunn 2019; Smith et al. 2011). Wet bulb temperature is calculated from dew point temperature and air temperature using the Stull (2011) formula. To ensure a high-quality final product, only stations with sufficient data completeness are included and the final grid boxes are filtered to remove those stations where large inhomogeneities are present (see Willett 2023a,b for more details). Importantly, the high-variability nature of extremes and dependence on a single daily observation ultimately means that uncertainty is larger than for monthly mean

quantities such as those provided by HadISDH.land (section 2d1).

There are many regions of the globe for which high T_w is rare or non-existent. Fig. SB.2.1 shows the percentage of days where the T_wX exceeded 25, 29, and 31°C over the 1973–2022 record (panels a,c,e), and the number of days for 2022 as an anomaly compared to the 1991–2020 baseline (panels b,d,f). Even the lower midlatitudes experience ‘moderate’ T_w (T_wX25 , Figs. SB.2.2a,b), but ‘high’ T_w (T_wX29 and T_wX31 , Figs. SB.2.1c–f) are so far mostly limited to the lower latitudes. In the Middle East, the Persian Gulf and Red Sea regions typically experience the most frequent ‘high’ T_w but

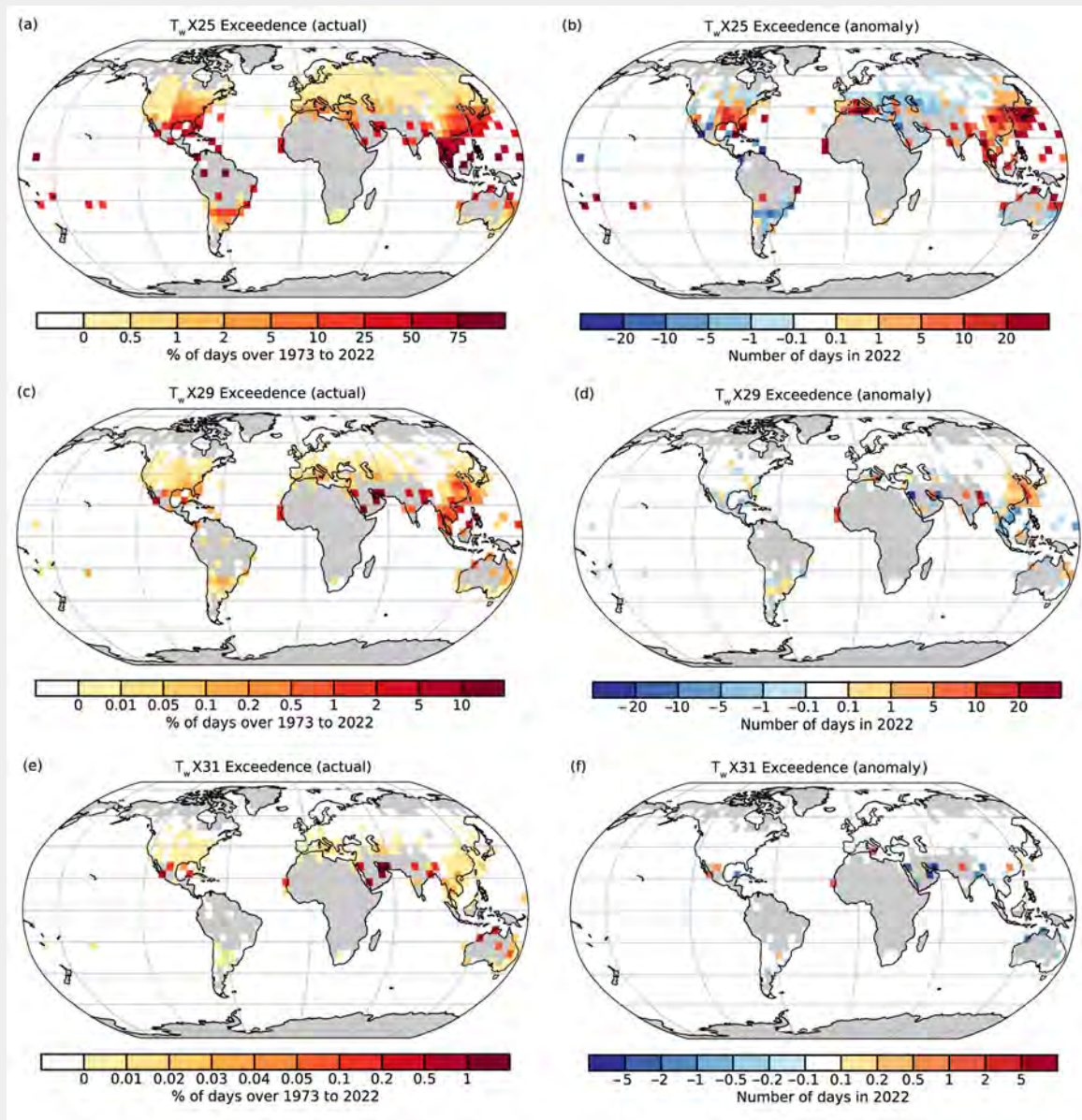


Fig. SB2.1. Number of days where the daily maximum wet bulb temperature is equal to or exceeds set thresholds from HadISDH.extremes. Data have been screened to remove grid boxes where temporal completeness is less than 70% (<35 of 50 yrs). (a),(c),(e) show the percentage of days over the 1973–2022 period and (b),(d),(f) show 2022 annual anomalies compared to the 1991–2020 base period as number of days per year. Panels (a), (c), and (e) identify land regions where there are no exceedances specifically as white grid boxes. This is different from the gray “missing data” regions.

did not during 2022. Interestingly, the 2022 heatwave in the United Kingdom (UK; sections 2b4, 7f2), despite record-breaking dry bulb temperatures, remained below the T_wX25 threshold and relatively dry in terms of humidity. When averaged globally (Fig. SB2.2a), the T_wX25 and T_wX29 indices show significant trends in days at 0.13 ± 0.03 days yr⁻¹ decade⁻¹ and 0.02 ± 0.01 days yr⁻¹ decade⁻¹, respectively.

The T_wX90p index is more globally applicable, though the current (1991–2020) 90th percentiles for higher latitude grid boxes are less likely to be at levels sufficient to cause significant health impacts. Plate 2.1ag shows eastern North America, the UK/Europe, India, China, Japan, much of Southeast Asia, and eastern Australia with widespread higher-than-average exceedances in 2022. When averaged globally (Fig. SB2.2b) it is clear that the frequency of these ‘moderate’ humid heat extremes are increasing, and 2022 saw a near-record-high number of day counts, surpassed only by 1998, 2016, 2020, and 2021. The long-term trend is 4.6 ± 1.08 days yr⁻¹ decade⁻¹. This time series also shows clearly that while high-humidity heat events are more common in El Niño years, with peaks occurring in 1998, 2010, and 2016, the more neutral and La Niña years of 2020 and 2021, respectively, were actually comparable.

The T_wX index shows that humid heat extremes are also becoming more severe. The global average T_wX has significantly increased since the 1970s at 0.13 ± 0.04 °C decade⁻¹ and was higher than average for 2022 (Fig. SB2.2c). The spatial anomalies (Plate 2.1ah) for 2022 follow the pattern of T_wX90p generally, demonstrating that many regions are experiencing both more frequent and more extreme humid heat events.

This new dataset, HadISDH.extremes, will be updated annually and so can be used to track changes in the frequency and severity of humid heat events. HadISDH.extremes also provides equivalent dry bulb temperature indices that have been identically processed, therefore uniquely enabling analysis of the varying contributions of dry and humid heat to a range of societal impacts.

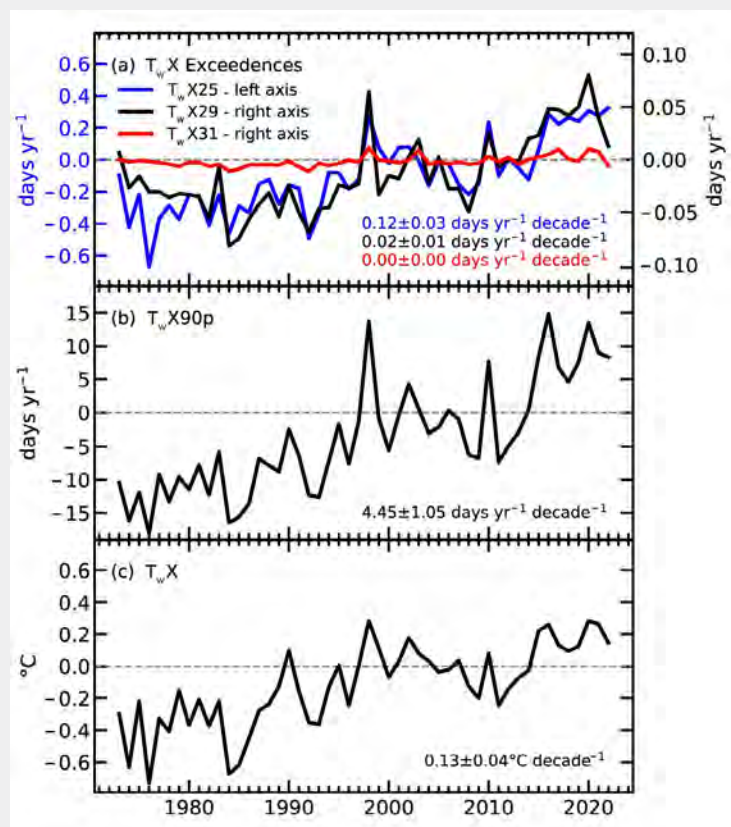


Fig. SB2.2. Global mean annual anomaly time series of various daily maximum wet bulb temperature indices from HadISDH.extremes relative to a 1991–2020 base period. Decadal trends are also shown. These were fitted using an ordinary least squares regression with AR(1) correction following Santer et al. (2008). (a) Annual sums of the daily maximum wet bulb temperature (T_wX) $\geq 25^\circ\text{C}$, $\geq 29^\circ\text{C}$, and $\geq 31^\circ\text{C}$ thresholds. (b) Annual sum of the daily maximum wet bulb temperature exceedances of the 90th percentile (T_wX90p). (c) Annual mean of the daily maximum wet bulb temperature (T_wX) of the month.

2. TOTAL COLUMN WATER VAPOR

—C. A. Mears, J. P. Nicolas, O. Bock, S. P. Ho, and X. Zhou

In 2022, the global land and ocean averages of total column water vapor (TCWV) were near or slightly above the 1991–2020 climatological averages, despite the ongoing presence of La Niña conditions in the tropical Pacific Ocean, which usually reduces the TCWV due to lower tropospheric temperatures. In reanalysis output, 2022 was the 8th (MERRA-2), 10th (JRA-55), and 14th (ERA5) highest/wettest vapor year since 1980. Time series of annual vapor anomalies from different products (Fig. 2.25) agree well for combined land and ocean averages and ocean-only averages. Over land, there is a considerable discrepancy between ERA5 and GPS-RO observations, which show a substantial decrease over land for the last two years, and ground-based GNSS observations and JRA-55 and MERRA-2, which do not show such a drop. The differences arise mainly over Africa and South America (not shown). Similar discrepancies are observed between ERA5 and surface-specific humidity and relative humidity for the last two to three years, where ERA5 is very dry compared to MERRA-2 and HadISDH (section 2d1).

The global map of TCWV anomalies (presented as percent of annual mean values to more clearly show extratropical changes) for 2022 (Plate 2.1i) shows a strong low vapor (or dry) anomaly in the central equatorial Pacific, with a strong high vapor (or wet) anomaly directly to the south and west, including much of Australia and the eastern Indian Ocean south of the equator. Much of the extratropical Northern Hemisphere shows high (wet) anomalies, which are most pronounced in the North Pacific, northern India, and the Tibetan Plateau.

Several regions had record-high or record-low vapor in the annual mean during 2022. Figure 2.26 shows a global map of the number of the three reanalysis products that indicated high or low records by evaluating annual means for the years 1980–2022. All three products agree that the central and eastern equatorial Pacific Ocean experienced a record-low anomaly; the general pattern

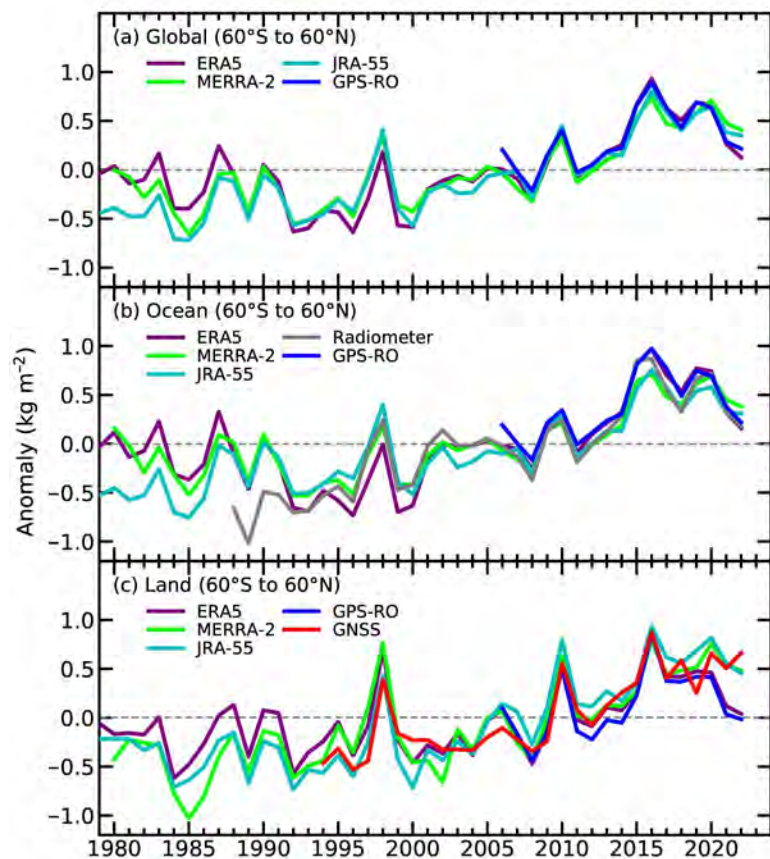


Fig. 2.25. Global mean total column water vapor annual anomalies (kg m^{-2}) over (a) land and ocean, (b) ocean only, and (c) land only from observations and reanalyses (ERA5, MERRA-2, JRA-55). The shorter time series from the observations have been adjusted so that there is zero mean difference relative to the ERA5 results during their respective periods of record.

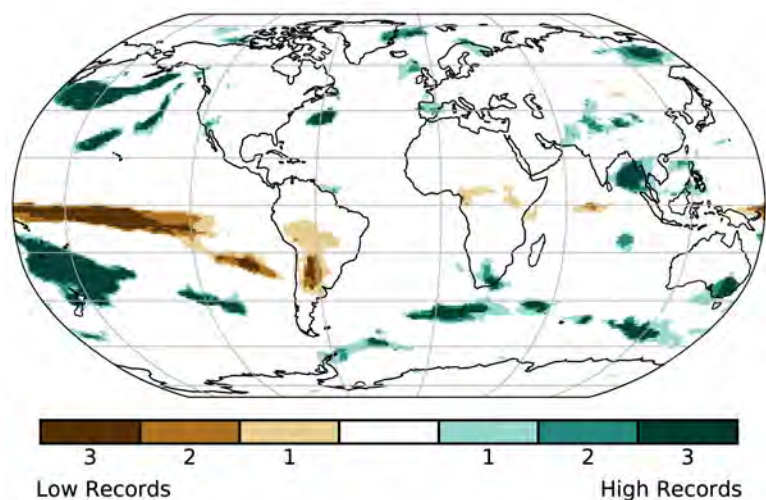


Fig. 2.26. Global map of the number of reanalysis products (out of three) that indicated a record-low or record-high annual mean total column water vapor (TCWV) anomaly during 2022 relative to the 1980–2022 period.

is consistent with typical La Niña behavior (Mears et al. 2022), but the reasons for the strength of the signal in 2022 are not yet understood. The dry anomaly extends into southern South America with slightly less agreement, where it is associated with a multiyear drought in Chile and Argentina (Heath 2022). Several regions of record-high vapor occurred over the midlatitude oceans in both hemispheres, as well as southeast Australia, which also experienced anomalously high rainfall (section 2d4), the north of New Zealand, the Bay of Bengal, and eastern Siberia.

This assessment used three global reanalysis products: ERA5 (Hersbach et al. 2020), MERRA-2 (Gelaro et al. 2017), and JRA-55 (Kobayashi et al. 2015). Measurements made over the oceans by satellite-borne microwave radiometers were used (Remote Sensing Systems Satellite; Mears et al. 2018). GPS-RO observations from the Constellation Observing System for Meteorology, Ionosphere, and Climate (COSMIC), Metop-A, -B, and -C, COSMIC2 (Ho et al. 2020a, b, 2010; Teng et al. 2013; Huang et al. 2013) and Spire satellite missions were used over both land and ocean. The approach to merge the RO data products from multiple RO missions into consistent climate data records is detailed in Shao et al. (2023). The ground-based GNSS dataset (Bock 2022) used in this analysis counts 240 stations, located mainly on continental land and a few islands, with more than 10 years of measurements (Plate 2.1i) among which 207 are located within 60°S–60°N (Fig. 2.25). All three reanalyses assimilate satellite microwave radiometer and GPS-RO data and are, therefore, not entirely independent from these two datasets. Ground-based GNSS measurements are not assimilated and serve as a completely independent dataset.

3. UPPER-TROPOSPHERIC HUMIDITY

—V. O. John, L. Shi, E.-S. Chung, R. P. Allan, S. A. Buehler, and B. J. Soden

Upper-tropospheric humidity (UTH) in 2022 was close to, or slightly below, the 2001–20 average (Fig. 2.27a). The mean and standard deviation of 2022 anomalies was -0.25 ± 0.28 %rh for the satellite microwave humidity sounder dataset (Chung et al. 2013), -0.15 ± 0.60 %rh for the satellite High Resolution Infrared Sounder (HIRS) dataset (Shi and Bates 2011), and -0.17 ± 0.33 %rh for the ERA5 reanalysis (Hersbach et al. 2020). Over the 44-year record, the HIRS and ERA5 time series have statistically insignificant trends of 0.007 ± 0.023 %rh decade⁻¹ and 0.008 ± 0.020 %rh decade⁻¹, respectively. This is consistent with the theoretical consideration that the large-scale relative humidity in the upper troposphere remains approximately constant (Ingram 2010) and implies that the absolute amount of water vapor in the upper troposphere has increased over time.

Increased upper-tropospheric water vapor is also depicted in Fig. 2.27b by a significant positive trend ($+0.105 \pm 0.008$ K decade⁻¹) in the difference between mid to upper-tropospheric brightness temperature data from satellite microwave sounding unit (MSU) and advanced microwave sounding unit (AMSU) instruments (Zou et al. 2023) and the HIRS upper-tropospheric (UT) water vapor brightness temperatures. MSU instruments measure the radiation emitted by oxygen molecules in the atmosphere. As the concentration of oxygen is not changing, the emission level of the

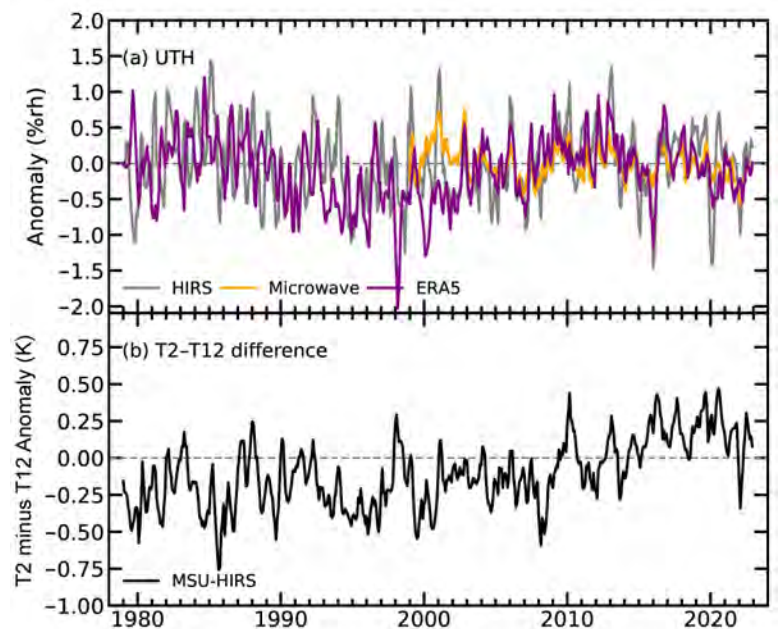


Fig. 2.27. Time series of 60°S–60°N monthly mean anomaly of (a) upper-tropospheric relative humidity (%rh) for the three datasets (see text for details) and (b) the difference between mid to upper-tropospheric temperature (MSU T2) and water vapor channel (HIRS T12) brightness temperatures (K). Anomalies are with respect to the 2001–20 base period.

oxygen channel (measuring UT temperature) is not changing, but as the temperature of the UT increases with time, there is a positive trend in the measurement of this channel (not shown). If there were no increase in water vapor, the emission level of the HIRS water vapor channel would also stay constant in time, which, due to the UT temperature increase, would result in a positive trend in the measurement of this channel and no trend in the difference between the two time series. However, as the water vapor in the UT increases, the water vapor emission level of the HIRS channel shifts higher in the troposphere and measures water vapor emissions from a colder temperature, diverging from the oxygen emission level of MSU. Differencing the time series removes the effect of the temperature increase and shows only the impact of the water vapor changes (e.g., see Soden et al. 2005; Chung et al. 2014).

Monitoring of upper-tropospheric water vapor is crucial to determining one of the strongest positive (amplifying) feedbacks contributing to anthropogenic warming due to its powerful greenhouse effect (see Coleman and Soden 2021 for a detailed description of water vapor feedback).

The agreement among the three UTH datasets is reasonable; the correlations of HIRS and ERA5 with the microwave series during their common period (1999–2022) are 0.6 and 0.5, respectively, despite their structural differences. For example, satellites represent a layer-average UTH with one satellite sampling the same location over Earth only twice a day while ERA5 represents the 400-hPa level RH with hourly sampling. The microwave data have almost all-sky sampling while the HIRS data sample only clear-sky conditions; this sampling difference is one reason for the higher interannual variability in the HIRS data as illustrated in John et al. (2011). Water vapor increases in the upper and lower troposphere since 1979 are captured by climate models when observed sea-surface temperatures are prescribed but smaller than those simulated by coupled climate simulations (Allan et al. 2022). This can be explained by the unusual spatial pattern and resulting magnitude of observed warming compared to that simulated by coupled climate models in the recent period, which included a number of strong La Niña events (Andrews et al. 2022) such as the extended event that affected 2022.

The spatial anomaly patterns (Plate 2.1j for microwave UTH; Fig. 2.28 for HIRS) relate to large-scale weather conditions, with positive (negative) anomalies associated with wetter (drier) conditions at the surface. This is because one of the main drivers of UTH is convection; therefore, UTH is useful for monitoring changes in large-scale dynamics in the atmosphere. Clear La Niña patterns are visible, with positive anomalies over the Maritime Continent and a strong dry signal in the western equatorial Pacific (centered near the date line). Prevailing drought conditions over the western United States, central Europe, and southern China are also reflected in lower-than-average UTH. Drought conditions affecting parts of South America and Angola/Namibia in Africa in 2021 may be associated with low UTH in these regions during 2022, yet severe drought affecting East Africa in 2022 is not, implying that the link between UTH and dry conditions is complex. Higher-than-average UTH over Pakistan, Nigeria, eastern Australia, and northern Brazil are associated with a series of substantial rainfall events with associated flooding in 2022.

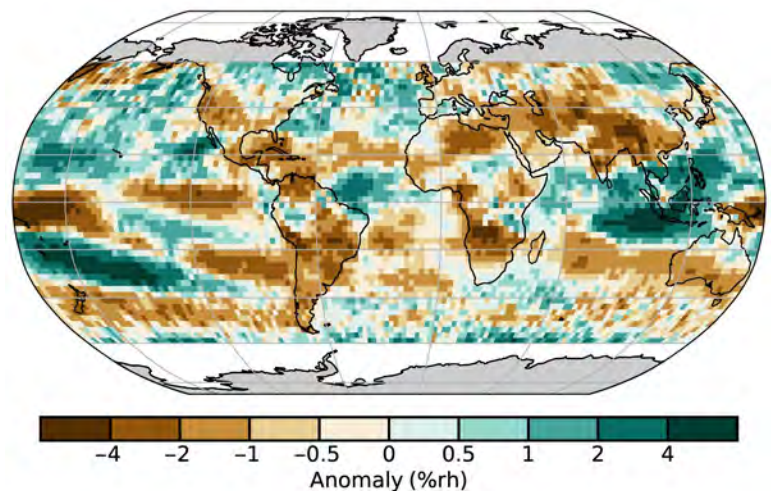


Fig. 2.28. Upper-tropospheric humidity anomaly map (%rh) for 2022 for the HIRS data record with respect to the 2001–20 base period.

4. PRECIPITATION

—R. S. Vose, R. Adler, G. Gu, U. Schneider, and X. Yin

Precipitation over global land areas in 2022, as estimated from two different monitoring products, was near or slightly below the 1991–2020 long-term average (Fig. 2.29a). In particular, the gauge-based product from the Global Precipitation Climatology Centre (GPCC; Becker et al. 2013) had an anomaly of -4.34 mm for 2022, and the blended gauge–satellite product from the Global Precipitation Climatology Project (GPCP; Adler et al. 2018) had an anomaly of -0.11 mm. Both products indicate that mean global land precipitation in 2022 was less negative than in 2021.

According to the GPCP product, the precipitation anomaly over the global ocean (Fig. 2.29b) was -18.03 mm, and the overall global (i.e., land plus ocean) anomaly (Fig. 2.29c) was -13.02 mm. Both anomalies are less negative than the previous year. The negative ocean and global anomalies are typical of La Niña, wherein below-normal sea-surface temperatures in the eastern tropical Pacific Ocean are associated with suppressed convection and rainfall. Overall, the GPCP product ranks 2022 as the fourth-driest year in the global record (Fig. 2.29c), which begins in 1979.

Over global land areas, the highest positive precipitation anomalies in 2022 were across northern South America and the Maritime Continent, and the greatest negative precipitation anomalies were over western and central North America, central South America, western Europe, and parts of southern and eastern Africa (Plate 2.1k). Over the global oceans, high positive precipitation anomalies extended from the eastern Indian Ocean southeastward to the tropical western Pacific Ocean. Parts of the equatorial Atlantic Ocean and the Southern Ocean near South America were also much wetter than average. In contrast, large negative precipitation anomalies were apparent over much of the central Pacific Ocean and the western Indian Ocean and, to a somewhat lesser extent, over parts of the north Atlantic Ocean.

La Niña, along with the Indian Ocean dipole, influenced precipitation patterns across the globe again in 2022, particularly in the tropics. The current La Niña began in 2020, and while it has varied in intensity since that time, there is a notable resemblance between the annual precipitation anomaly patterns of the past two years. For example, wetter-than-normal conditions once again extended from the Maritime Continent into the South Pacific Ocean and from northern South America into the equatorial Atlantic Ocean. Likewise, much of the central Pacific Ocean near and south of the equator were drier than normal again in 2022, as was much of the North Atlantic Ocean. The largest anomalies at the core of these wet and dry features exceeded 500 mm per year. These tropical La Niña features in 2022 helped to fuel frequent flood and landslide conditions (section 2d5), for example, in Indonesia and Malaysia, Indochina, southern India, Pakistan, and the southeast quadrant of Australia. Floods and landslides were also more prevalent across northern South America and eastern Brazil.

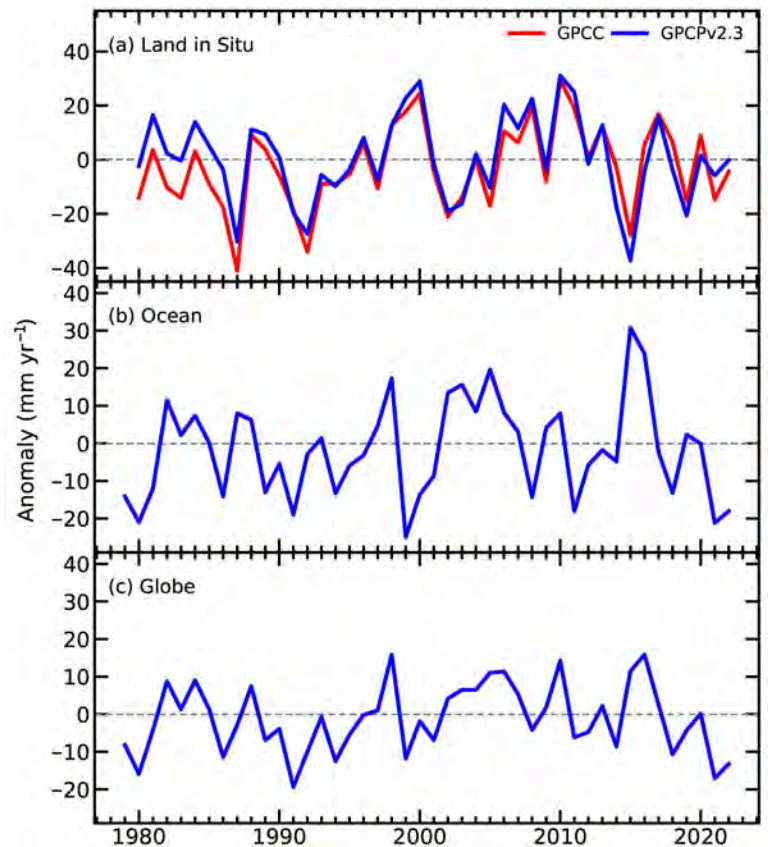


Fig. 2.29. Globally averaged precipitation anomalies (mm yr^{-1} ; 1991–2020 base period) over (a) land, (b) ocean, and (c) the globe (land and ocean). Land and ocean time series were created using a proportional land/sea mask at the $1^\circ \times 1^\circ$ scale.

5. LAND SURFACE PRECIPITATION EXTREMES

—M. R. Tye, S. Blenkinsop, M. G. Bosilovich, M. G. Donat, I. Durre, C. Lennard, I. Pinto, A. J. Simmons, and M. Ziese

Continuing La Niña conditions (see Sidebar 3.1 and section 4b for details) contributed to lower maximum-intensity rainfall than the 1991–2020 mean in South America and southern Africa and higher maximum-intensity rainfall in eastern Australia (Plate 2.11; Figs. 2.30, 2.31), continuing the pattern from recent years. Some regions with less intense rainfall extremes than average, such as Bangladesh, China, southern Europe, and the central and southwestern United States, also experienced wide-spread drought, exacerbating the resultant floods and landslides when extreme precipitation occurred over dry land.

Here, we focus on rainfall intensity indices: Rx1day (maximum rainfall in 24 hours) and Rx5day (maximum accumulated rainfall over five consecutive days). These metrics reflect strong potential for societal impacts from flooding. We use a combination of gauge-based (Global Historical Climatology Network daily [GHCND], Menne et al. 2012; GPCC, Ziese et al. 2022), reanalysis (ERA5, Hersbach et al. 2020; MERRA-2, Gelaro et al. 2017) and satellite (Climate Hazards Group InfraRed Precipitation with Station data [CHIRPS], Funk et al. 2015) data. Records demonstrate that a proportion of the globe experiences extreme precipitation in any given year. The reported events were exceptional in terms of Rx1Day and Rx5Day but are not a comprehensive list. Details on extreme flooding events can also be found in Chapter 7.

Pakistan received around three times its normal volume of monsoon precipitation in August (ECMWF 2022), with some regions receiving up to eight times their expected monthly totals (PMDNWFC 2022). It was the wettest August since Pakistan records began in 1961. Figures 2.30 and 2.31 (and Plate 2.11) show widespread strong positive Rx5day anomalies over the region. The monsoon axis was farther south than normal and was accompanied by a strong land/sea heat contrast (PMDCDPC 2022). Approximately 15% of the South Asia region (as defined in Iturbide et al. 2020) received Rx1day and Rx5day precipitation totals up to 2.5 times greater than their previous records. Recent analysis indicates that Rx5day over the Sindh and Balochistan provinces is now about 75% more intense than it would have been without climate change (Otto et al. 2022). Similar to

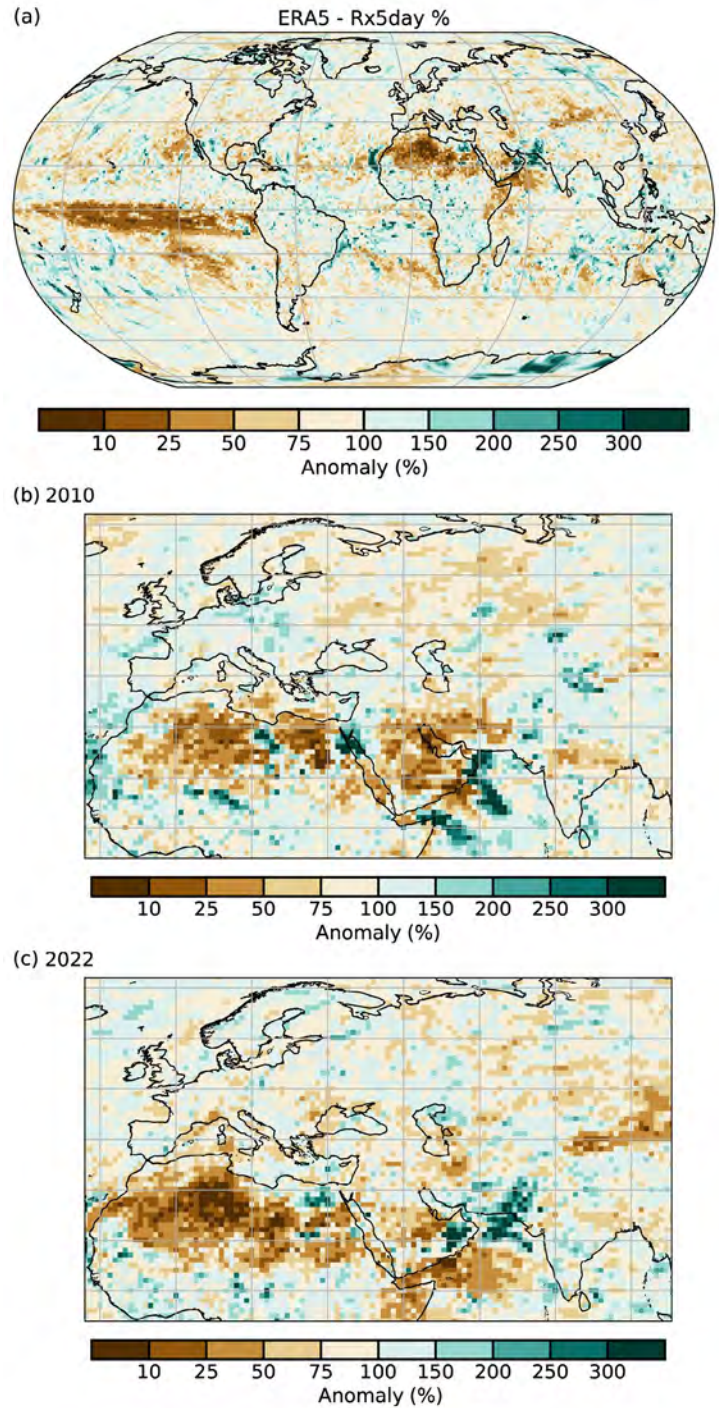


Fig. 2.30. Annual maximum five-day precipitation (Rx5day) as a percentage of the 1991–2020 average for (a) the globe and over Europe and South Asia in (b) 2010 and (c) 2022. (Source: ERA5.)

the 2010 La Niña, the duration and intensity of the most extreme rains over Pakistan in 2022 were abnormally high, while net monsoon rains over Bangladesh were below average (Rajeevan et al. 2011; Figs. 2.39b,c). Heavy rains in south and east China in June exceeded decades-old records (NCEI 2023; Fig. 2.30a), continuing a pattern of above-average Rx1day observed in this region in 2020 and 2021.

Australian floods in Queensland and eastern New South Wales between February and March caused 22 fatalities and were the costliest on record for the insurance sector (Aon 2023). Several locations had Rx5day >1000 mm during February, with Brisbane receiving 677 mm over three days and some locations doubling their previous five-day annual record (Fig. 2.31). Further flooding occurred in eastern Australia during October and November, with around 11% of Victoria gauges and 13% of New South Wales gauges reporting record Rx1day totals over the two months and around 67% of the area in the top 1% of recorded daily totals (Bureau of Meteorology [BOM] 2023; Plate 2.11; Fig. 2.30a).

Floods and landslides occurred following heavy rainfall between 11 and 13 April over southeastern South Africa (OCHA 2022a). Rx1day at Pennington South (307.2 mm) and at King Shaka Airport (221.2 mm) were more than three and four times their previous daily records, respectively (SAWS 2022). This resulted in more than \$3.6 billion in economic loss and 455 fatalities (Aon 2023).

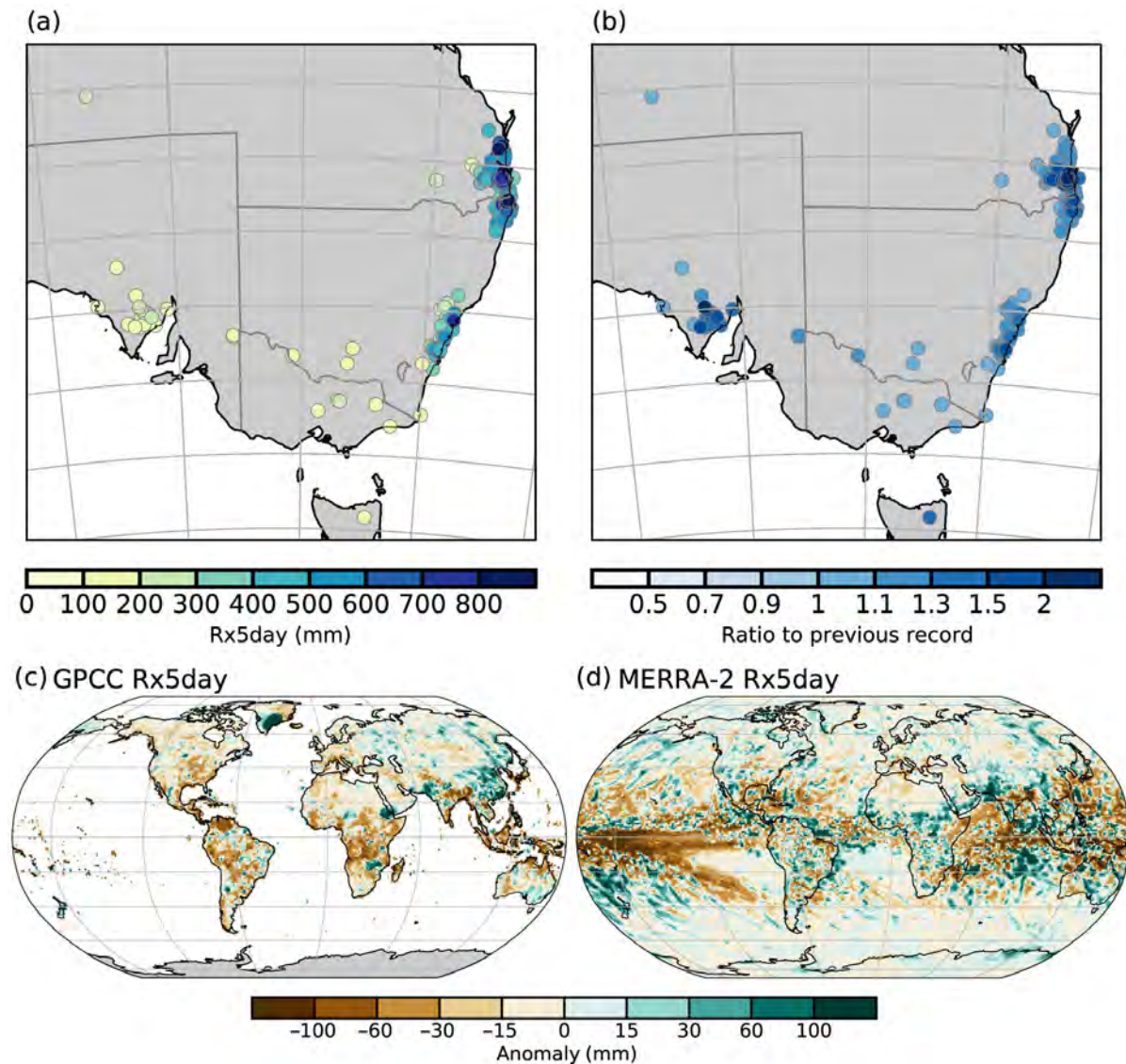


Fig. 2.31. Annual maximum five-day precipitation record-breaking totals from GHCN over southeastern Australia in Feb 2022 for (a) absolute values (mm) and (b) ratios to the previous record; (c) GPCP global Rx5day anomalies from 1981–2022 mean (mm); and (d) MERRA-2 global Rx5day anomalies from 1991–2020 mean (mm).

Heavy rainfall associated with a succession of four tropical cyclones between January and February 2022 over Madagascar, Mozambique, and Malawi caused severe humanitarian impacts and infrastructure destruction (see sections 4g6 and 7e5 for details).

Despite a wetter-than-average autumn over some parts of western and northern Europe, drier-than-average conditions persisted over most of Europe (section 7f) and were accompanied by ~67% of the Mediterranean and southern Europe region experiencing Rx1day up to 70% lower than normal (Plate 2.1l; Fig.2.30a). Exceptions to this pattern were Spain and Portugal during December. NOAA’s Climate Extremes Index component 4 (CEI4; Gleason et al. 2008) reported a slightly above-average year (12% compared to the long-term mean of 10.4%) for the percentage of the contiguous United States experiencing extreme one-day precipitation. While some regions had record-breaking values of CEI4 in summer and autumn, they do not include those affected by Hurricanes Fiona and Ian. Hurricane Ian was the second-costliest disaster on record (see Sidebar 4.1), bringing exceptional Rx1day and Rx5day to Florida as evidenced in Fig. 2.30a and Plate 2.1l.

6. CLOUDINESS

—C. Phillips and M. J. Foster

Cloudiness in 2022 was at its lowest coverage since the Pathfinder Atmospheres – Extended (PATMOS-x v6.0; Foster et al. 2023) satellite record began in 1980, with a mean global cloud area fraction of 65% (Figure 2.32). Dataset reliability is lower this year (see below), but the Clouds and the Earth’s Radiant Energy System Energy Balance and Filled (CERES EBAF) record, beginning in 2000 supports this by showing 2022 as having the second-lowest amount of solar radiation reflected by clouds relative to clear-sky. The eruption of the large Hunga Tonga–Hunga Ha’apai volcano in the South Pacific, which ended on 15 January, had the potential to impact the global or regional cloud amount, and a sharp decrease in global cloudiness was observed afterwards. However, Plate 2.1m and closer spatial analysis did not indicate any definitive connection to the eruption.

During 2022, there were several important satellite transitions, launches, and changes affecting cloud observation from space. Most relevant here, the *Aqua* satellite used previously (Platnick et al. 2015; Phillips and Foster 2022) started to drift significantly in orbit. The effective sampling time-of-day is no longer stable, and systematic diurnal variation of cloudiness must be accounted for. The PATMOS-x v6.0 cloud climate dataset (Foster et al. 2023) is used instead. Its constituent satellites also suffer from severe orbital drift and intersatellite differences, but the record starts in 1980 and is thus much longer than *Aqua* Moderate Resolution Imaging Spectroradiometer (MODIS), which begins in 2002.

Differences in sensors can make comparison difficult, as the errors in cloud area fraction are likely to be systematic and conditional on the cloud type, time of day, scan angle, surface type, etc. This is exemplified by the differing trends between the PATMOS-x cloudiness (Fig. 2.32) and the *Aqua* MODIS-C6.1 cloudiness. PATMOS-x shows a long-term decline in cloud area fraction, whereas *Aqua* MODIS-C6.1 previously showed an increase (Phillips and Foster 2022), and the drifting *Aqua* MODIS-C6.1 recorded the most cloud coverage on record for 2022 (not shown). For context, Fig. 2.33 shows the cloud radiative effects from CERES EBAF-top-of-atmosphere

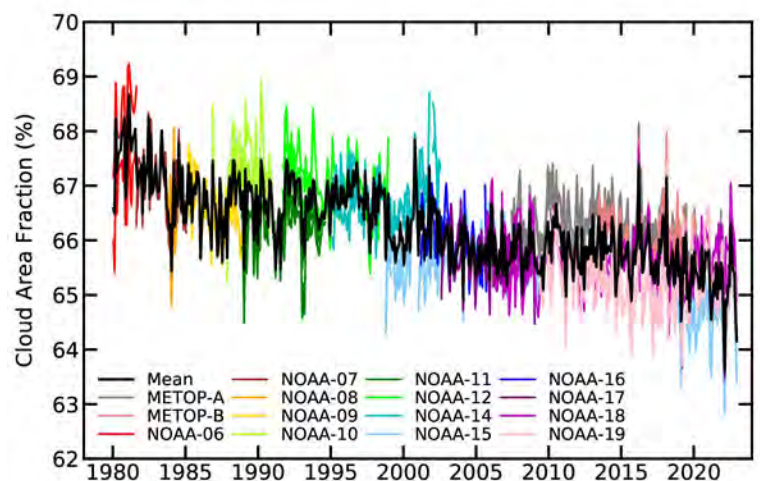


Fig. 2.32. Global mean cloud area fraction (%). (Source: PATMOS-x v6.0 [Foster et al. 2023].)

Ed4.2 through December 2022 (Loeb et al. 2018). Cloud radiative effect in this case is defined as the difference between average clear-sky observed radiative flux and average all-sky observed radiative flux. Shortwave cloud radiative effect (SWCRE) in 2022 was the second highest since the record began in 2000. This means that clouds had an anomalously large warming effect (less cooling) in the shortwave as a result of reflecting less radiation back out to space and permitting more to reach the surface. Conversely, the longwave cloud radiative effect (LWCRE) in 2022 was the second lowest. This corresponds to clouds having a stronger cooling effect (less warming) in the longwave as a result of permitting more radiation out into space and trapping less close to the surface. Added together, the shortwave and longwave cancel out such that the cloud radiative effect in 2022 was close to the mean value ($+0.05 \text{ W m}^{-2}$). More details on radiative flux and energy budget can be found in section 2f1.

Note that the cloud radiative effect can vary as the surface warms and/or changes albedo (section 2h1) without any change in cloud properties at all. However, if the cloud area fraction is indeed decreasing (as measured by PATMOS-x), this is consistent with the observed positive shortwave and negative longwave cloud radiative effect. Fewer clouds mean more absorbed solar radiation as opposed to reflected and also more longwave emission to space from the warm surface. Cloudiness has long been a difficult essential climate variable to quantify, and we conclude that uncertainty remains large.

7. LAKE WATER LEVELS

—B. M. Kraemer, H. A. Dugan, S. La Fuente, and M. F. Meyer

For 264 of the world's largest lakes, the 2022 mean water-level anomaly was 1.59 m above the 1992–2002 baseline, with 67% having higher-than-average levels (data from Birkett et al. [2022]; Birkett and Beckley [2010]; Crétaux et al. [2011]). Water-level anomalies ranged widely from -65.75 m to $+157.02 \text{ m}$, with the most extreme anomalies due to reservoir filling and drainage. The median water-level anomaly was $+0.28 \text{ m}$ with an interquartile range of -0.14 m to $+1.12 \text{ m}$. These measurements support understanding of global hydrological changes, water availability, drought, and the impact of human water diversions on lake water levels. Climate change affects these water levels by altering global precipitation patterns (Konapala et al. 2020) and increasing atmospheric water loss from inland waters due to higher evaporation rates (Zhao et al. 2022; Sharma et al. 2019).

Water-level anomalies in lakes varied greatly but with some regional consistency (Plate 2.1n). Lakes in the western United States, southern South America, the Middle East, and the Caucasus in eastern Europe had consistently below-normal water levels, due to a combination of a surface-vapor pressure deficit (as seen in Plate 2.1 and section 2d1), enhanced water evaporative loss, reduced precipitation, increasing human water use, and other factors (Friedrich et al. 2018;

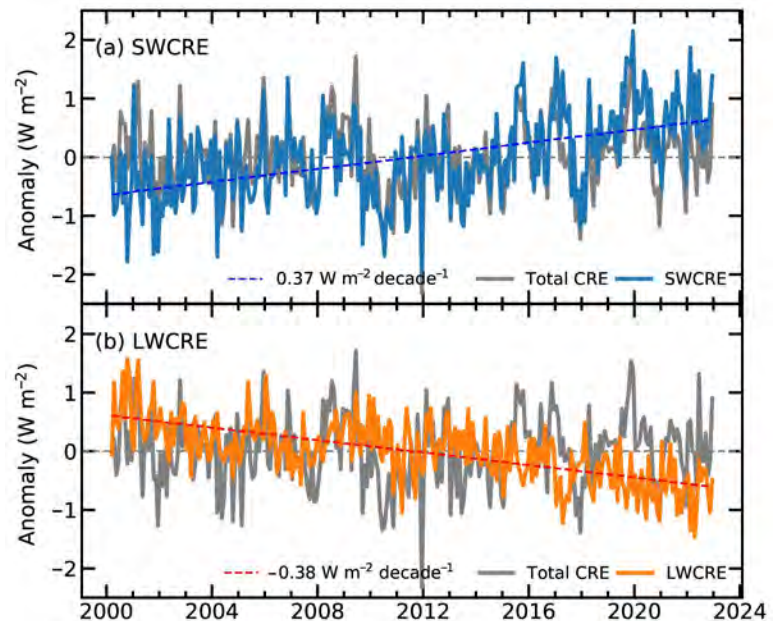


Fig. 2.33. Cloud radiative effect (CRE) anomaly (W m^{-2}) from the dataset CERES EBAF Ed4.2 (Loeb et al. 2018) representing the changes in top-of-atmosphere radiative forcing that are attributable to clouds (which could include both changes to clouds themselves and surface changes masked by clouds). Positive values indicate (a) cloudiness-related warming through more radiation reaching the surface and less being reflected back out to space (SWCRE, blue line) or (b) more being trapped close to the surface rather than escaping out to space (LWCRE, orange line). Gray line is total CRE. Negative values indicate cloudiness-related cooling.

Khazaei et al. 2019; Pisano et al. 2020). The largest negative volumetric anomalies (water-level anomalies multiplied by static lake surface area from HydroLAKES; Messenger et al. 2016) were all in the Middle East, including the Caspian Sea, Aral Sea, and Lake Urmia (Fig. 2.34). Lakes in Canada, the tropics, and southern Asia tended to have positive water-level anomalies. The six largest positive volumetric anomalies were all found in tropical Africa: Lakes Victoria, Tanganyika, Malawi/Nyasa, Turkana, Volta, and Nasser (Fig. 2.34) due to years of above-average precipitation (although the tropical African precipitation anomaly for 2022 was not above average, as seen in Plate 2.1k). Positive water-level anomalies can be explained in general by climate variability and change through increasing heavy precipitation, as well as by dam management and reductions in human water demand (Vanderkelen et al. 2018). Snowmelt may also contribute to higher water levels in northern and high-altitude regions (Zhang et al. 2019; Woolway et al. 2020; Kraemer et al. 2019). In general, the global patterns in water-level anomalies with radar altimetry match those observed using data from the Gravity Recovery and Climate Experiment (GRACE) satellite mission (as seen in Fig. 2.34 and section 2d8; Landerer and Swenson 2012) with exceptions in East Africa and northern North America where local lake conditions may cause water levels to diverge from terrestrial water storage patterns.

To detect water-level anomalies for 2022, we used radar altimeter measurements obtained from the NASA/CNES Topex/Poseidon and Jason satellite missions through the Global Reservoir and Lake Monitoring (G-REALM; https://ipad.fas.usda.gov/cropexplorer/global_reservoir/) project

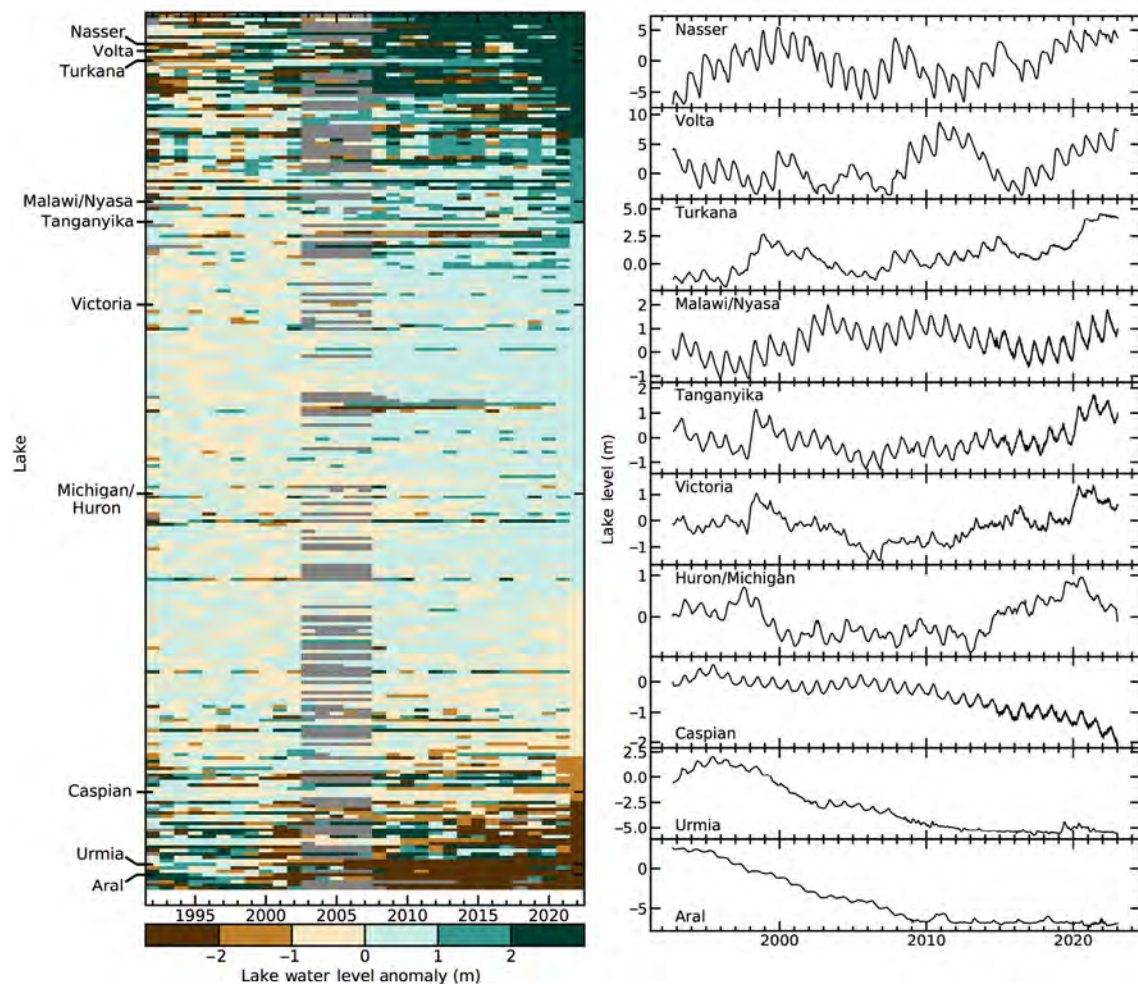


Fig. 2.34. Lake water-level anomaly (m) time series for 264 globally distributed lakes ranked by their 2022 anomaly relative to the 1992–2002 mean (based on data from Birkett et al. 2022; Birkett and Beckley 2010; Crétaux et al. 2011). Of the 264 water level time series, 106 had substantial data gaps from 2003 to 2008 due to changes in the orbital pathways of the satellite altimeters during that time period. The subset of lakes that are named on the y-axis of (a) and plotted in (b) are those with the 10 largest anomalies (either positive or negative) when water levels anomalies were weighted by the surface area of each lake. The time series plots (b) are sorted by volumetric anomalies with the largest positive anomaly on the top and the largest negative anomaly on the bottom.

version 2.5 (Birkett et al. 2022; Birkett and Beckley 2010) and Theia's Hydroweb database (downloaded 16 January 2022; <https://hydroweb.theia-land.fr/>; Crétaux et al. 2011). Lake surface areas are from the HydroLAKES database (Messenger et al. 2016). The 264 lakes in this analysis contain more than 90% of Earth's liquid surface freshwater (Messenger et al. 2016), have the longest (31+ years) and highest resolution time series, and are updated in near real-time. Water levels are usually measured every 10 days, but with some lake-to-lake variation. To ensure consistency, the lake time series were linearly interpolated to daily timescales. Due to changes in orbital pathways of the satellite altimeters, 103 of the 264 lakes had substantial data gaps from 2003 to 2008, thus a period before these gaps (1992–2002) was used as the baseline for calculating anomalies. Monitoring lake water levels on-site is important for verifying and adjusting satellite estimates of long-term water level changes. However, the lack of readily available, machine readable, and near-real-time data limits our ability to monitor global-scale changes using only on-site data. Comparisons between satellite altimeter and on-site measurements have a root mean square error of ~5 cm for large lakes (Birkett and Beckley 2010).

Satellite radar altimeters are an effective tool for monitoring volumetric change in inland waters, as they provide frequent coverage regardless of cloudiness. However, most satellite altimeters were designed for mapping ocean heights and are best used to monitor the largest lakes (Crétaux et al. 2011; >1000 km²). By chance, 155 smaller lakes (10 km²–1000 km²) are also included here because they had enough overpasses. Multispectral satellites like LandSat-8/9 and Sentinel-2 can detect changes in lake area (Khandelwal et al. 2022; Pekel et al. 2016; Meyer et al. 2020) at high-resolution (30 m) and frequent coverage (10 days–16 days), but require cloud-free conditions. The December 2022 launch of the Surface Water and Ocean Topography (SWOT) satellite is anticipated to revolutionize lake water-level monitoring due to its high spatial resolution (50 m) and frequent coverage (≤21 days) (Biancamaria et al. 2016). Meanwhile, efforts to harmonize existing lake water-level data sources and develop tools to improve accessibility will enhance our understanding of water cycle variations.

8. GROUNDWATER AND TERRESTRIAL WATER STORAGE

—M. Rodell and D. N. Wiese

Terrestrial Water Storage (TWS; the sum of groundwater, soil moisture, surface water, snow, and ice) reached 20-year highs or lows in several regions in 2022. Changes in mean annual TWS between 2022 and 2021 are plotted in Plate 2.10 as equivalent heights of water (cm). Drought and heat continued to affect southern Europe in 2022, with TWS reaching 20-year lows in the Danube River basin and in the Alps. Drought in western Iran also worsened with another year of large TWS losses (some >9 cm). Above-normal precipitation provided some relief to western Russia, but TWS remained below average. Large increases in TWS (some >12 cm) were seen in Southeast Asia, due in part to the heaviest rain in 60 years falling in southern China in June and Typhoon Noru causing flooding in Vietnam and Laos in September (see section 7g for details). TWS in central and southern India approached 20-year highs as well. Extreme drought struck the Yangtze River basin in the summer of 2022, causing the river to reach record-low levels and severely depressing TWS in the region. Southeastern Australia had a very wet year, with multiple episodes of extreme rain and flooding contributing to 20-year high TWS in the Murray-Darling River basin by the end of the year. Conversely, north-central Australia became notably drier (section 7h4). Wet weather caused TWS increases in the northern portion of sub-Saharan Africa and in South Africa, with the latter experiencing record-breaking rainfall in April. Drought affected a large area of south-central Africa centered on Lake Tanganyika, diminishing TWS, yet TWS remained above normal in almost all of sub-Saharan Africa. In North America, dry weather caused TWS declines up and down the U.S. Central Plains, while previously elevated TWS dropped closer to normal levels in the eastern United States. As a result, TWS in the Mississippi River basin dropped to a 20-year low, as water levels in October in the lower Mississippi River itself were the lowest since at least 1988. TWS in the southwestern United States was nearly unchanged from the low levels in that region in 2021. TWS increased in south-central Canada

and decreased in north-central Canada. In South America, eastern Brazil gained a huge amount of water, exceeding 12 cm over a large area, while northern Brazil added to already elevated TWS levels. Much of the western half of the continent's TWS experienced declines due to subpar rainfall.

Figures 2.35 and 2.36 depict zonal-mean and global-mean TWS anomalies, respectively, since April 2002 after removing the seasonal cycle. Data gaps occur during the interim between the GRACE and GRACE-FO missions and when onboard instruments were shut down for various reasons. In addition to excluding from these averages TWS declines associated with ice sheet and glacier losses in Antarctica, Greenland, the Gulf Coast of Alaska, and polar islands (as per Rodell and Wiese 2022), more areas where glacier ablation caused long-term trends in High Mountain Asia, western Canada, and in the southern Andes were also excluded this year. Most notably, 2022 witnessed intensification of both a dry zone between about 25°N and 45°N and a wet zone between about 8°S and 15°N (Fig. 2.35). The former is attributable to TWS declines in the central and eastern United States, southern Europe, the Caspian Sea and adjacent lands, and eastern China. The latter was caused by TWS gains in eastern Brazil, northern sub-Saharan Africa, southern India, and southeastern Asia. South of that zone of wetness, dryness that began in 2019 or earlier appears to be abating, also owing to TWS gains in eastern Brazil. At the global scale (Fig. 2.36), TWS, excluding ice sheets and glaciers, fluctuated by about 1 cm throughout the year, remaining stable with respect to 2021 and somewhat low overall.

TWS is a useful indicator of hydroclimatic variability because it reflects the integrated effects of weather over months to years. Groundwater and terrestrial water storage are not well monitored at regional and larger scales using conventional approaches, but the GRACE and GRACE Follow-On satellite missions have provided global, monthly time series of TWS anomalies (departures from the long-term mean) since 2002 (Tapley et al. 2004; Landerer et al. 2020). On a monthly scale, uncertainties are typically around 1 cm to 2 cm equivalent height of water over a 500,000 km² region at midlatitudes (Wiese et al. 2016). Groundwater typically dominates the interannual variations in TWS except in the wet tropics (dominated by surface water) and high latitude and alpine regions (dominated by ice and snow; Getirana et al. 2017).

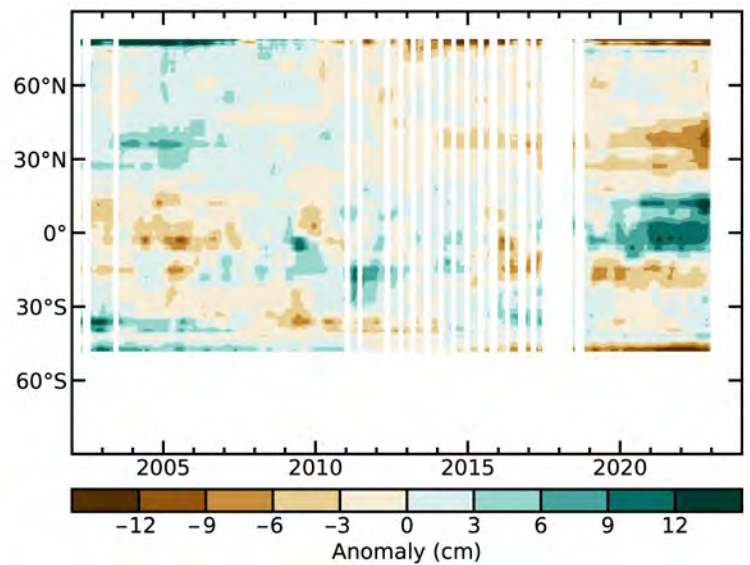


Fig. 2.35. Zonal means of monthly terrestrial water storage anomalies, excluding those in Antarctica, Greenland, the Gulf Coast of Alaska, polar islands, and major glacier systems, in cm equivalent height of water (cm), based on gravity observations from GRACE and GRACE-FO. Anomalies are relative to a 2003–20 base period.

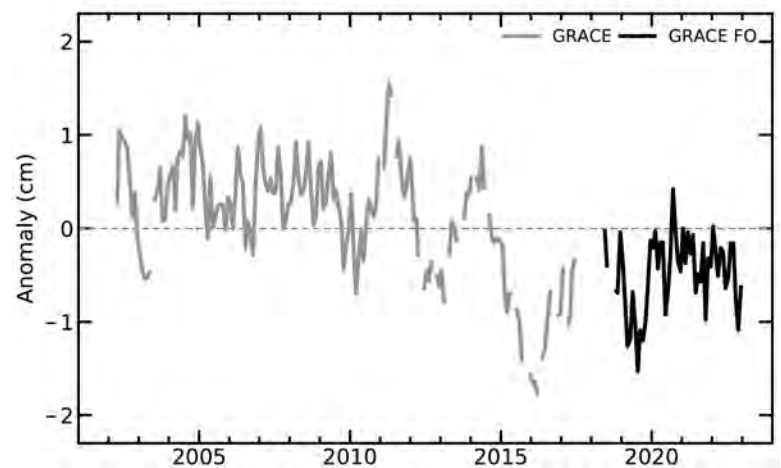


Fig. 2.36. Global average terrestrial water storage anomalies from GRACE (gray) and GRACE-FO (black), in cm equivalent height of water (cm), relative to a 2003–20 base period.

9. SOIL MOISTURE

—P. Stradiotti, W. Preimesberger, R. van der Schalie, R. Madelon, N. Rodriguez-Fernandez, M. Hirschi, A. Gruber, S. Hahn, W. A. Dorigo, R. A. M. de Jeu, and R. Kidd

The year 2022 saw a global increase in average soil moisture for the fourth consecutive year, with conditions close to the previous wet record of 2011 and of similar magnitude in both the Southern and Northern Hemisphere (SH and NH; Fig. 2.37). The year was generally a continuation of 2021 (van der Schalie et al. 2022), the largest difference between the two consisting of a transition from below- to above-average soil moisture (compared with the 1991–2020 base period) in parts of the SH (Fig. 2.38).

The third consecutive La Niña year (2020–22; see Sidebar 3.1 for details) brought about distinct patterns of precipitation (section 2d4) resulting regionally in above-average soil moisture. This was the case for eastern Australia, where wetter-than-normal conditions persisted throughout the year and turned into localized strong positive anomalies (above $0.1 \text{ m}^3 \text{ m}^{-3}$; Supp. Fig. A2.8). Widespread strong positive anomalies of similar magnitude also characterized most of South and mainland Southeast Asia since the start of the year, linked to the effect of La Niña on rainfall in the wet season (Hrudya et al. 2021). With the onset of the Indian summer monsoon, these conditions shifted from central and southern India to northwestern India and Pakistan, coinciding with severe floods (Smiljanic et al. 2022). Consistent with 2021, southeastern Africa (including southern Mozambique and South Africa) experienced a wetter-than-usual phase starting in April and characterizing the whole dry season until November. Northeast Brazil started the year with strong wet anomalies that dried to average conditions by April, only to strengthen again in November and December. Areas of above-average soil moisture were also noticeable in eastern Europe and in the coastal regions surrounding the Yellow Sea for most of 2022.

While on average 2022 recorded wetter-than-normal soil moisture conditions, dry conditions were dominant in several regions. The Great Plains of central North America experienced notable below-average conditions (consistent with the deeper layers; section 2d8) that worsened during the year. These likely intensified the summer heatwaves affecting the region through local land–atmosphere interactions (Benson and Dirmeyer 2021). The strong (below $-0.1 \text{ m}^3 \text{ m}^{-3}$) dry anomalies developed in the southern Great Plains and moved northward, reaching Montana and the Canadian Prairies

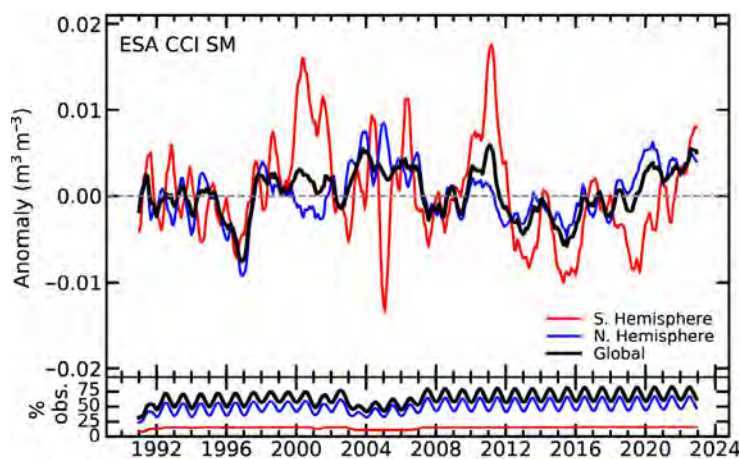


Fig. 2.37. Time series of global (black), Northern Hemisphere (blue), and Southern Hemisphere (red) monthly surface soil moisture anomalies for the period 1991–2022 (upper, $\text{m}^3 \text{ m}^{-3}$; 1991–2020 base period) and the valid observations as a percentage of total global land surface (lower, %). Data are masked where no retrieval is possible or where the quality is not assured and flagged, for example due to dense vegetation, frozen soil, or radio frequency interference. (Source: C3S Soil Moisture.)

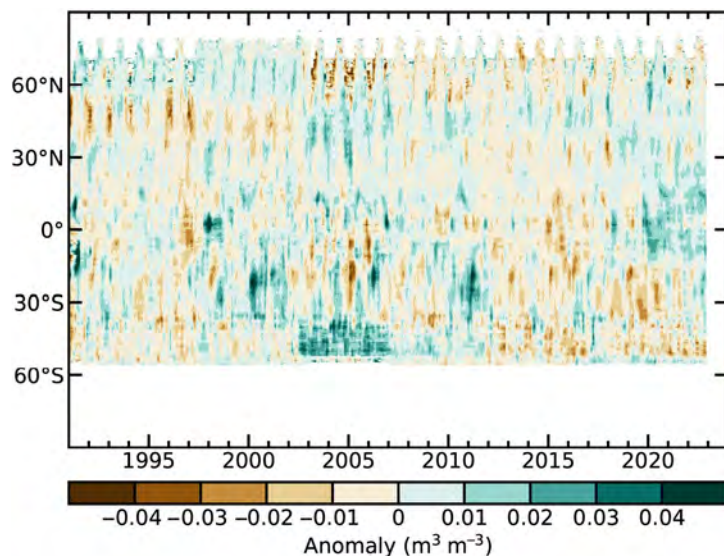


Fig. 2.38. Time–latitude diagram of monthly surface soil moisture anomalies ($\text{m}^3 \text{ m}^{-3}$; 1991–2020 base period) for the period 1991–2022. Data are masked where no retrieval is possible or where the quality is not assured and flagged, for example due to dense vegetation, frozen soil, or radio frequency interference. (Source: C3S Soil Moisture.)

in autumn. This aggravated the water deficit of the region for the second consecutive year (van der Schalie et al. 2022). Persistent dry conditions also continued in southern South America and were especially pronounced in the Rio Paraná basin and Patagonia, now in a four-year-long drought spell (Naumann et al. 2021). In eastern Africa, the Indian Ocean dipole (IOD) is one of the main drivers of intra-annual climatic variability along with the El Niño–Southern Oscillation (Nicholson 2017; Marchant et al. 2007; Anderson et al. 2022). The negative IOD mode, which lasted until October 2022 (see section 4f for details), is consistent with the below-average soil moisture observed for most of the Horn of Africa, northern Mozambique, and Madagascar, developing into very dry conditions toward the end of the year. Negative anomalies for the region are a continuation of the severe droughts in recent years (Anderson et al. 2022). Mild negative anomalies remained steady throughout 2022 around the Mediterranean Sea regions (Spain, northern Morocco, Libya, and Tunisia). In large parts of China and northern Asia, widespread negative anomalies persisted and intensified in the eastern Siberian tundra region at the end of the boreal autumn. However, the strong negative water deficit in the Yangtze River basin (section 2d8) is not as visible in the surface layer.

A strong intra-annual variation was observed in western and northern Australia, with average to very dry conditions (below $-0.1 \text{ m}^3 \text{ m}^{-3}$) in the first part of the year giving way to slightly positive anomalies from mid-year. A similar progression was observed for the Arabian Peninsula and the Persian plateau, northern Europe (Scandinavian peninsula), and the southern Sahel regions. In contrast, the Pacific Northwest region started 2022 with above-average conditions, which subsided toward the boreal summer, turning to below-average soil moisture by the end of the year.

Soil moisture was observed by microwave satellite remote sensing of the upper few centimeters of the soil layer, as provided by the COMBINED product of the Copernicus Climate Change Service (C3S) v202012 (Dorigo et al. 2017). C3S combines multi-sensor data in the 1978–2022 period through statistical merging (Gruber et al. 2017, 2019). Wet and dry anomalies here refer to the positive and negative deviations respectively from the 1991–2020 climatological average.

10. MONITORING GLOBAL DROUGHT USING THE SELF-CALIBRATING PALMER DROUGHT SEVERITY INDEX

—J. Barichivich, T. J. Osborn, I. Harris, G. van der Schrier, and P. D. Jones

The self-calibrating Palmer Drought Severity Index (scPDSI) over the period 1950–2022 shows that the ongoing increase in global drought since mid-2019 (Barichivich et al. 2020, 2021) reached a new historical peak in October 2022 (Fig. 2.39), surpassing the peak in August 2021 (Barichivich et al. 2022). A historical maximum of 6.2% of the global land area experienced extreme drought conditions ($\text{scPDSI} \leq -4$) in August 2022, slightly greater than the previous maximum in October 1984 (6.1%). The extent of severe plus extreme drought conditions ($\text{scPDSI} \leq -3$) in 2022 exceeded 15% of the global land area between July and November, reaching a historical maximum of 15.8% in August. Similarly, moderate or worse drought conditions ($\text{scPDSI} \leq -2$) peaked in October at a historical maximum of 29% of the global land area.

The global pattern of regional droughts in 2021 largely persisted through 2022 (Plate 2.1q). Drought severity through western

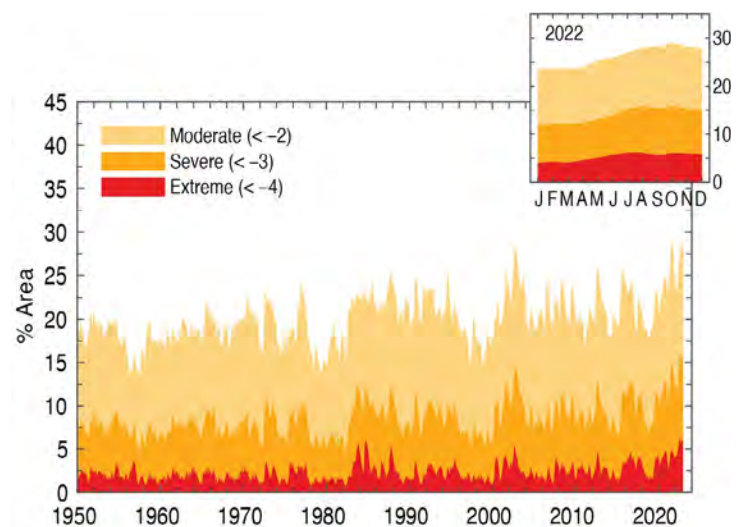


Fig. 2.39. Percentage of global land area (excluding ice sheets and deserts) with the self-calibrating Palmer Drought Severity Index (scPDSI) indicating moderate (<-2), severe (<-3), and extreme (<-4) drought for each month during 1950–2022. Inset: each month of 2022.

North America remained mostly unchanged from 2021 to 2022, but worsened in Europe, parts of South America, and the midlatitudes of Asia (Fig. 2.40). Despite persistent drought conditions in western North America, California experienced a milder fire season than in 2021 (section 2h3) but the west–east moisture contrast observed across the United States since 2017 persisted (Plate 2.1q). In South America, earlier drought hot spots through most of Chile and around the El Gran Chaco region in northern Argentina intensified (Barichivich et al. 2022). The record-breaking megadrought of central Chile reached its 13th consecutive year in 2022, and 80-year record-low river levels in northern Argentina and Paraguay (e.g., Bermejo and Paraná) disrupted fluvial transport.

A persistent lack of precipitation in large areas of Europe from winter to summer, together with warmer-than-usual conditions and a sequence of heatwaves (sections 2b4, 7f) triggered a severe-to-extreme drought (Plate 2.1q). At its peak, the drought affected more than two-thirds of Europe, becoming one of the worst historical droughts in France, Spain, Germany, and Italy. In northern Italy, the Po River and canals in Venice reached record-low levels. The drought did not extend into northern Europe, where wet conditions across Fennoscandia continued through 2022. In northern Africa, previous moderate drought intensified to extreme drought along the Mediterranean coast from Morocco to Tunisia (Plate 2.1q). Most of the Middle East from eastern Turkey to Pakistan also saw an intensification of drought to severe or extreme conditions.

Although changes in moisture anomalies through tropical Africa are uncertain due to the sparse coverage of meteorological station data, this region largely saw a continuation of the wet conditions that began in 2019 (Plate 2.1q). In southern Africa, drought conditions seen since 2018 continued through 2022 but eased slightly compared to 2021 (Fig. 2.40). In Australia, previous drought eased in the east but most of the country continued under moderate drought during 2022 (Plate 2.1q). In contrast, India and Southeast Asia experienced predominantly wet conditions. The Yangtze River basin in central-eastern China saw severe drought as a result of precipitation deficit combined with an extreme heatwave, though most of northern China saw wet conditions (see section 7g and Sidebar 7.2 for details). Previous moderate-to-severe drought in parts of northeastern Siberia and the Russian Far East continued in 2022 (Plate 2.1q).

The update of the scPDSI (Wells et al. 2004; van der Schrier et al. 2013) for this year uses global precipitation and Penman-Monteith Potential Evapotranspiration (ET) from an early update of the Climatic Research Unit gridded Time Series (CRU TS) 4.07 dataset (Harris et al. 2020). It incorporates new estimates of some variables in CRU TS4.07 compared with CRU TS4.06 used last year, affecting potential ET via an improved baseline climatology for cloud cover. These revisions modify the scPDSI drought index values throughout, notably a small reduction in the global areas of moderate and severe drought that is consistent throughout the time series.

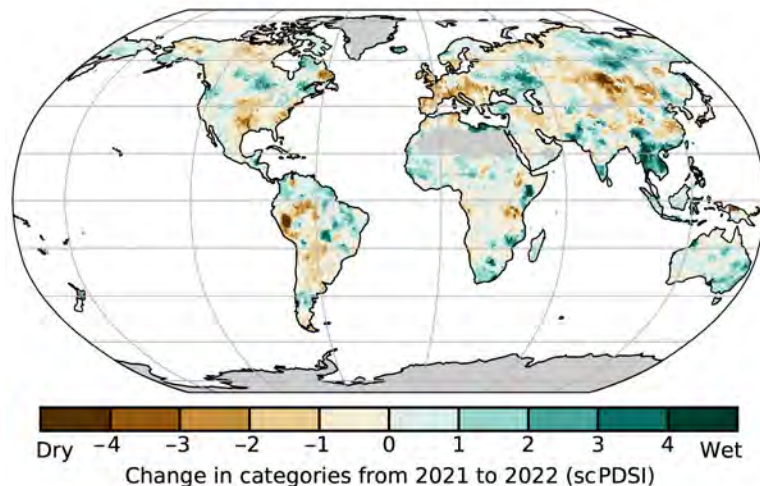


Fig. 2.40. Change in drought (self-calibrating Palmer Drought Severity Index [scPDSI]) from 2021 to 2022 (mean scPDSI for 2022 minus mean scPDSI for 2021). Increases in drought severity are indicated by negative values (brown), decreases by positive values (green). No calculation is made where a drought index is not physically meaningful (gray areas: ice sheets or deserts with approximately zero mean precipitation).

11. LAND EVAPORATION

—D. G. Miralles, A. Koppa, H. E. Beck, and M. F. McCabe

Around two-thirds of the precipitation that falls over land is returned to the atmosphere through evaporation (Dorigo et al. 2021). Understanding the spatial and temporal dynamics of evaporation is of key importance for agriculture and water management, as well as for diagnosing the influence of short-term climate variability and long-term climate changes on water resources (Miralles et al. 2014). In 2022, most land regions experienced positive (more than normal) evaporation anomalies relative to the 1991–2020 reference period (Plate 2.1r). Abnormally high values were observed in Amazonia, Southeast Asia and India, southern Africa, and eastern Australia. Most of these anomalies were linked to high precipitation (section 2d4) and coincided with reports of extreme-intensity events and floods (section 2d5). In the Amazon, precipitation enhances evaporation mainly through its influence on interception loss—the vaporization of rain stored on tree canopies and understory vegetation. For drier regions, such as eastern Australia or southern Africa, positive soil evaporation and transpiration anomalies occurred mostly in response to increased soil moisture availability (section 2d9). Conversely, anomalously low evaporation was observed across the Horn of Africa, the U.S. Central Plains, and parts of Brazil and Argentina. In water-limited regions, negative anomalies in evaporation are mainly caused by below-average precipitation (Orimoloye et al. 2022). In the Horn of Africa, the abnormally low evaporation can be linked to a prolonged meteorological drought that has already persisted for five consecutive rainfall seasons (section 7e; Anderson et al. 2023). Interestingly, despite the summer drought and heatwave events striking western Europe (sections 2d10, 7f2), no anomalously low evaporation was recorded in the region.

The global mean land evaporation in 2022 was above the 1991–2020 mean, and even above the expectation based on the positive 1980–2021 trend. This 28 mm yr^{-1} global mean anomaly is in fact the largest on record (Fig. 2.41). The geographical patterns shown in Plate 2.1r are typical of La Niña conditions (Miralles et al. 2014; Martens et al. 2018), which tend to cause an increase in global mean evaporation (see Southern Oscillation Index [SOI] in Fig. 2.41). This El Niño–Southern Oscillation-induced variability in evaporation is superimposed on a long-term trend of 0.78 mm yr^{-1} , which falls towards the high-end of trend estimates reported in the recent literature (Zhang et al. 2016; Brutsaert et al. 2017; Anabalón and Sharma 2017). This positive trend has been attributed to increasing global temperatures (Miralles et al. 2014) and terrestrial greening (Cheng et al. 2017). Both hemispheres experienced positive evaporation anomalies

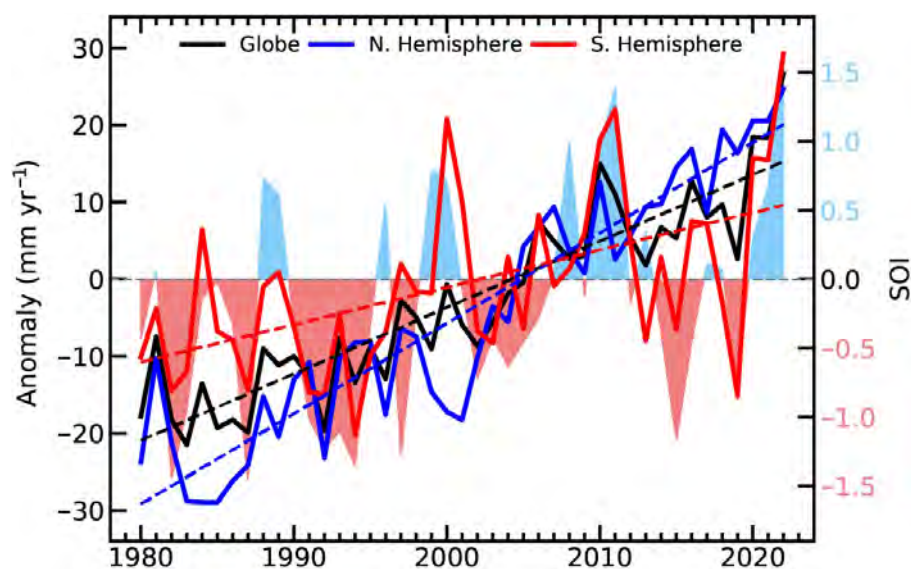


Fig. 2.41. Land evaporation anomalies (mm yr^{-1} ; 1991–2020 base period) for the Northern Hemisphere, Southern Hemisphere, and the entire globe (blue, red, and black solid lines, respectively). Linear trends in evaporation (dashed lines) and the Southern Oscillation Index (SOI) from CRU (right axis, shaded area) are also shown. (Sources: GLEAM; <https://crudata.uea.ac.uk/cru/data/soi/>.)

throughout the year, with the Southern Hemisphere in particular (Fig. 2.42) reflecting behavior consistent with La Niña conditions.

The evaporation results are based on version 3.7 of the Global Land Evaporation Assessment Model (GLEAM; Miralles et al. 2011). This version is driven by satellite observations of soil and vegetation water content (Dorigo et al. 2017; Moesinger et al. 2019), a blend of gauge, satellite, and reanalysis data for precipitation (Beck et al. 2019), and reanalysis data for radiation and air temperature (Beck et al. 2022). The reported long-term trends are affected by the indirect representation of the influence of carbon dioxide and atmospheric aridity on vegetation stress in GLEAM v3 (Martens et al. 2017). The unbiased root-mean square error is approximately 0.7 mm day^{-1} and the temporal correlation against in situ eddy-covariance measurements is around 0.8 on average (Martens et al. 2017).

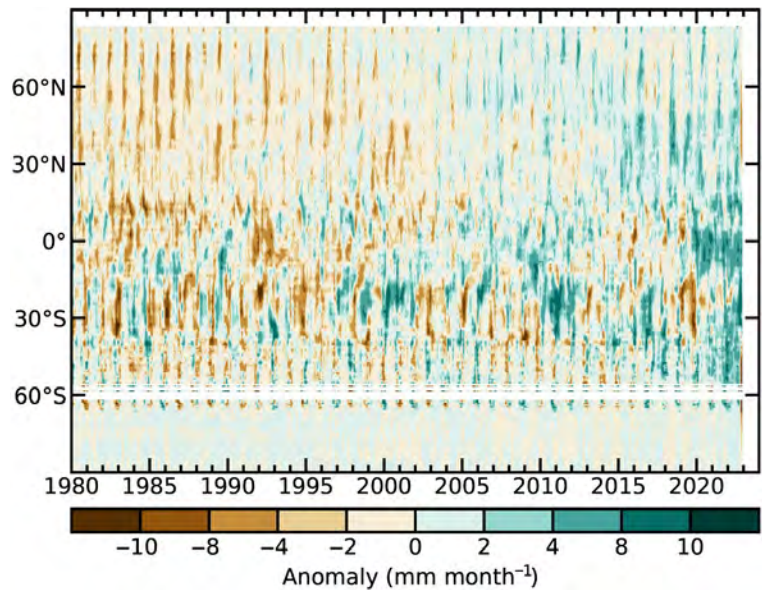


Fig. 2.42. Zonal mean terrestrial evaporation anomalies (mm month^{-1} ; 1991–2020 base period). (Source: GLEAM.)

e. Atmospheric circulation

1. MEAN SEA-LEVEL PRESSURE AND RELATED MODES OF VARIABILITY

—B. Noll, D. Fereday, and D. Campos

Mean sea-level pressure (MSLP) can be used to derive indices that describe globally important modes of atmospheric variability, which provide context to weather and climate anomalies and extremes. One of the most globally impactful modes is the El Niño–Southern Oscillation (ENSO), not only owing to its direct effects in the Indo-Pacific region but also to its teleconnections across the mid and high latitudes of both hemispheres (Capotondi et al. 2015). ENSO can be described by the Southern Oscillation Index (SOI), the normalized MSLP difference between Tahiti and Darwin (Allan et al. 1996; Kaplan 2011). The SOI was mostly positive from late 2020 through 2022, coinciding with an impactful, protracted La Niña event (following Allan and D’Arrigo 1999), which has been associated with heavy rainfall and floods in Australia and New Zealand (see sections 7h4 and 7h5, respectfully, for details), a wet summer and dry winter in south-central Chile (section 7d4), and a persistence of drought in the western United States (section 7b2).

In the tropical Indian Ocean, the Indian Ocean dipole (IOD) also influences MSLP patterns (Saji et al. 1999). The negative phase of the IOD, which developed during austral winter 2022, is associated with above-normal ocean temperatures in the tropical eastern Indian Ocean and below-normal ocean temperatures in the west (see section 4f for details). The development of an IOD event is correlated with ENSO by way of variations in the Walker Circulation (Behera et al. 2006). The combined effect of La Niña and a negative IOD contributed to a stronger-than-normal rising branch of the Walker Circulation in the eastern Indian Ocean, western Pacific, and across Australasia, which influenced regional moisture availability and global atmospheric circulation patterns during the year.

Variability in MSLP is also expressed at the regional scale by modes including the Arctic Oscillation (AO), the North Atlantic Oscillation (NAO), and the Pacific/North American (PNA) in the Northern Hemisphere (NH) as well as the Southern Annular Mode (SAM)/Antarctic Oscillation (AAO) in the Southern Hemisphere (SH; Kaplan 2011).

In the NH, the winter NAO is the leading winter mode of variability in the North Atlantic/European (NAE) region, comprising an MSLP dipole with centers over Iceland and the Azores. The NAO was positive in January and February (Fig. 2.43a), consistent with the strong

stratospheric polar vortex, while (as in 2021) the PNA index was mostly negative throughout the year, in line with the persistent La Niña event (Yeh et al. 2018). The winter NAO and PNA are generally independent (Soulard and Lin 2017). A prolonged high-pressure anomaly occurred over Europe in spring and summer (Figs. 2.43b,c) driving extreme dry and hot conditions (see section 7f for details). The summer NAO (the leading NAE-region mode of variability in July and August; Folland et al. 2009) is an MSLP dipole with centers over Greenland and northern Europe. The 2022 summer NAO index was the second highest in the series dating to 1959, underlining the strength of the MSLP anomaly (Fig. 2.43e). In December, the winter NAO was once again negative, as is weakly favored by La Niña in early winter (e.g., Moron and Plaut 2003).

The SAM, which contributes to up to 34% of the variability in the extratropical SH atmospheric circulation (Fogt and Marshall 2020), was positive for a record-tying 76% of days during 2022 (Fig. 2.44e). This matched the record set in 1998 and was the sixth time since 2015 that the SAM was positive for more than 60% of days. Positive SAM events often occur during La Niña, and the SOI and SAM show a positive correlation starting around 1990 (Clem and Fogt 2013). The upward SAM trend in recent decades, particularly during austral summer, has been associated with a poleward shift of the westerly wind belt in the SH (Fogt and Marshall 2020), which also

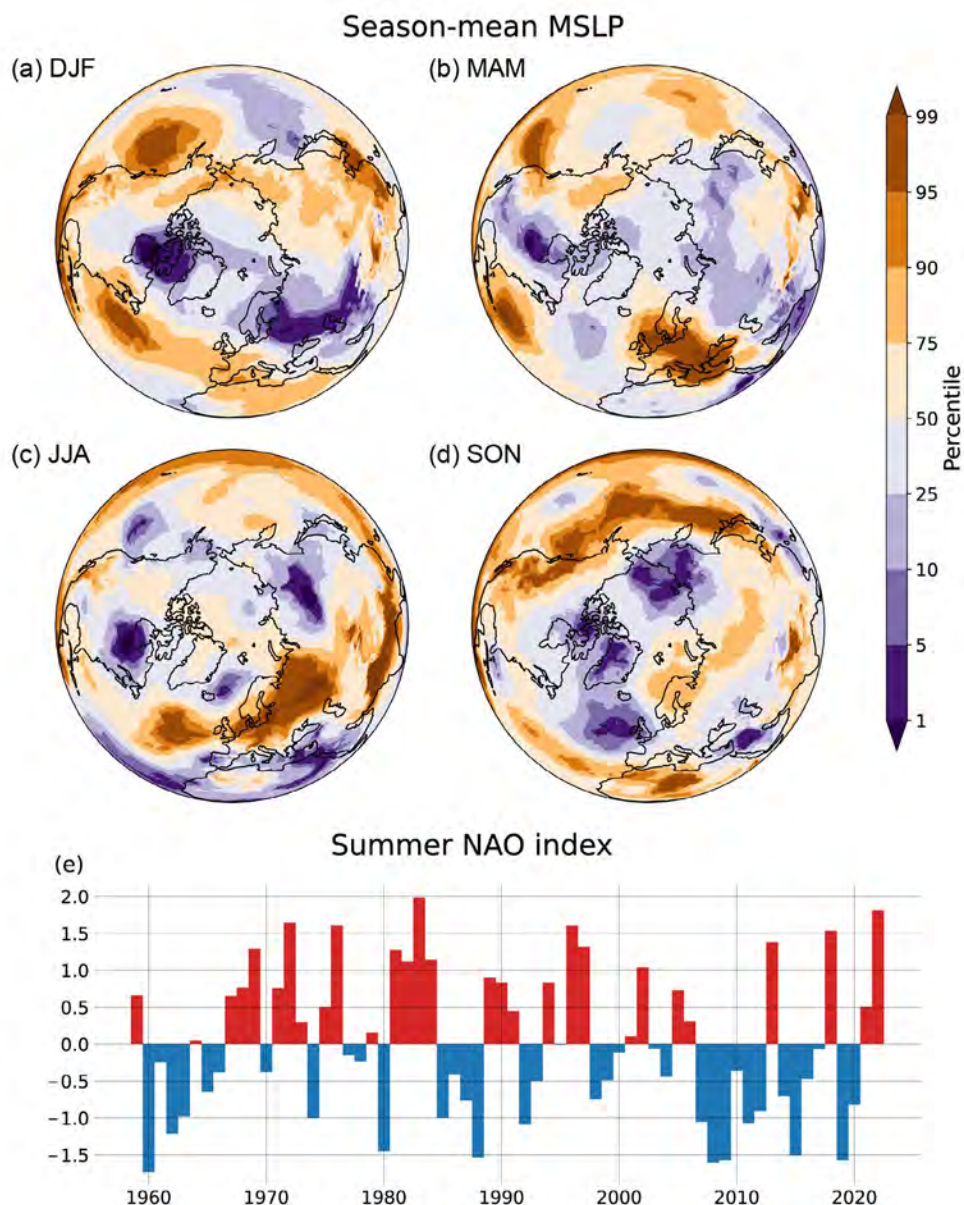


Fig. 2.43. Northern Hemisphere circulation in 2022. (a)–(d) seasonal mean sea-level pressure (MSLP) anomalies with respect to the 1991–2020 base period, shown as percentiles based on the 1959–2022 period. (e) Jul/Aug summer North Atlantic Oscillation (NAO) index for the period 1959–2022. (Source: ERA5 [Hersbach et al. 2020].)

occurred in 2022. This was associated with a prominent belt of higher-than-normal MSLP from the sub-Antarctic Indian Ocean, across New Zealand, and into southern South America (Fig. 2.44; Plate 2.1s), contributing to New Zealand’s warmest year on record (section 7h5). The combined effect of the SAM, ENSO, and IOD teleconnections contributed to lower-than-normal MSLP across Australia and the Maritime Continent. 2022 was Australia’s ninth-wettest year on record, with parts of New South Wales experiencing its wettest year on record (section 7h4). In association with higher-than-normal sea-surface temperatures (SSTs), annual precipitable water values were above normal in the tropical eastern Indian Ocean, across northern and eastern Australia, and into the southwestern Pacific, contributing to greater moisture availability for low-pressure systems in the region and culminating in some impactful atmospheric river events, such as New Zealand’s strongest August atmospheric river on record (see section 7h5; NIWA 2022b). In the South Pacific, a prominent pressure dipole was observed, especially during the winter, in response to La Niña, a positive SAM, and the presence of above-normal SST anomalies in the southwestern Pacific (Garreaud et al. 2021).

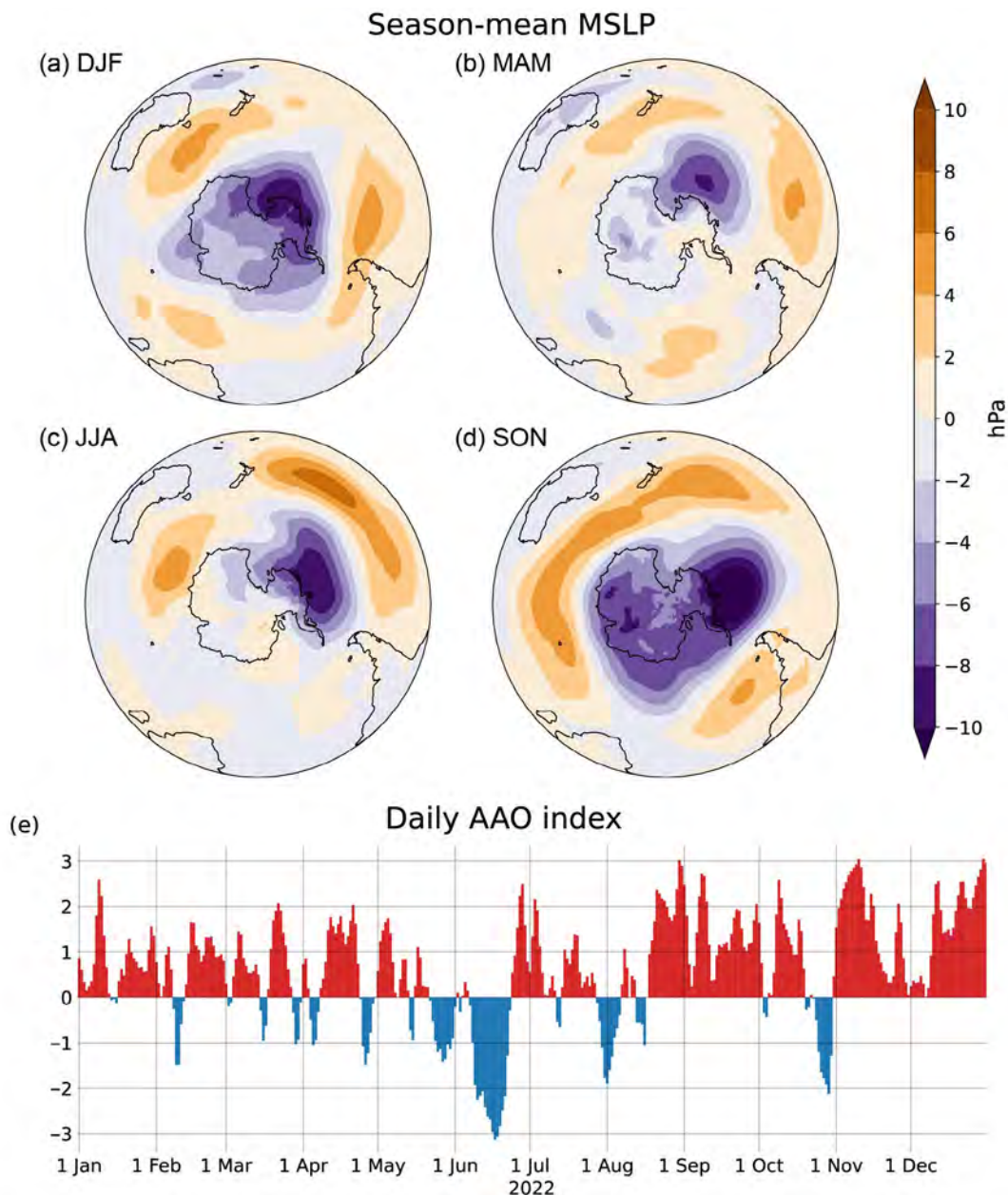


Fig. 2.44. Southern Hemisphere circulation in 2022. Seasonal mean sea-level pressure (MSLP) anomalies (hPa; 1991–2020 base period) for (a) DJF 2021/22, (b) MAM 2022, (c) JJA 2022, and (d) SON 2022. (Source: ERA5 reanalysis.) (e) Daily Antarctic Oscillation (AAO) index time series. (Source: NOAA Climate Prediction Center.)

2. LAND AND OCEAN SURFACE WINDS

—C. Azorin-Molina, R. J. H. Dunn, L. Ricciardulli, C.A. Mears, J. P. Nicolas, T. R. McVicar, Z. Zeng, and M. G. Bosilovich

Relative to the 1991–2020 climatology, land surface wind-speed anomalies at ~10 m above the ground in 2022 were dominated by positive values (Table 2.6). North and South America showed the highest positive anomalies relative to the climatology ($+0.070 \text{ m s}^{-1}$ and $+0.112 \text{ m s}^{-1}$, respectively), followed by East and Central Asia ($+0.012 \text{ m s}^{-1}$ and $+0.007 \text{ m s}^{-1}$, respectively). One exception was Europe, where annual mean wind speeds below the climatology persisted in 2022 (-0.072 m s^{-1} ; Plate 2.1t). The positive anomalies in 2022 agree with the recent reversal or stabilization of surface winds observed since the 2010s (Zeng et al. 2019) after decades of decrease, denoted as “stilling” (Roderick et al. 2007; McVicar et al. 2012; Fig. 2.45a). The changes in the frequency of wind intensities still show long-term trends since the 1970s, with no trends or weak declines for moderate winds ($>3 \text{ m s}^{-1}$; Fig. 2.45c) and clear slowdowns for the strongest winds ($>10 \text{ m s}^{-1}$; Fig. 2.45d).

Changes and variability of land surface winds were assessed using: 1) anemometer observations from the Hadley Centre Integrated Surface Database version 3 (HadISD3) dataset (1973–2022; Dunn et al. 2012, 2016; Dunn 2019) and 2) two reanalyses: European Centre for Medium-Range Weather Forecasts Reanalysis version 5

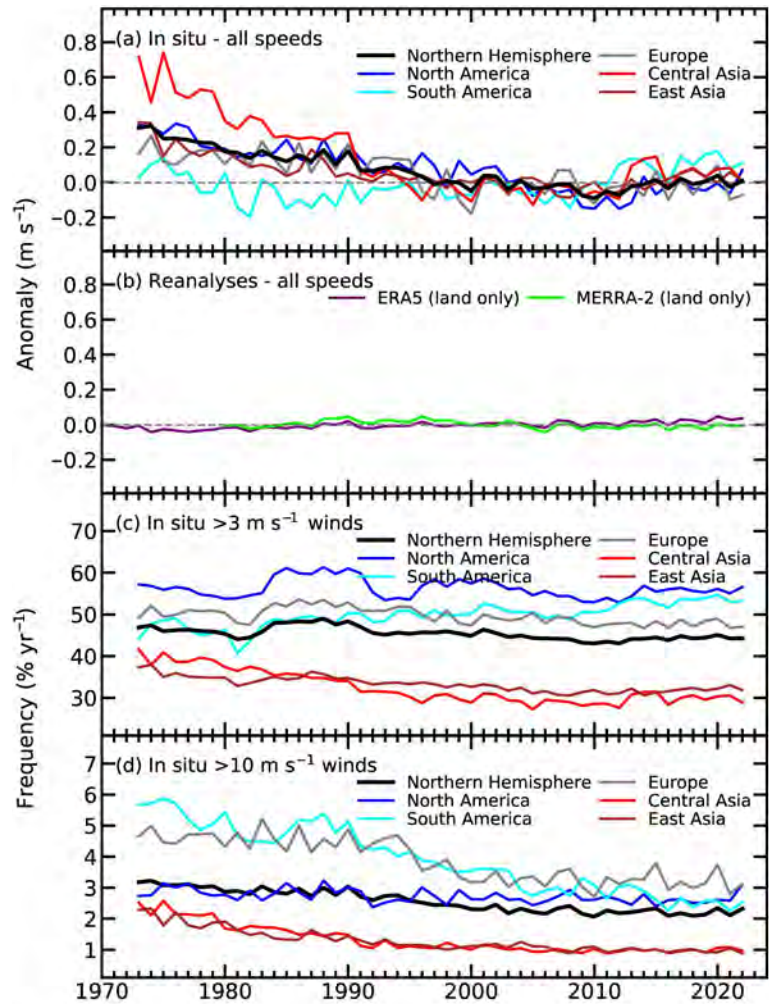


Fig. 2.45. Land surface Northern Hemisphere (20°N – 70°N) and regional surface wind-speed anomaly time series (m s^{-1} ; 1991–2020 base period). Panel (a) shows the HadISD3 observational dataset (1973–2022) and (b) ERA5 (1979–2022) and MERRA-2 (1980–2022) reanalyses. HadISD3 occurrence frequencies ($\% \text{ yr}^{-1}$) are shown for wind speeds (c) $>3 \text{ m s}^{-1}$, and (d) $>10 \text{ m s}^{-1}$.

Table 2.6. Northern Hemisphere (20°N – 70°N) and regional statistics for land surface wind speed (m s^{-1}) using the observational HadISD3 dataset for the period 1979–2022.

Region	Mean 1991–2020 (m s^{-1})	Anomaly 2022 (m s^{-1})	Trend 1979–2022 ($\text{m s}^{-1} \text{ decade}^{-1}$), and 5th to 95th percentile confidence range	Number of stations
Northern Hemisphere	3.308	+0.009	-0.055 ($-0.070 \rightarrow -0.041$)	2877
North America	3.643	+0.070	-0.068 ($-0.085 \rightarrow -0.051$)	842
Europe	3.648	-0.072	-0.050 ($-0.071 \rightarrow -0.035$)	934
Central Asia	2.738	+0.007	-0.072 ($-0.012 \rightarrow -0.046$)	304
East Asia	2.715	+0.012	-0.028 ($-0.044 \rightarrow -0.015$)	537
South America	3.452	+0.112	$+0.051$ ($+0.033 \rightarrow +0.069$)	101

(ERA5; 1979–2022, Hersbach et al. 2020; Bell et al. 2021) and Modern-Era Retrospective Analysis for Research and Applications version 2 (MERRA-2; 1980–2022, Gelaro et al. 2017). Note that surface wind-speed anomalies and trends differ between observations and reanalyses due to the difficulty that reanalysis systems have in reproducing long-term variability (Fig. 2.45b; e.g., Torralba et al. 2017; Ramon et al. 2019; Wohland et al. 2019).

Overall, observed trends of land surface winds for the past 44 years (i.e., since 1979) show a dominance of negative values (Fig. 2.46). In situ wind speeds declined by $0.055 \text{ m s}^{-1} \text{ decade}^{-1}$ across the NH over that time (Table 2.6). Over the last decade there has been a stabilization or reversal of wind speed trends globally (e.g. Zeng et al. 2019), which has also been observed regionally (e.g., Utrabo-Carazo et al. 2022). The exception is South America, where both the few observations and ERA5 reanalysis (Fig. 2.46) show positive trends, which support inter-hemispheric asymmetry of surface wind changes (Deng et al. 2022; Yu et al. 2022).

The recent reversal of the long-term surface wind speed decline over land has resulted in an increase in wind energy production over the last decade (e.g., over China; Liu et al. 2022). Observed surface wind speed changes are likely to be associated with internal decadal ocean–atmosphere oscillations (Zeng et al. 2019) along with temperature gradient variations arising from global warming (Zhang et al. 2021) but local-to-regional land use changes (Minola et al. 2022), instrumentation (Azorin-Molina et al. 2018), and encoding issues (Dunn et al. 2022) are also factors.

Compared to a 1991–2020 climatology, 2022 had positive anomalies over oceans recorded by satellite radiometers (Remote Sensing Systems [RSS]: $+0.11 \text{ m s}^{-1}$), slightly larger than satellite scatterometers (Advanced Scatterometer [ASCAT]: $+0.037 \text{ m s}^{-1}$) and reanalysis (ERA5: $+0.036 \text{ m s}^{-1}$; Fig. 2.47). The most prominent anomalies were recorded in the Pacific Ocean, with strong positive anomalies ($>+1.2 \text{ m s}^{-1}$) in the central tropical Pacific and negative ($<-1.2 \text{ m s}^{-1}$) in the western tropical Pacific and Maritime Continent, extending well into the eastern equatorial Indian Ocean—a strong signature of a persistent La Niña phase.

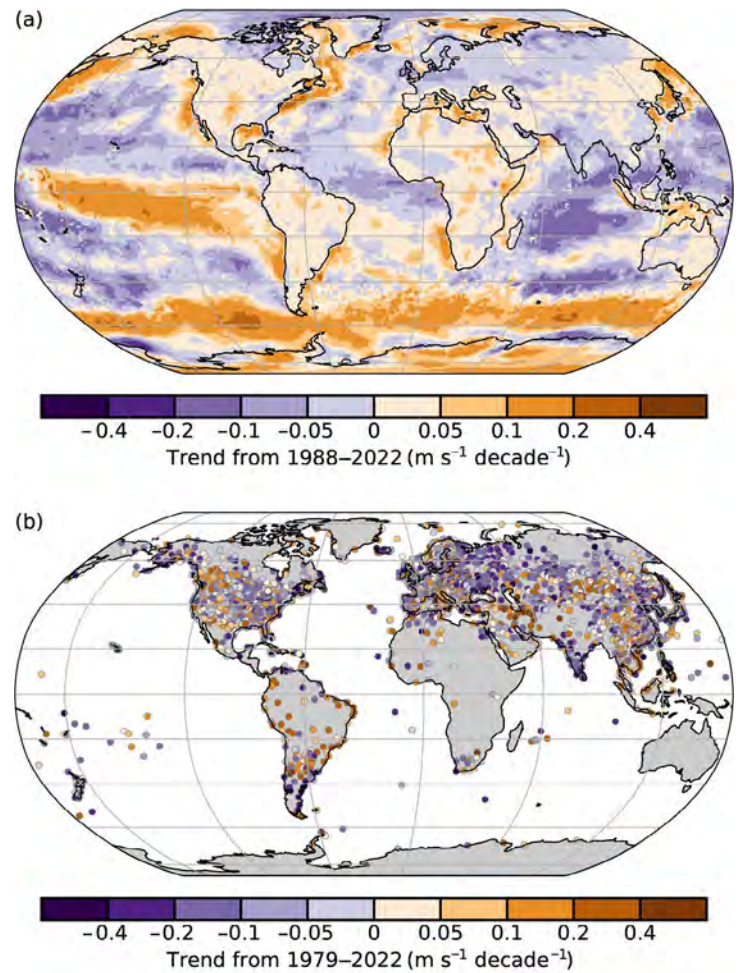


Fig. 2.46. Wind speed trends ($\text{m s}^{-1} \text{ decade}^{-1}$) from the (a) ERA5 reanalysis output over land/ice and Remote Sensing Systems (RSS) satellite radiometers (SSM/I, SSMIS, TMI, AMSR2, ASMR-E, and WindSat) over ocean for the period 1988–2022 (shaded areas) and (b) observational HadISD3 dataset over land (circles) for the period 1979–2022.

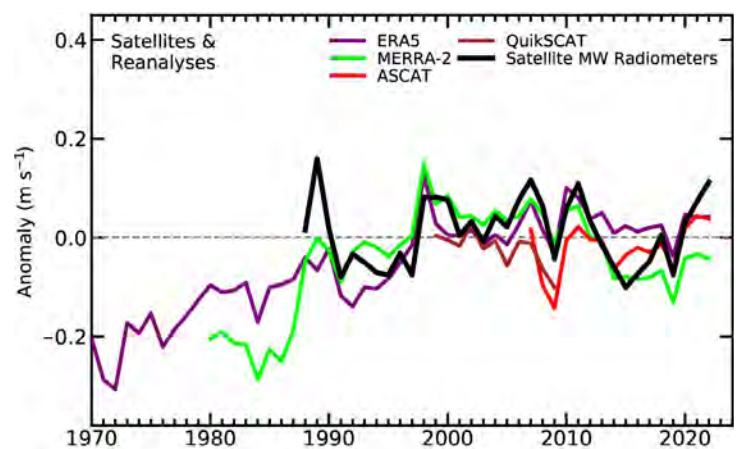


Fig. 2.47. Annual global mean wind speed anomalies (m s^{-1} ; 1991–2020 base period) over the ocean from satellite radiometers and scatterometers.

Similar to 2021, the mid-to-high latitude South Pacific Ocean experienced a strong positive anomaly ($>+1.2 \text{ m s}^{-1}$), consistent with the observed strengthening of the Southern Hemisphere westerlies (e.g., Deng et al. 2022; section 2e1). Strong positive anomalies were also seen in the Northern Hemisphere high-latitude regions (e.g., the Gulf of Alaska and the Greenland Sea).

Changes in ocean surface winds show widespread midlatitude negative trends for the period 1988–2022 and a strong negative trend in the Indian Ocean (Fig. 2.46). In contrast, positive trends prevail in the Pacific trade winds, the Southern Ocean, the Bering Sea, and near the coastlines (e.g., North America). The overall global ocean wind trend for 1988–2022 over 60°S – 60°N is close to zero (RSS Radiometers: $<+0.01 \text{ m s}^{-1} \text{ decade}^{-1}$; ERA5: $+0.036 \text{ m s}^{-1} \text{ decade}^{-1}$).

Over the ocean, surface winds were evaluated over the period 1988–2022 by 1) ERA5; and 2) satellite-based products: merged radiometer winds (including Special Sensor Microwave/Imager [SSM/I], the Special Sensor Microwave Imager/Sounder [SSMIS], the Advanced Microwave Scanning Radiometer-Earth Observing System [AMSRE], and the Advanced Microwave Scanning Radiometer 2 [AMSR2], Tropical Rainfall Measuring Mission [TRMM], Microwave Imager [TMI], and WindSat), and scatterometer winds Quick Scatterometer [QuikSCAT] and ASCAT (Wentz 1997, 2015; Wentz et al. 2007; Ricciardulli and Wentz 2015; Ricciardulli and Manaster 2021).

3. UPPER AIR WINDS

—M. Mayer, L. Haimberger, C. T. Sabeerali, V. Schenzinger, D. E. Surendran, and O. P. Sreejith

The 2022 global mean wind-speed anomaly at 850 hPa was about 0.1 m s^{-1} above the 1991–2020 climatology (Fig. 2.48a). The linear trend for the period 1991–2022 of $0.05 \text{ m s}^{-1} \text{ decade}^{-1}$ in the case of ERA5 and $0.04 \text{ m s}^{-1} \text{ decade}^{-1}$ for the Japanese 55-year Reanalysis (JRA55) is significant (p -value <0.01) but not statistically significant in MERRA-2. It is worth noting that the time series has been extended to the 1940s due to a recent backward extension of ERA5 (Hersbach et al. 2023).

Figure 2.48b together with Plate 2.1u indicate the mostly strongly positive zonal 850-hPa wind-speed anomalies at 50°S – 70°S in 2022. The increase in wind speed in this latitude belt

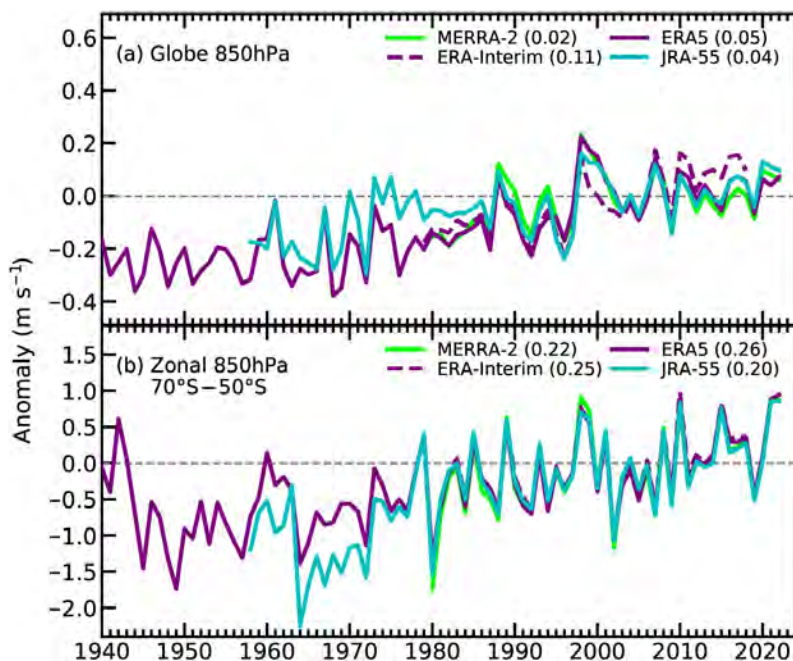


Fig. 2.48. Annual anomalies of (a) global mean and (b) 70°S – 50°S belt mean eastward wind speed (m s^{-1} ; 1991–2020 base period) at 850 hPa from four reanalyses (ERA5 [Hersbach et al. 2020], ERA-Interim [Dee et al. 2011], MERRA-2 [Gelaro et al. 2017], and JRA-55 [Kobayashi et al. 2015]). The numbers in parentheses are linear trends in $\text{m s}^{-1} \text{ decade}^{-1}$ for the period 1991–2020. The ERA-Interim time series ends in 2019.

has therefore continued, with 2022 close to the absolute maxima of the shown time series. The linear trends of the annual means are highly significant (p -value <0.002) for the period 1991–2022, between 0.20 and $0.26 \text{ m s}^{-1} \text{ decade}^{-1}$. This result is consistent with the high positive SAM (Marshall 2003) that continued to increase from the already high annual value of 1.2 in 2021 to 1.5 in 2022 (see also section 2e1). The AAO index, which is closely related to the SAM, was also strongly positive (0.79 in 2021 and 0.71 in 2022).

Plate 2.1u shows the annual zonal wind anomaly speed map at 850 hPa, averaged over September–December (SOND) 2022. The high (3 m s^{-1} near 60°S) wind speed anomaly in the Southern Ocean is the most prominent feature there. It is consistent with higher-than-average baroclinicity that was caused by record-high lower-tropospheric temperatures just north of the 50°S – 70°S belt (section 2b5).

2022 was the third La Niña year in a row (see Sidebar 3.1 and section 4b for details), the first time such an event has formed in the twenty-first century and only the third time in the last 50 years. The last “triple La Niña” occurred after the intense 1997/98 El Niño. Figures 2.49a,b show how similar the 200-hPa velocity potential patterns are for these events, indicating persistent and widespread circulation anomalies in the tropics during the three consecutive peak La Niña phases. Negative velocity potential anomalies over the Indo-Pacific Warm Pool are consistent with enhanced convective activity in this region, and the positive anomalies to the west and east are consistent with the expected changes to the Walker Circulation. The latter describes tropospheric circulation in the zonal-vertical plane in the equatorial regions in association with zonally varying sea-surface temperatures and convective activity (Bjerknes 1969). Figures 2.49c,d show the composite anomalies of pressure vertical velocity and zonal/vertical velocities averaged over 10°S–10°N, which complements the picture of the Walker circulation. The similarity is striking in this view, particularly for the main centers of activity over Indonesia and near the date line. Even the weaker maxima and minima over eastern Africa and northeastern Brazil look qualitatively similar.

In terms of equatorial stratospheric winds, the quasi-biennial oscillation (QBO) of 2022 was quite regular in terms of wind speeds and evolution of the easterly and westerly zones, comparable to 1982, 1992, or 2015. Despite the 2021 westerly lingering around 70 hPa until mid-April,

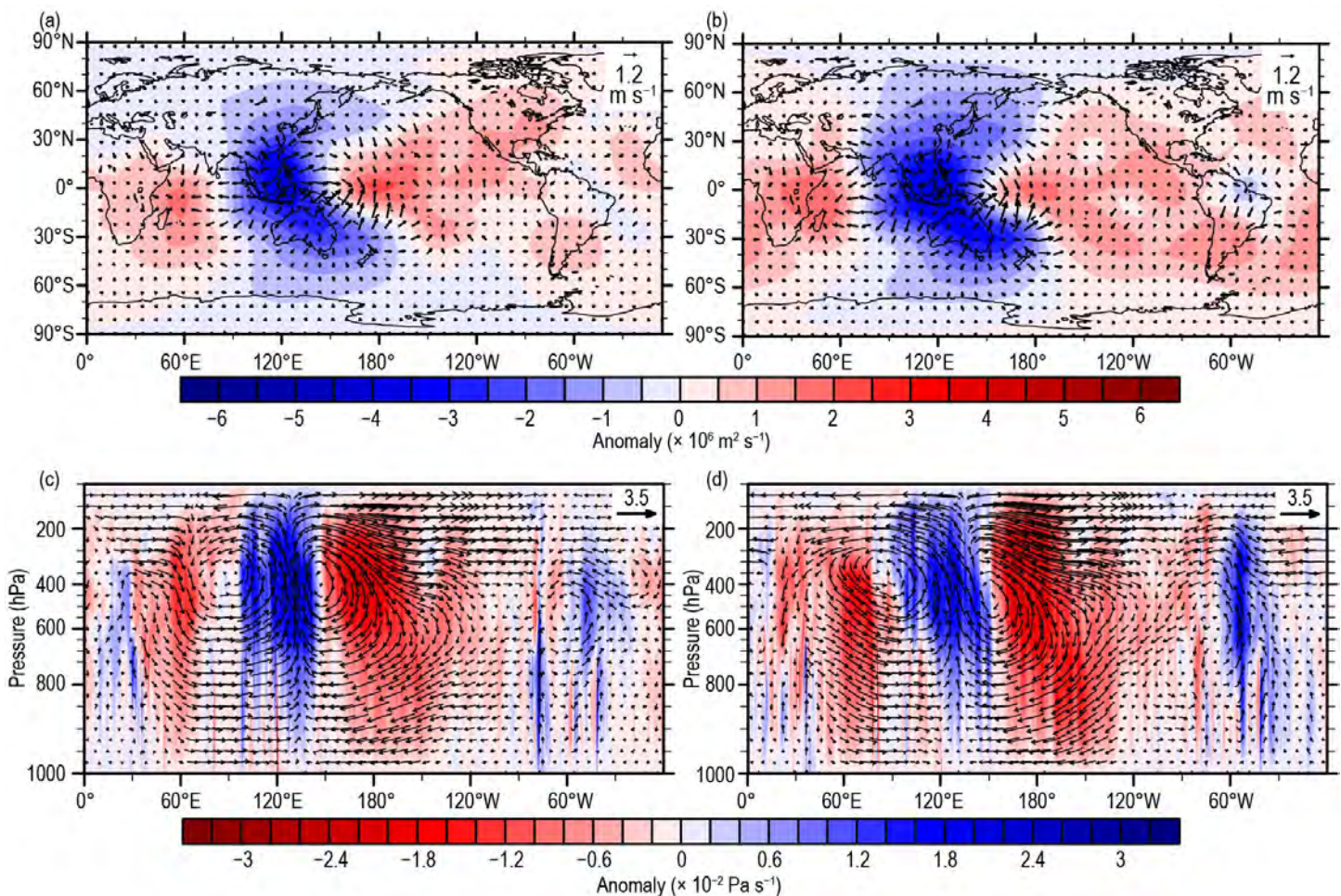


Fig. 2.49. Composites of 200-hPa velocity potential (colors; $\times 10^6 \text{ m}^2 \text{ s}^{-1}$) and divergent wind anomalies (arrows; 1991–2020 base period) for three consecutive OND seasons: (a) 1998–2000 and (b) 2020–22. Composite of 10°S–10°N averaged pressure vertical velocity anomalies (colors; $\times 10^{-2} \text{ Pa s}^{-1}$) and u/ω anomalies (arrows; zonal wind anomaly u : m s^{-1}) for three consecutive OND seasons: (c) 1998–2000 and (d) 2020–22. (Source: ERA5.)

thus stalling the easterly zone for this period of time, the already-formed westerly at 10 hPa descended with a normal speed of 1.13 km yr^{-1} . Its amplitude reached a maximum at the 10-hPa level in February, with a speed of 19.2 m s^{-1} , which is also within its usual range. A plot of zonal wind as a function of height and season over Singapore, which serves as a proxy for the global state of the QBO due to its zonal symmetry, is shown in Fig. 2.50a. The stratospheric state at the end of the year with one westerly shear zone present from 10 hPa to 80 hPa resembles that of 2015 (see Fig. 2.50b for a comparison of recent years), when the first major disruption of the QBO took place (Osprey et al. 2016).

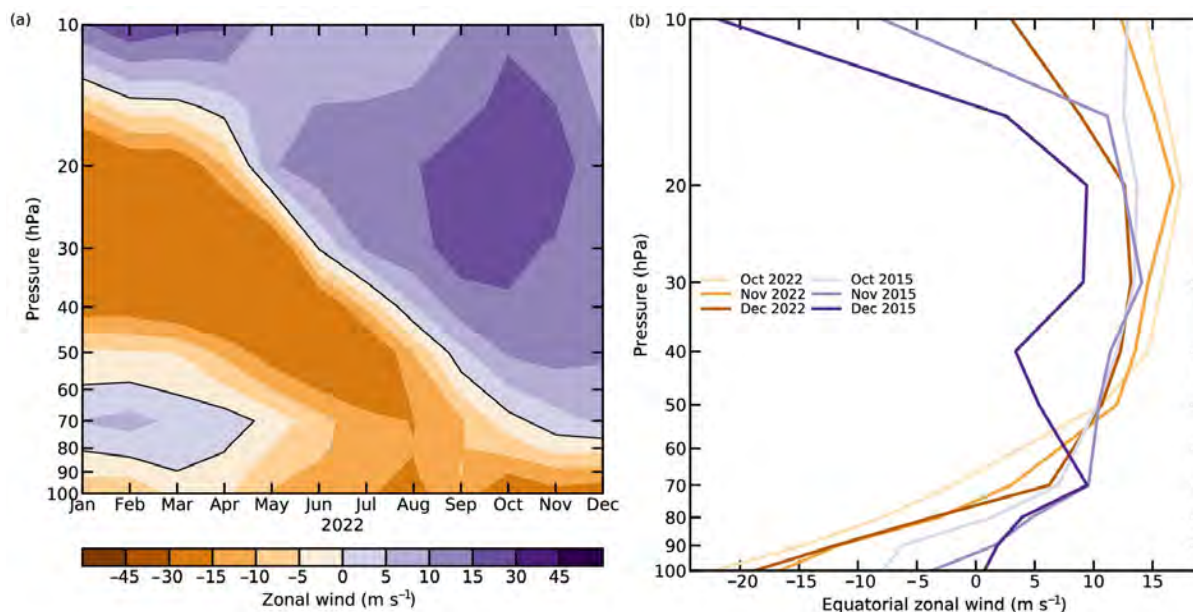


Fig. 2.50. (a) Stratospheric monthly mean zonal-wind values (m s^{-1}) based on daily measurements in Singapore. Easterlies (negative values) are shown in brown, westerlies (positive) in purple. (b) Monthly profiles of Singapore zonal wind averaged for Oct, Nov, and Dec in 2015 and 2022. Westerly winds are prominent above 70 hPa for both years, though the weakening of the westerlies at 40 hPa in 2015, which lead up to the first observed quasi-biennial oscillation disruption, is already visible in Dec.

4. LIGHTNING

—M. Füllekrug, E. Williams, C. Price, S. Goodman, R. Holzworth, K. Virts, D. Buechler, T. Lang, and Y. Liu

The Geostationary Lightning Mapper (GLM) on Geostationary Operational Environmental Satellites 16 and 17 reported the first lightning anomaly map covering the Western Hemisphere Americas and adjacent oceans, while the Lightning Imaging Sensor (LIS) on board the International Space Station (ISS LIS) has recorded lightning from February 2017 to present and thereby extends over 25 years of global lightning observations with previous satellites in low-Earth orbit (Blakeslee et al. 2020).

Figure 2.51a displays the average lightning density over the Americas and the Pacific Ocean calculated over 2019–22 from the GLMs. Coastlines and some topographic features, such as the Cordilleras in Central America and the Andes in South America, can act as meteorological divides for lightning densities to change on relatively small spatial scales. Over the oceans, lightning flashes indicate the tracks of thunderstorms that follow the trade winds, the westerlies at midlatitudes, and the easterlies at low latitudes. The Intertropical Convergence Zone over the Pacific Ocean is located slightly north of the equator.

The spatial distribution of anomalies in lightning density for 2022 is shown in Fig. 2.51b. Given the relatively short period of the record, it is currently expected that these anomalies exhibit an annual variability caused primarily by the long-term varying state of the climate (Williams 2020); in the case of the period 2020–22, the ongoing La Niña conditions following the El Niño event in 2018/19.

During El Niño, the three-dimensional structure of deep convection is taller and stronger (Hamid et al. 2001) than it is during La Niña. In South America, deeper storms during El Niño relate to increased convective available potential energy, a strengthening of the South American low-level jet, and a stronger upper-level jet stream (Bruick et al. 2019). Velasco and Fritsch (1987) report that large mesoscale convective systems (MCS), the most extreme lightning-producing weather systems on Earth (Zipser et al. 2006), are concentrated downwind of major mountain ranges in both North and South America. In North America, latitudinal shifts of storm tracks occur in association with El Niño and jet stream steering winds (Goodman et al. 2000). El Niño may contribute to extreme lightning climatology anomalies relative to the mean, as ~25% of the annual lightning at a single location has been shown to occur during the passage of a single MCS at midlatitudes during the strong El Niño years of 1982/83 (Goodman and MacGorman 1986).

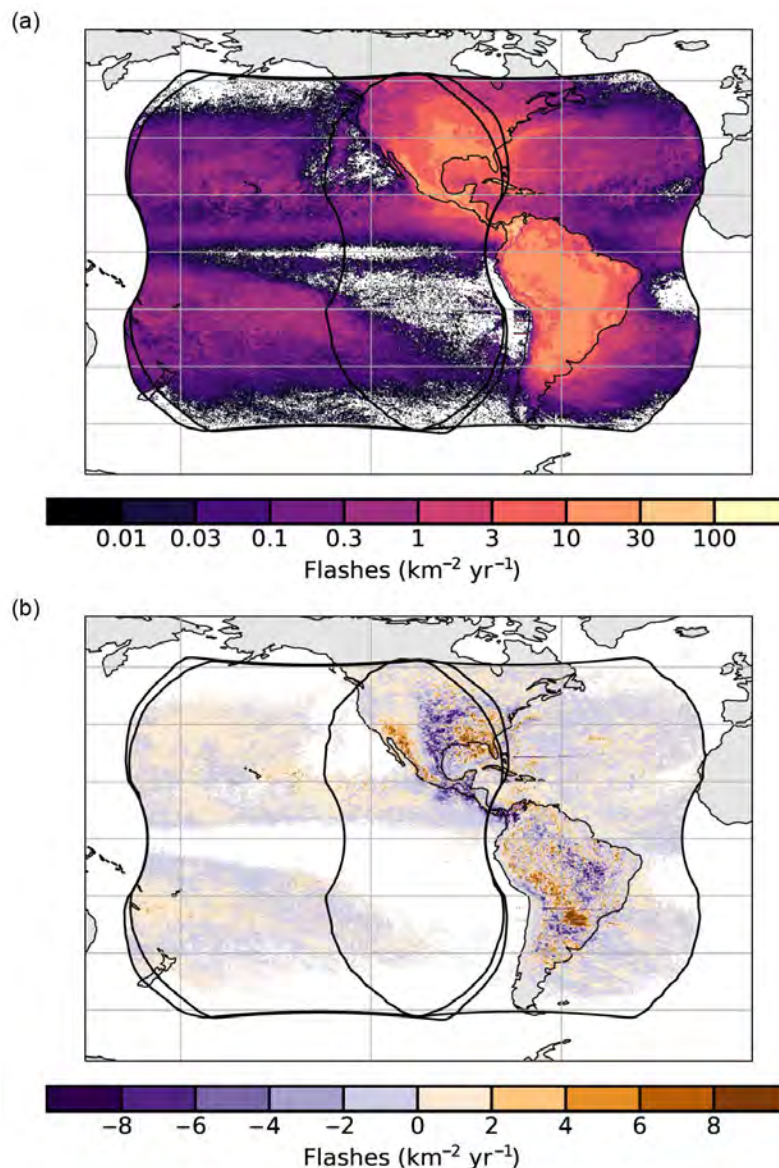


Fig. 2.51. (a) Lightning flash rate density for the period 2019–22 from NOAA’s Geostationary Lightning Mapper (GLM) on GOES 16 & 17. The black outline indicates the nominal GLM field of view for each satellite. (b) Western Hemisphere anomalies in lightning density for 2022 that are calculated relative to the 2019–21 mean. Units are $\text{fl km}^{-2} \text{yr}^{-1}$.

In Füllekrug et al. (2022), a distinct downturn in the reference year 2020 was apparent in the longest available uniform record of global lightning (LIS on TRMM), in a matched detector on the ISS, and in the GLM record for lightning over the Western Hemisphere (Virts et al. 2023). In contrast, the LIS record for the period 1998–2014 (Williams et al. 2019) was statistically flat. Two sustained events beginning in early 2020 could have caused the 2020 downturn: the transition from El Niño to La Niña and the aerosol reduction during the first COVID lockdown in many countries. Evidence for tropical lightning reductions in La Niña relative to El Niño is abundant (Williams 1992; Hamid et al. 2001; Yoshida et al. 2007; Satori et al. 2009; Goodman et al. 2000; Williams et al. 2021). Lightning reductions with reduced aerosol (Altaratz et al. 2017; Thornton et al. 2017; Fan et al. 2018; Wang et al. 2018; Liu et al. 2020) have a microphysical basis (Rosenfeld and Woodley 2003; Rosenfeld et al. 2008), and a global reduction in aerosol optical depth in satellite observations in 2020 (Sanap 2021) arises from reduced fossil fuel consumption and associated aerosol emissions during the COVID lockdowns (e.g., Rémy et al. 2021).

The 2019–21 reference period might therefore be slightly biased during the main COVID lockdown that occurred between March and May 2020 (Fig. 2.52). During this three-month period, the lightning densities over the Gulf of Mexico exhibit larger densities than during the 2019–21 reference period, while the central regions of North America and South America exhibit lower lightning densities, as reported by GLM16 (Fig. 2.52a). This is consistent with lightning densities measured by ISS LIS, which offers a global view of lightning density changes (Fig. 2.52b). As a result, the two main confounding variables affecting lightning density (ENSO and aerosol loading) need to be disentangled and require some in-depth discussion in the future.

La Niña kept 2022 globally cooler than years with El Niño or ENSO-neutral conditions (section 2b1). Both the ISS LIS and the GLM records are consistent in showing that global lightning totals during the present La Niña phase have not returned to the levels of the previous El Niño in 2019. Despite the identification of consistent physical connections and a La Niña that is behaving similarly to earlier La Niñas (Williams et al. 2020), the global reductions in lightning in 2020 and thereafter are not yet fully understood.

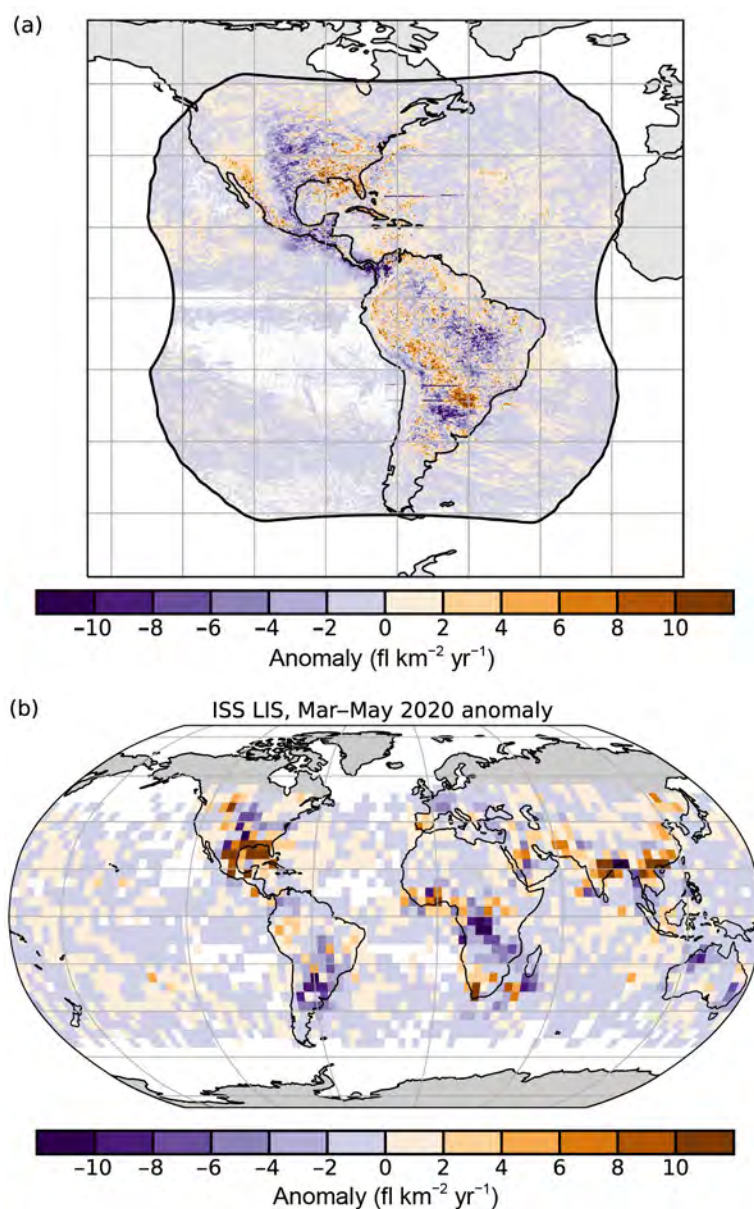


Fig. 2.52. Seasonal lightning density anomalies ($\text{fl km}^{-2} \text{yr}^{-1}$) for Mar–May 2020, potentially associated with the reduction of aerosol during the first COVID lockdown in many countries. (a) Spatial distribution of anomalies in seasonal lightning density from GLM16. (b) Global distribution of anomalies (relative to MAM 2017–19) in seasonal lightning density observed from the Lightning Imaging Sensor on board the International Space Station.

f. Earth radiation budget

1. EARTH RADIATION BUDGET AT TOP-OF-ATMOSPHERE

—T. Wong, P. W. Stackhouse Jr., P. Sawaengphokhai, J. Garg, and N. G. Loeb

The top-of-atmosphere (TOA) Earth radiation budget (ERB) is defined as the difference between incoming total solar irradiance (TSI) and outgoing radiation from Earth given by the sum of reflected shortwave (RSW) and outgoing longwave radiation (OLR). Regional imbalances in TOA ERB drive atmospheric and oceanic circulations. Thus, monitoring the variability in TOA ERB is essential for understanding the changes in the climate system.

An analysis of Clouds and the Earth's Radiant Energy System (CERES) TOA ERB measurements (Table 2.7) shows that the global annual mean OLR and TSI increased by 0.30 W m^{-2} and 0.15 W m^{-2} , respectively, in 2022 relative to 2021 (rounded to the nearest 0.05 W m^{-2}). In contrast, the global annual-mean RSW and net radiation decreased by 0.10 W m^{-2} and 0.05 W m^{-2} , respectively, over the same period. Fig. 2.53 shows regional annual-mean maps of the difference between 2022 and 2021 in TOA OLR and TOA RSW. The largest increases in OLR and decreases in RSW are observed over a large extent of the equatorial Pacific Ocean between New Guinea and 120°W longitude. Reductions in OLR and increases in RSW are observed over Southeast Asia, the northeastern Indian Ocean, the Philippines, Indonesia, Australia, and the tropical southwestern Pacific Ocean. These regional changes are associated with La Niña conditions that

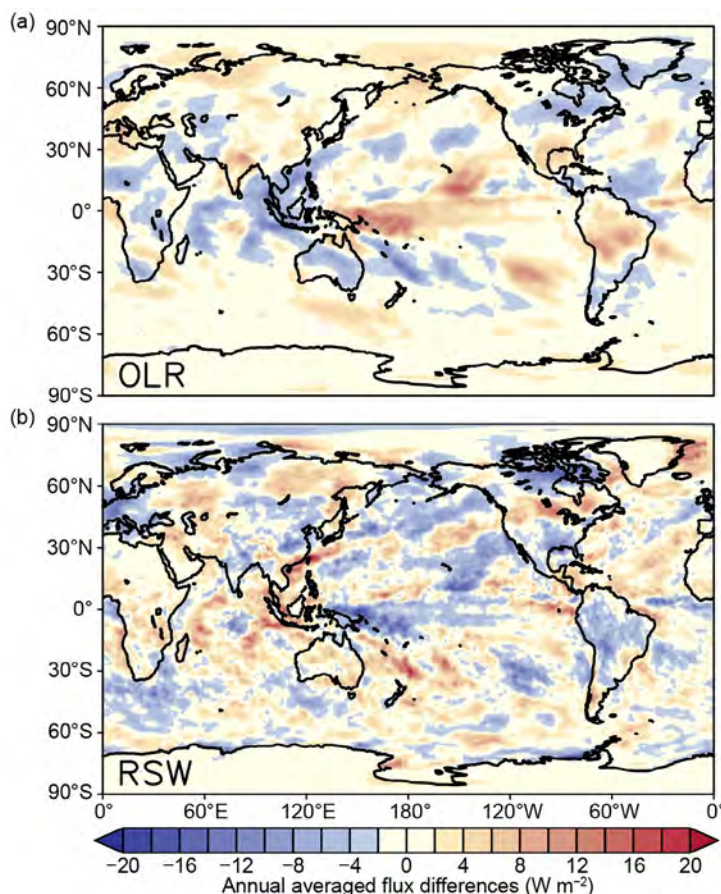


Fig. 2.53. Annual average top-of-atmosphere (TOA) flux differences (W m^{-2}) between 2022 and 2021 for (a) outgoing longwave radiation (OLR) and (b) reflected shortwave radiation (RSW). The annual-mean maps for 2022 were derived after adjusting Dec 2022 FLASHFlux version 4A data using the difference between CERES EBAF Ed4.2 and CERES FLASHFlux version 4A data in 2021.

Table 2.7. Global annual mean top-of-atmosphere (TOA) radiative flux changes between 2021 and 2022, the 2022 global annual mean radiative flux anomalies relative to their corresponding 2001–21 mean climatological values, and the $2\text{-}\sigma$ interannual variabilities of the 2001–21 global annual mean fluxes (all units in W m^{-2}) for the outgoing longwave radiation (OLR), total solar irradiance (TSI), reflected shortwave (RSW), absorbed solar radiation (ASR, determined from $\text{TSI} - \text{RSW}$), and total net fluxes. All flux values have been rounded to the nearest 0.05 W m^{-2} and only balance to that level of significance.

Global	One Year Change (2022 minus 2021) (W m^{-2})	2022 Anomaly (Relative to 2001–21) (W m^{-2})	Climatological Mean (2001–21) (W m^{-2})	Interannual Variability (2001–21) (W m^{-2})
OLR	+0.30	+0.30	240.35	± 0.60
TSI	+0.15	+0.20	340.20	± 0.15
RSW	-0.10	-0.75	99.00	± 1.00
ASR	+0.25	+0.95	241.15	± 0.95
Net	-0.05	+0.65	0.80	± 0.80

persisted and intensified between 2020 and 2022, according to the Multivariate El Niño–Southern Oscillation (ENSO) index (Wolter and Timlin 1998; section 2e1). Relative to the multiyear average from 2001 to 2021, the 2022 global annual mean TOA flux anomalies are +0.30 for OLR, +0.20 for TSI, −0.75 for RSW, and +0.65 $W m^{-2}$ for total net flux (Table 2.7). These anomalies are near or within their respective 2- σ interannual variability (Table 2.7) for this period.

Throughout 2022, the global monthly mean TOA OLR anomaly remained largely positive (Fig. 2.54). The OLR anomaly dipped to a value of −0.50 $W m^{-2}$ for one month in August but recovered quickly back to positive values in the following months. These results are generally consistent with NOAA High Resolution Infrared Sounder (HIRS; Lee and NOAA CDR Program 2018) and NASA Atmospheric Infrared Sounder (AIRS; Susskind et al. 2012) OLR datasets (not shown). For the year as a whole, the 2022 global mean TOA OLR anomaly was +0.30 $W m^{-2}$. The global monthly mean TOA absorbed solar radiation (ASR; determined from TSI minus RSW) anomaly remained positive throughout 2022, peaking at +1.80 $W m^{-2}$ in June. For the year as a whole, the 2022 global mean TOA ASR anomaly was +0.95 $W m^{-2}$. The global monthly mean TOA total net anomaly, which is calculated from ASR anomaly minus OLR anomaly, also stayed mostly positive throughout 2022, reaching a maximum of +1.65 $W m^{-2}$ in June. For the year as a whole, the 2022 global mean TOA total net anomaly was +0.65 $W m^{-2}$. In terms of the global annual mean TOA ERB, the positive 2022 ASR anomaly was much larger than the negative effect of the 2022 OLR anomaly to produce the observed positive 2022 total net anomaly. Further analyses are needed to understand the significances and impacts of these observed global changes.

The TSI data were obtained from the Total Irradiance Monitor aboard the Solar Radiation and Climate Experiment (SORCE) mission (Kopp and Lean 2011), the Royal Meteorological Institute of Belgium composite dataset (Dewitte et al. 2004), and the Total Solar and Spectral Irradiance Sensor-1 (Coddington 2017) mission, all renormalized to the SORCE Version 15. The TOA RSW and TOA OLR data come from two different CERES datasets. The data for March 2000–November 2022 are based on the CERES Energy Balance and Filled (EBAF) Ed4.2 product (Loeb et al. 2009,

2012, 2018), which are constructed with measurements from the CERES instruments (Wielicki et al. 1996, 1998) aboard *Terra*, *Aqua*, and NOAA-20 spacecraft. The data for December 2022 comes from the CERES Fast Longwave and Shortwave Radiative Fluxes (FLASHFlux) version 4A product (Kratz et al. 2014), which are created using CERES measurements from *Terra* and *Aqua* spacecraft. The FLASHFlux to EBAF data normalization procedure (Stackhouse et al. 2016) results in 2- σ monthly uncertainties of ± 0.35 , ± 0.05 , ± 0.15 , and ± 0.50 $W m^{-2}$ for the OLR, TSI, RSW, and total net radiation, respectively (rounded to nearest 0.05 $W m^{-2}$).

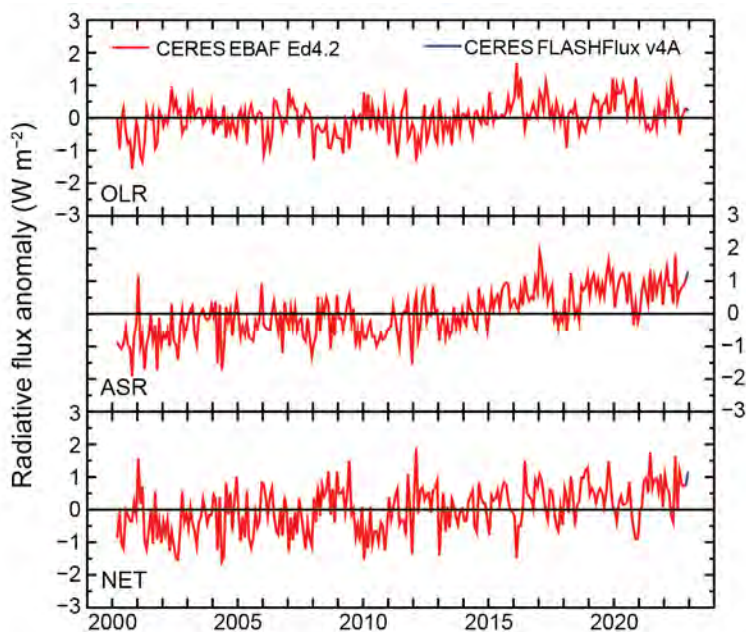


Fig. 2.54. Time series of global monthly mean deseasonalized anomalies ($W m^{-2}$) of top-of-atmosphere (TOA) Earth radiation budget for outgoing longwave radiation (OLR; upper), absorbed solar radiation (ASR, determined from total solar irradiance (TSI) minus RSW; middle), and total net (TSI-RSW-OLR; lower) from Mar 2000 to Dec 2022. Anomalies are relative to their calendar month climatology (2001–21). The time series show the CERES EBAF Ed4.2 1-Deg data (Mar 2000–Nov 2022) in red and the CERES FLASHFlux version 4A data (Dec 2022) in blue; see text for merging procedure. (Sources: <https://ceres-tool.larc.nasa.gov/ord-tool/jsp/EBAFTOA42Selection.jsp> and https://ceres-tool.larc.nasa.gov/ord-tool/jsp/FLASH_TISASelection.jsp.)

2. MAUNA LOA APPARENT TRANSMISSION RECORD

—J. A. Augustine, K. O. Lantz, J.-P. Vernier, and J. E. Barnes

The Mauna Loa Observatory (MLO) on Hawaii (19.536°N, 155.576°W) at 3397 m a.s.l. has made pyrhelimeter measurements since 1958. Because of its high elevation, morning apparent atmospheric transmission computed from those measurements is a good proxy for stratospheric extinction.

The apparent transmission time series from 1958 through 2022 is shown in Fig. 2.55; the inset highlights new data for 2022. January and February 2022 transmissions continue at relatively stable levels of ~0.928 observed at the end of 2021. This relatively low transmission has been maintained since 2019 by a series of volcanic eruptions and wildfires (Augustine et al. 2020, 2021). A broad reduction in transmission began in March 2022 and reached a minimum of 0.919 in May. A sharp recovery in June to values observed earlier was followed by relatively stable transmissions through November (Mauna Loa erupted on 27 November, ending data collection for 2022). The springtime reduction in transmission coincided with the violent underwater eruption in January of Hunga Tonga–Hunga Ha‘apai (HTHH; 20.536°S, 175.382°W; Sidebar 2.2) and the seasonal passage of dust from Asia.

Most of the 70+ volcanic eruptions in 2022 had Volcanic Explosivity Indexes (VEI) less than 2, limiting their effect on the stratosphere. HTHH’s initial eruption on 13 January sent material as high as 20 km. A second more powerful eruption on 15 January (VEI 5) reached the lower mesosphere (~58 km) but within the day settled to between 25 km and 35 km (Proud et al. 2022). The westerly phase of the quasi-biennial oscillation of stratospheric winds (QBO) propagated the HTHH plume westward. The plume was concentrated at ~10°S but Cloud-Aerosol LIDAR and Infrared Pathfinder Satellite Observations (CALIPSO) imagery shows lateral transport branches in the 19 km–27 km layer reaching 30°S and 20°N in March (see supplemental material), in agreement with the Ozone Mapping and Profiler Suite (OMPS) and the Stratospheric Aerosol and Gas Experiment (SAGE) limb sounder (Taha et al. 2022). Discrete CALIPSO images at 19-day intervals in Legras et al. (2022) show the northern extent of Tonga’s stratospheric plume near 20°N at least through 3 May, but by 22 May it retreated south and remained there at least through 18 July (no published data thereafter). Lidar observations at MLO first sensed the HTHH plume on 1 March at an altitude of 24.5 km. A much larger signal was observed near 24 km on 14 March, in agreement with CALIPSO, which shows the northern periphery of the plume over MLO from 14 to 16 March (see supplemental material).

Distinguishing HTHH from other large volcanic stratospheric events is its relatively small sulfur dioxide injection, ~50 times less than Mt. Pinatubo (Taha et al. 2022), and stratospheric aerosol optical depth (AOD) six times less than Pinatubo at 0.015, which represents a 4–5 factor increase from background (Khaykin et al. 2022). Those discrepancies are likely due to wet deposition (Proud et al. 2022) as HTHH increased stratospheric water by 10%–13% (Millan et al. 2022; Khaykin et al. 2022). Zhu et al. (2022) suggests the added water promoted faster sulfate aerosol formation and greater extinction but shortened its long-term effect on surface radiation.

While there were several springtime dust storms in Asia in 2022, none were as severe as those in 2021. Monthly average

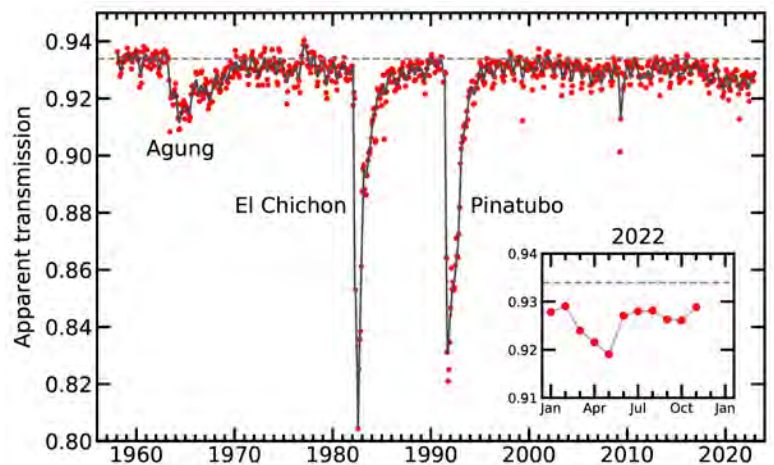


Fig. 2.55. Apparent transmission at Mauna Loa, Hawaii, from 1958 through 2022. Red dots are monthly averages of morning apparent transmission, and the gray curve is a locally weighted scatterplot smoothing (LOWESS) fit with a six-month smoother applied. The insert is an enlargement of the newest data for 2022. The horizontal dashed gray lines represent the average transmission of the clean period before the eruption of Agung. The Dec 2022 transmission is not available because the eruption of Mauna Loa in late Nov cut power to the station.

global AOD images for 2022 from the Moderate Resolution Imaging Spectroradiometer (MODIS [Barnes et al. 1998]; https://earthobservatory.nasa.gov/global-maps/MODAL2_M_AER_OD) show slightly elevated AOD over Hawaii in March, peak AOD in April, a reduction in May, and gone by June.

In summary, HTHH’s plume and Asian dust were primary contributors to the reduction of apparent transmission over MLO from March through May 2022. Both sources of enhanced extinction vanished by June, returning transmission to levels observed in January and February for the remainder of the 2022 record, which ended in November.

Atmospheric transmission is calculated from the ratio of direct-normal pyrheliometer measurements at two integer solar elevations (Ellis and Pueschel 1971). Three ratios from clear-morning measurements at 2, 3, 4, and 5 atmospheric pathlengths are averaged to get representative daily value. Daily transmissions are then averaged over monthly periods. Our calculation is referred to as an “apparent” transmission because atmospheric variability at longer pathlengths adds to the uncertainty.

Sidebar 2.2: Hunga Tonga–Hunga Ha’apai eruption

— S. DAVIS, W. RANDEL, J. AUGUSTINE, B. FRANZ, N. KRAMAROVA, T. LEBLANC, J.-P. VERNIER, X. WANG, AND M. WEBER

On 14–15 January 2022, the Hunga Tonga–Hunga Ha’apai (HTHH) submarine volcano (20.54°S, 175.4°W) erupted multiple times, injecting ash, water vapor, and sulfur dioxide (SO₂, an aerosol precursor) into the atmosphere. The underwater eruption on 15 January was among the strongest in the modern geophysical record, with an estimated Volcanic Explosivity Index (VEI) similar to that of Mt. Pinatubo in 1991 (VEI=6; Poli and Shapiro, 2022). The eruption produced a number of impacts, including audible sound heard ~10,000 km away, perturbations to the ionosphere, global tsunamis, as well as a Lamb wave and seismic activity similar in magnitude

to the 1883 eruption of Krakatau (Kubota et al. 2022; Matoza et al. 2022).

The plume from the HTHH eruption was observed to reach as high as ~55 km, a record in the geostationary satellite era that exceeded the ~40 km height reported for Mt. Pinatubo (Fig. SB.2.3; Carr et al. 2022). Following this transient peak in the plume height reaching the mesosphere, an umbrella of gas and ash spread out in the stratosphere between approximately 26 km and 34 km. The trace gases and aerosols injected into the stratosphere by the HTHH eruptions quickly spread as far north as 20°N in the month following the eruption, before

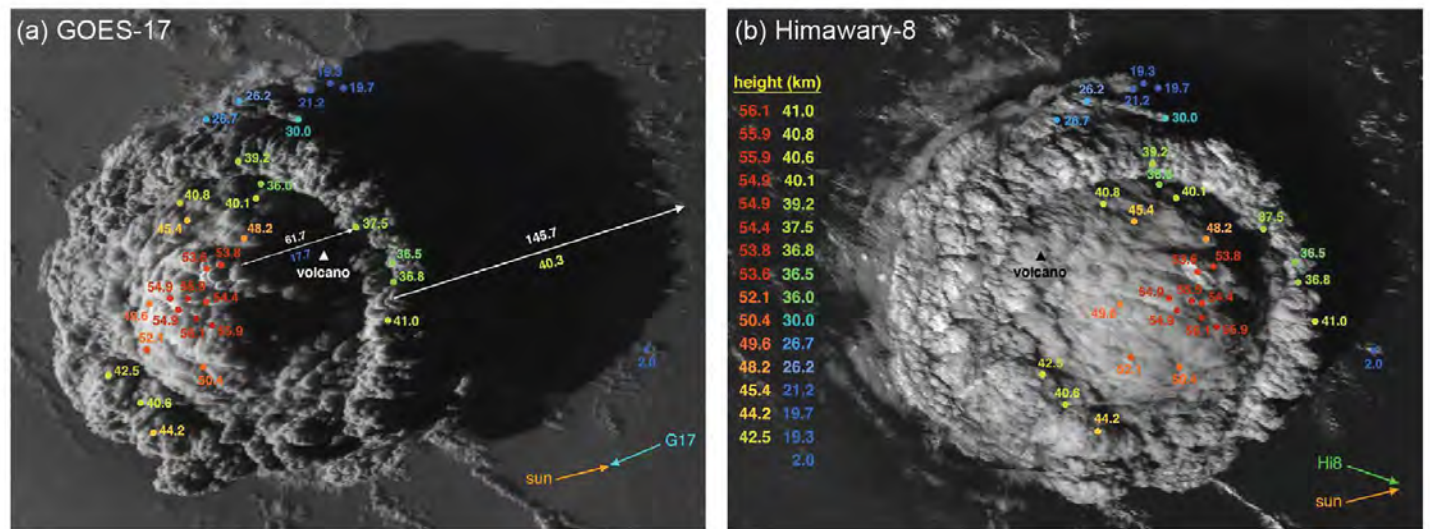


Fig. SB2.3. (From Carr et al. 2022, their caption. Figure used under **CC BY 4.0**): Image of the plume on 15 Jan 2022 at 0430 UTC from (a) GOES-17 and (b) Himawari-8. Colored dots mark manual stereo height estimates (in km), and the white/black triangles show the volcano’s location. The white arrows in panel (a) depict the shadow of a plume edge feature and a dome feature, with the shadow length and the derived height given above/below the arrow. Arrows in the lower right of each panel indicate the sun-to-pixel and satellite-to-pixel azimuths.

being transported to higher Southern Hemisphere (SH) latitudes in subsequent months and into the northern midlatitudes by the end of 2022. Here, we elaborate on some of the notable perturbations to the atmosphere, as well as some of the possible chemical and climate effects that are likely to occur in the coming years.

As the HTHH eruption occurred underwater, a vast amount of water vapor (WV) was present in the eruption plume, and this water vapor-enriched plume has had a dramatic impact on the stratosphere. By injecting water vapor and ice directly into the stratosphere, the HTHH eruption bypassed the typical tropical tropopause layer “cold trap” that normally limits the amount of water vapor entering the stratosphere (section 2g5). While previous volcanic eruptions and pyrocumulonimbus events have also injected water vapor into the stratosphere,

HTHH injected ~ 50 Tg H_2O to ~ 150 Tg H_2O , which is unprecedented in the satellite record and represents upwards of 10% of the entire stratospheric burden of WV (Khaykin et al. 2022; Millán et al. 2022; Randel et al. 2023; Vömel et al. 2022). Measurements from within the HTHH plume in the week immediately after the eruption showed water vapor mixing ratios exceeding 1000 ppmv between 25 km and 30 km (Khaykin et al. 2022; Randel et al. 2023; Vömel et al. 2022), in contrast to typical background stratospheric values of ~ 5 ppmv and enhancements on the order of 10 ppmv from other recent volcanoes and the early 2020 Australian wildfires (e.g., Sioris et al. 2016; Kablick et al. 2020; Schwartz et al. 2020). Enhanced water vapor amounts persisted in the stratosphere throughout 2022 (Fig. SB.2.4a). As an example, the quasi-global monthly anomaly (averaged over $\sim 80^\circ S$ – $80^\circ N$, relative to the

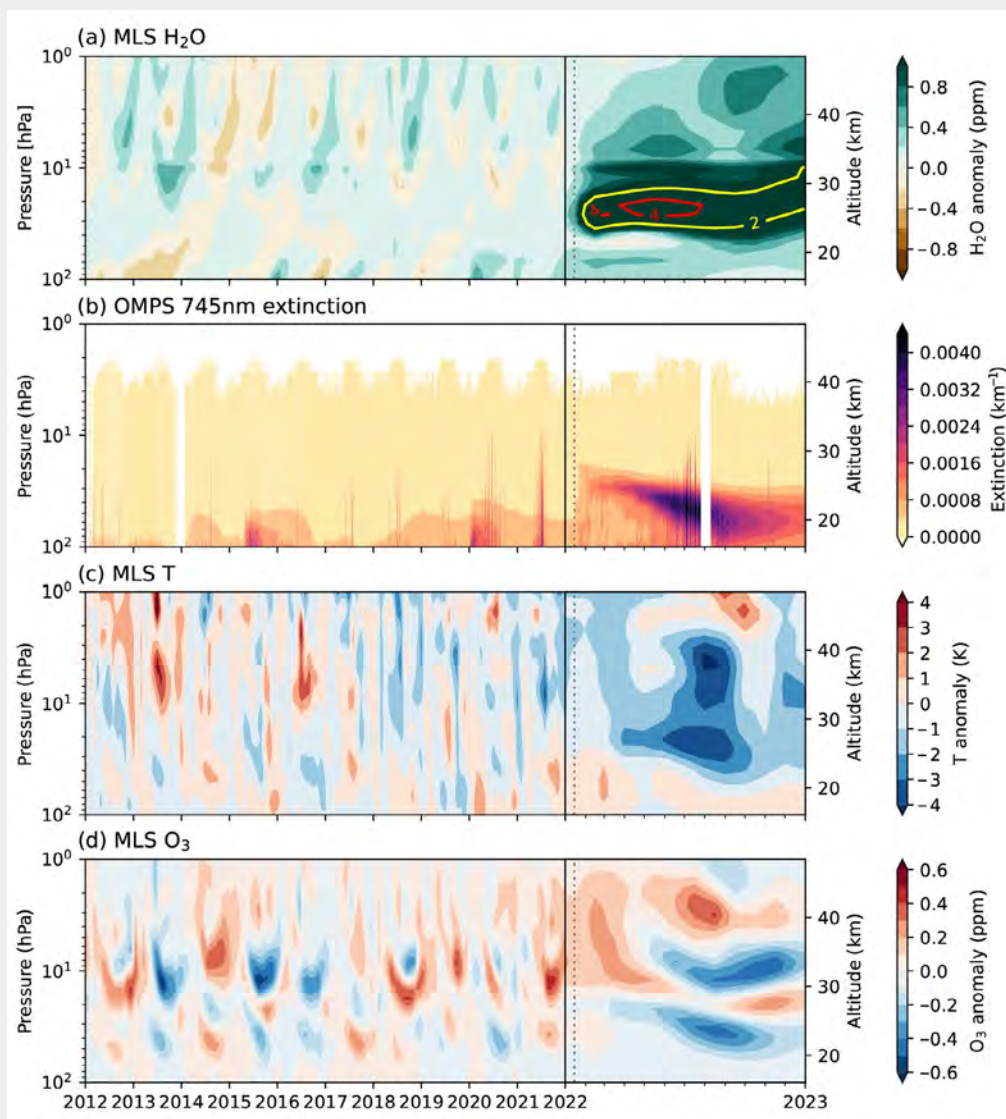


Fig. SB2.4. Southern Hemisphere ($10^\circ S$ – $50^\circ S$) average (a) stratospheric water vapor (H_2O) anomaly (ppm), (b) aerosol extinction (km^{-1}), (c) temperature anomaly (K), and (d) ozone (O_3) anomaly (ppm) for the period 2012–22. The start of 2022 is indicated by the vertical solid line, and the HTHH eruption is indicated by the vertical dotted line. Water vapor, ozone, and temperature anomaly data are from the Aura MLS and calculated as departures from the 2004–21 mean. Aerosol extinction at 745 nm is based on Suomi National Polar-Orbiting Partnership OMPS Limb Profiler data.

2004–21 average) in December 2022 at 26 hPa (~25 km) from the Aura Microwave Limb Sounder (MLS) satellite was +1.1 ppmv, which corresponds to a 12-sigma and 24% deviation from the mean for that month. Because the main WV removal process is due to the slow stratospheric overturning circulation, it is expected that anomalous stratospheric water vapor will persist for a number of years.

It is estimated that HTHH emitted ~0.5 Tg SO₂ (Carn et al. 2022), which is relatively small compared to the ~20 Tg SO₂ emitted by the similarly sized Mt. Pinatubo eruption (Guo et al. 2004). Stratospheric sulfate aerosols formed anomalously quickly in the HTHH plume, likely influenced by rapid oxidation of SO₂ in the extreme water vapor plume (Carn et al. 2022; Zhu et al. 2022). The sulfate aerosol layer gradually separated from the water vapor plume and descended into the SH lower stratosphere due to gravitational settling (Fig. SB.2.4b; see also Legras et al. 2022; Wang et al. 2022), dispersing over latitudes from the tropics to the Antarctic after several months. This resulted in a five-fold increase in the stratospheric aerosol load, which is the highest in the last three decades (Khaykin et al. 2022; see also section 2g3). This stratospheric perturbation had a visible impact on SH aerosol optical depth at 550-nm anomalies in 2022 (section 2g3).

As water vapor and aerosols are radiatively active and persisted in the stratosphere throughout 2022, there are expected impacts on stratospheric temperatures (section 2b6). Enhanced stratospheric water vapor is expected to lead to local (stratospheric) cooling, while elevated stratospheric sulfate aerosol concentrations lead to local warming. Observations show cold stratospheric temperatures in 2022 that were well outside the range of previous variability (Figs. SB.2.4c, 2.11a), with corresponding anomalies in stratospheric winds and circulation that are in balance with the anomalous temperatures (Coy et al. 2022; Wang et al. 2022).

Elevated stratospheric water vapor and aerosol concentrations are expected to affect surface climate and tropospheric temperatures in a manner opposite to their stratospheric impacts (e.g., enhanced stratospheric water vapor leads to surface warming). Although unambiguous detection of a tropospheric/surface temperature signal may be nearly impossible given the potentially small magnitude of any perturbation relative to natural variability, it is estimated that the HTHH eruption increases the likelihood of exceeding an annual mean global surface temperature anomaly of 1.5°C by 7% in the five years following the eruption (Jenkins et al. 2023).

The HTHH eruption is also likely to have effects on stratospheric ozone (Fig. SB.2.4d; sections 2g4, 6h). Impacts from HTHH on stratospheric aerosols and water vapor (and other species) may be perturbing stratospheric ozone chemistry in both midlatitudes and in the polar regions, in addition to the ozone changes from forced circulation changes (Wang et al. 2022). Since the HTHH plume was primarily confined to the SH during 2022, the greatest potential effects are on SH midlatitude ozone (as already evident in Fig. SB.2.4d) and the Antarctic ozone hole. Ozone profile data and total column ozone data in 2022 reveal anomalously low ozone in the SH midlatitude lower stratosphere during 2022, in general agreement with these expectations (section 2g4). However, MLS observations inside the Antarctic vortex showed near-average water vapor (Fig. 6.15h), and other stratospheric perturbations in recent years (e.g., Australian wildfires in early 2020 and earlier volcanic eruptions such as that of La Soufrière in April 2021) as well as anomalously weak planetary wave activity in austral spring have also likely impacted the 2022 Antarctic ozone hole. Further studies are needed to quantify the role of HTHH in perturbing stratospheric ozone.

g. Atmospheric composition

1. LONG-LIVED GREENHOUSE GASES

—X. Lan, B. D. Hall, G. Dutton, and I. Vimont

Increases in atmospheric greenhouse gas burdens, especially the long-lived greenhouse gases (LLGHGs) carbon dioxide (CO₂), methane (CH₄), and nitrous oxide (N₂O), are largely responsible for increasing global temperature (Foster et al. 2021).

Carbon dioxide is the most important and prevalent anthropogenic GHG. The atmospheric pre-industrial abundance of CO₂ is estimated to be ~278 ppm (parts per million by moles in dry air), based on air extracted from ice in Greenland and Antarctica (Etheridge et al. 1996). Globally averaged CO₂ derived from remote marine boundary layer measurements made by NOAA's Global Monitoring Laboratory was 417.1±0.1 ppm in 2022 (Fig. 2.56a), 50% higher than the pre-industrial level. Annual growth in global mean CO₂ has risen steadily from 0.6±0.1 ppm yr⁻¹ in the early 1960s to an average of 2.4 ppm yr⁻¹ during 2013–22 with the 2022 annual growth rate at 2.2 ppm yr⁻¹ (Fig. 2.56a; the global trend is updated monthly on www.gml.noaa.gov/ccgg/trends, and uncertainties are reported as one sigma in this section).

The main driver of increasing atmospheric CO₂ is fossil fuel (FF) burning, with total fossil emissions (including ~5% from cement production) increasing from 3.0±0.2 Pg C yr⁻¹ in the 1960s to 9.6±0.5 Pg C yr⁻¹ in the past decade (2012–21; Friedlingstein et al. 2022). Comparing fossil emissions to the atmospheric increase, we can conclude that only about half of the fossil CO₂ emitted since 1958 has remained in the atmosphere, with the other half taken up by the oceans and terrestrial biosphere. While emissions of CO₂ from FF combustion drive its increasing atmospheric burden, the interannual variability in the CO₂ growth rate is mostly driven by terrestrial biosphere exchange of CO₂ driven by climate variability such as El Niño–Southern Oscillation (ENSO), which is confirmed by measurements of stable (¹³C:¹²C) carbon isotope ratios (e.g., Keeling and Revelle 1985; Alden et al. 2010).

Fossil CO₂ emissions are estimated to have declined by 5.4% in 2020 relative to 2019 due to the COVID-19 pandemic but returned to pre-COVID levels in 2021

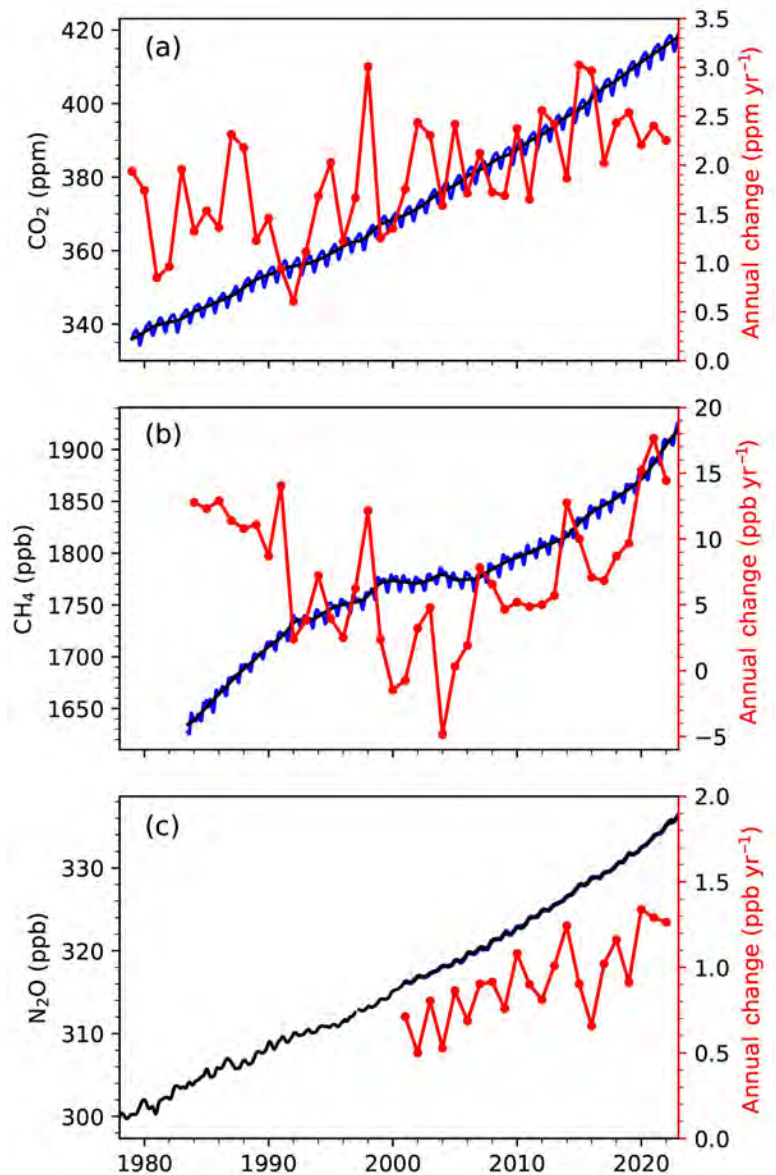


Fig. 2.56. Global mean dry-air remote surface mole fractions (approximately weekly data in blue and deseasonalized trend in black [see Dlugokencky et al. 1994b for methods], left axis) and annual change (red, right axis) of (a) carbon dioxide (CO₂, ppm), (b) methane (CH₄, ppb), and (c) nitrous oxide (N₂O, ppb) derived from the NOAA Global Greenhouse Gases Reference Network. N₂O data prior to 2000 are insufficient and noisy and thus hinder the calculation of a growth rate.

(Friedlingstein et al. 2022). However, these emission changes are not reflected in observed global atmospheric CO₂ signals, because it is a relatively small signal compared to the natural variability that is driven by the large fluxes from photosynthesis and respiration of ecosystems on land.

The impacts of LLGHGs on global climate are estimated using the effective radiative forcings (ERFs) of LLGHGs, following the Intergovernmental Panel on Climate Change Sixth Assessment Report (Forster et al. 2021). Increasing atmospheric CO₂ has accounted for 66% increase in ERF by LLGHGs, by 2.26 W m⁻² in 2022 compared with preindustrial times (before 1750). The rate of increase in CO₂ ERF during 2018–22 accounted for 78% of the total increase by LLGHGs. A pulse of CO₂ will remain in the atmosphere for thousands of years (Archer and Brovkin 2008) and cause long-lasting warming (Pierrehumbert 2014).

Atmospheric CH₄ has a lifetime of ~9 years, meaning that its atmospheric abundance and ERF can be reduced much more quickly by reducing emissions compared to CO₂ (United Nations Global Methane Assessment 2021). Global mean tropospheric CH₄ abundance increased to 1911.8±0.6 ppb (parts per billion by moles in dry air) in 2022, a 165% increase compared to its pre-industrial level of 729±9 ppb (Mitchell et al. 2013). Global CH₄ increased by an average of 12±1 ppb yr⁻¹ between 1984 and 1991, followed by a smaller increase of 4±2 ppb yr⁻¹ between 1992 and 1998, and further reduced to near zero (1±3 ppb yr⁻¹) during 1999–2006. Atmospheric CH₄ growth restarted in 2007 and has significantly accelerated since 2014 (Fig. 2.56b). The highest annual CH₄ growth rates were recorded in 2020 and 2021 at 15.2±0.4 ppb and 17.7±0.4 ppb, respectively, since the beginning of NOAA's systematic CH₄ measurements in 1983. Preliminary results also reveal large growth in 2022 of 14.4±0.4 ppb. The increase in CH₄ contributed to a 0.56 W m⁻² increase in ERF in 2022 from preindustrial times while the CH₄-related production of tropospheric ozone (O₃) and stratospheric H₂O also contributes to ~0.30 W m⁻² indirect radiative forcing (Myhre et al. 2014).

Atmospheric measurements of ¹³C:¹²C of CH₄ (denoted δ¹³C-CH₄) are sensitive to different CH₄ emission and sink processes (Lan et al. 2021). The ongoing reduction in δ¹³C-CH₄ since 2008 (Michel et al. 2022) indicates increased emissions from microbial sources (Basu et al. 2022), including both anthropogenic emissions from livestock and waste/landfills and natural wetland and lakes, which have more negative δ¹³C-CH₄ signatures. A decrease in biomass burning (Worden et al. 2017) and a small increase in FF emissions (leakage, not combustion) may also play a smaller role in 2007–16 global CH₄ change (Lan et al. 2019, 2021; Oh et al. 2022; Basu et al. 2022).

Recent studies suggest a dominant role of increased tropical wetland emissions in the 2020 CH₄ surge (Feng et al. 2021; Peng et al. 2022). An increased contribution from wetland emissions also agrees with the acceleration of atmospheric δ¹³C-CH₄ reductions in 2020 and 2021 (Michel et al. 2022). Rapid increases in wetland CH₄ emissions can be an indication of ongoing climate feedback. A reduction in the hydroxyl radical (OH, the main sink for CH₄) may have contributed to the growth in 2020 due to the COVID-19 pandemic impact on major OH precursors, NO_x, and CO (Laughner et al. 2021; Peng et al. 2022). However, COVID-19-related processes are unlikely to explain the continued rapid increase in 2021 and 2022. Additionally, Lan et al. (2021) showed that the reduction in the OH sink portion would push atmospheric δ¹³C-CH₄ upward when the atmospheric CH₄ mass balance is satisfied.

Nitrous oxide is an ozone-depleting LLGHG (Ravishankara et al. 2009) produced by microbes that rely on nitrogen substrates from natural and agricultural soils, animal manure, and the oceans (Davidson 2009). Atmospheric N₂O has been increasing steadily throughout the industrial era, except for a brief period in the 1940s (MacFarling Meure et al. 2006; Thompson et al. 2019). The mean global atmospheric N₂O abundance in 2022 was 335.7±0.1 ppb, a 24% increase over its preindustrial level of 270 ppb. The annual increase of 1.3±0.1 ppb in 2020 was the largest in NOAA's measurement record since 2000, while similarly large growth rates were observed in 2021 and 2022 at 1.3±0.1 ppb and 1.3±0.1 ppb (Fig. 2.56c). Recent growth rates are larger than the average increase during 2010–19 (1.0 ± 0.2 ppb), suggesting increased emissions. The increase in atmospheric N₂O abundance contributed to a 0.22 W m⁻² increase in ERF in 2022. The rate of increase in N₂O contributed to 9% of the rate of increase in radiative forcing by all LLGHGs

in the past five years (2018–22), comparable to the 11% contribution from CH₄ increase.

The combined radiative forcing in 2022 from all LLGHGs was 3.44 W m⁻² (Fig. 2.57), which is 3.6 times larger than in 1950. The post-industrial increases in atmospheric CO₂, CH₄, and N₂O abundances have contributed to 88% of ERF increase (Fig. 2.57a), while the mean rate of ERF increase for CO₂, CH₄, and N₂O in the past five years (2018–22) accounts for 98% of the mean rate of ERF increase resulting from growth of all LLGHGs (Fig. 2.57b).

2. OZONE-DEPLETING SUBSTANCES AND THEIR SUBSTITUTES

—I. J. Vimont, B. D. Hall, G. Dutton, S. A. Montzka, J. Mühle, M. Crotwell, K. Petersen, S. Clingan, and D. Nance

Ozone-depleting substances (ODSs) include chlorofluorocarbons (CFCs), methyl bromide, various chlorinated hydrocarbons, halons, and the CFC replacements hydrochlorofluorocarbons (HCFCs). These compounds influence global climate both through direct absorption of infrared energy and via their ability to deplete stratospheric ozone, a strong greenhouse gas (Karpechko and Maycock 2018). Hydrofluorocarbons (HFCs) are increasingly used as ODS replacements that do not destroy ozone, but they are highly efficient infrared absorbers.

The consumption and production of these classes of halogenated compounds is controlled by the 1987 Montreal Protocol (hereafter referred to as The Protocol), and its subsequent amendments, both of which aim to limit damage to the stratospheric ozone layer and the climate. The Protocol first specified the phase-out of production and consumption for dispersive uses of ODSs starting with the CFCs, followed by halons and then HCFCs. More recently, a phase down of select HFCs with high global warming potentials (GWPs) used as ODS substitutes has been mandated through the Kigali Amendment to The Protocol. Importantly, the Kigali Amendment was signed by China in 2021 and by the United States in 2022, further strengthening the ability of The Protocol and the global community to reduce the impacts of these gases on the climate.

Even as production of these controlled substances ends, other factors affect their atmospheric abundance. Their atmospheric lifetimes vary considerably, such that long-lived chlorofluorocarbons like CFC-11 and CFC-12 have only declined 18% and 10% from their peak atmospheric abundances (in 1994 and 2003, respectively), while the shorter-lived solvent methyl chloroform has declined by 99% (Fig. 2.58). Production of CFC-11 and CFC-12 was reported to have been globally phased out in 2010, while methyl chloroform (CH₃CCl₃) was reported to have been globally phased out by 2015. Additionally, the slow long-term release or sudden leakage of chemicals from some applications (e.g., insulating foams and refrigeration units) plays an important role in maintaining emissions even after production has been phased out.

It is important to note that for compounds controlled by The Protocol, the scheduled phase-down or phase-out of production of these compounds is agreed upon, and efforts to accomplish this are self-reported by individual countries to the United Nation's Ozone Secretariat. Recent studies of CFC-11 exemplify the critical need for continued monitoring of these compounds in the atmosphere to ensure the success of The Protocol. The unexpected slowdown in the reduction of the atmospheric abundance of CFC-11 after 2012 led to the discovery of renewed, unreported emissions through to 2018 in an apparent violation of The Protocol (Montzka et al.

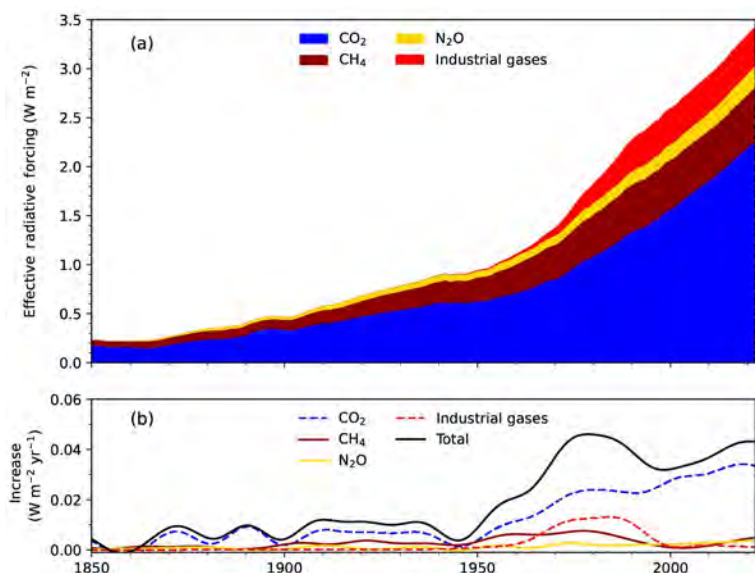


Fig. 2.57. (a) Effective radiative forcing (W m⁻²) due to long-lived greenhouse gases (LLGHGs; see Table 2.8 for details on industrial gases). (b) Annual increase in direct radiative forcing (W m⁻²).

2018; Rigby et al. 2019). Since then, an accelerated decline in abundance has been measured, suggesting that the problem may be mostly resolved (Montzka et al. 2021; Park et al. 2021).

Tangentially, signatories to the Kigali Amendment pledged to begin controlling select HFCs under The Protocol, including HFC-23 and HFC-134a. Reported abatement of HFC-23 independent of the Kigali Amendment suggests that emissions of this high-GWP compound should have been decreasing in recent years (e.g., Stanley et al. 2020 and references therein). However, measurements show its global abundance increasing by about 1.0 ppt (parts per trillion by moles in dry air) per year (since 2013), reaching 35.9 ppt in 2022 (Table 2.8 and Fig. 2.58), indicating that emissions are instead increasing (Stanley et al. 2020; Park et al. 2023). Likewise, the most abundant

Table 2.8. Summary table of long-lived greenhouse gases for 2022 (CO₂ mixing ratios are in ppm, N₂O and CH₄ in ppb, and all others in ppt).

Compound Class	Industrial Designation or Common Name	Chemical Formula	ERF ^a	Rad. Efficiency (W m ⁻² ppb ⁻¹) ^b	Rad. Forcing ^a (ERF/SARF) (W m ⁻²)	Mean surface mole fraction, 2022 [change from prior year] ^c	Lifetime (yrs) ^b
Acidic oxide	Carbon Dioxide	CO ₂	Y	1.33 × 10 ⁻⁵	2.3	417.1 [2.4]	
Alkane	Methane	CH ₄	Y	3.88 × 10 ⁻⁴	0.56	1911.9 [13.0]	9.1
Nitride	Nitrous Oxide	N ₂ O	Y	3.2 × 10 ⁻³	0.22	335.7 [1.3] ^d	123
Chlorofluorocarbon	CFC-11	CCl ₃ F	N(Y) ^e	0.26	0.057(0.064)	219.6 [−2.1] ^d	52
Chlorofluorocarbon	CFC-12	CCl ₂ F ₂	N(Y) ^e	0.32	0.157(0.176)	489.7 [−3.5] ^d	102
Chlorofluorocarbon	CFC-113	CCl ₂ FCClF ₂	N	0.30	0.020	67.8 [−0.5] ^d	93
Hydrochlorofluorocarbon	HCFC-22	CHClF ₂	N	0.21	0.052	248.8 [−0.1]	11.9
Hydrochlorofluorocarbon	HCFC-141b	CH ₃ CCl ₂ F	N	0.16	0.004	24.6 [0.0]	9.4
Hydrochlorofluorocarbon	HCFC-142b	CH ₃ CClF ₂	N	0.19	0.004	21.2 [−0.3]	18
Hydrofluorocarbon	HFC-134a	CH ₂ FCF ₃	N	0.17	0.021	124.5 [5.6]	14
Hydrofluorocarbon	HFC-152a	CH ₃ CHF ₂	N	0.10	<0.001	7.4 [0.2]	1.6
Hydrofluorocarbon	HFC-143a	CH ₃ CF ₃	N	0.17	0.005	27.5 [1.8]	51

^a Effective Radiative Forcing (ERF) calculated by multiplying the stratospheric-temperature adjusted radiative efficiency (SARF) by the global mole fraction (in ppb) and then applying a tropospheric adjustment factor for the species indicated based on recommended values from chapters 6 and 7 in the IPCC AR6 WGI Report. The Radiative Forcing column is either ERF (where indicated) or SARF. The adjustments to the SARF are CO₂: 5% ± 5%, CH₄: −14% ± 15%, N₂O: 7% ± 13–16%.

^b Radiative efficiencies and lifetimes were taken from Appendix A in WMO (2018) and Hodnebrog et al. (2020a), except for SF₆ lifetime from Ray et al. (2017), CH₄ lifetime from Prather et al. (2012). For CO₂, numerous removal processes complicate the derivation of a global lifetime. AGGI = Annual Greenhouse Gas Index. For radiative forcing, see <https://www.esrl.noaa.gov/gmd/aggi/aggi.html>.

^c Mole fractions are global, annual, midyear surface means determined from the NOAA cooperative global air sampling network (Hofmann et al. 2006), except for PFC-14, PFC-116, PFC-218, PFC-318, and HFC-23, which were measured by AGAGE (Mühle et al. 2010; Miller et al. 2010). Changes indicated in brackets are the differences between the 2022 and 2021 means, the relevant quantities for calculating radiative forcing. These changes are somewhat different from the 2022 annual increases reported in (LLGHG SECTION), which are determined as the difference between 1 Jan 2022 and 1 Jan 2021. All values are preliminary and subject to minor updates.

^d Global mean estimates derived from multiple NOAA measurement programs (“Combined Dataset”).

^e ERF calculated values for CFC-11 and CFC-12 are highly uncertain but recommended by the IPCC AR6 WGI Report. Thus, they are included in parentheses here as the lower confidence value. The adjustment to the SARF for these values is 12% ± 13% (Hodnebrog et al. (2020b)).

Compound Class	Industrial Designation or Common Name	Chemical Formula	ERF ^a	Rad. Efficiency (W m ⁻² ppb ⁻¹) ^b	Rad. Forcing ^a (ERF/SARF) (W m ⁻²)	Mean surface mole fraction, 2022 [change from prior year] ^c	Lifetime (yrs) ^b
Hydrofluorocarbon	HFC-125	CHF ₂ CF ₃	N	0.23	0.007	37.0 [3.7]	30
Hydrofluorocarbon	HFC-32	CH ₂ F ₂	N	0.11	0.002	26.3 [3.5]	5.4
Hydrofluorocarbon	HFC-23	CHF ₃	N	0.18	0.006	35.9 [0.9]	228
Hydrofluorocarbon	HFC-365mfc	CH ₃ CF ₂ CH ₂ CF ₃	N	0.22	<0.001	1.07 [0.02]	8.9
Hydrofluorocarbon	HFC-227ea	CF ₃ CHFCF ₃	N	0.26	<0.001	2.04 [0.17]	36
Chlorocarbon	Methyl Chloroform	CH ₃ CCl ₃	N	0.07	<0.001	1.1 [-0.1]	5.0
Chlorocarbon	Carbon Tetrachloride	CCl ₄	N	0.17	0.013	75.5 [-1.2] ^d	32
Chlorocarbon	Methyl Chloride	CH ₃ Cl	N	0.01	<0.001	547.5 [0.2]	0.9
Chlorocarbon	Methyl Bromide	CH ₃ Br	N	0.004	<<0.001	6.61 [-0.06]	0.8
Chlorocarbon	Halon 1211	CBrClF ₂	N	0.29	0.001	2.93 [-0.1]	16
Chlorocarbon	Halon 1301	CBrF ₃	N	0.30	0.001	3.31 [0.0]	72
Chlorocarbon	Halon 2402	CBrF ₂ CBrF ₂	N	0.31	<0.001	0.397 [0.001]	28
Fully fluorinated species	Sulfur Hexafluoride	SF ₆	N	0.57	0.006	11.02 [0.37]	>600
Fully fluorinated species	PFC-14	CF ₄	N	0.09	0.005	88.5 [1.0]	~50,000
Fully fluorinated species	PFC-116	C ₂ F ₆	N	0.25	0.001	5.15 [0.12]	~10,000
Fully fluorinated species	PFC-218	C ₃ F ₈	N	0.28	<0.001	0.74 [0.02]	~2600
Fully fluorinated species	PFC-318	c-C ₄ F ₈	N	0.32	<0.001	1.99 [0.09]	~3200

^a Effective Radiative Forcing (ERF) calculated by multiplying the stratospheric-temperature adjusted radiative efficiency (SARF) by the global mole fraction (in ppb) and then applying a tropospheric adjustment factor for the species indicated based on recommended values from chapters 6 and 7 in the IPCC AR6 WGI Report. The Radiative Forcing column is either ERF (where indicated) or SARF. The adjustments to the SARF are CO₂: 5% ± 5%, CH₄: -14% ± 15%, N₂O: 7% ± 13–16%.

^b Radiative efficiencies and lifetimes were taken from Appendix A in WMO (2018) and Hodnebrog et al. (2020a), except for SF₆ lifetime from Ray et al. (2017), CH₄ lifetime from Prather et al. (2012). For CO₂, numerous removal processes complicate the derivation of a global lifetime. AGGI = Annual Greenhouse Gas Index. For radiative forcing, see <https://www.esrl.noaa.gov/gmd/aggi/aggi.html>.

^c Mole fractions are global, annual, midyear surface means determined from the NOAA cooperative global air sampling network (Hofmann et al. 2006), except for PFC-14, PFC-116, PFC-218, PFC-318, and HFC-23, which were measured by AGAGE (Mühle et al. 2010; Miller et al. 2010). Changes indicated in brackets are the differences between the 2022 and 2021 means, the relevant quantities for calculating radiative forcing. These changes are somewhat different from the 2022 annual increases reported in {LLGHG SECTION}, which are determined as the difference between 1 Jan 2022 and 1 Jan 2021. All values are preliminary and subject to minor updates.

^d Global mean estimates derived from multiple NOAA measurement programs (“Combined Dataset”).

^e ERF calculated values for CFC-11 and CFC-12 are highly uncertain but recommended by the IPCC AR6 WGI Report. Thus, they are included in parentheses here as the lower confidence value. The adjustment to the SARF for these values is 12% ± 13% (Hodnebrog et al. (2020b)).

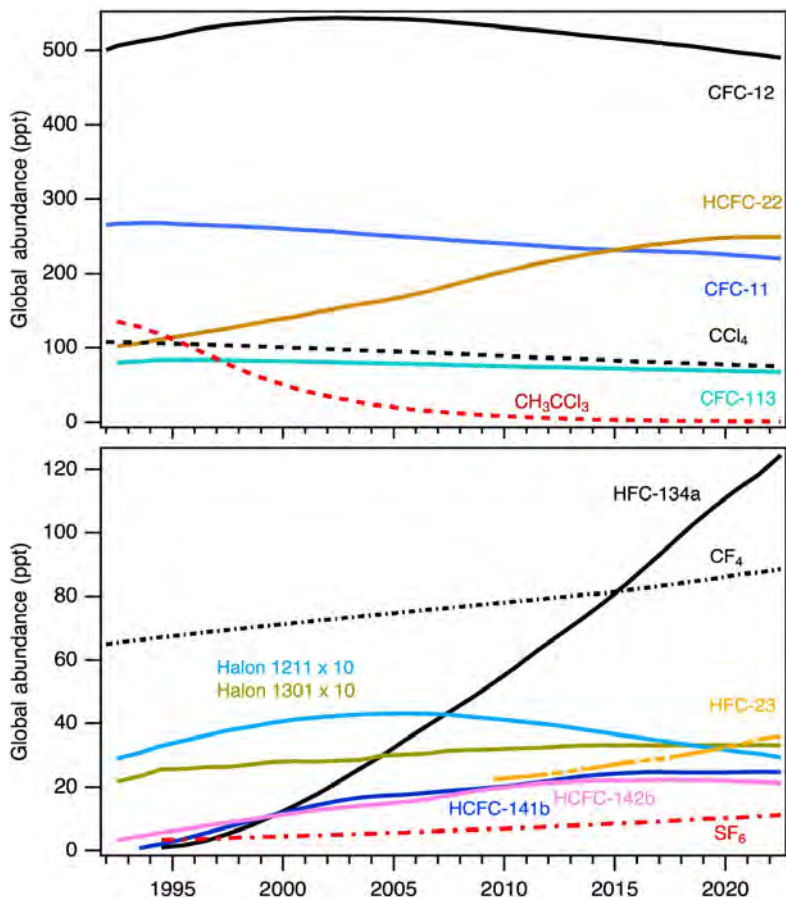


Fig. 2.58. Global mean abundances (mole fractions) at Earth's surface (ppt = nmol mol⁻¹ in dry air) for a suite of halogenated gases, most of which deplete stratospheric ozone. See Table 2.8 for the 2022 global mean mole fractions of these and other gases. All compounds, except hydrofluorocarbon (HFC)-23, are mid-year global means taken from <https://gml.noaa.gov/aftp/data/hats/>. HFC-23 data derived from AGAGE mid-year global means taken from https://agage2.eas.gatech.edu/data_archive/global_mean/global_mean_ms.txt.

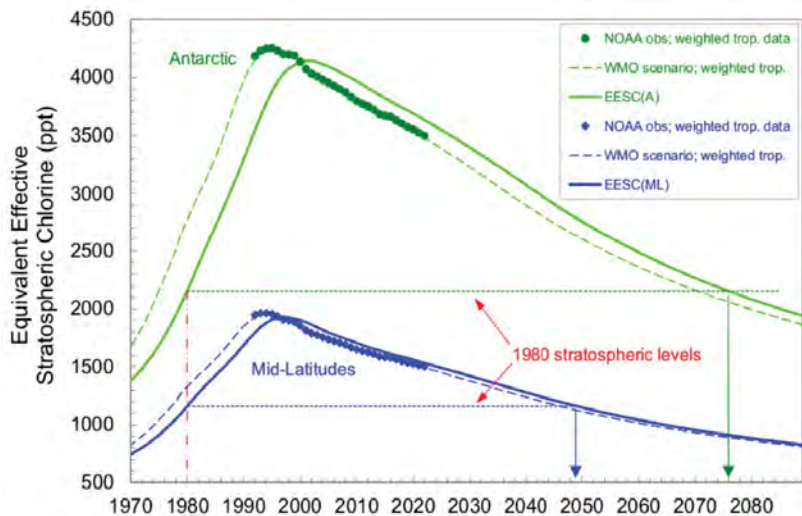


Fig. 2.59. The equivalent effective stratospheric chlorine in the Antarctic and midlatitudes (EESC(A) and EESC(ML), respectively) values represent EESC on 1 Jan of each year since 1970. Dashed lines represent tropospheric measurement-derived scenarios, based on past measurements and, for the future, full adherence to all controls from The Protocol based on the WMO/UNEP 2018 Ozone Assessment. Solid lines depict inferred stratospheric changes based on the measured tropospheric curves. In 2022, midlatitude and Antarctic EESC were at 1537 ppt and 3635 ppt, which represent reductions of 21% and 12.5% in stratospheric reactive halogen loading from their peaks. Translating this to the Ozone Depleting Gas Index (ODGI), the midlatitude ODGI is 48.6 and the Antarctic ODGI is 74.1, meaning the stratospheric reactive halogen loading has declined 52.4% and 25.9% relative to the 1980 benchmark reactive halogen abundance.

HFC, HFC-134a, a common mobile air-conditioning fluid, has increased by an average of 5.8 ppt yr⁻¹ since 2012, reaching 124.5 ppt in 2022 (Table 2.8; Fig. 2.58).

One measure of the reactive halogen loading at a given time and place in the stratosphere is the equivalent effective stratospheric chlorine (EESC; Daniel et al. 1995; Montzka et al. 1996; Newman et al. 2007). The presence of reactive halogen radicals in the stratosphere is mostly due to the breakdown of CFCs, which still have high abundances in the atmosphere and contribute strongly to EESC. While EESC provides a measure of reactive stratospheric halogen (Fig. 2.59), it is useful to scale the EESC to provide context relative to stratospheric ozone recovery, and thus the Ozone Depleting Gas Index (ODGI) was developed (Hoffmann and Montzka 2009). For a full description of both EESC and ODGI, see <https://gml.noaa.gov/odgi/>. Briefly, EESC and the ODGI are separated

into two categories, midlatitude and Antarctic, because transport processes cause widely different reactive halogen abundances in these stratospheric regions. ODGI is derived from a simple scaling of EESC such that an ODGI of 100 represents the peak EESC value, and an ODGI of 0 represents the value of EESC in 1980 (Hoffmann and Montzka 2009). Using the ODGI, recovery of the stratospheric ozone layer is expected to reach 1980 levels in 2049 for the midlatitudes and 2076 in the Antarctic (Fig. 2.59).

3. AEROSOLS

—S. Rémy, N. Bellouin, M. Ades, M. Alexe, A. Benedetti, O. Boucher, and Z. Kipling

Atmospheric aerosols play an important role in the climate system by scattering and absorbing radiation and by affecting the life cycle, optical properties, and precipitation activity of clouds (IPCC AR6, chapter 6; Szopa et al. 2021). Aerosols also represent a serious public health issue in many countries, and hence are subject to monitoring and forecasting as part of air quality policies. There is also growing evidence that aerosols influence ecosystems through changes in the quality and quantity of light and deposition flux of nutrients over land and ocean (Mahowald et al. 2017).

The Copernicus Atmosphere Monitoring Service (CAMS; <http://atmosphere.copernicus.eu>) runs a near-real-time global analysis of aerosols and trace gases. It also produces a reanalysis of global aerosols and trace gases covering the years 2003–22 (CAMS Reanalysis [CAMRA]; Inness et al. 2019), by combining state-of-the-art numerical modeling and in the case of aerosols, remote sensing retrievals from the Moderate Resolution Imaging Spectroradiometer (MODIS; Levy et al. 2013) and the Advanced Along Track Scanning Radiometer (AATSR; Popp et al. 2016).

Aerosol optical depth (AOD) at 550 nm and particulate matter $\leq 2.5\mu\text{m}$ (PM_{2.5}) concentrations ($\mu\text{g m}^{-3}$) in 2022 (Figs. 2.60a,b) show maxima over India and China, mostly from anthropogenic sources, as well as from dust over the Sahara and the Middle East. High values from seasonal or occasional extreme fires are noted over equatorial Africa, Siberia, parts of North America, and the Amazon basin. There is strong seasonality in AOD (Fig. 2.60c), driven mainly by dust episodes

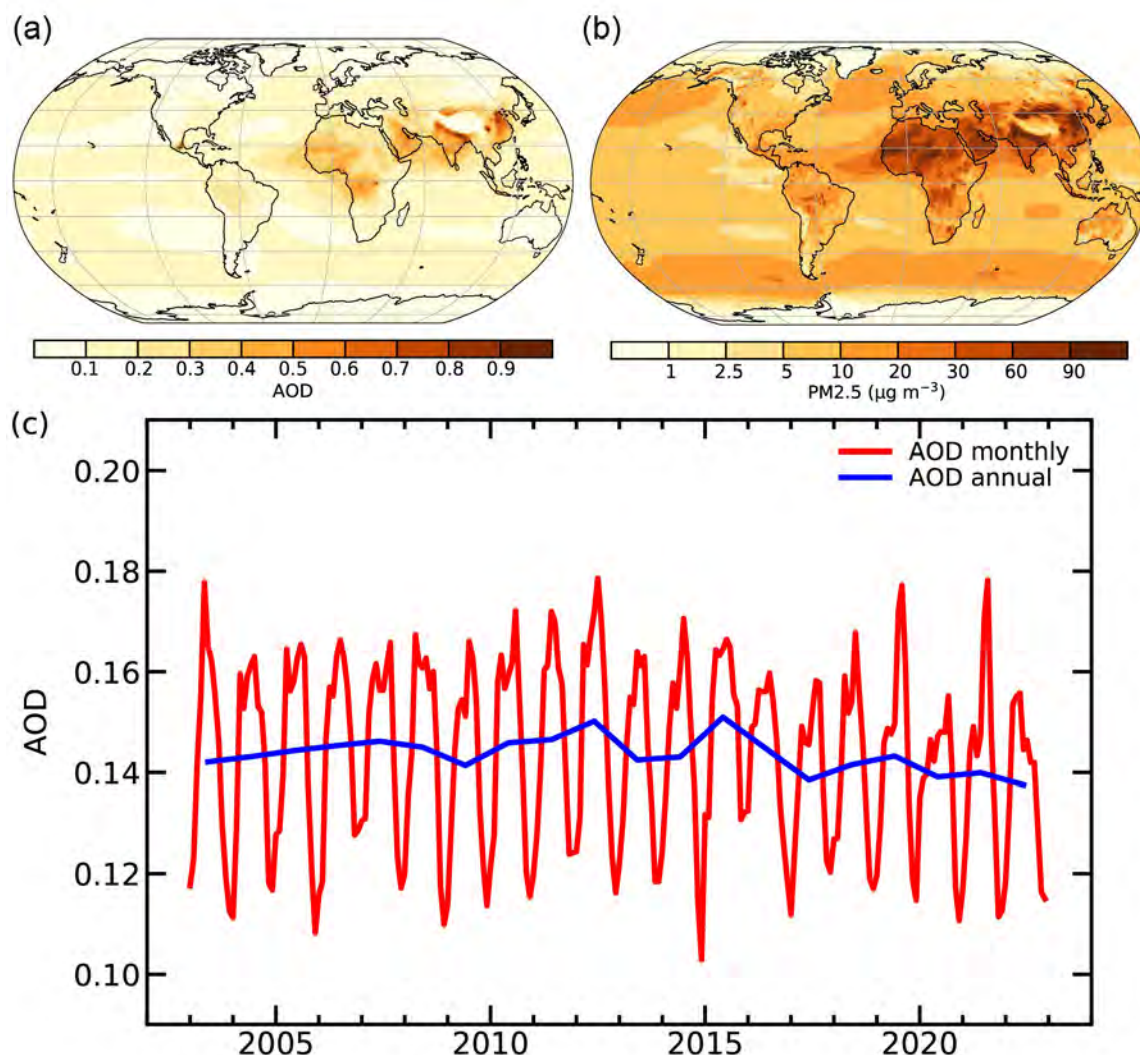


Fig. 2.60. (a) Global aerosol optical depth (AOD) at 550 nm in 2022; (b) global surface PM_{2.5} concentrations ($\mu\text{g m}^{-3}$) in 2022; and (c) global average of total AOD at 550 nm averaged over monthly (red) and annual (blue) periods for 2003–22.

between March and July in the Sahara, Middle East, and Taklimakan/Gobi desert and seasonal biomass burning in Africa, South America, and Indonesia. Globally averaged AOD in 2022 was the lowest on record, slightly lower than in 2021 and 2020. The summer maximum was much less pronounced than in 2021, as there were fewer fire emissions in 2022.

The 2022 AOD (Plates 2.1v,w) was much less impacted by large fire events than in 2021. Positive anomalies due to fires are found above parts of the Amazon basin, following an active fire season in July and August 2022, and parts of Alaska. South Africa also experienced exceptional fires from the end of July to early October, which led to a large positive AOD anomaly and a number of exceptional AOD days (Plate 2.1x). Dust storm activity was in general lower than usual over most of the Sahara except over its northwest fringe, while the Taklimakan and most of the Arabian Peninsula experienced a higher-than-usual amount of dust. Most of the Southern Hemisphere witnessed a small positive AOD anomaly (see Plates 2.1v,w) between January and March 2022 associated with the Hunga Tonga–Hunga Ha’apai (HTHH) eruption of 13–15 January. This eruption led to the largest stratospheric aerosol disturbance since the June 1991 Mt. Pinatubo eruption (Legras et al. 2022), although HTHH mostly impacted the Southern Hemisphere (see Sidebar 2.2). Monthly stratospheric AOD increased by 0.05 to 0.1 AOD units over the most affected areas (west of Australia, eastern equatorial Pacific Ocean), where there were also signals in terms of number of extreme AOD days. The negative anomalies of AOD over East Asia, Europe, and the Amazon basin (positive anomalies over India and Iran) are associated with ongoing decreasing (increasing) trends in these regions.

The AOD and PM_{2.5} 2003–22 and 2012–22 trends are shown in Figs. 2.61a–d and are generally consistent. Between 2003 and 2022, there is a strong negative trend over most of United States, Europe, East Asia, and parts of the Amazon basin, the latter from reduced deforestation activity. Positive trends are noted over parts of Siberia, driven by biomass burning events, as well as over India and Iran, driven by an increase in anthropogenic emissions of aerosol constituents (e.g., Wang et al. 2021). Between 2012 and 2022, the picture is slightly different: there is no decreasing

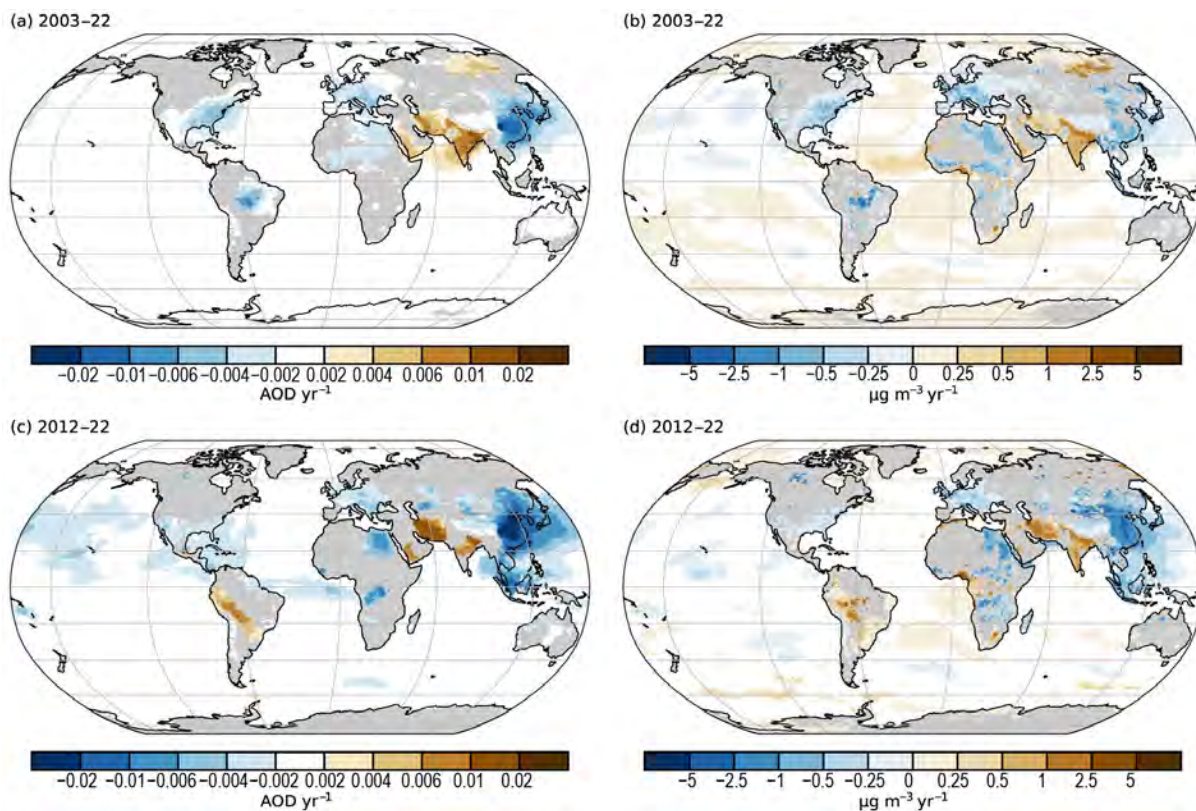


Fig. 2.61. (a),(b) linear trends of total aerosol optical depth (AOD unit yr⁻¹) and PM_{2.5} (μg m⁻³ yr⁻¹) for 2003–22; and (c),(d) linear trends of total AOD (AOD unit yr⁻¹) and PM_{2.5} (μg m⁻³ yr⁻¹) for 2012–22. Only trends that are statistically significant (95% confidence level) are shown. Regions with decreasing trends include the eastern United States, most of Europe, parts of Brazil and China, as well as the Korean Peninsula and Japan.

trend over the Amazon basin, showing that most of the 2003–22 reduction can be explained by the evolution from 2003 to 2012. The 2012–22 negative trend over Europe and the eastern United States is weaker than the 2003–22 trend, while over East Asia it is stronger, which is consistent with the observed decrease of anthropogenic emissions predominantly occurring since 2012 (Li et al. 2017; Wang et al. 2021). A stronger positive trend between 2012 and 2022 is noted over most of Iran, while over the same period the positive trend over India is smaller than the 2003–22 trend.

Anthropogenic AOD and radiative forcing resulting from aerosol-radiation (RFari) and aerosol-cloud interactions (RFaci; see Bellouin et al. 2020 for details) are shown in Fig. 2.62 for 2022 and the period 2003–22. 2022 is the fifth consecutive year showing a decrease in the average anthropogenic AOD and of the absolute magnitude of RFari and RFaci. This is qualitatively consistent with a reduction in anthropogenic aerosol load (Quaas et al. 2022).

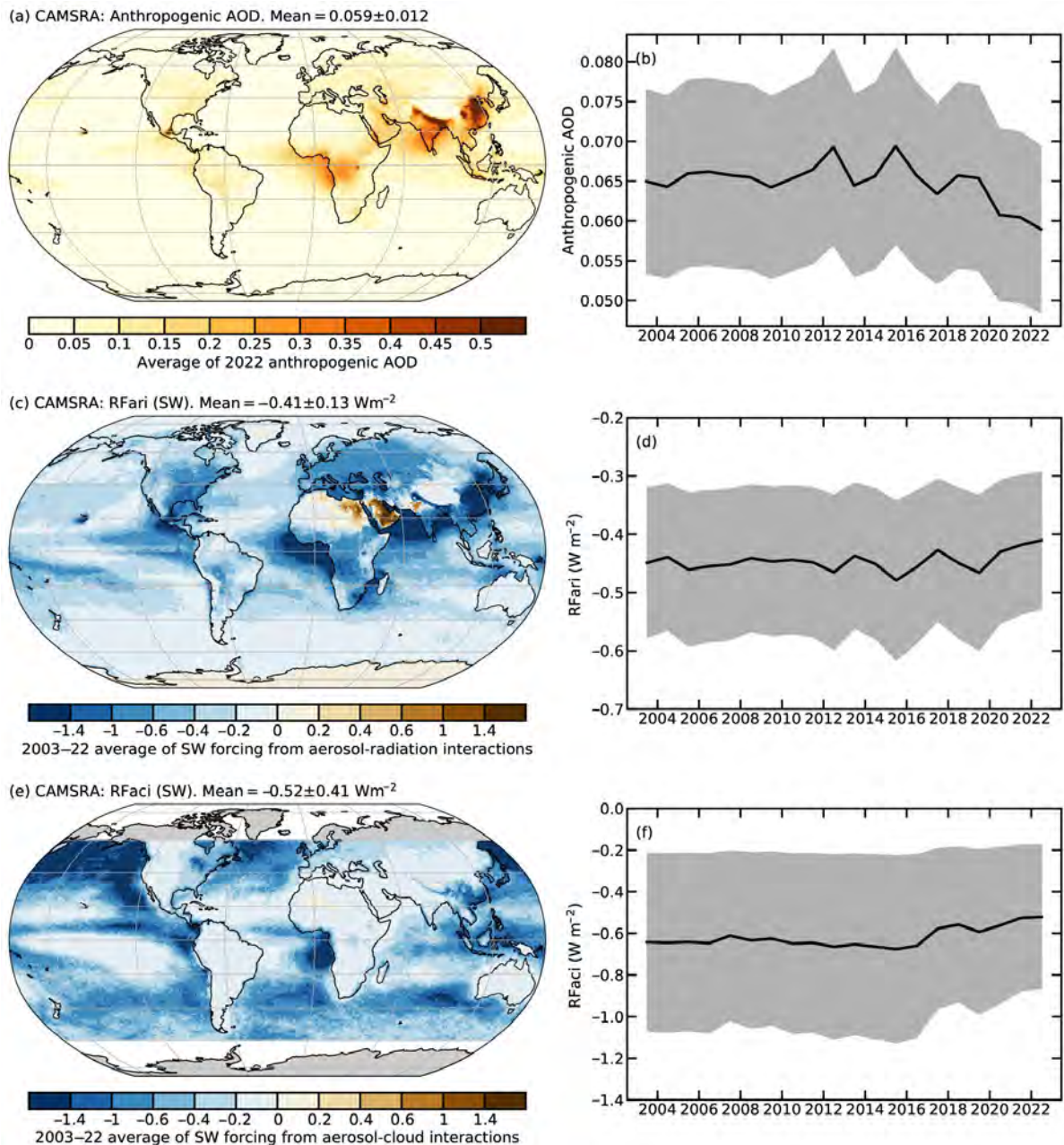


Fig. 2.62. CAMSRA (a) 2022 average of anthropogenic aerosol optical depth (AOD); (b) global annual average of anthropogenic AOD from 2003 to 2022. Radiative forcing in the shortwave (SW) spectrum due to (c),(d) aerosol-radiation (RFari) and (e),(f) aerosol-cloud interactions (RFaci). The left column shows the distributions for the year 2022. The right column shows time series of global averages for the period 2003–22, with the $1\text{-}\sigma$ uncertainties of these estimates shown in gray.

4. STRATOSPHERIC OZONE

—M. Weber, W. Steinbrecht, C. Arosio, R. van der A, S. M. Frith, J. Anderson, L. M. Ciasto, M. Coldewey-Egbers, S. Davis, D. Degenstein, V. E. Fioletov, L. Froidevaux, D. Loyola, A. Rozanov, V. Sofieva, K. Tourpali, R. Wang, T. Warnock, and J. D. Wild

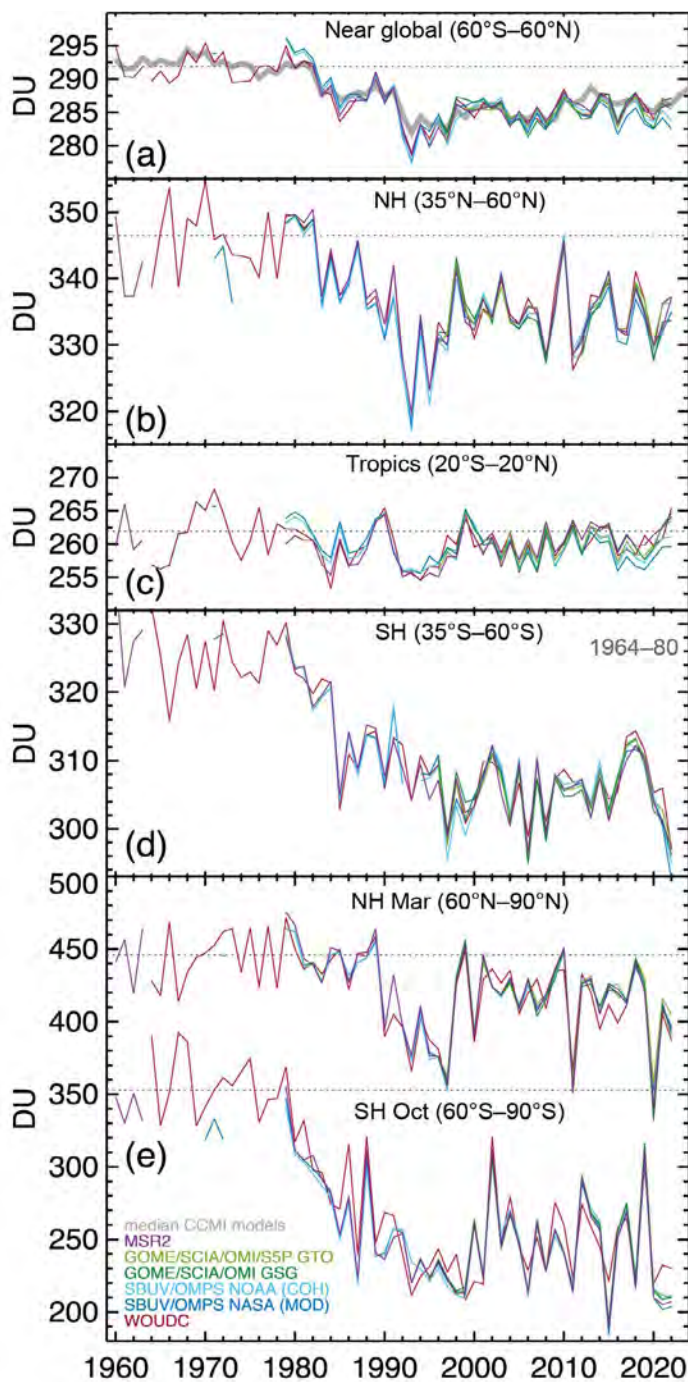


Fig. 2.63. Time series of annual mean total column ozone (DU) in (a)–(d) four zonal bands and (e) polar (60°–90°) total column ozone in Mar (Northern Hemisphere, NH) and Oct (Southern Hemisphere, SH), the months when polar ozone losses usually are largest. Data are from World Ozone and Ultraviolet Radiation Data Centre (WOUDC) ground-based measurements combining Brewer, Dobson, Système D’Analyse par Observations Zénithales (SAOZ), and filter spectrometer data (red; Fioletov et al. 2002, 2008); the BUV/SBUV/SBUV2/OMPS merged products from NASA (V8.7; dark blue; Frith et al. 2014, 2017), and NOAA (SBUV V8.6, OMPS V4r1; light blue; Wild and Long pers. comm., 2019); the GOME/SCIAMACHY/GOME-2/OMPS/(TROPOMI) products GSG from University of Bremen (dark green; Weber et al. 2022), and GTO from the ESA/DLR dataset (light green; Coldewey-Egbers et al. 2015; Garane et al. 2018). MSR2 (purple) assimilates nearly all ozone datasets after corrections based on the ground-based data (van der A et al. 2015). All datasets have been bias-corrected by subtracting averages for the reference period 1998–2008 and adding back the mean of these averages. The dotted gray lines in each panel show the average ozone level for 1964–80 calculated from the WOUDC data. The thick gray lines in (a) show the median ozone level from CCM1-1 ref C2 model runs (SPARC/IO3C/GAW 2019). Most of the observational data for 2022 are preliminary.

Stratospheric ozone protects Earth’s biosphere from harmful ultraviolet (UV) radiation. The phase-out of ozone-depleting substances (ODSs) mandated by the Montreal Protocol and its Amendments (section 2g2) stopped the continuous decline of stratospheric ozone observed before the mid-1990s (Fig. 2.63). Some regions indicate a slow recovery attributed to the ODS decline, most notably the upper stratosphere (Figs. 2.64a–c; WMO 2022; Arosio et al. 2019; Sofieva, et al. 2021; Coldewey-Egbers et al. 2022; Godin-Beekmann et al. 2022; Weber et al. 2022). The rate and the sign of long-term ozone changes depend on changes in chemical composition (e.g., ODSs) and stratospheric circulation, which vary by region and altitude and are partly due to increasing long-lived greenhouse gases (LLGHGs). Both stratospheric cooling due to LLGHG and ODS decline are expected to reduce stratospheric ozone loss outside the polar region (Stolarski et al. 2015).

Relative to a base period of 1998–2008, 2022 annual mean total ozone anomalies poleward of 30° latitude in each hemisphere were mostly negative, while positive anomalies were observed at lower latitudes and in the tropics (Plate 2.1y). These anomalies are related to the La Niña (<https://psl.noaa.gov/enso/mei/>) and the mostly westerly shear phase of the quasi-biennial oscillation (above 30 hPa) in 2022. The associated weakening of the tropical upwelling and Brewer-Dobson circulation (BDC) leads to higher ozone in the tropics and reduced ozone transport into high latitudes and, at the same time, decreases polar stratospheric temperatures in winter/spring, thereby enhancing spring polar ozone losses (Domeisen et al. 2019).

The variability in lower stratospheric ozone is largest in winter/spring in both hemispheres, which drives the annual mean variations, as seen in Figs. 2.63 and 2.64.

The various annual mean time series of total ozone (Fig. 2.63) convey the same picture as observed in Plate 2.1y. At midlatitudes (35°–60°) in both hemispheres (Figs. 2.63b,d), the annual mean total ozone in 2022 was close to the long-term mean (1998–2008) in the Northern Hemisphere and at the lower end of values during the last decade in the Southern Hemisphere (SH). Particularly striking are the very low 2022 values in the SH, which are close to the all-time low of the previous sixty years. Very low stratospheric ozone is also evident at the 50-hPa level (Fig. 2.64f). Contrastingly, 50-hPa ozone and total columns from selected datasets (WOUDC,

GSG, GTO) are close to the maximum observed during the last two decades (Figs. 2.63c, 2.64e).

In addition to the effect of La Niña, the underwater volcanic eruption from Hunga Tonga–Hunga Ha’pai (HTHH) in January 2022 may have contributed to this low annual mean SH ozone in 2022. HTHH injected large quantities of aerosols and water vapor into the stratosphere that reduced stratospheric temperatures and modified chemical reaction cycles (sections 2g5, 2g3; Sidebar 2.2; Bourassa et al. 2022; Millán et al. 2022; Vömel et al. 2022). The weakening of the residual BDC in the SH caused by HTHH contributed to the drop in SH middle lower stratospheric and column ozone in 2022 (Coy et al. 2022; Wang et al. 2022). The transport of enhanced aerosol levels into the polar region, and circulation-driven lower polar temperatures may have caused additional Antarctic ozone losses (Wang et al. 2022). While the anomalously weak planetary wave activity in austral spring was the main cause of the deeper Antarctic ozone holes during the last three years (section 6i), recent studies suggest that Australian wildfires in December 2019, volcanic events of La Soufrière in April 2021, and HTHH in early 2022 contributed to the low ozone levels in the lower stratosphere at southern midlatitudes

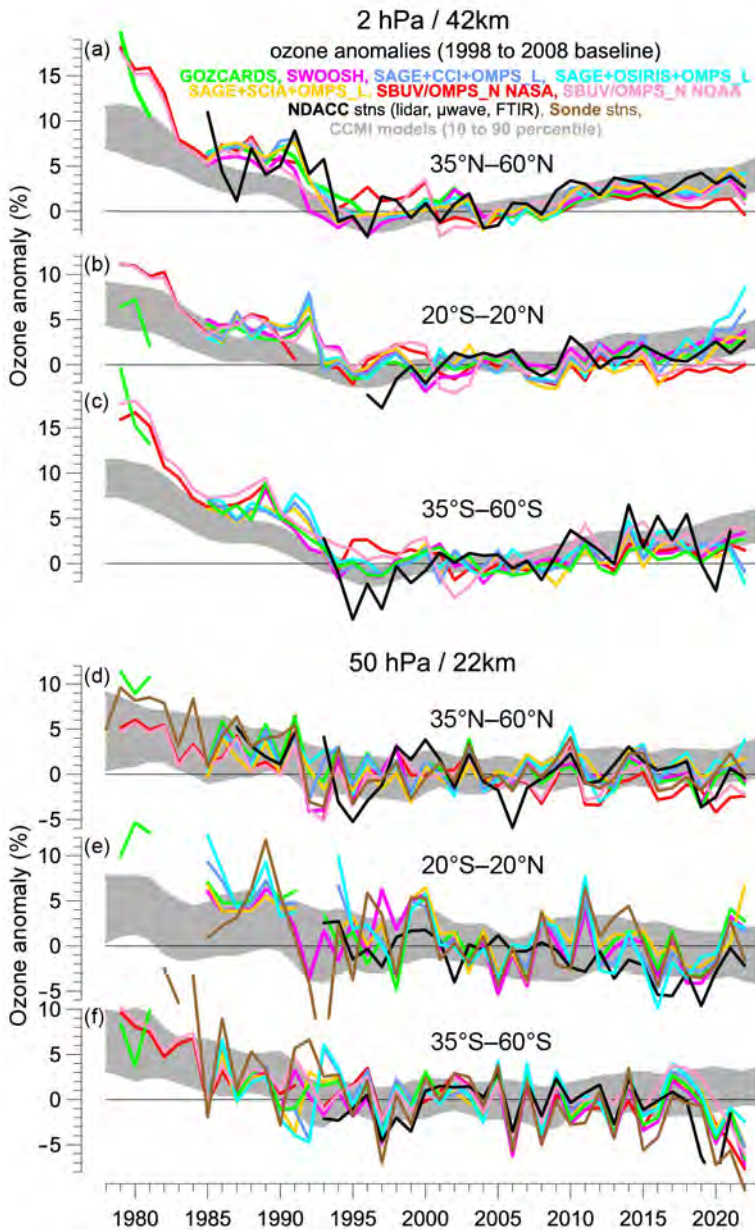


Fig. 2.64. Annual mean anomalies of ozone in (a)–(c) the upper stratosphere near 42-km altitude or 2-hPa pressure, and (d)–(f) in the lower stratosphere near 22 km or 50-hPa pressure for three zonal bands: (a),(d) 35°N–60°N, (b),(e) 20°S–20°N (tropics), and (c),(f) 35°S–60°S. Anomalies are with respect to the 1998–2008 base period. Colored lines are long-term records obtained by merging different limb (GOZCARDS, SWOOSH, SAGE+CCI+OMPS-L, SAGE+SCIAMACHY+OMPS-L) or nadir-viewing (SBUV, OMPS-N) satellite instruments. The nadir-viewing instruments have much coarser altitude resolution than the limb-viewing instruments. This can cause differences in some years, especially at 50 hPa. The black line is from merging ground-based ozone records at seven Network for the Detection of Atmospheric Composition Changes (NDACC) stations employing differential absorption lidars and microwave radiometers. See Steinbrecht et al. (2017), WMO (2018), and Arosio et al. (2018) for details on the various datasets. Gray shaded area shows the range of chemistry-climate model simulations from CCM1 refC2 (SPARC/IO3C/GAW 2019). Ozone data for 2022 are not yet complete for all instruments and are still preliminary.

(Figs. 2.63d, 2.64f) and deeper Antarctic ozone holes (Figs. 2.64f; Rieger et al. 2021; Ansmann et al. 2022; Yook et al. 2022; Strahan et al. 2022; Wang et al. 2022, Solomon et al. 2023).

Ozone profile data (Fig. 2.64f) confirm the low total ozone at southern midlatitudes. Apart from this, Fig. 2.64 shows ozone values in 2022 that are generally consistent with expectations from model simulations of the Phase 1 Chemistry Climate Model Initiative (CCMI) based on current scenarios of ODS and greenhouse gas changes (thick gray line in Fig. 2.63a; shaded area in Fig. 2.64; SPARC/IO3C/GAW 2019): 1) slow but noticeable recovery of ozone in the upper stratosphere over the last 20 years (WMO 2022; Godin-Beekmann et al. 2022), with observations in recent years closer to the lower end of the model simulations; and 2) little or no recovery of ozone in the lower stratosphere, with recent midlatitude observations at the lower end of the simulations (Ball et al. 2020; Thompson et al. 2021; Godin-Beekmann et al. 2022; WMO 2022).

5. STRATOSPHERIC WATER VAPOR

—S. M. Davis, K. H. Rosenlof, D. F. Hurst, H. Vömel, and R. Stauffer

Normally, water vapor (WV) entering the stratosphere is regulated by temperatures in the tropical tropopause layer (TTL; ~14 km–19 km), with higher WV concentrations occurring when TTL temperatures are higher. However, the 14–15 January 2022 eruptions of the Hunga Tonga–Hunga Ha’apai (HTHH) submarine volcano (20.54°S, 175.4°W) injected an amount of

water vapor (~50 Tg–150 Tg) into the stratosphere that is unprecedented in the satellite record and represents upwards of 10% of the entire stratospheric burden of WV (Carr et al. 2022; Khaykin et al. 2022; Legras et al. 2022; Millán et al. 2022; Proud et al. 2022; Vömel et al. 2022; see also Sidebar 2.2). By being injected at between approximately 26 km and 34 km, WV associated with the HTHH eruption bypassed the TTL “cold trap” and resulted in a dramatic perturbation to WV and other stratospheric species (e.g., ozone, section 2g4) that will likely persist for years.

This direct injection of WV into the stratosphere by HTHH is evident in the so-called “tropical tape recorder” (Mote et al. 1996) plot (Fig. 2.65a). The WV anomaly appears suddenly in early 2022 between roughly 40 hPa and 10 hPa and then ascends through the stratosphere as part of the meridional overturning circulation. Within the tropical latitude band (15°S–15°N), this unprecedented zonal-mean monthly-mean anomaly (relative to the 2004–21 mean) peaked at 6.4 ppm (parts per million, i.e., $\mu\text{mol mol}^{-1}$) above the climatological normal of 4.1 ppm

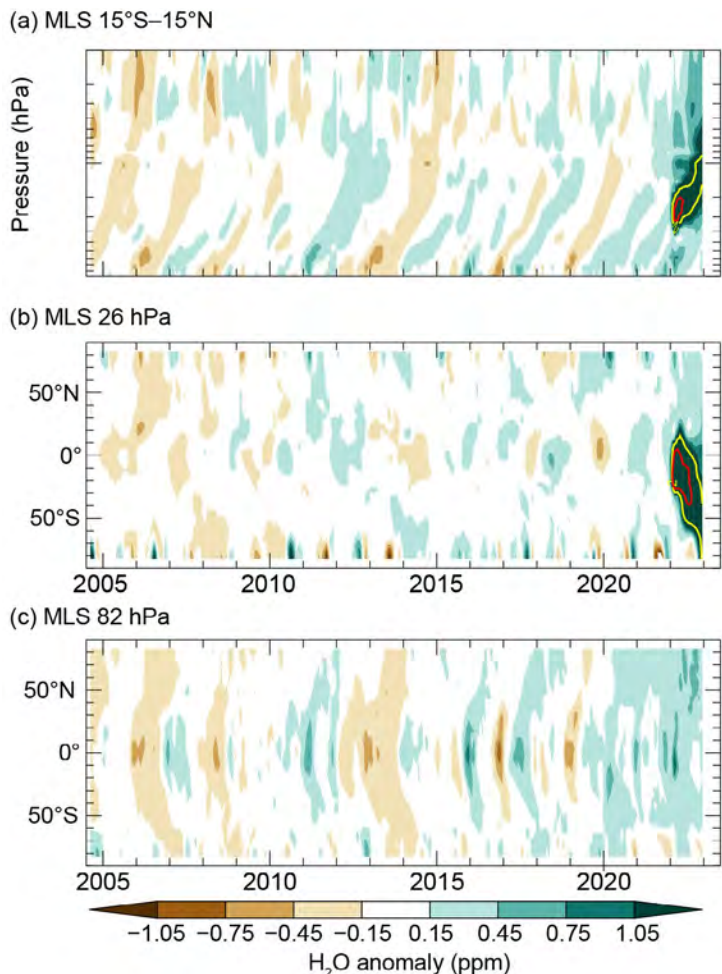


Fig. 2.65. (a) Latitude–time contour of tropical (15°S–15°N) lower-stratospheric water vapor (WV) anomalies, with the +2 ppm and +4 ppm values shown as yellow and red contour lines, respectively. (b),(c) Latitude–time contour of WV anomalies at (b) 26 hPa and (c) 82 hPa, respectively. All panels are based on version 5.01 Aura MLS data, which has collected near-global (82°S–82°N) measurements since Aug 2004. Anomalies are differences from the mean 2004–21 WV mixing ratios (ppm) for each month. (a) shows the unprecedented injection of water vapor directly into the stratosphere by the Hunga Tonga–Hunga Ha’apai eruption. (b) shows the southward propagation of the plume at 26 hPa, while (c) shows a more general propagation of tropical lower-stratospheric WV anomalies to higher latitudes in both hemispheres as well as the influences of dehydrated air masses from the Antarctic polar vortex as they are transported toward the Southern Hemisphere midlatitudes at the end of each year. Tick marks denote the beginning of each year.

at 26 hPa (~25 km) in March after the enhancement spread northward to fill this band, corresponding to a deviation from the climatological monthly zonal mean of 160% (31 standard deviations). A latitude–time cross-section of WV anomalies at 26 hPa (Fig. 2.65b) shows that the HTHH plume quickly spread as far north as 20°N immediately following the eruption, before being transported into the Southern Hemisphere in subsequent months. Maps of WV anomalies at 82 hPa (~17 km) and 26 hPa reveal the impact on lower- and mid-stratospheric WV, respectively, from the quiescent period in December 2021 through to the aftermath of the eruption in February (Fig. 2.66).

Even though they pale in comparison to the mid-stratospheric impacts, tropical lower stratospheric WV anomalies were positive (wet) for all months in 2022 (Figs. 2.65a,c). These anomalies were greatest in February (the first full month post-eruption of HTHH), with values of +1.1 ppm, corresponding to deviations from the climatological monthly mean of 40%. Over the tropical latitude band, anomalies were either the most positive on record or second-most positive between February and July. In addition to propagating upwards, the 82-hPa WV anomalies also propagated poleward in each hemisphere (Fig. 2.65c).

Lower stratospheric WV observed by Aura Microwave Limb Sounder (MLS) is consistent with balloon-borne frost point hygrometer soundings (Fig. 2.67). As is well known, at the tropical stations the WV anomalies are highly correlated with the tropical cold-point tropopause (CPT) temperature anomalies (Figs. 2.67c,d).

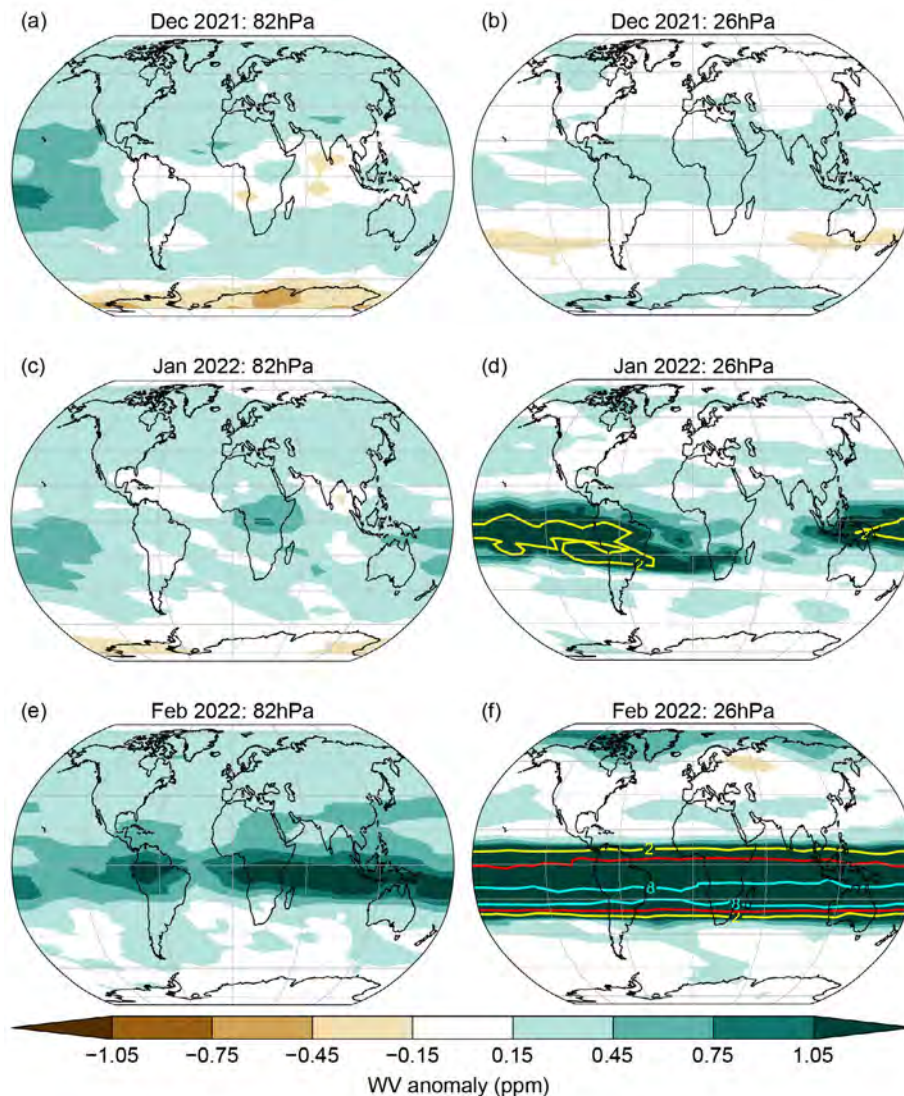


Fig. 2.66. Deseasonalized monthly lower stratospheric Aura MLS vapor (WV) anomalies (ppm; 2004–21 base period) at (a),(c),(e) 82 hPa and (b),(d),(f) 26 hPa for (a),(b) Dec 2021, (c),(d) Jan 2022, and (e),(f) Feb 2022. Contours of WV anomalies of +2, +4, and +8 ppm are shown in yellow, red, and cyan, respectively.

In 2022, the tropical CPT temperatures were anomalously high throughout the entire year except for July (deseasonalized monthly anomaly of -0.04 K), with an annual mean anomaly of $+0.73$ K. Interannual variations in CPT temperatures are correlated with interannual variability in climate modes, such as ENSO and the quasi-biennial oscillation (QBO) in equatorial stratospheric winds (e.g., Randel et al. 2004), so these are briefly discussed below.

The criteria for La Niña was met throughout 2022 (see section 4b for details). La Niña conditions in boreal winter

are typified by weaker tropical lower stratospheric upwelling, anomalously warmer CPTs, and enhanced WV in the tropical lower stratosphere (e.g., Garfinkel et al. 2021). The observed positive anomalies in tropical lower-stratospheric WV at the beginning and end of 2022 are thus consistent with the expected behavior associated with a La Niña.

The QBO phase was easterly through to September until switching to westerly for the remainder of 2022. The QBO westerly phase is associated with anomalously weak tropical upwelling and warm temperatures. Thus, the La Niña and QBO easterlies had offsetting effects on CPTs (and hence WV) at the beginning of 2022, whereas the QBO westerlies and La Niña at the end of 2022 likely contributed to the anomalously warm CPTs and enhanced lower-stratospheric WV at that time.

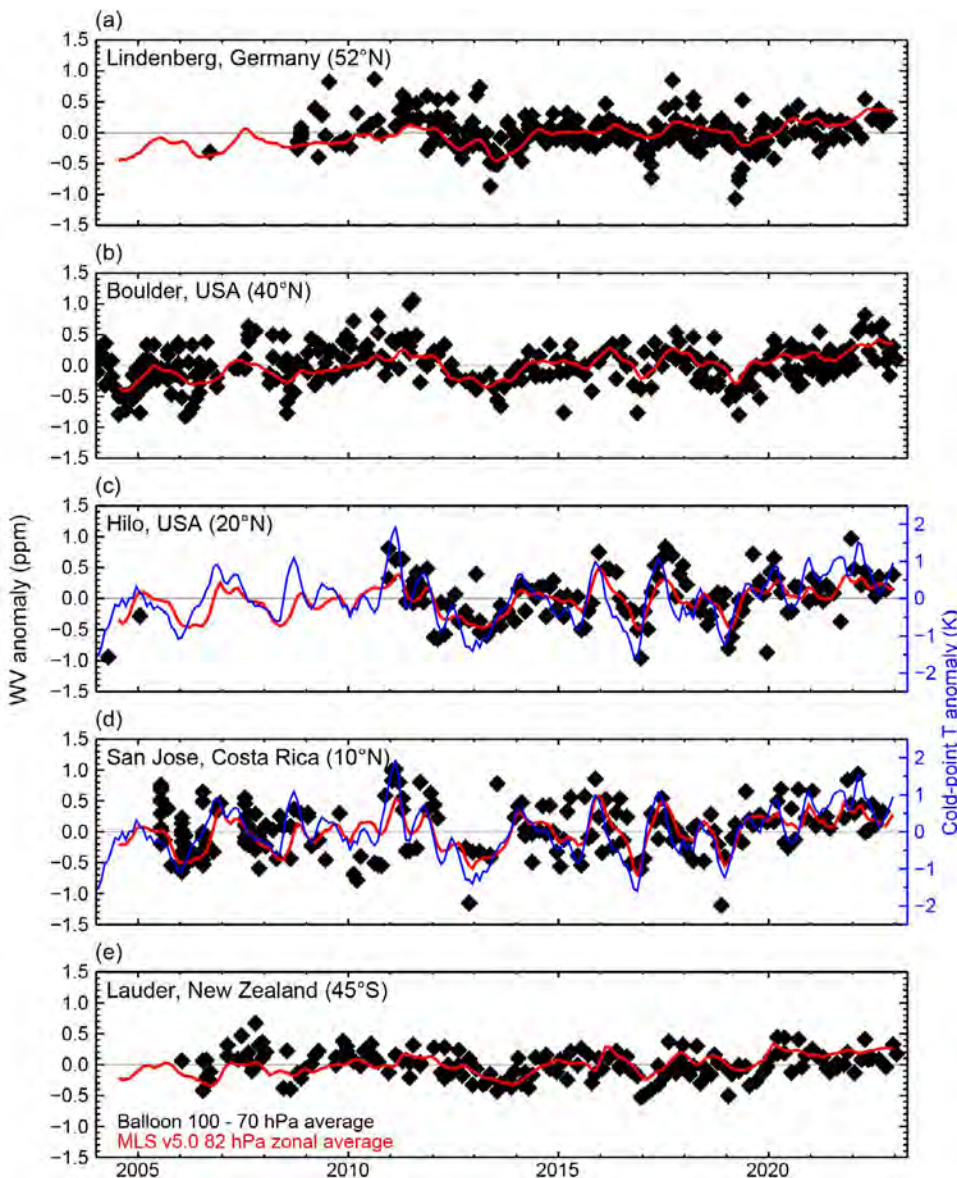


Fig. 2.67. Lower-stratospheric water vapor (WV) anomalies (ppm) over five balloon-borne frost point (FP) hygrometer stations. Each panel shows the lower stratospheric anomalies of individual FP soundings (black) and of monthly zonal averages from MLS data at 82 hPa in the 5° latitude band containing the FP station (red). High-resolution FP vertical profile data were averaged between 70 hPa and 100 hPa to emulate the MLS averaging kernel for 82 hPa. Each MLS monthly zonal mean was determined from 2000–3000 profiles. Anomalies for MLS and FP data are calculated relative to the 2004–21 period for all sites except for Lindenberg (2009–21) and Hilo (2011–21). Tropical cold-point tropopause temperature (CPT) anomalies based on the MERRA-2 reanalysis (c,d, blue curve) are generally well correlated with the tropical lower stratospheric WV.

6. TROPOSPHERIC OZONE

—O. R. Cooper, J. R. Ziemke, and K.-L. Chang

Tropospheric ozone is the third most important greenhouse gas, after carbon dioxide and methane. It contributes to almost all of the effective radiative forcing due to ozone (tropospheric and stratospheric), estimated by the IPCC Sixth Assessment Report to be 0.47 (0.24 to 0.70) $W m^{-2}$ (Forster et al. 2021). A short-lived climate forcer, its lifetime is on the order of three to

four weeks (Archibald et al. 2020) and, therefore, its global distribution is highly variable (Gaudel et al. 2018). In situ observations are too sparse and infrequent to provide an accurate quantification of the global distribution and trends in tropospheric ozone, although in some areas they are abundant enough to provide reliable regional-scale trends (Tarasick et al. 2019; Cooper et al. 2020; Gaudel et al. 2020; Gulev et al. 2021; Chang et al. 2022).

While the current generation of atmospheric chemistry models is showing reasonable skill in quantifying the global tropospheric ozone burden (TOB) and reproducing long-term trends (Skeie et al. 2020; Szopa et al. 2021; Christiansen et al. 2022; Fiore et al. 2022; Wang et al. 2022), their estimates vary, and further development is required before they can provide reliable near-real time estimates of the global ozone distribution. Instruments on polar-orbiting satellites are our best means for monitoring tropospheric ozone on the global scale. While currently available satellite products have limited vertical resolution, they can report tropospheric column ozone values, which can be summed to provide near-global estimates of the tropospheric ozone burden.

Since 2012, *State of the Climate* reports have relied on the combined Aura Ozone Monitoring Instrument and Microwave Limb Sounder satellite ozone measurements (OMI/MLS) to quantify the near-global tropospheric ozone burden and trends (Ziemke et al. 2019). Vertical resolution of OMI/MLS monthly tropospheric column ozone (TCO) is ~ 3 km near the tropopause with ~ 2 Dobson units (DU; 7%) precision regionally; trend uncertainties are about $0.5 \text{ DU decade}^{-1}$ ($1.5\% \text{ decade}^{-1}$). In 2022, the strongest positive TCO anomalies (relative to 2005–21) occurred from East Asia to the northeastern North Pacific ($\sim 1.2 \text{ DU}$; 3%), while the negative anomalies were weak and were limited to Australia and New Zealand (Plate 2.1z). Hemispheric and global TOB were $160 \pm 6 \text{ Tg}$ ($0^\circ\text{--}60^\circ\text{N}$), $149 \pm 6 \text{ Tg}$ ($0^\circ\text{--}60^\circ\text{S}$), and $309 \pm 8 \text{ Tg}$ ($60^\circ\text{S--}60^\circ\text{N}$) for 2022 (95% confidence ranges). Globally ($60^\circ\text{S--}60^\circ\text{N}$), the 2004–22 TOB increase was approximately $1.50 \pm 0.37 \text{ Tg yr}^{-1}$, equal to a total increase of $\sim 8\%$ since 2004 (Fig. 2.68). Spatially, the trends are overwhelmingly positive (Fig. 2.69), with the strongest trends occurring in the tropics, consistent with the conclusions of the IPCC AR6, which assessed

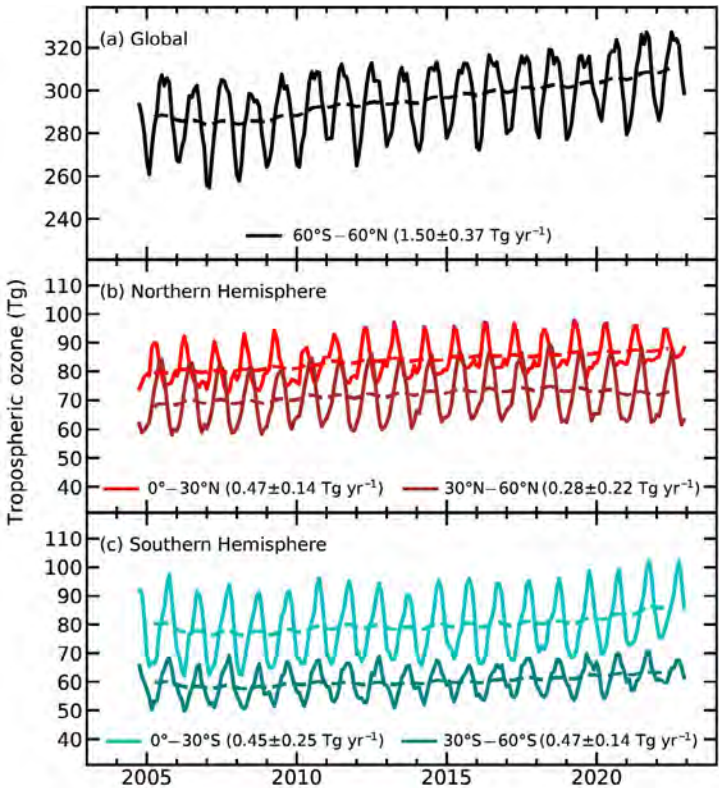


Fig. 2.68. Monthly averages (solid lines) and 12-month running means (dashed lines) of OMI/MLS tropospheric ozone burdens (Tg) from Oct 2004 through Dec 2022 for (a) $60^\circ\text{S--}60^\circ\text{N}$ (black), (b) the Northern Hemisphere tropics (red) and midlatitudes (dark red), and (c) the Southern Hemisphere tropics (light blue) and midlatitudes (dark green). Slopes of linear fits to the data are presented with their 95% confidence-level uncertainties.

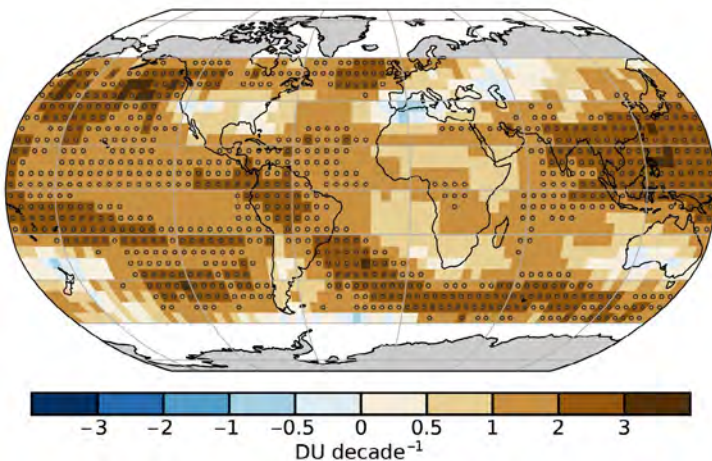


Fig. 2.69. Linear trends in OMI/MLS tropospheric column ozone (DU decade^{-1}) on a $5^\circ \times 5^\circ$ grid from Oct 2004 through Dec 2022. Circles denote trends with p -values < 0.05 . Trends were calculated using a multivariate linear regression model (e.g., Randel and Cobb 1994 and references therein) that included a seasonal cycle fit and the Niño-3.4 index as an El Niño–Southern Oscillation proxy; trend uncertainties included autoregressive adjustment via Weatherhead et al. (1998).

observed tropospheric ozone trends from the late twentieth century to 2016–18 (Gulev et al. 2021).

At the surface, six baseline sites are available for quantifying multi-decadal ozone trends through the end of 2022 (Fig. 2.70; Table 2.9). Trends are estimated by the generalized least squares method, based on monthly anomalies referenced to the monthly climatological values over 2000–20 (Chang et al. 2021). At northern high latitudes, ozone has increased at the rate of 0.50 ± 0.32 ppbv decade⁻¹ ($p < 0.01$) since 1973 at Barrow Observatory, Alaska, while ozone at Summit, Greenland, has decreased by 2.25 ± 0.92 ppbv decade⁻¹ ($p < 0.01$) since 2000. At northern midlatitudes, ozone has decreased by 0.97 ± 1.15 ppbv decade⁻¹ ($p = 0.09$) since 1988 at Tudor Hill, Bermuda, but with large fluctuations. Nighttime observations at Mauna Loa Observatory (MLO), Hawaii, are representative of the lower free troposphere of the central North Pacific Ocean and show a positive trend of 0.92 ± 0.40 ppbv decade⁻¹ ($p < 0.01$) since 1973. In the southern high latitudes, ozone at Arrival Heights, Antarctica, changed little since 1996, with a weak increase of 0.27 ± 0.56 ppbv decade⁻¹ ($p = 0.33$). Ozone at South Pole, the most remote location on Earth, increased by 0.35 ± 0.35 ppbv decade⁻¹ ($p = 0.05$) since 1975. While these data provide a range of trends at remote locations, they are too sparse to provide a global mean surface trend, and surface trends do not necessarily reflect trends in the free troposphere, which have been overwhelmingly positive since the 1990s (Gulev et al. 2021; Fiore et al. 2022), in agreement with OMI/MLS tropospheric column product.

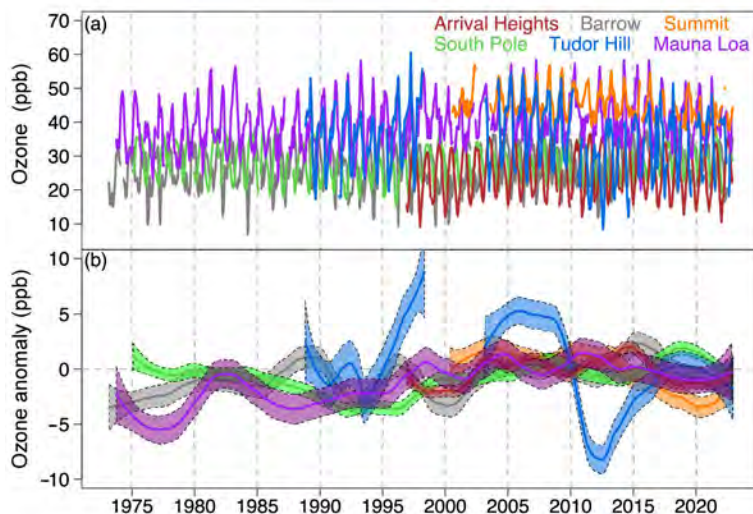


Fig. 2.70. (a) Monthly mean surface ozone (ppb) at Barrow Observatory, Alaska (gray), Summit, Greenland (orange), Tudor Hill, Bermuda (blue), Mauna Loa, Hawaii (purple), Arrival Heights, Antarctica (red), and South Pole (green). Monthly means are produced for months with at least 50% data availability using observations from all 24 hours of the day. The locations of each site are listed in Table 2.9. (b) The same time series after conversion to monthly anomalies referenced to the monthly climatological values over 2000–20 and smoothed variability based on the locally weighted scatterplot smoothing (LOWESS) regression.

Table 2.9. Ozone trends at the six baseline monitoring sites shown in Fig. 2.70. Trends are estimated by the generalized least squares method, based on monthly anomalies referenced to the monthly 2000–20 base period (Chang et al. 2021), and reported with 95% confidence intervals and p-values.

Site name — latitude, longitude, elevation (m)	Yrs with data	Trend, ppbv decade ⁻¹	p-value
Summit, Greenland — 72.6°N, 38.5°W, 3238 m	2000–present	-2.25 ± 0.92	$p < 0.01$
Barrow, Alaska — 71.3°N, 156.6°W, 11 m	1973–present	0.50 ± 0.32	$p < 0.01$
Tudor Hill, Bermuda — 32.3°N, 64.9°W, 30 m	1988–1998, 2003–present	-0.97 ± 1.15	$p = 0.09$
Mauna Loa Observatory (MLO), Hawaii — 19.5°N, 155.6°W, 3397 m	1973–present	0.92 ± 0.40	$p < 0.01$
Arrival Heights, Antarctica — 77.8°S, 166.8°W, 50 m	1996–present	0.27 ± 0.56	$p = 0.33$
South Pole, Antarctica — 90.0°S, 59.0°E, 2840 m	1975–present	0.35 ± 0.35	$p = 0.05$

7. CARBON MONOXIDE

—J. Flemming and A. Inness

Carbon monoxide (CO) is an indirect climate forcing agent because of its chemical feedbacks with the hydroxyl radical (OH), which controls the atmospheric lifetime of methane (CH₄), and because of its role as a precursor for tropospheric ozone (Szopa et al. 2021, section 6.3.3.2). Both methane and tropospheric ozone are also short-lived climate pollutants. CO is emitted into the atmosphere by combustion processes originating from anthropogenic sources, such as road transport and energy generation, as well as from natural sources, such as wildfires and biogenic emissions. Of similar or larger size than these emissions is the chemical production of CO in the atmosphere from formaldehyde as part of the oxidation chains of CH₄, isoprene, and other volatile organic trace gases (Zheng et al. 2019). Oxidation of CO by reaction with OH is the main loss process for CO, resulting in an atmospheric lifetime of one to two months. The greater abundance of OH in the summer of each hemisphere is a main reason for the typical CO seasonal cycle that peaks in winter.

Monthly and annual global mean total columns of CO together with combined annual anthropogenic and wildfire emissions for the period 2003–22 are shown in Fig. 2.71. The year 2022 has the lowest overall global CO burden and the lowest total CO emissions in the period. The low emissions in 2022 were a consequence of less intense wildfire activity and a general decrease in anthropogenic CO emissions. Figure 2.71 suggests a good qualitative agreement between the variability and trends of global CO burden (lines) and global CO emissions (points) for the study period. However, the CO emissions and the CO burden are not perfectly correlated, which is an indication of the additional influence of the varied chemical production and destruction of CO on its global burden. Furthermore, while the CO wildfire emissions and CO burden were inferred from satellite observations, the anthropogenic emissions are only projections based on inventories and the biogenic emissions are from a modeled multi-year climatology, both with considerable uncertainties for the details for 2022.

The spatial distribution of the annual anomalies of 2022 with respect to the period 2003–22 is shown in Plate 2.1aa. The mid and high latitudes show large-scale negative anomalies throughout the year. These were most pronounced in the summer seasons when the wildfire activity was lower than in some previous years (e.g., 2021, 2019) that saw strong wildfires. The positive CO anomalies in northern India can be attributed to anthropogenic sources, such as agricultural fires. The continuation of La Niña conditions in the tropical Pacific resulted in a pronounced negative anomaly over Maritime Southeast Asia during September–November. Stronger-than-usual wildfire activity in tropical and southern Africa and tropical South America led to positive CO anomalies, particularly in the second half of 2022.

The Copernicus Atmosphere Monitoring Service (CAMS; <https://atmosphere.copernicus.eu/>) has produced a retrospective analysis of CO, aerosols, and ozone since 2003 by assimilating satellite retrievals of atmospheric composition with the European Centre for Medium-Range Weather Forecasts (ECMWF) model (Inness et al. 2019). This CAMS reanalysis assimilated global Thermal Infra-Red total column CO retrievals (V6 from 2003 to 2016; Near Real Time [NRT] V7 from January 2017 to June 2019; NRT V8 from July 2019 to present) of the Measurement of Pollution in the Troposphere instrument (Deeter et al. 2014, 2017, 2019), excluding observations poleward of 65° N/S, using the ECMWF 4D-VAR data assimilation system. The anthropogenic emissions were taken from the Monitoring Atmospheric Composition and Climate megacity (MACCity) inventory

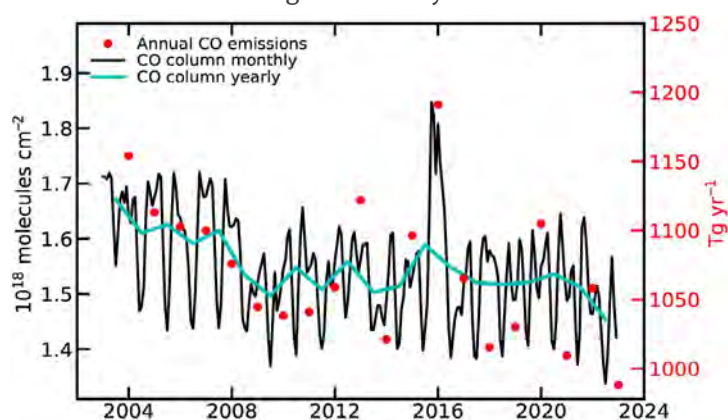


Fig. 2.71. Time series of the area-averaged global total column of carbon monoxide (CO) from the CAMS reanalysis ($\times 10^{18}$ molecules cm^{-2} , left axis, black: monthly mean values; cyan: annual mean values) and annual total global CO emissions (Tg yr^{-1} , right axis, red circles) for the period 2003–22.

(Granier et al. 2011) that accounts for projected emission trends according to the Representative Concentration Pathway (RCP) 8.5 scenario, but COVID-19-related emissions modifications were not applied. Biomass burning emissions were taken from the Global Fire Assimilation System (v1.2; Kaiser et al. 2012; section 2h3) that is based on MODIS fire radiative power retrievals (Giglio et al. 2016). Monthly mean biogenic CO emissions simulated by the Model of Emissions of Gases and Aerosols from Nature version 2.1 (MEGAN2.1) model following Sindelarova et al. (2014) were used for the period 2003–17, after a monthly-mean climatology derived from the 2003–17 simulations was applied.

h. Land surface properties

1. TERRESTRIAL SURFACE ALBEDO DYNAMICS

—G. Duveiller and N. Gobron

The changes in brightness of the land’s surface, referred to as its albedo, emerge from the combined effect of multiple land processes, notably a darkening in the visible part of the spectrum caused by increased vegetation growth, a brightening due to dry conditions, and a strong effect depending on the presence of snow. In 2022, the land surface was overall darker compared to the reference period of 2003–20. This darkening can be attributed to a combination of greener-than-usual regions along with considerable snow cover deficits in the Northern Hemisphere (section 2c5), which were not offset by the brightening that could have been expected following the multiple heatwaves that occurred in 2022 (section 2b4).

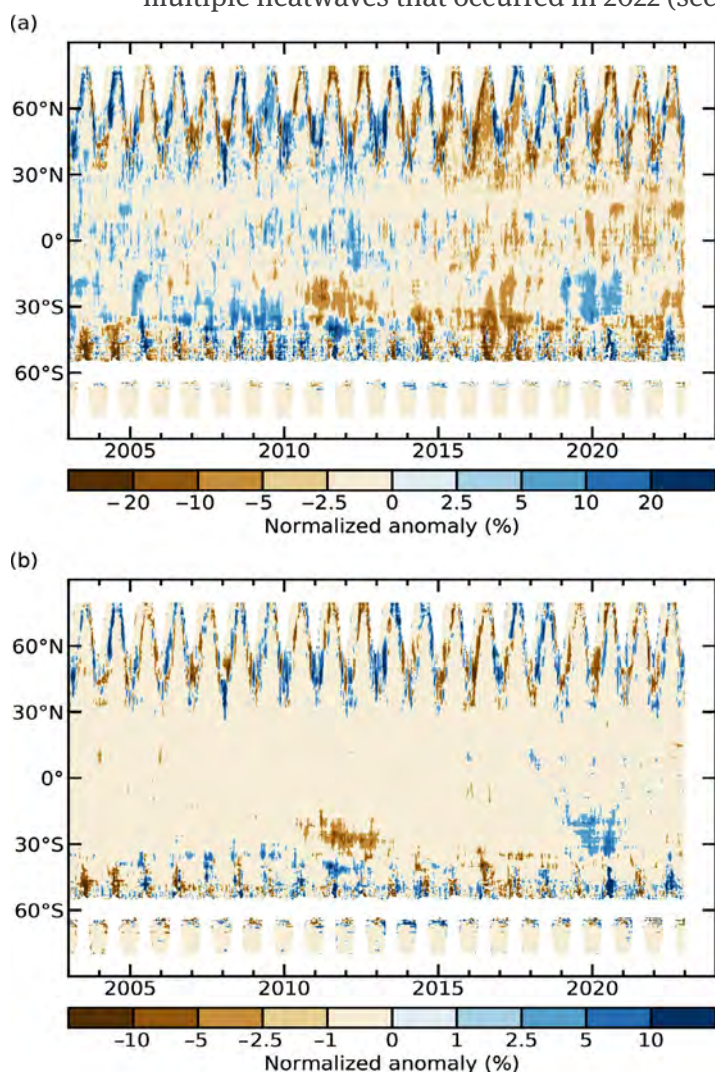


Fig. 2.72. Zonally averaged (a) white sky visible (%) and (b) near infrared (%) albedo anomalies for the period 2003–22 using a 2003–20 base period.

La Niña was responsible for increased precipitation in several areas during 2022, leading to greening (and thus darkening), generating distinct features in the global anomaly maps (see Plate 2.1ab for anomalies in visible albedo and compare to anomalies in precipitation), notably in southern Africa, eastern Australia, and northeastern Brazil. Snow deficits in the Arctic, in Eastern Europe, and in a small area of the midwestern United States further characterize the darkening patterns in 2022, while larger and longer extents of snow cover in North America and Tibet brightened these latter areas. Drier conditions following heatwaves did not offset the darkening effects, with localized exceptions in eastern Africa, Paraguay and Argentina, Mexico and the central United States, and Turkey.

The patterns of surface albedo anomalies consolidate the darkening trend over the years, specifically for visible albedo (Figs. 2.72, 2.73). Surface albedo is generally known to be decreasing considerably in the Arctic due to reductions of terrestrial snow cover, snow cover fraction over sea ice, and sea-ice extent, driven mostly by increasing surface air temperature and declining snowfall (Zhang et al. 2019; see Chapter 5). Negative trends of albedo have also been reported over the vegetated surfaces in various regions, even though land-cover change and other effects can

brighten the land as well (Chrysoulakis et al. 2019). The non-snow-related albedo reductions are in line with increasing trends in the fraction of absorbed photosynthetically active radiation (FAPAR; section 2h2), that could possibly be associated with increasing trends in greening across some areas, while browning occurs in others (Cortés et al. 2021).

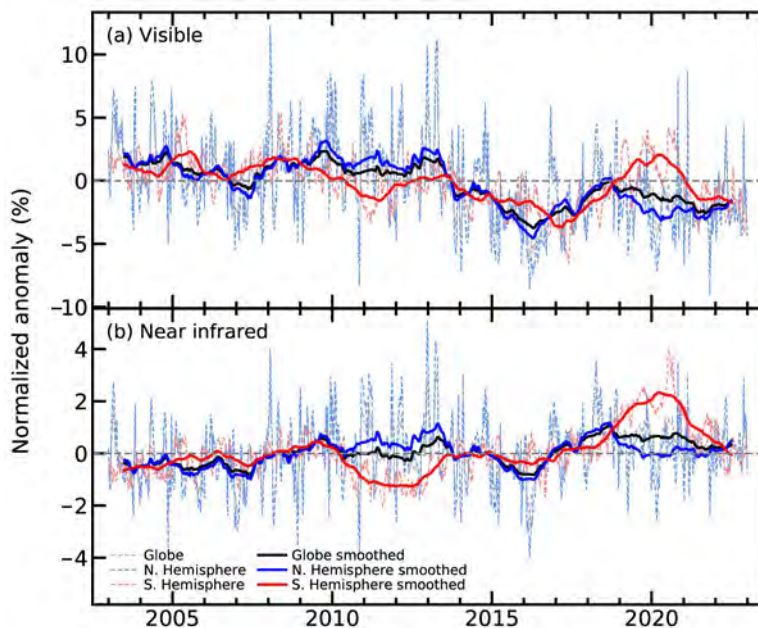


Fig. 2.73. Global (black lines), Northern Hemisphere (blue), and Southern Hemisphere (red) land surface (a) visible and (b) near infrared albedo anomalies (%; 2003–20 base period) for the period 2003–22. Dotted lines denote each monthly period; solid lines indicate the six-month running averaged mean.

This analysis is based on satellite records of visible and near-infrared white-sky albedo estimated from the Moderate Resolution Imaging Spectroradiometer (MODIS) instrument onboard the *Aqua* and *Terra* satellite platforms (Schaaf et al. 2002). Also known as bi-hemispherical reflectance, it is defined as the fraction of radiation that is reflected by the surface in the absence of a direct radiation component and when the diffuse radiation component is isotropic. This situation would correspond to a hypothetical overcast or foggy day, in which the sky would be white (and hence the name: white-sky albedo). Various studies have shown that these products represent ground properties well, whether it be ice sheets (Stroeve et al. 2013) or vegetation (Cescatti et al. 2012). The baseline reference period used here is 2003–20, covering the extent of the MODIS record where data from both satellite platforms (*Terra* and *Aqua*) are available.

2. TERRESTRIAL VEGETATION DYNAMICS

—N. Gobron

The fraction of absorbed photosynthetically active radiation (FAPAR) provides evidence on the amount of vegetation and its health status, and is, therefore, important in assessing the primary productivity of the vegetative cover, the associated fixing of atmospheric carbon dioxide and the energy balance at the surface. FAPAR anomalies in 2022 compared to the 1998–2020 average show wide variations in terms of value and geographic coverage of vegetation productivity worldwide (Plate 2.1ad).

The largest negative anomalies (decreased plant photosynthesis) occurred in North America, across Alaska and the Yukon territory, Kansas, and Texas through to northeast Mexico and in East Africa (Somalia, Ethiopia, Kenya, Uganda, and Tanzania). Negative anomalies also occurred in South America (Argentina, Paraguay, and Bolivia). To a lesser extent, negative anomalies appeared on the Pacific zones of Colombia and Ecuador, southern zone of Chile, and Atlantic coast of Angola and Namibia. Madagascar, Morocco, and northern Algeria were also affected. Several negative hotspots concerned southwest and northern Australia, western Russia, and central Europe.

The most noticeable positive anomalies (increased vegetated photosynthesis) appeared over northern Canada, northeastern Brazil, Botswana, southern Africa, southern and eastern Asia, and eastern Australia. Smaller anomalies were noticeable over the Sahel region and over northern Russia.

The negative anomalies over the boreal forest in Alaska and the Yukon were due to spring wildfires associated with earlier snowmelt. Summer rainfall was lower and later than normal, with higher temperatures than usual (see section 7b). There were precipitation deficits from Kansas in the United States to the northeast of Mexico throughout the year, which affected shrubland growth. Heatwaves occurred in January and July over northern Argentina and Paraguay,

respectively, and temperatures were the highest on record at both the start and the end of 2022 with a strong deficit of precipitation over these regions, as well as Bolivia (see section 7d). East African vegetation health declined in the spring as the temperature was higher than normal with a rainy season ending with cumulatively low rainfall. Strong seasonal negative anomalies occurred over Europe in spring and summer and over the northern United States in autumn;

however, these seasonal events were not detectable in the annual anomaly as positive anomalies occurred in other seasons.

The Arctic ecosystem, characterized by low tundra vegetation over northern Canada (Nunavut) and northern Russia (Kara Sea) shows a greening trend due to higher temperatures during the summer. Terrestrial photosynthesis was enhanced over eastern China and India, with vegetation growth increasing since 2015 due to land use changes, along with an intensification of the production of multiple crops (Gobron 2019; Chen et al. 2019). Northeastern Brazil, with tropical forests along the coast and savanna, had a positive FAPAR annual anomaly of above +0.4, as both precipitation and temperature were above normal. Similar conditions occurred over Botswana, South Africa, and eastern Australia, which correspond to the typical impact of La Niña.

Figure 2.74 shows the average latitudinal anomalies from 1998 to 2022 compared to the reference period 1998–2020. In 2022, the anomaly was positive at nearly all latitudes, apart from a few places such as above the equator and south of 30°S, highlighting the greening of land surfaces. The Southern Hemisphere (SH) was affected by negative anomalies (i.e., less than -0.04), from 2002 to 2014, except in 2010–12, and in 2019/20.

Figure 2.75 shows the global and hemispheric anomalies, with more seasonal variability in the SH than in the Northern Hemisphere (NH). FAPAR anomalies over the SH were positive before 2002, started to be

negative until 2010/11 and during the summer periods in 2015/16, 2018/19, and 2019/20, but were positive for all of 2022. The NH experienced fewer negative events compared to the SH. Since 2021/22, both the SH and NH recorded only positive FAPAR anomalies.

Space-based earth observations are crucial for monitoring terrestrial photosynthetic activity worldwide. Optical sensors are used to infer FAPAR, an essential climate variable (as defined by GCOS [2016, 2022]). The 2022 analysis merges 25 years of global FAPAR monthly products based on three optical sensors from 1998 to 2022 (Gobron et al. 2010; Pinty et al. 2011; Gobron and Robustelli 2013). Uncertainties of each dataset were derived through error propagation techniques and comparisons against multiple proxies using ground-based measurements and radiative transfer simulations that all provide an estimate of the uncertainties and biases. This long-term FAPAR dataset has an estimated uncertainty close to 5%–10%.

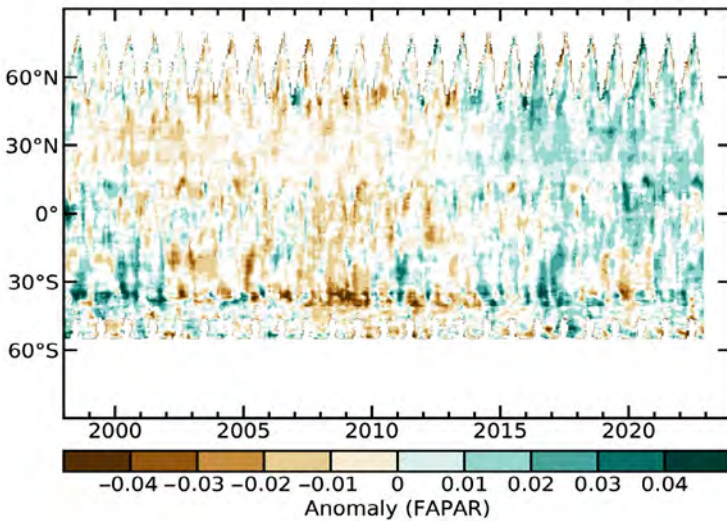


Fig. 2.74. Zonally averaged fraction of absorbed photosynthetically active radiation (FAPAR) anomalies for 1998–2022 (1998–2020 base period).

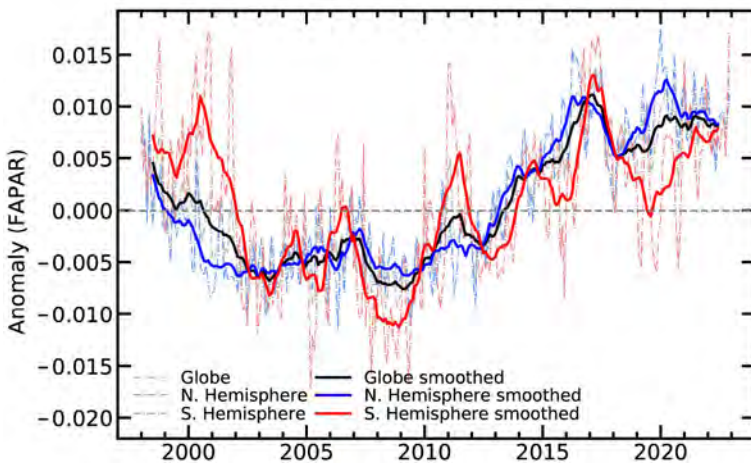


Fig. 2.75. Global (black lines), Northern Hemisphere (blue), and Southern Hemisphere (red) fraction of absorbed photosynthetically active radiation (FAPAR) anomalies for 1998–2022 (1998–2020 base period). Dotted lines denote each monthly period; solid lines indicate the six-month running averaged mean.

3. BIOMASS BURNING

—J. W. Kaiser and M. Parrington

The year 2022 continued to illustrate the two distinct trends that have emerged in global biomass burning over the last decade that are shaping current pyrogeography: a declining trend in many savanna regions related to agricultural expansion and an increasing trend in many forested regions where climate change with severe drought periods increases the flammability of the landscape (Plate 2.1ae). Here we characterize the amount of biomass burning, also referred to here as “fire activity” and more widely as wildfires, with the amount of carbon that is consumed by fire; 80%–95% of this is emitted as carbon dioxide, depending on fire type (smoldering vs. flaming), 1%–2% is emitted as particulate matter and subject to deposition within a few days, and the remainder (CO, CH₄, and others) is further oxidized to carbon dioxide in the atmosphere. In a stable ecosystem, virtually all of this carbon dioxide is assimilated again on time scales of years by re-growth of vegetation. In the current situation however, 20% is estimated to contribute to the long-term buildup of atmospheric carbon dioxide (Zheng et al. 2023).

On one hand, 2022 had the lowest fire activity in the Global Fire Assimilation System (GFAS) record (1603 Tg C, 22% below the 2003–20 average; Table 2.10; Plate 1.1), with fire activity in tropical Asia at its lowest since at least 2003. On the other hand, there was significant regional fire activity in boreal North America, southwestern and Central Europe, and central South

Table 2.10. Annual continental-scale biomass burning budgets in terms of carbon emission (Tg C yr⁻¹) from GFASv1.4. The Arctic and western United States are listed as subregions of frequent interest; their values are contained in those for North America plus Northern Asia.

Name of Region	Location	2003–20 Mean value ^a (min–max)	2022 Value ^a	2022 Anomaly ^a (%)
Global	–	2062 (1781–2421)	1603	–460 (–22%)
North America	30°N–75°N, 190°E–330°E	85 (57–114)	77	–8 (–10%)
Central America	13°N–30°N, 190°E–330°E	52 (38–72)	45	–7 (–14%)
South America	60°S–13°N, 190°E–330°E	368 (242–537)	376	+9 (+2%)
Europe and Mediterranean	30°N–75°N, 330°E–60°E	42 (28–72)	37	–5 (–12%)
N. Hem. Africa	0°–30°N, 330°E–60°E	421 (308–494)	333	–88 (–21%)
S. Hem. Africa	0°–35°S, 330°E–60°E	477 (429–532)	450	–27 (–6%)
Northern Asia	30°N–75°N, 60°E–190°E	199 (116–436)	110	–89 (–45%)
Southeast Asia	10°N–30°N, 60°E–190°E	122 (86–162)	69	–53 (–44%)
Tropical Asia	10°N°–10°S, 60°E–190°E	166 (27–475)	22	–144 (–87%)
Australia	10°S–50°S, 60°E–190°E	129 (60–232)	83	–46 (–36%)
Arctic (sub-region)	67°N–90°N, 0°–360°	8 (1–37)	7	–1 (–17%)
Western United States (sub-region)	30°N–49°N, 230°E–260°E	19 (8–42)	16	–2 (–12%)

^a Quantity given in Tg C yr⁻¹

America (Plate 2.1ae; Fig. 2.76). After the extreme fires of 2019 and 2020, fire activity in the Arctic Circle and southeast Australia was again near and below average, respectively.

Global fire emissions are dominated by savanna burning except for rare episodes of extreme tropical peat burning during El Niño conditions. African fire emissions account for roughly half of the total fire carbon emissions in the Global Fire Emissions Database (GFED) and GFAS time series, and fires over savanna regions have decreased over the past decade (Andela et al. 2017). This trend continued in 2022 over Northern Hemisphere Africa with emissions 21% below the 2003–20 average, marking the third successive year with lower fire activity than any years in the record before 2019 (Fig. 2.77a). Southern Hemisphere Africa also contributed to the trend, albeit to a lesser degree. Fire activity in tropical Asia—including Indonesia—was the lowest on record (Fig. 2.77c); here, wet La Niña-related conditions continued as the dominant physical driver. While the long-term global trend is partly driven by agricultural expansion into savanna ecosystems and its associated fragmentation of the landscape, unusual patterns of high or low rainfall and more or less environmental protection also influence interannual variability on top of the declining trend.

South America was the only continental region to experience above-average activity (+2%; Fig. 2.77b) in 2022, due to the increased numbers of fires across northern Argentina, Paraguay, Bolivia, and some parts of the Amazon. In this region, 2020 and 2022 saw the highest fire activity of the last 12 years, which is consistent with the significant droughts in much of this region (section 2d10) as well as increased deforestation in the Amazon since 2019 for Brazil (<http://www.obt.inpe.br/OBT/assuntos/programas/amazonia/prodes>). At higher northern latitudes, North America and northern Asia experienced negative anomalies (−10% and −45%, respectively) overall, although there was regionally increased fire activity during the summer months for Alaska, the Yukon and Northwest Territories, and Khabarovsk Krai.

GFAS is operated to produce global fire emission estimates in near real-time by the Copernicus Atmosphere Monitoring Service (CAMS; Kaiser et al. 2012). It is based on the MODIS

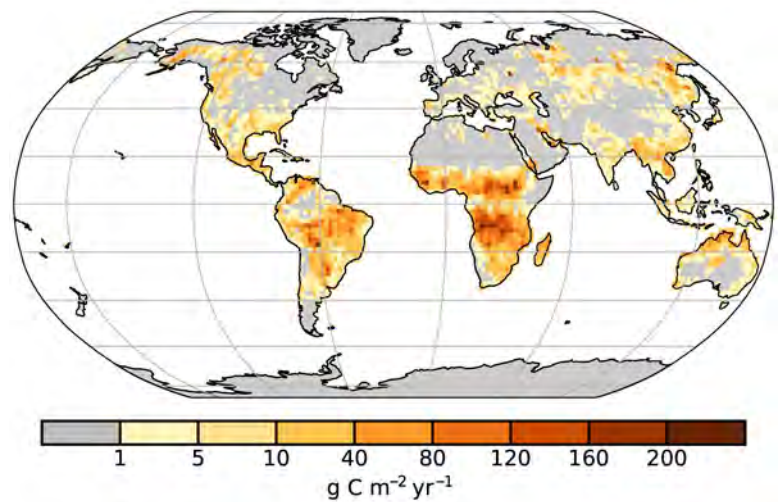


Fig. 2.76. Global map of fire activity in 2022 in terms of carbon consumption ($\text{g C m}^{-2} \text{yr}^{-1}$). (Source: GFASv1.4.)

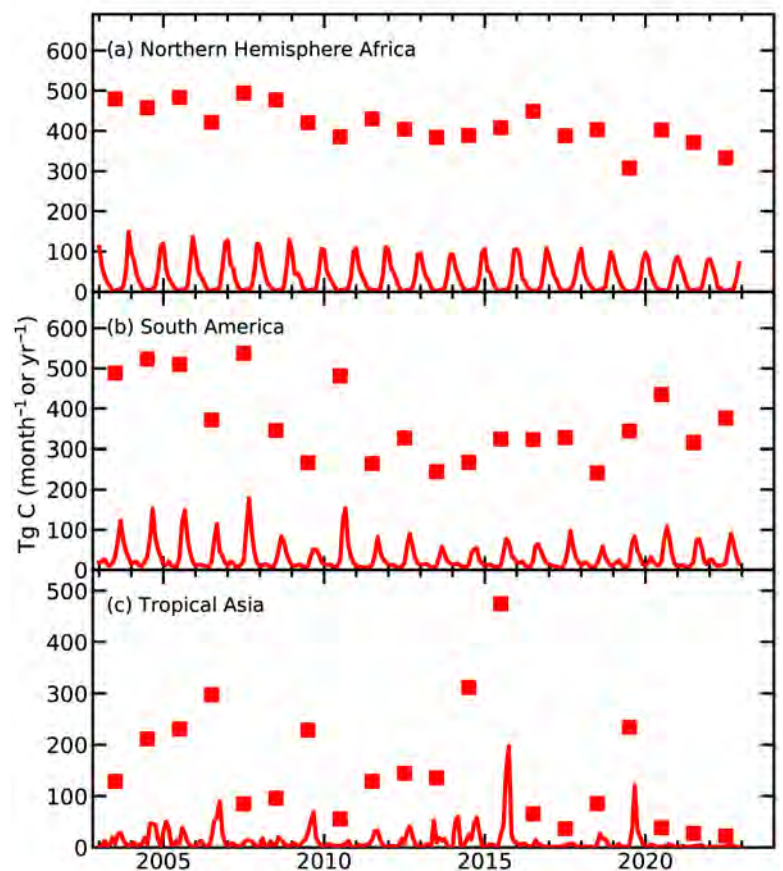


Fig. 2.77. Regional time series of monthly (lines in Tg C month^{-1}) and annual (squares in Tg C yr^{-1}) biomass burning activity in (a) Northern Hemisphere Africa, (b) South America, and (c) tropical Asia.

Fire Radiative Power products (Giglio et al. 2016). Here, we use consistent reprocessing with input from MODIS Collection 6 for the entire period of 2003–22. The 14% bias with respect to Collection 5 has been corrected, and the satellite- and observation time-specific bias correction factors from Hüser et al. (2018) have been applied in order to compensate for several outages of observations from the MODIS instruments during 2022. The *Aqua* and *Terra* satellites carrying MODIS have been in drifting orbits during 2022 with an overall shift of the local equator crossing times of <15 minutes (<https://aqua.nasa.gov/sites/default/files/AquaStatus.pdf>; <https://terra.nasa.gov/wp-content/uploads/2022/09/Orbit-Changes-Terra.pdf>); we consider this to be negligible for GFAS. The time series in Plate 1.1 also puts GFAS in the context of GFED4s, which is mostly based on burnt area observation and dates back to 1997 (van der Werf et al. 2017).

4. PHENOLOGY OF PRIMARY PRODUCERS

—D. L. Hemming, O. Anneville, Y. Aono, T. Crimmins, N. Estrella, A. Menzel, I. Mrekaj, J. O’Keefe, T. Park, A. D. Richardson, J. Rozkošný, T. Rutishauser, T. H. Sparks, S. J. Thackeray, A. J. H. van Vliet, and F. West.

During 2022, land surface phenology derived from the MODIS Normalized Difference Vegetation Index (NDVI, a dimensionless index of the difference between visible and near-infrared reflectance of vegetation cover, where higher values indicate denser, green vegetation) over the Northern Hemisphere (>30°N; Park et al. 2016), was compared to NDVI over the 2000–20 baseline period (Fig. 2.78). The hemispheric mean Start and End of Season (SOS_M and EOS_M) for the

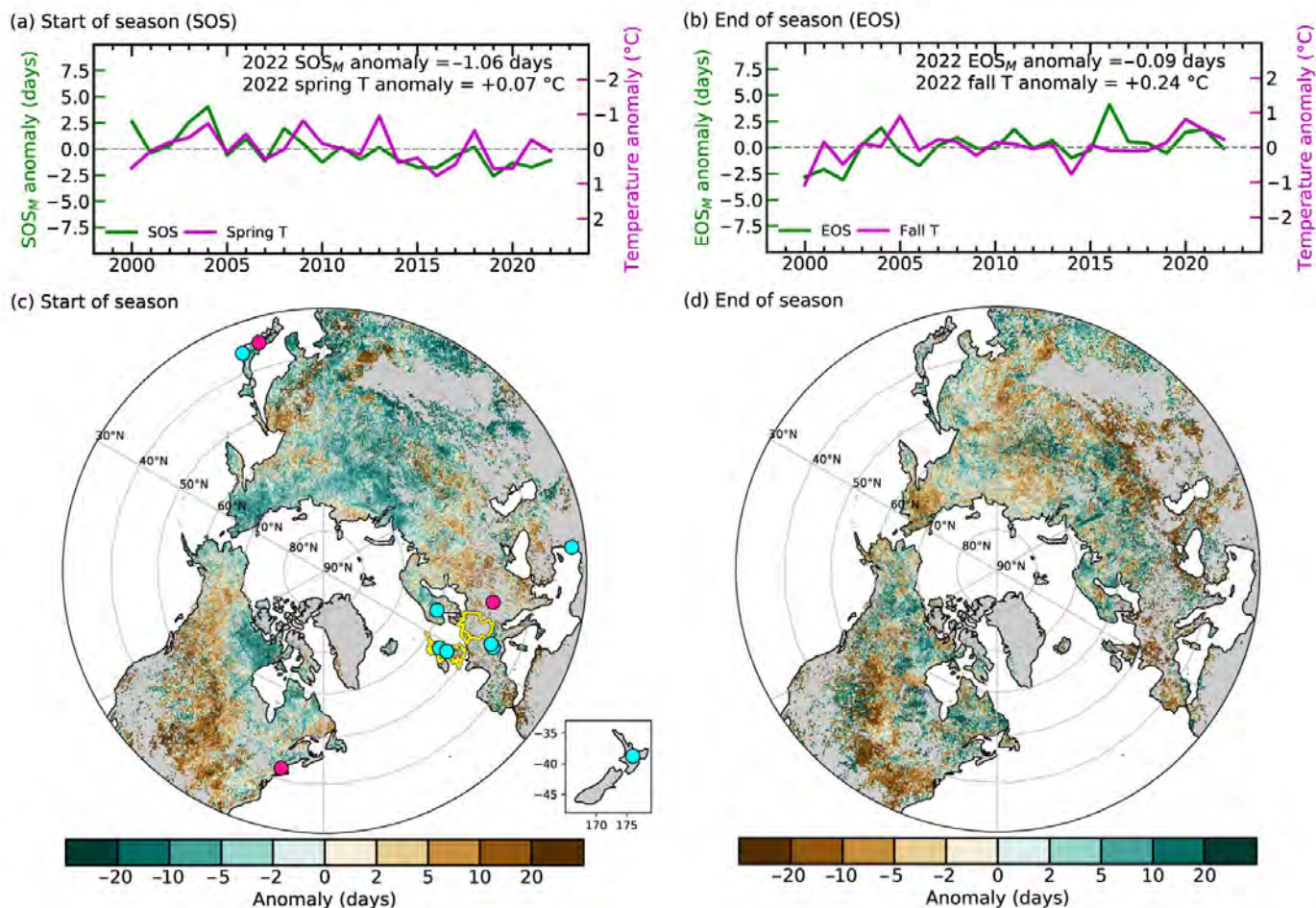


Fig. 2.78. (a) Time series of area-mean anomalies (days relative to 2000–20 baseline) in MODIS Normalized Difference Vegetation Index (NDVI)-based vegetation-growing-season onset (start of season, SOS_M , green) and satellite-derived (MERRA-2) spring (Mar–May, pink) temperature for the Northern Hemisphere. (b) Same as (a) but for growing season end (end of season, EOS_M , green) and autumn (Sep–Nov, pink) temperature. Note the temperature scale reversal for (a). (c),(d) Spatial pattern of (c) SOS_M and (d) EOS_M anomalies in 2022 with respect to the baseline. Highlights identify the location of sites shown in Figs. 2.79 and 2.80 and discussed in the text (country mean phenology data, yellow; site PhenoCam and phenology observations, magenta; lake phytoplankton, blue).

baseline period is 16 May and 11 October, respectively, and in 2022, SOS_M was 1.1 days earlier and EOS_M was similar to the baseline (Figs. 2.78a,b; Table 2.11). Regionally, earlier SOS_M occurred across central and northeastern Eurasia (EA), Alaska, and northern Canada. The warmer spring ($+0.23^\circ\text{C}$) led to 2.5 days earlier SOS_M in EA. Most of North America (NA) experienced later SOS_M ($+1.7$ days) in 2022 (Fig. 2.78c) due to the colder (-0.18°C) and wetter ($+0.05$ mm day $^{-1}$) spring, particularly over U.S. croplands. Northern NA and western EA showed later EOS_M ($+0.8$ days) whereas earlier EOS_M (-0.4 days) was observed in southern NA and eastern EA (Fig. 2.78d). Time series of the two decades of the MODIS record show continuous advancement and delay trends in SOS_M and EOS_M (SOS_M : -1.6 ± 0.4 days decade $^{-1}$, $p < 0.001$; EOS_M : $+1.2 \pm 0.5$ days decade $^{-1}$, $p = 0.07$).

PhenoCam data (Seyednasrollah et al. 2019) helped link the coarse resolution of satellite-derived phenology with fine-resolution visual observations on organisms and ecosystems (Richardson 2019). PhenoCam estimates (2008–22) of SOS (SOS_{PC}) and EOS (EOS_{PC}) at Harvard Forest, a deciduous forest in Massachusetts (United States) were compared with ground observations of red oak (*Quercus rubra*; SOS_{RO} and EOS_{RO} ; Richardson and O’Keefe 2009; O’Keefe

Table 2.11. Start of season (SOS), end of season (EOS), and full bloom dates (FBD; for native cherry tree observations only) for MODIS mean across the Northern Hemisphere (NH MODIS, $>30^\circ\text{N}$), land phenology records in USA (Harvard: PhenoCam, red oak, and MODIS mean across Harvard Forest; USA National Phenology Network, USA-NPN, mean covering northeastern United States), Europe oak records (Germany, Netherlands, Slovakia, UK, and MODIS mean across UK) and Japan (native cherry tree observations and MODIS mean across Japan). The baseline period is 2000–20 for all records except PhenoCam and NPN, which have baseline periods of 2008–22 and 2011–22, respectively, spanning the available observations. Negative/positive values represent earlier/later dates.

Location/Record	SOS/FBD 2022 (date)	SOS/FBD Baseline (date)	SOS/FBD Difference 2022-Baseline (days)	EOS 2022 (date)	EOS Baseline (date)	EOS Difference 2022-Baseline (days)
NH MODIS	15 May	16 May	-1	11 Oct	11 Oct	0
Harvard MODIS	26 Apr	24 Apr	-2	1 Dec	5 Dec	+3
Harvard PhenoCam	9 May	7 May	-2	16 Oct	22 Oct	+5
Harvard red oak	13 May	6 May	-7	18 Oct	19 Oct	0
USA-NPN	7 May	6 May	-1	27 Sep	3 Oct	+6
UK MODIS	6 Apr	30 Mar	-7	23 Dec	12 Dec	-10
Germany	29 Apr	28 Apr	+1	12 Nov	6 Nov	+6
Netherlands	17 Apr	20 Apr	-3	19 Dec	27 Nov	+22
Slovakia	1 May	26 Apr	+6	14 Oct	18 Oct	-4
UK	19 Apr	24 Apr	-5	10 Dec	1 Dec	+9
Japan MODIS	9 Apr	21 Apr	-12	-	-	-
Japan	1 Apr	6 Apr	-5	-	-	-

2021) and MODIS (SOS_M and EOS_M) for the associated pixel (Figs. 2.79a,b). These were also compared with red oak observations contributed to *Nature's Notebook*, the United States National Phenology Network's (NPN) monitoring across the northeastern United States (Rosemartin et al. 2014; Crimmins et al. 2022). In 2022, SOS_{PC} , SOS_{RO} , and SOS_M were zero, three, and two days later, respectively, compared to 2021. EOS_{PC} , EOS_{RO} , and EOS_M were 17, 7, and 13 days earlier compared to 2021 (Figs. 2.79a,b). Interannual variability of start and end of season for Harvard Forest are broadly consistent with those from the NPN, which underscore the value of volunteer-contributed data for tracking phenology at local to continental scales. The earlier EOS_{PC} in 2022 yielded a growing season of 160 days, more than two weeks shorter compared to 2021 and a full week shorter compared to the 2011–20 average (167 ± 7 days; Table 2.11).

'First leaf'/'start of leaf unfolding' (SOS_0) and 'leaf falling'/'bare tree' (EOS_0) dates for oak (*Quercus robur* and/or *Q. petraea*) from Germany (D), the United Kingdom (UK), Netherlands (NL), and Slovakia (SK) are presented (Figs. 2.79c,d). In 2022, SOS_0 dates varied across Europe from 5 and 3 days earlier than the baseline (in UK and NL) to 1 and 6 days later (in D and SK), while EOS_0 dates were earlier by 4 days (SK) and later by 6, 9, and 22 days (D, UK, and NL; Table 2.11).

Start- and end-of-season events across Europe are strongly influenced by temperature (Menzel et al. 2020); SOS_0 advances by four to six days per 1°C increase in the mean February–April temperature, and EOS_0 is delayed by two to four days per 1°C increase in the mean September–October temperature. In 2022, the later EOS_0 dates in D, UK, and NL were, in part, associated with unusually high autumn temperatures, encouraging leaf activity and resulting in a longer 2022 'oak season' at these locations (for UK, see Kendon et al. 2022). In SK, high spring, summer, and autumn air temperatures and soil moisture deficits in 2022 encouraged later leaf out and early leaf fall and led to the shortest oak season since 2000.

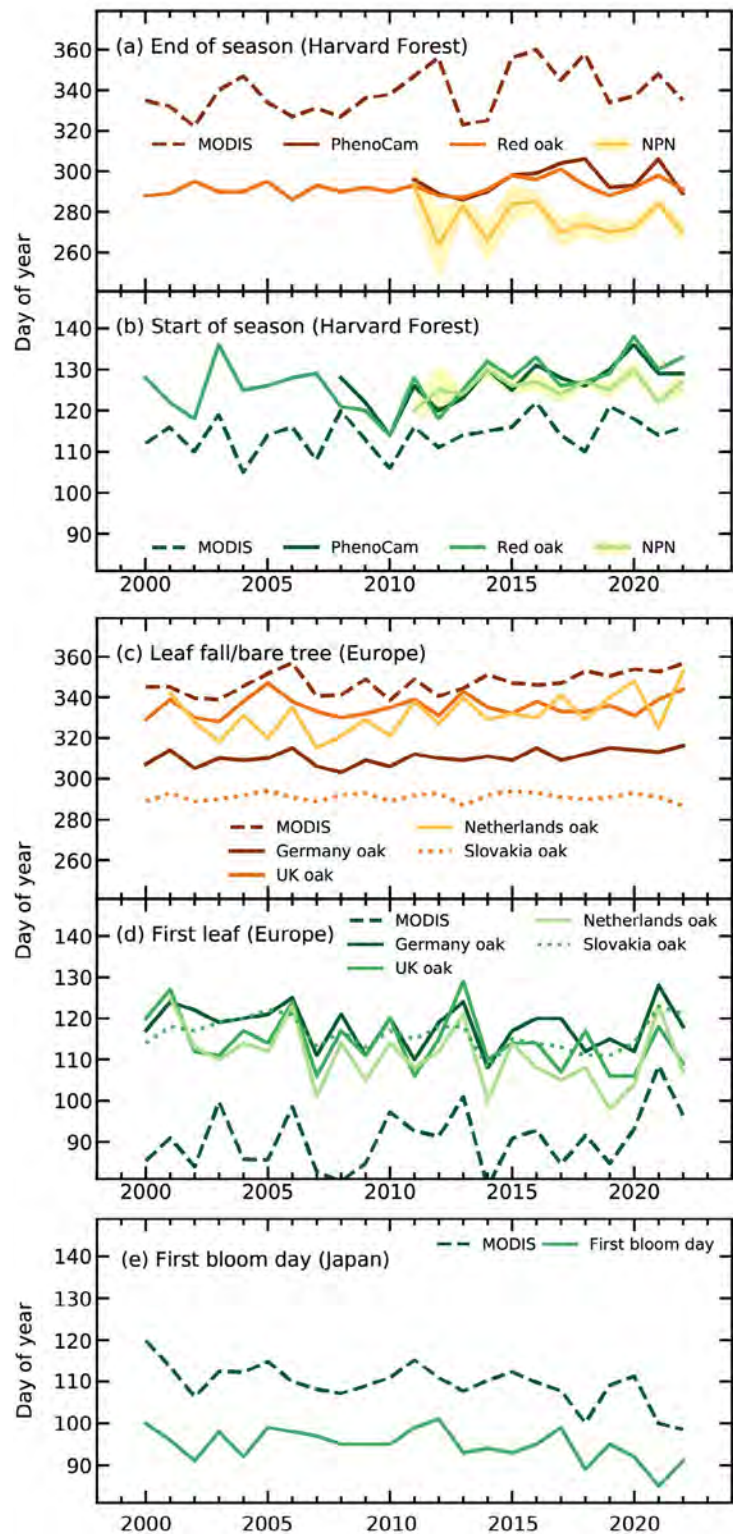


Fig. 2.79. Day of year of spring (green shades) and autumn (orange and brown) vegetation phenology indicators for (a),(b) Harvard Forest, Massachusetts, derived from PhenoCam, red oak ground observations, MODIS remote sensing (dashed), and USA-National Phenology Network (NPN) regional-scale means for red oak (calculated across the northeastern states of Pennsylvania, New Jersey, New York, Connecticut, Rhode Island, Massachusetts, Vermont, New Hampshire, and Maine, ± 1 std. error shaded), (c),(d), Germany, UK, Netherlands, and Slovakia mean oak and MODIS Europe mean, and (e) Kyoto, Japan, full bloom day observations for cherry trees and MODIS Japan mean start of season.

In Kyoto, Japan, full bloom dates (FBD) for a native cherry tree species, *Prunus jamasakura*, were acquired from historical documents dating back to 812 AD (Aono and Kazui 2008) and updated with current observations at Arashiyama, which are compiled from daily observations made by railway passengers at train stations and recorded in newspapers and on web sites (Fig. 2.79e). In 2022, FBD was five days earlier than the 2000–20 mean (Table. 2.11).

Monitoring data on lake water concentrations of the photosynthetic pigment chlorophyll-*a* were available to estimate spring phytoplankton phenology in 1 Southern Hemisphere and 10 Northern Hemisphere lakes (Fig. 2.80). Seasonal timing was quantified for start of season (SOS_L ; Park et al. 2016), day of maximum concentration (DOM_L), and center of gravity (COG_L , an estimate of the mid-point of the plankton bloom; Edwards and Richardson 2004). Lake basins showed great interannual variation and mixed phenological behavior in 2022 relative to the 2000–20 baseline. The Norway lake, Mjøsa, and the Southern Hemisphere lake in New Zealand, Taupo, showed different seasonal changes to other lakes related to snow melt and southern season, respectively. SOS_L occurred earlier than the baseline median for most (8 of 11) lakes, and DOM_L occurred later in most lakes (8 of 11). For COG_L , no consistent pattern was observed.

5. VEGETATION OPTICAL DEPTH

—R. M. Zotta, R. van der Schalie,
W. Preimesberger, L. Moesinger,
R. A. M. de Jeu, and W. Dorigo

Microwave radiation emitted or reflected by Earth's surface is strongly affected by available surface water, including that which is stored in living biomass. The portion of the radiance attenuated by the canopy is expressed by vegetation optical depth (VOD), a parameter used in radiative transfer models to describe radiance interaction with vegetation. VOD is closely related to canopy water content (Konings et al. 2017), leaf area index (Vreugdenhil et al. 2017), and gross primary production (Teubner et al. 2019; Wild et al. 2022) and is a good indicator of vegetation response to climate variability. Positive

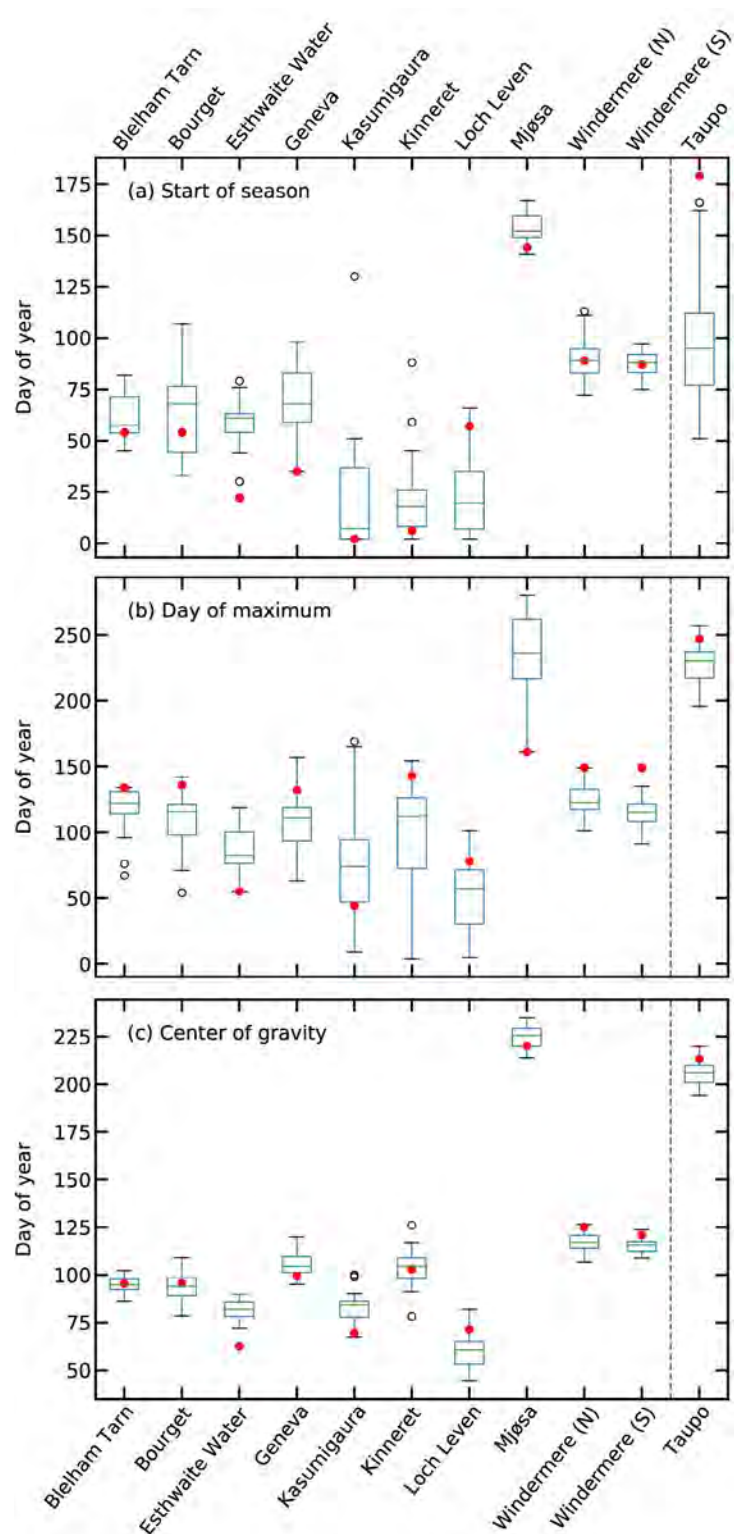


Fig. 2.80. Phenological metrics based on lake chlorophyll-*a* concentrations, as a proxy of phytoplankton biomass: (a) start of season, (b) day of maximum, and (c) center of gravity. Boxplots show variation during the 2000–20 baseline period, and red dots show 2022 values. Dashed line identifies Northern Hemisphere (Blelham Tarn in UK, Bourget in France, Esthwaite Water in UK, Geneva in France/Switzerland, Kasumigaura in Japan, Kinneret in Israel, Loch Leven in UK, Mjøsa in Norway, north and south basins of Windermere in UK) and Southern Hemisphere (Taupo in New Zealand) lakes.

VOD anomalies correspond to above-average vegetation development, while negative VOD anomalies indicate stressed or underdeveloped vegetation.

Globally, the year 2022 saw similar annual VOD anomaly patterns to 2021 and 2020 (Dorigo et al. 2022, 2021). In the Southern Hemisphere, where there is a clear connection between vegetation activity and variations in the El Niño–Southern Oscillation (Miralles et al. 2014; Martens et al. 2017), anomalies became positive (Figs. 2.81, 2.82). The relationship with climate modes is not straightforward, however, as VOD is also affected by drivers such as moisture availability, temperature, radiation, carbon dioxide fertilization, and land management (Gonsamo et al. 2021; Reichstein et al. 2013).

Widespread positive anomalies are seen in southern Africa and Australia (Plate 2.1af). In these regions, the patterns became more positive compared to 2021 (Supp. Fig. A2.9), coinciding with the persistence of La Niña throughout 2022, which brought above-average rainfall (see sections 7e5, 7h4). Other regions where positive patterns have prevailed include the Sahel, India, and northeastern China. Negative VOD anomalies occurred in the Great Plains in North America, the Parana River Basin in South America, and eastern Africa (Plate 2.1af). Most of these negative patterns coincided with precipitation deficits associated with La Niña and/or the negative Indian Ocean dipole mode (section 2e1; Mo et al. 2009; Santos et al. 2021; Anderson et al. 2022; Barlow et al. 2002). The negative VOD anomalies in the Great Plains (Plate 2.1af) coincide with reports of poor vegetation health issued by the NOAA National Centers for Environmental Information (NOAA 2023) for the American West, central and southern Plains, through the Mississippi Valley, and into the northeast. The negative patterns in the Parana River basin occurred in a region with intense wildfire activity (section 2h3), facilitated by dry conditions that persisted for a fourth consecutive year (Neumann et al. 2021). Below-average precipitation trends continued in East Africa (Anderson et al. 2022) and intensified towards the end of the year, leading to strong negative VOD anomalies (Plate 2.1af). Other remarkable negative VOD anomalies were observed in Europe from July to September (Supp. Fig. A2.10). Notably, in Spain, France, central and northern Italy, central Germany, Hungary, Romania, Slovenia,

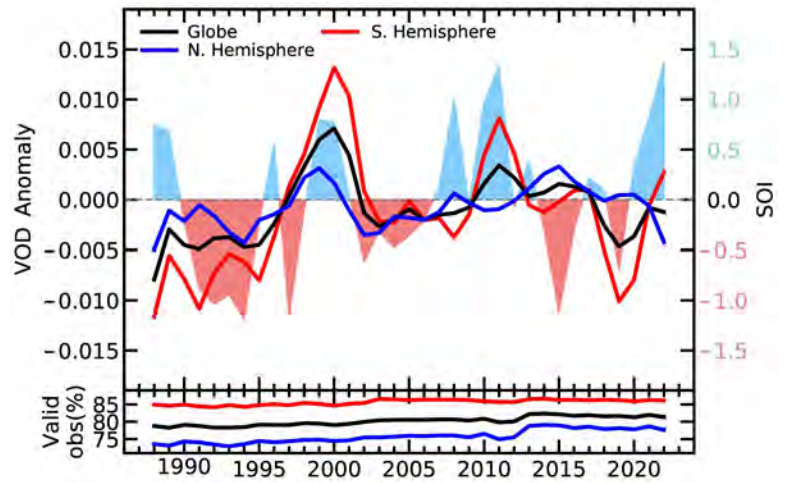


Fig. 2.81. Yearly CXKu vegetation optical depth (VOD) anomalies computed from the 1991–2020 climatology and their agreement with the Southern Oscillation Index (SOI). SOI tracks the state of the El Niño–Southern Oscillation. The SOI has been divided by 10, so that values >0.7 indicate La Niña and values <-0.7 indicate El Niño episodes. (Source: VODCA; <http://www.bom.gov.au/climate/enso/soi/>.)

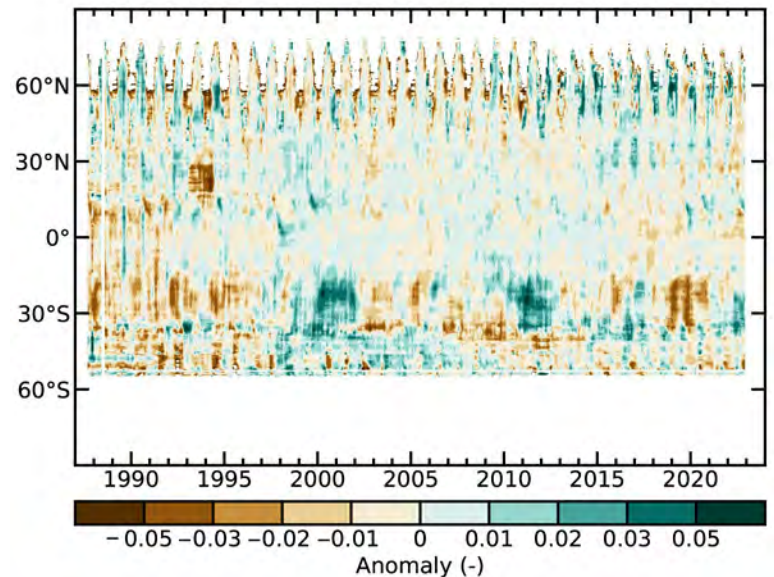


Fig. 2.82. Time–latitude diagram of vegetation optical depth (VOD) anomalies (1991–2020 base period). Data are masked where no retrievals is possible, where no vegetation is present (bare soil), or where the quality is not assured and flagged due to frozen soil, radio frequency interference, etc. (Source: VODCA.)

and Croatia, the main summer crops were severely affected due to exceptionally hot and dry weather conditions (Baruth et al. 2022). Negative VOD prevailed in Algeria and Morocco (Plate 2.1af) as well, with the Food and Agriculture Organization (FAO) reporting below-average cereal production due to widespread drought (FAO 2022). In China, vegetation conditions were affected by a precipitation deficit and heatwave in August (Toreti et al. 2022), which appear as negative VOD anomalies in central China, especially during July, August, and September (Supp. Fig. A2.10).

Several long-term patterns resulting from land-use change also prevailed in 2022 (Plate 2.1af; Dorigo et al. 2021). Due to deforestation and land degradation, below-average VOD occurred in Mongolia, Bolivia, Paraguay, and Brazil (Song et al. 2018). The intensification of agricultural production and reforestation led to above-average VOD in India and northeastern China, respectively (Song et al. 2018).

The VOD anomalies were computed from the VOD Climate Archive (VODCA; Moesinger et al. 2020). VODCA fuses VOD observations derived from several space-borne radiometers (Special Sensor Microwave/Imager [SSM/I], Tropical Rainfall Measuring Mission [TRMM], WindSat, Advanced Microwave Scanning Radiometer-Earth Observing System [AMSR-E] and Advanced Microwave Scanning Radiometer 2 [AMSR2]) through the Land Parameter Retrieval Model (Meesters et al. 2005; van der Schalie et al. 2017) into a harmonized, long-term (1987–2022) dataset. VODCA version 2 contains individual products for Ku-band (covering 1987–2022), X-band (1997–2022), C-band (2002–22), and L-band (2010–22), as well as a multi-frequency product called VODCA CXXu (1987–2022) which blends the highly correlated Ku-, X-, and C-band observations. All VODCA products are at 0.25° spatial and daily temporal resolutions. Here, we used VODCA CXXu to compute anomalies from the long-term (1991–2020) climatology. VODCA CXXu is indicative of upper canopy dynamics.

Acknowledgments

2.a.1 Overview

The editors thank the BAMS special editor, Mike Alexander, the five anonymous reviewers, as well as David Parker, John Kennedy, Katrina MacNeill, and Josh Blannin for their insight, thoughts, and suggestions when developing this chapter. We also thank Fumi Sezaki (JMA), Julien Nicolas (ECMWF), and Mike Bosilovich (NASA) for their help in providing the reanalysis data used in this chapter. R. J. H. Dunn and K. M. Willett were supported by the Met Office Hadley Centre Climate Programme funded by BEIS. R. J. H. Dunn also thanks Bill Little for his assistance with the plots.

2.b.2 Lake surface water temperature

Lake surface water temperatures from satellite data have been generated within the Climate Change Initiative Lakes project funded by the European Space Agency (4000125030/18/I-NB) with adaptation and extensions funded by the EU Copernicus Climate Change Service (C3S) programme. Part of the in situ data used for the validation of the satellite data and for this report have kindly been made publicly available by the Fisheries and Oceans Canada (FOC), the National Data Buoy Center from NOAA, the Hungarian Meteorological Office, the Upper Great Lakes Observing System (UGLOS), the North Temperate Lakes Long-Term Ecological Research (NTL-LTER), and the Swedish Infrastructure for Ecosystem Science (SITES), and the King County Water and Land Resources Division, Washington. The authors gratefully acknowledge the late Alon Rimmer for always supplying data for Lake Kinneret. The in situ temperature measurements for Lake Baikal were supported by Foundation for support of applied ecological studies "Lake Baikal" (<https://baikalfoundation.ru/project/tochka-1/>). Temperature data for the UK lakes were supported by the Natural Environment Research Council award number NE/R016429/1 as part of the UK-SCaPE program delivering National Capability.

2.b.3 Night marine air temperature

R. C. Cornes, T. Cropper and E. C. Kent were supported by the NERC NC CLASS programme (NE/R015953/1) and the NERC GloSAT project (NE/S015647/2). R. Junod was supported by funding from the U.S. Department of Energy (DE-SC0023332).

2.b.4 Surface temperature extremes

R. J. H. Dunn was supported by the Met Office Hadley Centre Climate Programme funded by BEIS.

2.b.5 Tropospheric temperature

Work performed by Stephen Po-Chedley at Lawrence Livermore National Laboratory (LLNL) was supported by LDRD 23-FS-009 and performed under the auspices of the DOE under Contract DE-AC52-07NA27344.

2.c.1 Permafrost temperatures and active layer thickness

The Circumpolar Active Layer Monitoring (CALM) program is funded by the US NSF Project OPP-1836377. The Swiss Permafrost Monitoring Network (PERMOS) is financially supported by MeteoSwiss (in the framework of GCOS Switzerland), the Federal Office for the Environment, and the Swiss Academy of Sciences and acknowledges the important contribution of its partner institutions and principal investigators. The French Network PermaFRANCE is financially supported by the Observatoire des Sciences de l'Univers Grenoble and the French Research Infrastructure OZCAR. Research on James Ross Island was supported by the Czech Antarctic Research Programme and the Czech Science Foundation project (GM22-28659M). The Chinese Permafrost Monitoring Network is financially supported by the Chinese National Science Foundation (41931180) and the Cryosphere Research Station on Qinghai-Xizang Plateau, CAS.

2.c.2 Rock glacier velocity

Rock glacier monitoring at Hinteres Langtalkar and Dösen rock glaciers (AT) is supported by the Hohe Tauern National Park Carinthia through its long-term permafrost monitoring program. The Laurichard (FR) survey is supported by CryobsClim “Long-term Observation and Experimentation System for Environmental Research” (SOERE/All’envi-OZCAR Research Infrastructure) and the PermaFrance observatory “monitoring the mountain permafrost in the French Alps” as well as French National Research Agency in the framework of the Investissements d’Avenir programs: Risk@UGA (ANR-15-IDEX-02) and LabEx OSUG@2020 (ANR10 LABX56). The Ecrins National Park helps field surveys since the early 2000s. The Swiss Permafrost Monitoring Network (PERMOS) is financially supported by MeteoSwiss in the framework of GCOS Switzerland, the Federal Office for the Environment and the Swiss Academy of Sciences. PERMOS acknowledges the important contribution of the partner institutions and principal investigators. The time series for Central Asian rock glaciers was compiled with the ESA Permafrost_CCI project (4000123681/18/I-NB). The time series for the Dry Andes was supported by the Centro de Estudios Avanzados en Zonas Áridas (CEAZA) and the Leading House for the Latin American Region (University of St. Gallen), grant number MOB1829.

2.c.3 Alpine glaciers

The World Glacier Monitoring Service data collection system is the basis for nearly all data used in this section.

2.c.4 Lake ice

We thank Alexander Mills, Huaxia Yao, Merja Pulkkanen, Shin-Ichiro Matsuzaki, Jan Henning L’Abée-Lund, Don Pierson, Lars Rudstam, Beth Kohlman, BJ Bauer, Douglas Pierzina, Bonny Pederson, Brendan Wiltse, Carol Wendorf, Cheryl and Dorothy Zingler, Craig Hillman, Calvin Maurer, Dale Robertson, David Kahan, Doug Fitzgerald, Earl Cook, Gay Alberts Ruby, Greg Sass, John Maier, James and Sharon Fenner, Susan Reineking, Jerry Evans, Jerry Sondreal, Tom Stangl, Jim and Judy Daugherty, Joel Rasmussen, John and Catherine Bart, Joy Krubsack, Kay and Rich Rezanka, Kay Wepfer, Ken Blumenfeld, Pete Boulay, Holly Waterfield, Larry Peterson, Lolita Olson, Lowell Dague, Marge Kellor, Mark Biller, Michael Kolecheck, Michael Bradley, Michael Allen, Michael Traufler, Mike, Jeff, and Thomm Backus, Mickey and Dennis Chick, Ann LaLiberte, Nancy Steenport, Patricia Bebak, Patrick Collins, Peter Bearup, Joe Jenkins, Bob Katzenberger, Ronald Jones, Sandra Anderson, Scott Schoepp, Travis Campbell, Susan Verhaalen, Thomas Sommerfeldt, Water Dahlke III, Rachel Dahlke, William Hanson, and Clare and Dan Shirley for their dedication and efforts in collecting and sharing *in situ* ice phenological records over the past 32+ years with us.

2.c.5 Northern Hemisphere snow cover extent

This work is funded in part by NOAA’s Climate Data Record (CDR) Program at the National Centers for Environmental Information.

2.d.1 Surface humidity

Kate Willett was supported by the Met Office Hadley Centre Climate Programme funded by BEIS. Adrian Simmons and David Lavers were supported by the Copernicus Climate Change Service implemented by ECMWF on behalf of the European Commission.

2.d.5 Precipitation extremes

The National Center for Atmospheric Research is sponsored by the National Science Foundation under Cooperative Agreement No. 1852977.

2.d.6 Cloudiness

CERES EBAF data were obtained from the NASA Langley Research Center CERES ordering tool at <https://ceres.larc.nasa.gov/data/>.

2.d.7 Lake water level

B. M. Kraemer recognizes support from the grant “SeeWandel: Life in Lake Constance - the Past, Present and Future” within the framework of the Interreg V programme “Alpenrhein-Bodensee-Hochrhein (Germany/Austria/Switzerland/Liechtenstein)” whose funds are provided by the European Regional Development Fund as well as the Swiss Confederation and cantons. M.F. Meyer was supported by a USGS Mendenhall Fellowship from the Water Mission Area. The funders had no role in study design, data collection and analysis, decision to publish, or preparation of the manuscript. Any use of trade, firm, or product names is for descriptive purposes only and does not imply endorsement by the U.S. Government.

2.d.8 Groundwater and terrestrial water storage

Work on the Groundwater and Terrestrial Water Storage section was funded by NASA’s GRACE-FO Science Team.

2.d.9 Soil moisture

This study uses satellite soil moisture observations from the Copernicus Climate Change Service (C3S) Climate Data Store (CDS): Soil moisture gridded data from 1978 to present. (Accessed on 19-01-2023), 10.24381/cds.d7782f18

2.d.10 Drought

Jonathan Barichivich was supported by the European Research Council (ERC) under the Horizon Europe research and innovation programme (ERC-starting grant CATES, grant agreement No. 101043214). Tim Osborn received funding from UK NERC (NE/S015582/1). Ian Harris received funding from UK National Centre for Atmospheric Science (NCAS). The research presented in the drought section was carried out on the High-Performance Computing Cluster supported by the Research and Specialist Computing Support service at the University of East Anglia.

2.d.11 Land evaporation

D. G. Miralles acknowledges support from the European Research Council (ERC) under grant agreement no. 101088405 (HEAT). M.F. McCabe and H.E. Beck are supported by the King Abdullah University of Science and Technology.

2.e.2 Surface winds

C. Azorin-Molina was supported by CSIC-UV-GVA and funded by AICO/2021/023, LINGLOBAL-CSIC ref. INCGLO0023, INTRAMURAL-CSIC ref. 202230I068, and PTI-CLIMA.R. J. H. Dunn was supported by the Met Office Hadley Centre Climate Programme funded by BEIS. L. Ricciardulli was supported by NASA Ocean Vector Wind Science Team grant 80HQTR19C0003. Z. Zeng was supported by the National Natural Science Foundation of China grant 42071022.

2.e.4 Lightning

The work of M. Füllekrug was sponsored by the Royal Society (UK) grant NMG/R1/180252 and the Natural Environment Research Council (UK) under grants NE/L012669/1 and NE/H024921/1.

E. Williams is supported for studies on global circuit response to climate change from the Physical and Dynamic Meteorology Program at the National Science Foundation on grant no. 6942679.

C. Price was supported in his lightning research by the Israel Science Foundation (ISF) grant 2701/17, and the Ministry of Energy grant no. 220-17-002. S. Goodman was supported by NASA Grant 80NSSC21K0923 and NASA Contract 80GSFC20C044. K.Virts is supported in part by the GOES-R Series Science, Demonstration, and Cal/Val Program at Marshall Space Flight Center. D. Buechler is supported by the NASA MSFC/UAH Cooperative Agreement NNM11AA01A. The authors wish to thank Peter Thorne at Maynooth University in Ireland and at the European Centre for Medium Range Weather Forecast (ECMWF) for suggesting and initiating this work and for recommending that lightning be made an essential climate variable. ISS LIS acknowledges support from the NASA Science Mission Directorate.

2.f.1 Earth radiation budget at top of atmosphere

This research has been supported by the NASA CERES project. The NASA Langley Atmospheric Sciences Data Center processed the instantaneous Single Scanner Footprint (SSF) data used as input to EBAF Ed4.2 and processes the FLASHFlux TISA version 4A.

2.g.3 Aerosols

Samuel Rémy, Melanie Ades, and Mihai Alexe are grateful to the EU Copernicus Atmosphere Monitoring Service (CAMS), which supports the CAMS reanalysis used in the aerosols section.

2.g.4 Stratospheric ozone

Carlo Arosio, Melanie Coldewey-Egbers, Diego Loyola, Viktoria Sofieva, Alexei Rozanov, and Mark Weber are grateful to the EU Copernicus Climate Change Service, 312b Lot4 Ozone and to ESA's Climate Change Initiative Ozone (CCI+) projects for supporting the generation and extension of the GTO-ECV total ozone and SAGE-CCI-OMPS data records. Mark Weber, Carlo Arosio, Kleareti Tourpali, and Alexei Rozanov are grateful for the support by the ESA project "Ozone Recovery from Merged Observational Data and Model Analysis (OREGANO)". Stacey M. Frith is supported by the NASA Long Term Measurement of Ozone program WBS 479717. Lucien Froidevaux's contribution, with the assistance of Ryan Fuller, was performed at the Jet Propulsion Laboratory, California Institute of Technology, under contract with NASA. Jeannette Wild was supported by NOAA grant NA19NES4320002 (Cooperative Institute for Satellite Earth System Studies - CISESS) at the University of Maryland/ESSIC. Melanie Coldewey-Egbers and Diego Loyola acknowledge the partial support by the DLR projects MABAK and INPULS.

2.g.6 Tropospheric ozone

O. R. Cooper and K.-L. Chang were supported by NOAA cooperative agreement NA22OAR4320151.

2.g.7 Carbon monoxide

The Copernicus Atmosphere Monitoring Service is funded by the European Union.

2.h.2 Terrestrial vegetation dynamics

N. Gobron thanks Mirko Marioni for his technical support and the providers of the remote sensing dataset needed to perform this research, i.e. the SeaWiFS Project (Code 970.2) and the Goddard Earth Sciences Data and Information Services Center/Distributed Active Archive Center (Code 902) at the Goddard Space Flight Center, Greenbelt, MD 20771. MERIS products were processed at the Grid On Demand facility of the European Space Agency (ESA/ESRIN) using JRC software code.

2.h.1 Albedo

The authors thank Mirko Marioni for his technical support and NASA's Land Processes Distributed Active Archive Center (LP DAAC) for providing access to the remote sensing data.

2.h.3 Biomass burning

J. W Kaiser and M. Parrington were supported by the Copernicus Atmosphere Monitoring Service implemented by ECMWF on behalf of the European Commission. Data processing facilities were provided by the Max Planck Institute for Chemistry, Mainz, Germany.

2.h.4 Phenology of primary producers

Debbie Hemming acknowledges support from the Met Office Hadley Centre Climate Programme funded by BEIS, and thanks all co-authors for their interesting and helpful contributions. Taejin Park acknowledges support from the NASA Earth Science Directorate (grants NNX16AO34H and 80NSSC18K0173-CMS). Andrew Richardson acknowledges support from the National Science Foundation through the Macrosystems Biology (award 1702697) and LTER (award 1832210) programs. John O'Keefe also acknowledges support from the National Science Foundation through the LTER (award 1832210) program. Nature's Calendar (Woodland Trust) in the UK thanks all its volunteer recorders and support from players of People's Postcode

Lottery. Theresa Crimmins and the USA-NPN acknowledge support from the National Science Foundation through the Division of Biological Infrastructure (award 2031660), the US Fish and Wildlife Service (agreements F16AC01075 and F19AC00168), and the US Geological Survey (G14AC00405 and G18AC00135). The USA National Phenology Network thanks the many participants contributing phenology observations to *Nature's Notebook*. De Natuurkalender (Nature's Calendar) program in the Netherlands thanks all the volunteers and school children in the GLOBE program for their many observations. Annette Menzel and Nicole Estrella acknowledge support from the Bavarian State Ministry of Science and the Arts in the context of the Bavarian Climate Research Network (BayKlif) (Bavarian Citizen Science Portal for Climate Research and Science Communication [BAYSICS project]). The Slovak Hydrometeorological Institute thanks all its volunteer observers for participating in the phenological observation program. Orlane Anneville acknowledges support from INRAE. Stephen Thackeray thanks Werner Eckert, Heidrun Feuchtmayr, Shin-Ichiro Matsuzaki, Linda May, Ryuichiro Shinohara, Jan-Erik Thrane, Piet Verburg, Tamar Zohary and all field and lab workers associated with the provision of the lake chlorophyll-a data. We acknowledge funding from Vassdragsforbundet for Mjøsa med tilløpselver (<https://www.vassdragsforbundet.no/om-oss/>) and Natural Environment Research Council award number NE/R016429/1 as part of the UK-SCAPE programme delivering National Capability. Data for Lakes Geneva and Bourget were contributed by the Observatory of alpine LAKes (OLA), © SOERE OLA-IS, AnaEE-France, INRAE of Thonon-les-Bains, CIPEL, CISALB.

2.h.5 Vegetation optical depth

R. M. Zotta and W. Dorigo acknowledge the TU Wien Wissenschaftspreis 2015, a personal grant awarded to W. Dorigo.

We also acknowledge support from the ESA Climate Change Initiative and the Copernicus Climate Change Service (C3S).

Sidebar 2.1 Humid heat extremes

Kate Willett was supported by the Met Office Hadley Centre Climate Programme funded by BEIS.

Appendix 1: Chapter 2 – Acronyms

4D-VAR	four-dimensional variational data assimilation
AAO	Antarctic Oscillation
AATSR	Advanced Along Track Scanning Radiometer
AGAGE	Advanced Global Atmospheric Gases Experiment
AIRS	Atmospheric Infrared Sounder
ALT	active layer thickness
AMSR2	Advanced Microwave Scanning Radiometer 2
AMSR-E	Advanced Microwave Scanning Radiometer-Earth Observing System
AMSU	Advanced Microwave Sounding Unit
AO	Arctic Oscillation
AOD	aerosol optical depth
ASCAT	Advanced Scatterometer
ASR	absorbed solar radiation
BDC	Brewer-Dobson circulation
BOM	Bureau of Meteorology
BUV	backscattering ultraviolet
C3S	Copernicus Climate Change Service
CALIPSO	Cloud-Aerosol LIDAR and Infrared Pathfinder Satellite Observations
CAMS	Copernicus Atmosphere Monitoring Service
CAMSRA	Copernicus Atmosphere Monitoring Service Reanalysis
CCI	Climate Change Initiative
CCMI	Chemistry Climate Model Initiative
CDR	climate data record
CEI4	Climate Extremes Index component 4
CERES EBAF	Clouds and the Earth's Radiant Energy System Energy Balance and Filled
CFC-11	trichlorofluoromethane
CFC	chlorofluorocarbon
CH ₃ CCl ₃	methyl chloroform
CH ₄	methane
CHIRPS	Climate Hazards Group Infrared Precipitation with Station data
CLASSmat	Climate Linked Atlantic Sector Science night marine air temperature
CMIP	Coupled Model Intercomparison Project
CMIP6	Phase 6 of the Coupled Model Intercomparison Project
CO	carbon monoxide
CO ₂	carbon dioxide
COG _L	center of gravity
COSMIC	Constellation Observing System for Meteorology, Ionosphere, and Climate
CPT	cold-point tropopause
CRU TS	Climatic Research Unit Gridded Time Series
DOM _L	day of maximum concentration
DU	Dobson units
EBAF	Energy Balance and Filled
ECMWF	European Centre for Medium-Range Weather Forecasts
ECV	essential climate variable
EESC	equivalent effective stratospheric chlorine
ENSO	El Niño–Southern Oscillation
EOS	end of season
ERA5	European Centre for Medium-Range Weather Forecasts Reanalysis version 5
ERB	Earth radiation budget

ERFs	effective radiative forcings
ESA	European Space Agency
ET	Penman-Monteith Potential Evapotranspiration
ETCCDI	Expert Team in Climate Change Detection and Indices
EUR	Eurasia
EUR	Europe
FAO	Food and Agriculture Organization
FAPAR	fraction of absorbed photosynthetically active radiation
FBD	full bloom dates
FF	fossil fuel
FLASHFlux	Fast Longwave and Shortwave Radiative Fluxes
FP	frost point
GAW	Global Atmosphere Watch
GCM	general circulation model
GCOS	Global Climate Observing System
GFAS	Global Fire Assimilation System
GFED	Global Fire Emissions Database
GHCND	Global Historical Climatology Network Daily
GHCNDEX	Global Historical Climatology Network Index
GISTEMP	GISS Surface Temperature Analysis
GLEAM	Global Land Evaporation Assessment Model
GLM	Geostationary Lightning Mapper
GNSS	global navigation satellite system
GOES	Geostationary Operational Environmental Satellite
GOME	Global Ozone Monitoring Experiment
GOZCARDS	Global Ozone Chemistry and Related Trace Gas Data Records for the Stratosphere
GPCP	Global Precipitation Climatology Centre
GPCP	Global Precipitation Climatology Project
GPS-RO	GPS radio occultation
GRACE	Gravity Recovery and Climate Experiment
GRACE-FO	Gravity Recovery and Climate Experiment Follow-On
G-REALM	Global Reservoir and Lake Monitoring
GSL	Global Snow Lab
GTN-P	Global Terrestrial Network for Permafrost
GWP	global warming potential
H ₂ O	water vapor
HadCRUT5	Hadley Centre/Climatic Research Unit Temperature version 5
HadISD3	Hadley Centre Integrated Surface Database version 3
HadISDH	Hadley Centre Integrated Surface Database Humidity
HadSST	The Met Office Hadley Centre's sea surface temperature dataset
HCFC	hydrochlorofluorocarbon
HFC	hydrofluorocarbon
HIRS	High-Resolution Infrared Sounder
HTHH	Hunga Tonga–Hunga Ha'apai
IOD	Indian Ocean dipole
IPCC AR6	Intergovernmental Panel on Climate Change Sixth Assessment Report
ISS	International Space Station
ITCZ	Intertropical Convergence Zone
JRA-55	Japanese 55-year Reanalysis
LIS	Lightning Imaging Sensor
LLGHG	long-lived greenhouse gases
LOWESS	locally weighted scatterplot smoothing

LSWT	lake-surface water temperature
LTT	lower-tropospheric temperature
LWCRE	longwave cloud radiative effect
MACCity	Monitoring Atmospheric Composition and Climate megacity
MAT	marine air temperature
MCS	marine cold-spell
MCS	mesoscale convective systems
MEGAN2.1	Model of Emissions of Gases and Aerosols from Nature version 2.1
MERRA-2	Modern-Era Retrospective Analysis for Research and Applications version 2
MHW	marine heatwave
MLO	Mauna Loa Observatory
MLS	Microwave Limb Sounder
MODIS	Moderate Resolution Imaging Spectroradiometer
MOPITT	Measurement of Pollution in the Troposphere
MSLP	mean sea-level pressure
MSU	Microwave Sounding Unit
N ₂ O	nitrous oxide
NA	North America
NAE	North Atlantic/European
NAO	North Atlantic Oscillation
NDACC	Network for the Detection of Atmospheric Composition Changes
NDVI	Normalized Difference Vegetation Index
NH	Northern Hemisphere
NIWA	National Institute of Water and Atmospheric Research
NMAT	night marine air temperature
NOAAGlobalTemp	NOAA Merged Land Ocean Global Surface Temperature Analysis
NPN	National Phenology Network
NRT	near real time
O ₃	tropospheric ozone
ODGI	Ozone Depleting Gas Index
ODS	Ozone-depleting substance
OH	hydroxyl radical
OISST	Optimum Interpolation Sea Surface Temperature
OLR	outgoing longwave radiation
OMI	Ozone Monitoring Instrument
OMPS	Ozone Mapping and Profiler Suite
OMPS-L	Ozone Mapping and Profiler Suite-Limb
OMPS-N	Ozone Mapping and Profiler Suite-Nadir
PATMOS-X	Pathfinder Atmospheres – Extended
PERMOS	Swiss Permafrost Monitoring Network
PNA	Pacific/North American
q	specific humidity
QBO	quasi-biennial oscillation
QuikSCAT	Quick Scatterometer
RCP	Representative Concentration Pathway
RFaci	aerosol-cloud interactions
RFari	aerosol-radiation
RGIK	rock glacier inventories and kinematics
RGV	rock glacier velocities
RH	relative humidity
RSS	Remote Sensing Systems
RSW	reflected shortwave

SAGE	Stratospheric Aerosol and Gas Experiment
SAM	Southern Annular Mode
SAOZ	Système D'Analyse par Observations Zénithales
SAWS	South African Weather Service
SBUV	Solar Backscatter Ultraviolet Radiometer
SCE	snow-cover extent
SCIAMACHY	Scanning Imaging Absorption Spectrometer for Atmospheric Cartography
scPDSI	self-calibrating Palmer Drought Severity Index
SH	Southern Hemisphere
SLSTR	Sea and Land Surface Temperature Radiometer
SO ₂	sulfur dioxide
SOI	Southern Oscillation Index
SORCE	Solar Radiation and Climate Experiment
SOS	start of season
SPARC	Spatial Analysis and Resource Characterization
SSM/I	Special Sensor Microwave/Imager
SSMIS	Special Sensor Microwave Imager/Sounder
SST	sea-surface temperature
SW	shortwave
SWCRE	shortwave cloud radiative effect
SWOT	Surface Water and Ocean Topography
TCO	tropospheric column ozone
TCWV	total column water vapor
TMI	TRMM Microwave Imager
TOA	top-of-atmosphere
TOB	tropospheric ozone burden
TRMM	Tropical Rainfall Measuring Mission
TSI	total solar irradiance
TSIS-1	Total Solar and Spectral Irradiance Sensor-1
TTL	tropical tropopause layer
TTT	tropical tropospheric temperature
T _w	wet bulb temperature
TWS	terrestrial water storage
UAHNMAT	University of Alabama in Huntsville night-time marine air temperature
UT	upper tropospheric
UTH	upper-tropospheric humidity
UV	ultraviolet
VEI	Volcanic Explosivity Index
VOD	vegetation optical depth
VODCA	Vegetation Optical Depth Climate Archive
w.e.	water equivalent
WGMS	World Glacier Monitoring Service
WMO	World Meteorological Organization
WOUDC	World Ozone and Ultraviolet Radiation Data Centre
WV	water vapor

Appendix 2: Chapter 2 – Supplemental Material

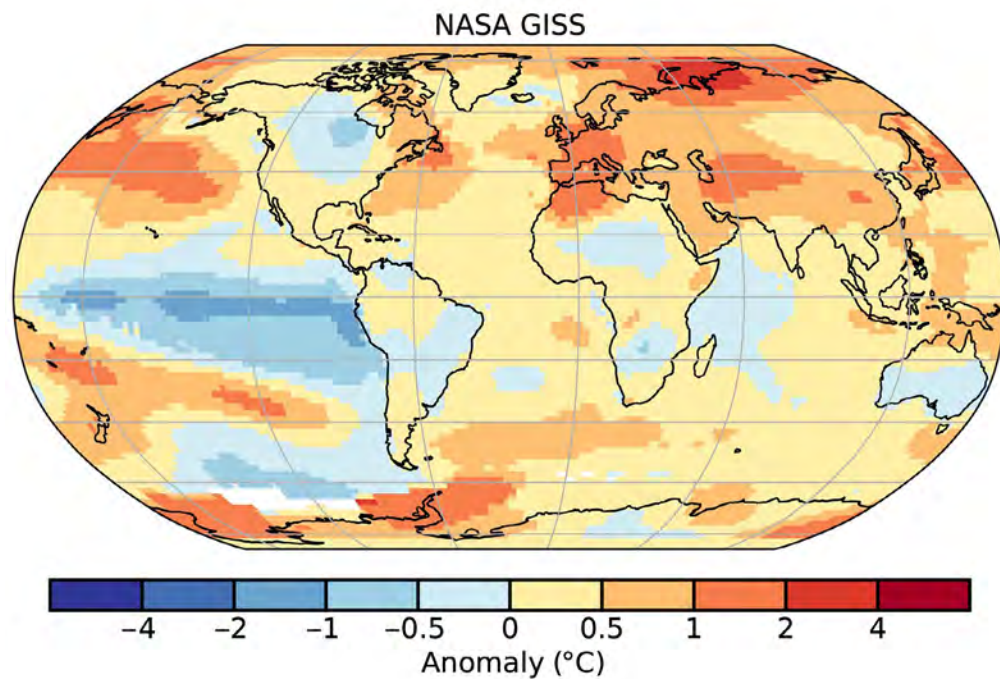


Fig. A2.1. NASA GISS 2-m surface temperature anomalies (°C; 1991–2020 base period).

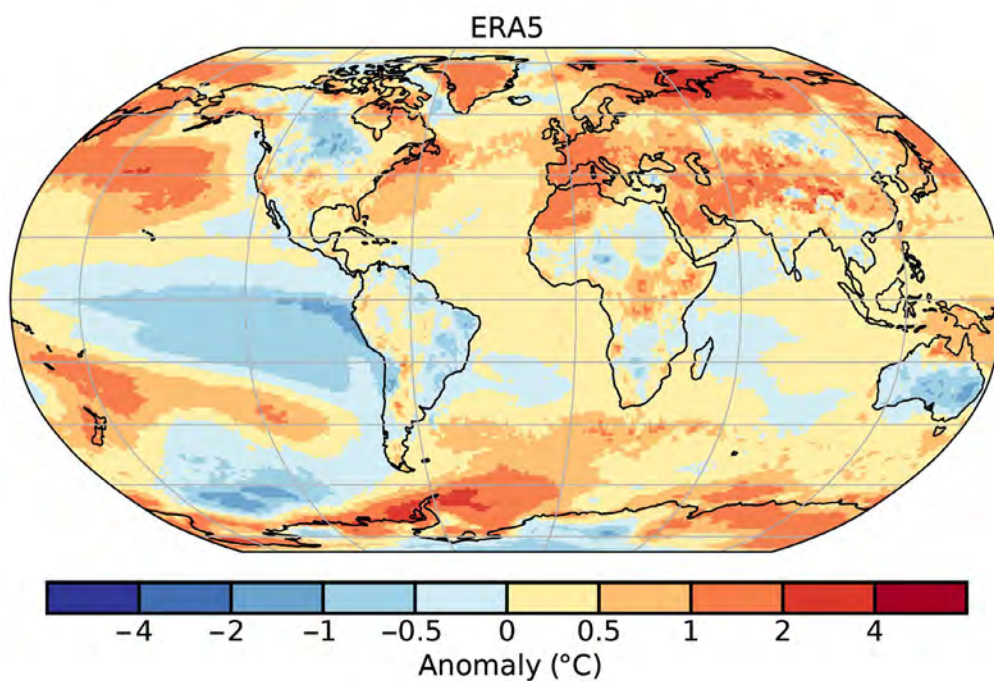


Fig. A2.2. ERA5 2-m surface temperature anomalies (°C; 1991–2020 base period).

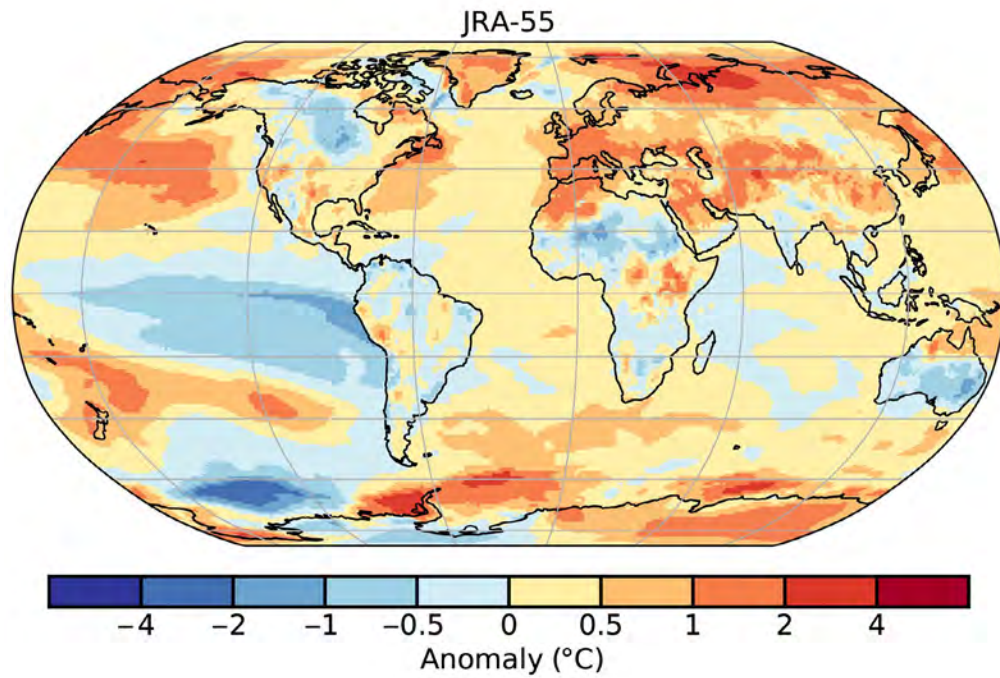


Fig. A2.3. JRA-55 2-m surface temperature anomalies (°C; 1991–2020 base period).

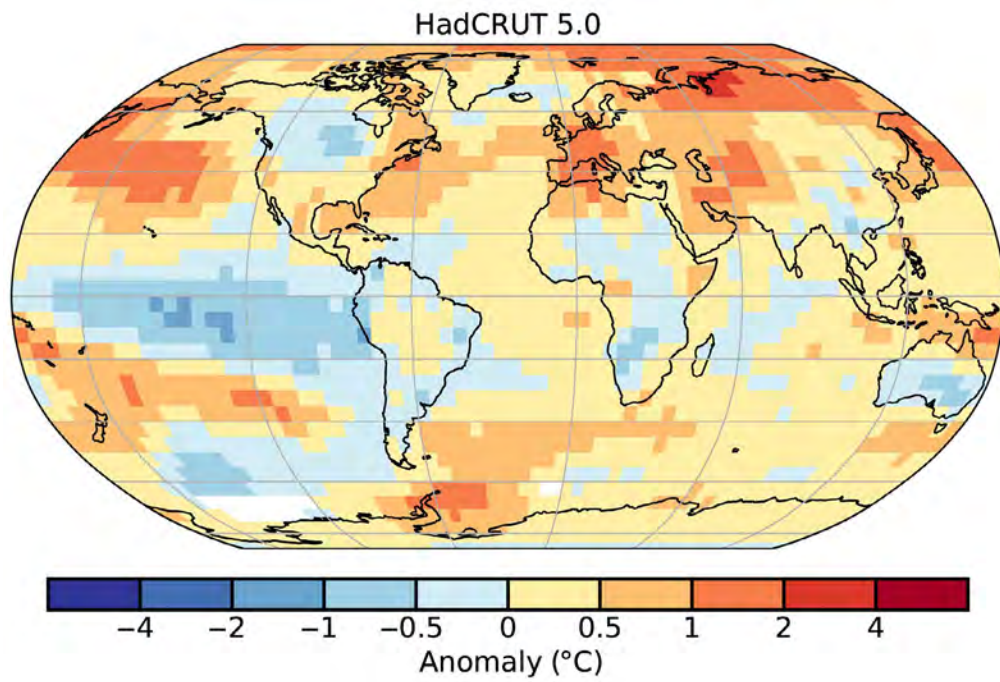


Fig. A2.4. HadCRUT5 2-m surface temperature anomalies (°C; 1991–2020 base period).

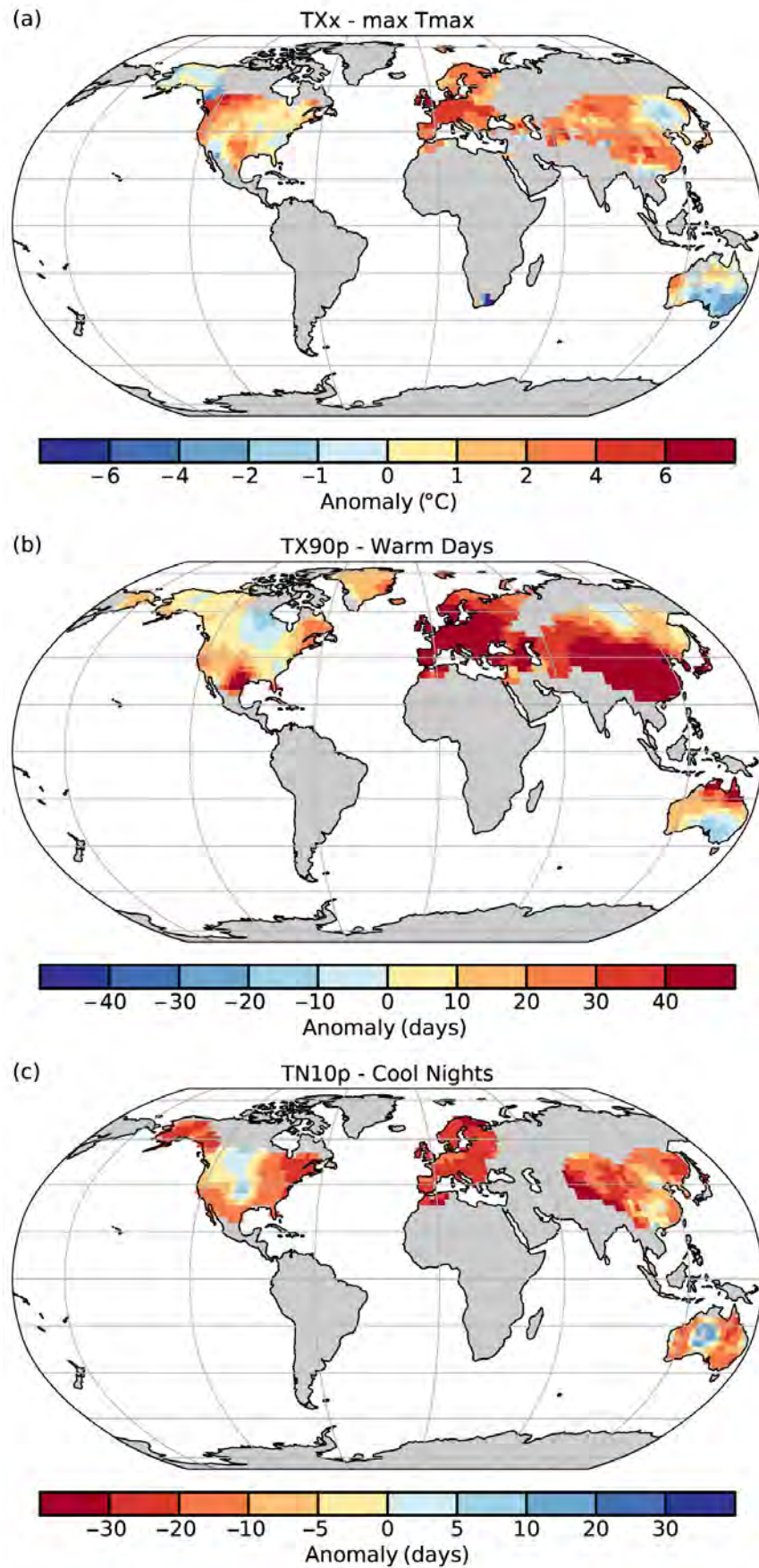


Fig. A2.5. (a) Extreme temperature anomalies in 2022 based on GHCNDEX for (a) hottest day of the year ($^{\circ}\text{C}$; TXx), (b) annual number of warm days (TX90p), and (c) annual number of cool nights (TN10p). Base period is 1961–90.

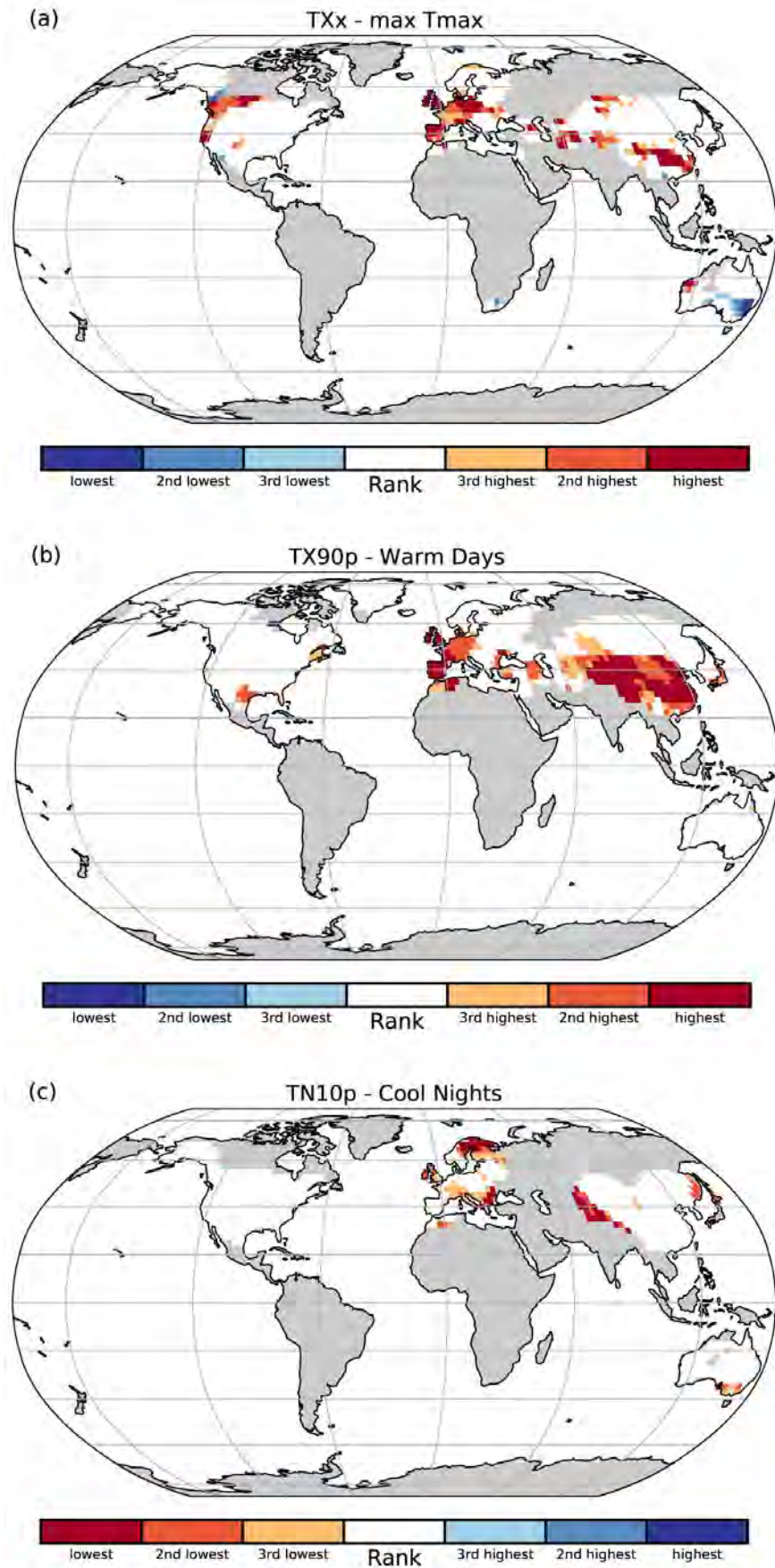


Fig. A2.6. Maps indicating grid cells where the temperature indices for 2022 ranked in the three highest or three lowest values based on GHCNDEX since 1951 for (a) hottest day of the year (TXx), (b) annual number of warm days (TX90p), and (c) annual number of cool nights (TN10p).

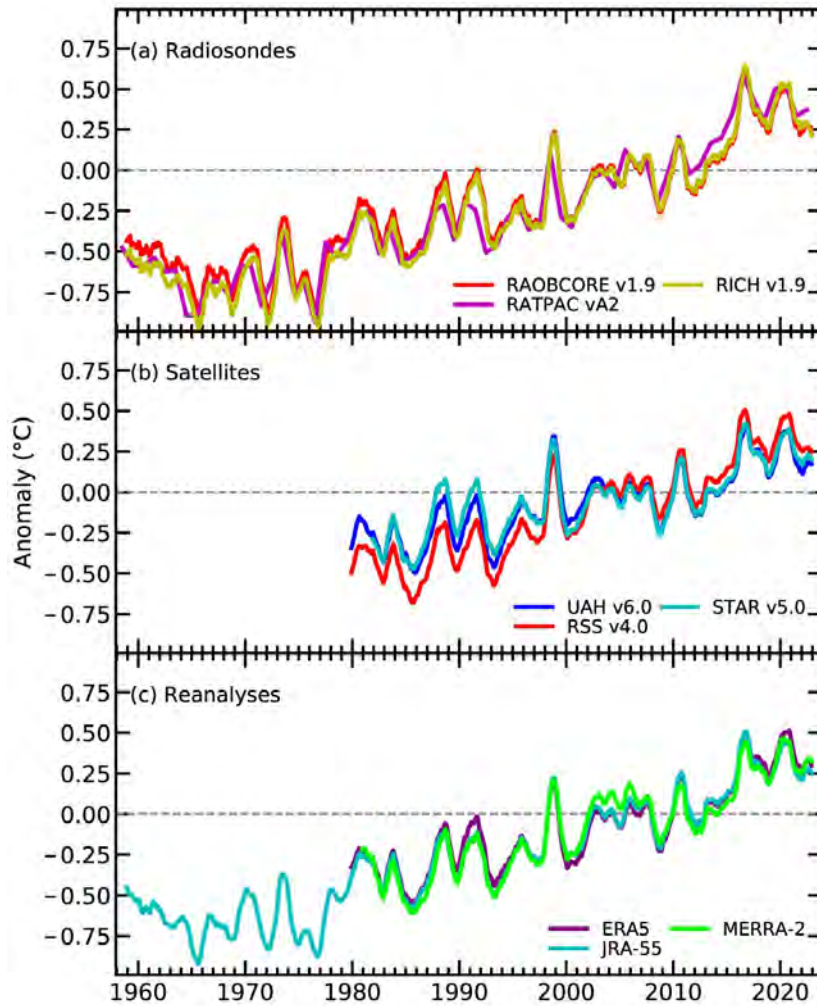


Fig. A2.7. Monthly average global lower-tropospheric temperature (LTT) anomalies ($^{\circ}\text{C}$; 1991–2020 base period) for (a) radiosonde, (b) satellite, and (c) reanalysis datasets. Time series are smoothed using a 12-month running average. Annual averages are displayed for the RATPAC dataset.

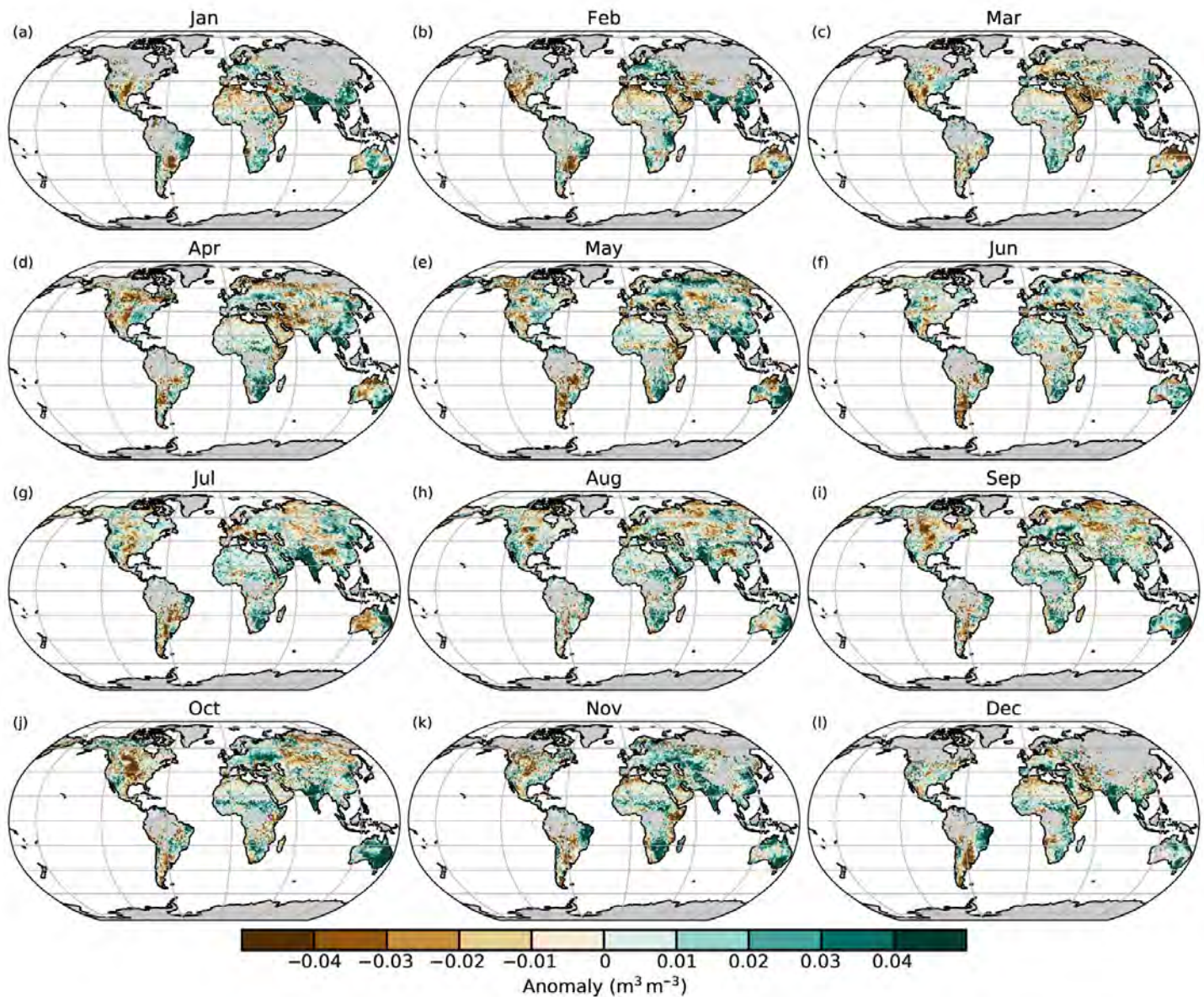


Fig. A2.8. Monthly average soil moisture anomalies for 2022 ($\text{m}^3 \text{m}^{-3}$; 1991–2020 base period). Data are masked where no retrieval is possible or where the quality is not assured and flagged, for example due to dense vegetation, frozen soil, or radio frequency interference. (Source: C3S Soil Moisture.)

2.f.2 Mauna Loa Apparent Transmission

Simulation of Tonga aerosol dispersion in the layer 19–27 km for 8–18 Mar 2022, derived from Cloud-Aerosol Lidar and Infrared Pathfinder Satellite Observations (CALIPSO) data.

https://figshare.com/articles/media/CALIOP_Latm-GMAO-19_27km_v2-10_20MAR-22_mp4/22704607/1

2.h.5 Vegetation Optical Depth

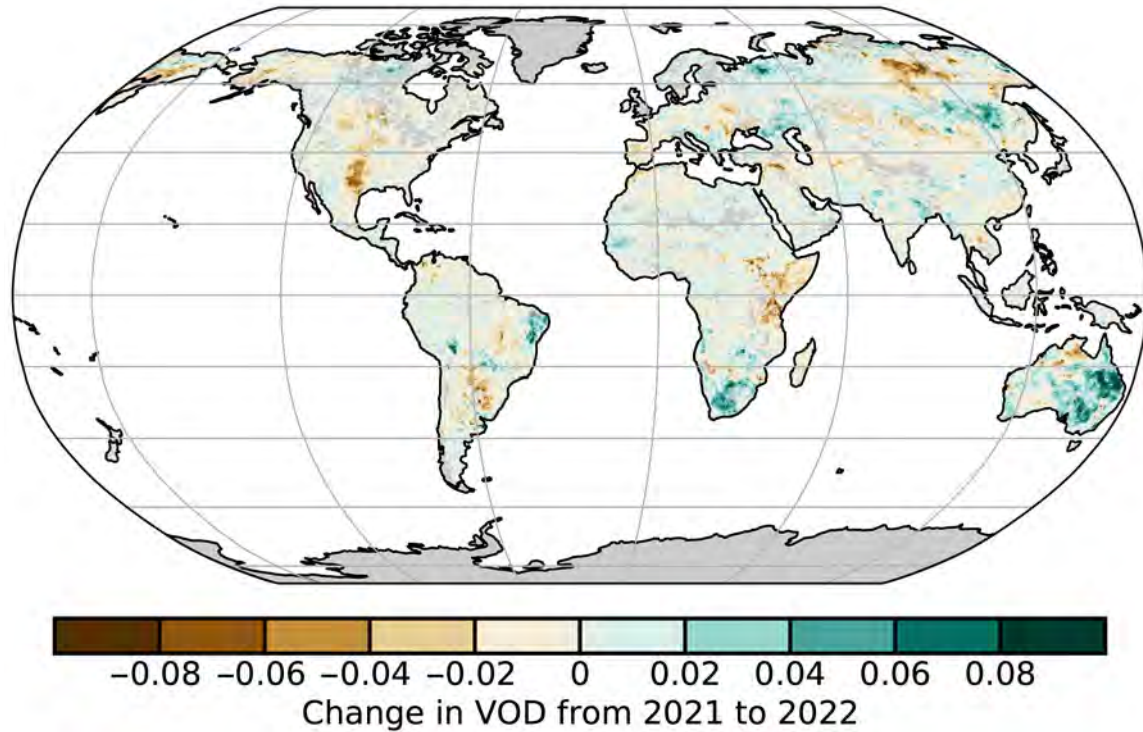


Fig. A2.9. Difference in average CXKu vegetation optical depth (VOD) between the years 2022 and 2021. Brown/green colors indicate areas where VOD in 2022 was lower/higher than in 2021. (Source: VODCA.)

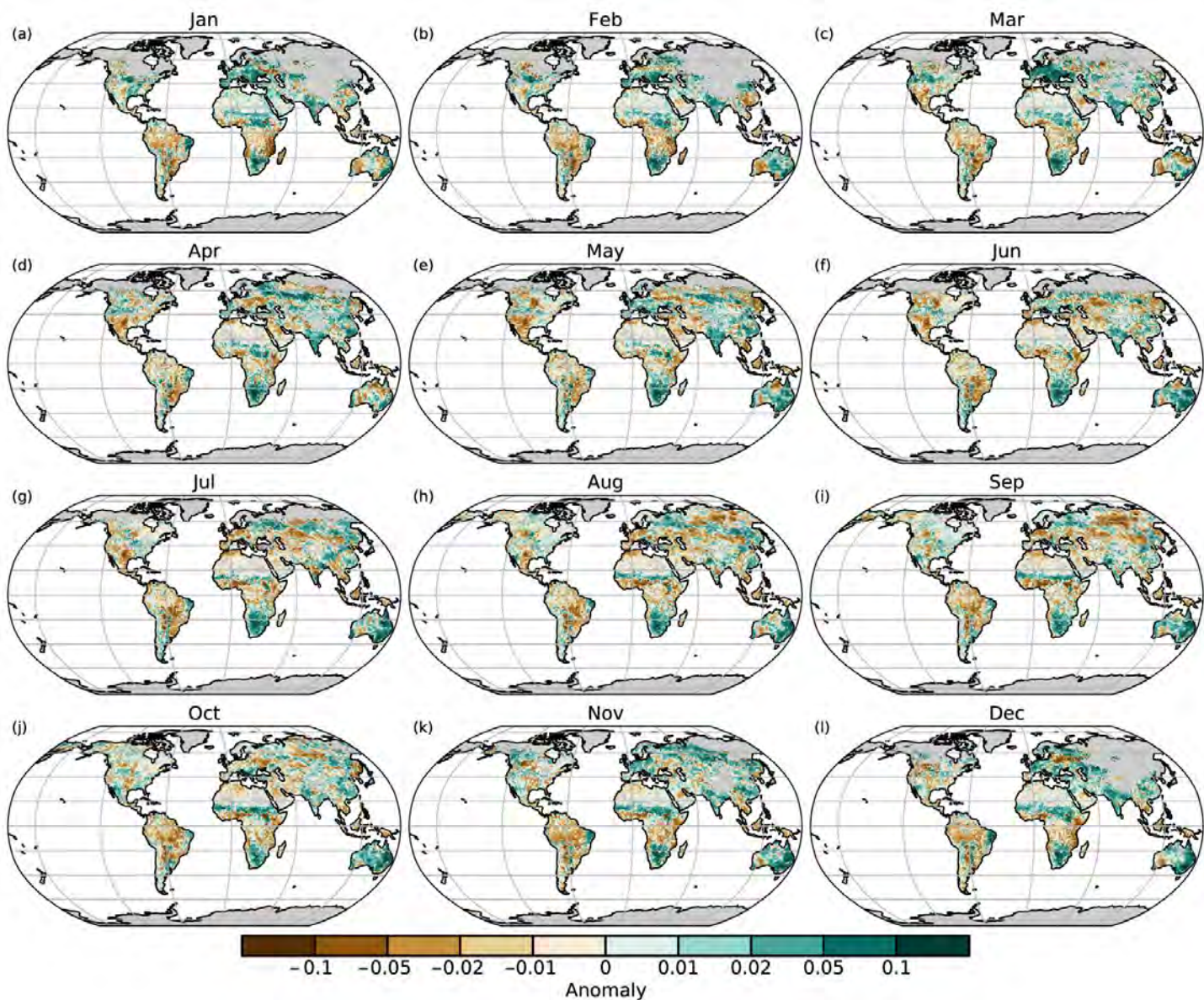


Fig. A2.10. VODCA monthly CXXu vegetation optical depth (VOD) anomalies for 2022 (1991–2020 base period). VOD cannot be retrieved over frozen or snow-covered areas, which is why they are masked in winter.

References

- Adler, R., and Coauthors, 2018: The Global Precipitation Climatology Project (GPCP) monthly analysis (new version 2.3) and a review of 2017 global precipitation. *Atmosphere*, **9**, 138, <https://doi.org/10.3390/atmos9040138>.
- Alden, C. B., J. B. Miller, and J. W. C. White, 2010: Can bottom-ocean CO₂ fluxes be reconciled with atmospheric ¹³C observations?. *Tellus*, **62B**, 369–388, <https://doi.org/10.1111/j.1600-0889.2010.00481.x>.
- Allan, R. J., and R. D. D'Arrigo, 1999: 'Persistent' ENSO sequences: How unusual was the 1990–1995 El Niño? *Holocene*, **9**, 101–118, <https://doi.org/10.1191/095968399669125102>.
- , J. A. Lindsay, and D. E. Parker, 1996: *El Niño Southern Oscillation and Climatic Variability*. CSIRO Publishing, 405 pp.
- Allan, R. P., K. M. Willett, V. O. John, and T. Trent, 2022: Global changes in water vapor 1979–2020. *J. Geophys. Res. Atmos.*, **127**, e2022JD036728, <https://doi.org/10.1029/2022JD036728>.
- Altaratz, O., B. Kucienska, A. Kostinski, G. B. Raga, and I. Koren, 2017: Global association of aerosol with flash density of intense lightning. *Environ. Res. Lett.*, **12**, 114037, <https://doi.org/10.1088/1748-9326/aa922b>.
- Anabalón, A., and A. Sharma, 2017: On the divergence of potential and actual evapotranspiration trends: An assessment across alternate global datasets. *Earth's Future*, **5**, 905–917, <https://doi.org/10.1002/2016EF000499>.
- Andela, N., and Coauthors, 2017: A human-driven decline in global burned area. *Science*, **356**, 1356–1362, <https://doi.org/10.1126/science.aal4108>.
- Anderson, W., B. I. Cook, K. Slinski, K. Schwarzwald, A. McNally, and C. Funk, 2023: Multiyear La Niña events and multiseason drought in the Horn of Africa. *J. Hydrometeorol.*, **24**, 119–131, <https://doi.org/10.1175/JHM-D-22-0043.1>.
- Andrews, T., and Coauthors, 2022: On the effect of historical SST patterns on radiative feedback. *J. Geophys. Res. Atmos.*, **127**, e2022JD036675, <https://doi.org/10.1029/2022JD036675>.
- Ansmann, A., and Coauthors, 2022: Ozone depletion in the Arctic and Antarctic stratosphere induced by wildfire smoke. *Atmos. Chem. Phys.*, **22**, 11 701–11 726, <https://doi.org/10.5194/acp-22-11701-2022>.
- Aon, 2023: Weather, climate and catastrophe insight. Aon plc, 115 pp., <https://www.aon.com/getmedia/f34ec133-3175-406c-9e0b-25cea768c5cf/20230125-weather-climate-catastrophe-insight.pdf>.
- Aono, Y., and K. Kazui, 2008: Phenological data series of cherry tree flowering in Kyoto, Japan, and its application to reconstruction of springtime temperatures since the 9th century. *Int. J. Climatol.*, **28**, 905–914, <https://doi.org/10.1002/joc.1594>.
- Archer, D., and V. Brovkin, 2008: The millennial atmospheric lifetime of anthropogenic CO₂. *Climatic Change*, **90**, 283–297, <https://doi.org/10.1007/s10584-008-9413-1>.
- Archibald, A. T., and Coauthors, 2020: Tropospheric Ozone Assessment Report: A critical review of changes in the tropospheric ozone burden and budget from 1850 to 2100. *Elementa*, **8**, 034, <https://doi.org/10.1525/elementa.2020.034>.
- Arguez, A., S. Hurley, A. Inamdar, L. Mahoney, A. Sanchez-Lugo, and L. Yang, 2020: Should we expect each year in the next decade (2019–28) to be ranked among the top 10 warmest years globally? *Bull. Amer. Meteor. Soc.*, **101**, E655–E663, <https://doi.org/10.1175/BAMS-D-19-0215.1>.
- Armstrong, B., and Coauthors, 2019: The role of humidity in associations of high temperature with mortality: A multicountry, multicity study. *Environ. Health Perspect.*, **127**, 097007, <https://doi.org/10.1289/EHP5430>.
- Arosio, C., A. Rozanov, E. Malinina, K.-U. Eichmann, T. von Clarman, and J. P. Burrows, 2018: Retrieval of ozone profiles from OMPS limb scattering observations. *Atmos. Meas. Tech.*, **11**, 2135–2149, <https://doi.org/10.5194/amt-11-2135-2018>.
- , —, —, M. Weber, and J. P. Burrows, 2019: Merging of ozone profiles from SCIAMACHY, OMPS and SAGE II observations to study stratospheric ozone changes. *Atmos. Meas. Tech.*, **12**, 2423–2444, <https://doi.org/10.5194/amt-12-2423-2019>.
- Augustine, J. A., K. O. Lantz, J.-P. Vernier, and H. Telg, 2020: Mauna Loa clear-sky "apparent" solar transmission [in "State of the Climate in 2019"]. *Bull. Amer. Meteor. Soc.*, **101** (8), S61–S62, <https://doi.org/10.1175/BAMS-D-20-0104.1>.
- , —, and —, 2021: Mauna Loa apparent transmission [in "State of the Climate in 2020"]. *Bull. Amer. Meteor. Soc.*, **102** (8), S82–S83, <https://doi.org/10.1175/BAMS-D-21-0098.1>.
- Azorin-Molina, C., J. Asin, T. R. McVicar, L. Minola, J. I. Lopez-Moreno, S. M. Vicente-Serrano, and D. Chen, 2018: Evaluating anemometer drift: A statistical approach to correct biases in wind speed measurement. *Atmos. Res.*, **203**, 175–188, <https://doi.org/10.1016/j.atmosres.2017.12.010>.
- Ball, W. T., G. Chiodo, M. Abalos, J. Alsing, and A. Stenke, 2020: Inconsistencies between chemistry–climate models and observed lower stratospheric ozone trends since 1998. *Atmos. Chem. Phys.*, **20**, 9737–9752, <https://doi.org/10.5194/acp-20-9737-2020>.
- Barichovich, J., T. J. Osborn, I. Harris, G. van der Schrier, and P. D. Jones, 2020: Monitoring global drought using the self-calibrating Palmer Drought Severity Index [in "State of the Climate in 2019"]. *Bull. Amer. Meteor. Soc.*, **101** (8), S59–S60, <https://doi.org/10.1175/BAMS-D-20-0104.1>.
- , —, —, —, and —, 2021: Monitoring global drought using the self-calibrating Palmer Drought Severity Index [in "State of the Climate in 2020"]. *Bull. Amer. Meteor. Soc.*, **102** (8), S68–S70, <https://doi.org/10.1175/BAMS-D-21-0098.1>.
- , —, —, —, and —, 2022: Monitoring global drought using the self-calibrating Palmer Drought Severity Index [in "State of the Climate in 2021"]. *Bull. Amer. Meteor. Soc.*, **103** (8), S66–S67, <https://doi.org/10.1175/BAMS-D-22-0092.1>.
- Barlow, M., H. Cullen, and B. Lyon, 2002: Drought in central and southwest Asia: La Niña, the warm pool, and Indian Ocean precipitation. *J. Climate*, **15**, 697–700, [https://doi.org/10.1175/1520-0442\(2002\)0152.0.CO;2](https://doi.org/10.1175/1520-0442(2002)0152.0.CO;2).
- Barnes, W. L., T. S. Pagano, and V. V. Salomonson, 1998: Prelaunch characteristics of the Moderate Resolution Imaging Spectroradiometer (MODIS) on EOS-AM1. *IEEE Trans. Geosci. Remote Sens.*, **36**, 1088–1100, <https://doi.org/10.1109/36.700993>.
- Baruth, B., and Coauthors, 2022: Crop monitoring in Europe. *JRC MARS Bulletin*, Vol. 30, No 8, European Commission, Luxembourg, Luxembourg, <https://doi.org/10.2760/31930>.
- Basu, S., and Coauthors, 2022: Estimating emissions of methane consistent with atmospheric measurements of methane and δ¹³C of methane. *Atmos. Chem. Phys.*, **22**, 15 351–15 377, <https://doi.org/10.5194/acp-22-15351-2022>.

- Beck, H. E., E. F. Wood, M. Pazn, C. K. Fisher, D. G. Miralles, A. I. J. M. van Dijk, T. R. McVicar, and R. F. Adler, 2019: MSWEP V2 global 3-hourly 0.1° precipitation: Methodology and quantitative assessment. *Bull. Amer. Meteor. Soc.*, **100**, 473–500, <https://doi.org/10.1175/BAMS-D-17-0138.1>.
- , A. I. J. M. van Dijk, P. R. Larraondo, T. R. McVicar, M. Pan, E. Dutra, and D. G. Miralles, 2022: MSWX: Global 3-hourly 0.1° bias-corrected meteorological data including near real-time updates and forecast ensembles. *Bull. Amer. Meteor. Soc.*, **103**, E710–E732, <https://doi.org/10.1175/BAMS-D-21-0145.1>.
- Becker, A., P. Finger, A. Meyer-Christoffer, B. Rudolf, K. Schamm, U. Schneider, and M. Ziese, 2013: A description of the global land-surface precipitation data products of the Global Precipitation Climatology Centre with sample applications including centennial (trend) analysis from 1901–present. *Earth Syst. Sci. Data*, **5**, 71–99, <https://doi.org/10.5194/essd-5-71-2013>.
- Behera, S. K., J. J. Luo, S. Masson, S. A. Rao, H. Sakuma, and T. Yamagata, 2006: A CGCM study on the interaction between IOD and ENSO. *J. Climate*, **19**, 1688–1705, <https://doi.org/10.1175/JCLI3797.1>.
- Bell, B., and Coauthors, 2021: The ERA5 global reanalysis: Preliminary extension to 1950. *Quart. J. Roy. Meteor. Soc.*, **147**, 4186–4227, <https://doi.org/10.1002/qj.4174>.
- Bellouin, N., and Coauthors, 2020: Radiative forcing of climate change from the Copernicus reanalysis of atmospheric composition. *Earth Syst. Sci. Data*, **12**, 1649–1677, <https://doi.org/10.5194/essd-12-1649-2020>.
- Benson, B., J. Magnuson, and S. Sharma, 2000: Global Lake and River Ice Phenology Database, version 1. National Snow and Ice Data Center, accessed 1 February 2023, <https://doi.org/10.7265/N5W66HP8>.
- Benson, D. O., and P. A. Dirmeyer, 2021: Characterizing the relationship between temperature and soil moisture extremes and their role in the exacerbation of heat waves over the contiguous United States. *J. Climate*, **34**, 2175–2187, <https://doi.org/10.1175/JCLI-D-20-0440.1>.
- Biancamaria, S., D. P. Lettenmaier, and T. M. Pavelsky, 2016: The SWOT mission and its capabilities for land hydrology. *Remote Sensing and Water Resources*, A. Cazenave et al., Eds., Springer, 117–147, https://doi.org/10.1007/978-3-319-32449-4_6.
- Birkett, C. M., and B. Beckley, 2010: Investigating the performance of the Jason-2/OSTM radar altimeter over lakes and reservoirs. *Mar. Geod.*, **33**, 204–238, <https://doi.org/10.1080/01490419.2010.488983>.
- , K. O'Brien, S. Kinsey, M. Ricko, and Y. Li, 2022: Enhancement of a global lake and reservoir database to aid climate studies and resource monitoring utilizing satellite radar altimetry. *J. Great Lakes Res.*, **48**, 37–51, <https://doi.org/10.1016/j.jglr.2021.11.013>.
- Biskaborn, B. K., and Coauthors, 2019: Permafrost is warming at a global scale. *Nat. Commun.*, **10**, 264, <https://doi.org/10.1038/s41467-018-08240-4>.
- Bjerknes, J., 1969: Atmospheric teleconnections from the equatorial Pacific. *Mon. Wea. Rev.*, **97**, 163–172, [https://doi.org/10.1175/1520-0493\(1969\)097<2.3.CO;2](https://doi.org/10.1175/1520-0493(1969)097<2.3.CO;2).
- Blakeslee, R. J., and Coauthors, 2020: Three years of the Lightning Imaging Sensor onboard the International Space Station: Expanded global coverage and enhanced applications. *J. Geophys. Res. Atmos.*, **125**, e2020JD032918, <https://doi.org/10.1029/2020JD032918>.
- Blunden, J., and T. Boyer, Eds., 2022: "State of the Climate in 2021." *Bull. Amer. Meteor. Soc.*, **103** (8) Si–S465, <https://doi.org/10.1175/2022BAMSStateoftheClimate.1>.
- Bock, O., 2022: Global GNSS integrated water vapour data, 1994–2022. AERIS, accessed 24 July 2023, <https://doi.org/10.25326/68>.
- Bourassa, A. E., D. J. Zawada, L. A. Rieger, T. W. Warnock, M. Toohey, and D. A. Degenstein, 2023: Tomographic retrievals of Hunga Tonga-Hunga Ha'apai volcanic aerosol. *Geophys. Res. Lett.*, **50**, e2022GL101978, <https://doi.org/10.1029/2022GL101978>.
- Brohan, P., J. J. Kennedy, I. Harris, S. F. Tett, and P. D. Jones, 2006: Uncertainty estimates in regional and global observed temperature changes: A new data set from 1850. *J. Geophys. Res.*, **111**, D12106, <https://doi.org/10.1029/2005JD006548>.
- Bruick, Z. S., K. L. Rasmussen, A. K. Rowe, and L. A. McMurdie, 2019: Characteristics of intense convection in subtropical South America as influenced by El Niño–Southern Oscillation. *Mon. Wea. Rev.*, **147**, 1947–1966, <https://doi.org/10.1175/MWR-D-18-0342.1>.
- Brutsaert, W., 2017: Global land surface evaporation trend during the past half century: Corroboration by Clausius-Clapeyron scaling. *Adv. Water Resour.*, **106**, 3–5, <https://doi.org/10.1016/j.advwatres.2016.08.014>.
- Bureau of Meteorology, 2023: Daily rainfall extremes graph(s) for Australia. Accessed 7 February 2023, http://www.bom.gov.au/cgi-bin/climate/extremes/extreme_graphs_annual.cgi?graph=rain&year=2022&area=qld&percent=99.
- Capotondi, A., and Coauthors, 2015: Understanding ENSO diversity. *Bull. Amer. Meteor. Soc.*, **96**, 921–938, <https://doi.org/10.1175/BAMS-D-13-00117.1>.
- Carn, S. A., N. A. Krotkov, B. L. Fisher, and C. Li, 2022: Out of the blue: Volcanic SO₂ emissions during the 2021–2022 eruptions of Hunga Tonga—Hunga Ha'apai (Tonga). *Front. Earth Sci.*, **10**, 976962, <https://doi.org/10.3389/feart.2022.976962>.
- Carr, J. L., Á. Horváth, D. L. Wu, and M. D. Friberg, 2022: Stereo plume height and motion retrievals for the record-setting Hunga Tonga-Hunga Ha'apai eruption of 15 January 2022. *Geophys. Res. Lett.*, **49**, e2022GL098131, <https://doi.org/10.1029/2022GL098131>.
- Carrea, L., O. Embury, and C. J. Merchant, 2015: Datasets related to in-land water for limnology and remote sensing applications: Distance-to-land, distance-to-water, water-body identifier and lake-centre co-ordinates. *Geosci. Data J.*, **2**, 83–97, <https://doi.org/10.1002/gdj3.32>.
- , and Coauthors, 2020: Lake surface temperature [in "State of the Climate in 2019"]. *Bull. Amer. Meteor. Soc.*, **101** (8), S26–S28, <https://doi.org/10.1175/BAMS-D-20-0104.1>.
- , C. Merchant, B. Calmettes, and J.-F. Cretaux, 2021: Lake surface water temperature [in "State of the Climate in 2020"]. *Bull. Amer. Meteor. Soc.*, **102** (8), S28–S31, <https://doi.org/10.1175/BAMS-D-21-0098.1>.
- , —, and R. I. Woolway, 2022a: Lake surface water temperature [in "State of the Climate in 2021"]. *Bull. Amer. Meteor. Soc.*, **103** (8), S28–S30, <https://doi.org/10.1175/BAMS-D-22-0092.1>.
- , and Coauthors, 2022b: ESA Lakes Climate Change Initiative (Lakes_cci): Lake products, version 2.0.2. NERC EDS Centre for Environmental Data Analysis, accessed 24 July 2023, <https://doi.org/10.5285/a07deacaffb8453e93d57ee214676304>.
- , and Coauthors, 2023: Satellite-derived multivariate worldwide lake physical variable timeseries for climate studies. *Sci. Data*, **10**, 30, <https://doi.org/10.1038/s41597-022-01889-z>.
- Cescatti, A., and Coauthors, 2012: Intercomparison of MODIS albedo retrievals and in situ measurements across the global FLUXNET network. *Remote Sens. Environ.*, **121**, 323–334, <https://doi.org/10.1016/j.rse.2012.02.019>.

- Chang, K.-L., M. G. Schultz, X. Lan, A. McClure-Begley, I. Petropavlovskikh, X. Xu, and J. R. Ziemke, 2021: Trend detection of atmospheric time series: Incorporating appropriate uncertainty estimates and handling extreme events. *Elementa*, **9**, 00035, <https://doi.org/10.1525/elementa.2021.00035>.
- , and Coauthors, 2022: Impact of the COVID-19 economic downturn on tropospheric ozone trends: An uncertainty weighted data synthesis for quantifying regional anomalies above western North America and Europe. *AGU Adv.*, **3**, e2021AV000542, <https://doi.org/10.1029/2021AV000542>.
- Chen, C., and Coauthors, 2019: China and India lead in greening of the world through land-use management. *Nat. Sustainability*, **2**, 122–129, <https://doi.org/10.1038/s41893-019-0220-7>.
- Cheng, L., and Coauthors, 2017: Recent increases in terrestrial carbon uptake at little cost to the water cycle. *Nat. Commun.*, **8**, 110, <https://doi.org/10.1038/s41467-017-00114-5>.
- Christiansen, A., L. J. Mickley, J. Liu, L. D. Oman, and L. Hu, 2022: Multidecadal increases in global tropospheric ozone derived from ozonesonde and surface site observations: Can models reproduce ozone trends? *Atmos. Chem. Phys.*, **22**, 14751–14782, <https://doi.org/10.5194/acp-22-14751-2022>.
- Christy, J. R., and R. T. McNider, 2017: Satellite bulk tropospheric temperatures as a metric for climate sensitivity. *Asia-Pac. J. Atmos. Sci.*, **53**, 511–518, <https://doi.org/10.1007/s13143-017-0070-z>.
- Chrysoulakis, N., Z. Mitraka, and N. Gorelick, 2019: Exploiting satellite observations for global surface albedo trends monitoring. *Theor. Appl. Climatol.*, **137**, 1171–1179, <https://doi.org/10.1007/s00704-018-2663-6>.
- Chung, E.-S., B. Soden, and V. O. John, 2013: Intercalibrating microwave satellite observations for monitoring long-term variations in upper- and midtropospheric water vapor. *J. Atmos. Oceanic Technol.*, **30**, 2303–2319, <https://doi.org/10.1175/JTECH-D-13-00001.1>.
- , —, B. J. Sohn, and L. Shi, 2014: Upper-tropospheric moistening in response to anthropogenic warming. *Proc. Natl. Acad. Sci. USA*, **111**, 11636–11641, <https://doi.org/10.1073/pnas.1409659111>.
- Cicoira, A., J. Beutel, J. Faillettaz, and A. Vieli, 2019: Water controls the seasonal rhythm of rock glacier flow. *Earth Planet. Sci. Lett.*, **528**, 115844, <https://doi.org/10.1016/j.epsl.2019.115844>.
- Clem, K. R., and R. L. Fogt, 2013: Varying roles of ENSO and SAM on the Antarctic Peninsula climate in austral spring. *J. Geophys. Res. Atmos.*, **118**, 11481–11492, <https://doi.org/10.1002/jgrd.50860>.
- Coddington, O. M., 2017: TSIS Algorithm Theoretical Basis Document. Laboratory for Atmospheres and Space Physics (LASP) Document 151430 RevA, 108 pp., https://docserver.gesdisc.eosdis.nasa.gov/public/project/TSIS/TSIS_Algorithm_Theoretical_Basis_Document_151430RevA.pdf.
- Coldewey-Egbers, M., and Coauthors, 2015: The GOME-type Total Ozone Essential Climate Variable (GTO-ECV) data record from the ESA Climate Change Initiative. *Atmos. Meas. Tech.*, **8**, 3923–3940, <https://doi.org/10.5194/amt-8-3923-2015>.
- , D. G. Loyola, C. Lerot, and M. Van Roozendaal, 2022: Global, regional and seasonal analysis of total ozone trends derived from the 1995–2020 GTO-ECV climate data record. *Atmos. Chem. Phys.*, **22**, 6861–6878, <https://doi.org/10.5194/acp-22-6861-2022>.
- Coleman, R., and B. J. Soden, 2021: Water vapor and lapse rate feedbacks in the climate system. *Rev. Mod. Phys.*, **93**, 045002, <https://doi.org/10.1103/RevModPhys.93.045002>.
- Cooper, O. R., and Coauthors, 2020: Multi-decadal surface ozone trends at globally distributed remote locations. *Elementa*, **8**, 23, <https://doi.org/10.1525/elementa.420>.
- Copernicus, 2023a: 2022 Global Climate Highlights of the Copernicus Climate Change Service (C3S). Accessed 6 February 2023, <https://climate.copernicus.eu/global-climate-highlights-2022>.
- Cornes, R. C., E. C. Kent, D. I. Berry, and J. J. Kennedy, 2020: CLASSnmat: A global night marine air temperature data set, 1880–2019. *Geosci. Data J.*, **7**, 170–184, <https://doi.org/10.1002/gdj3.100>.
- , T. Cropper, R. Junod, and E. C. Kent, 2022: Night marine air temperature [in “State of the Climate in 2021”]. *Bull. Amer. Meteor. Soc.*, **103** (8), S31–S33, <https://doi.org/10.1175/BAMS-D-22-0092.1>.
- Cortés, J., M. D. Mahecha, M. Reichstein, R. B. Myneni, C. Chen, and A. Brenning, 2021: Where are global vegetation greening and browning trends significant? *Geophys. Res. Lett.*, **48**, e2020GL091496, <https://doi.org/10.1029/2020GL091496>.
- Coy, L., P. A. Newman, K. Wargan, G. Partyka, S. E. Strahan, and S. Pawson, 2022: Stratospheric circulation changes associated with the Hunga Tonga-Hunga Ha’apai eruption. *Geophys. Res. Lett.*, **49**, e2022GL100982, <https://doi.org/10.1029/2022GL100982>.
- Cremona, A., M. Huss, J. Landmann, J. Borner, and D. Farinotti, 2023: European heat waves 2022: Contribution to extreme glacier melt in Switzerland inferred from automated ablation readings. *Cryosphere*, **17**, 1895–1912, <https://doi.org/10.5194/tc-17-1895-2023>.
- Crétau, J. F., and Coauthors, 2011: SOLS: A lake database to monitor in the near real time water level and storage variations from remote sensing data. *Adv. Space Res.*, **47**, 1497–1507, <https://doi.org/10.1016/j.asr.2011.01.004>.
- Crimmins, T. M., E. G. Denny, E. E. Posthumus, A. H. Rosemartin, R. Croll, M. Montano, and H. Panci, 2022: Science and management advancements made possible by the USA National Phenology Network’s Nature’s Notebook platform. *BioScience*, **72**, 908–920, <https://doi.org/10.1093/biosci/biac061>.
- Cusicanqui, D., A. Rabatel, C. Vincent, X. Bodin, E. Thibert, and B. Francou, 2021: Interpretation of volume and flux changes of the Laurichard rock glacier between 1952 and 2019, French Alps. *J. Geophys. Res. Earth Surf.*, **126**, e2021JF006161, <https://doi.org/10.1029/2021JF006161>.
- Daniel, J. S., S. Solomon, and D. L. Albritton, 1995: On the evaluation of halocarbon radiative forcing and global warming potentials. *J. Geophys. Res.*, **100**, 1271–1285, <https://doi.org/10.1029/94JD02516>.
- Davidson, E. A., 2009: The contribution of manure and fertilizer nitrogen to atmospheric nitrous oxide since 1860. *Nat. Geosci.*, **2**, 659–662, <https://doi.org/10.1038/ngeo608>.
- Davis, S. M., and Coauthors, 2016: The Stratospheric Water and Ozone Satellite Homogenized (SWOOSH) database: A long-term database for climate studies. *Earth Syst. Sci. Data*, **8**, 461–490, <https://doi.org/10.5194/essd-8-461-2016>.
- Dee, D. P., and Coauthors, 2011: The ERA-Interim reanalysis: Configuration and performance of the data assimilation system. *Quart. J. Roy. Meteor. Soc.*, **137**, 553–597, <https://doi.org/10.1002/qj.828>.
- Deeter, M. N., and Coauthors, 2014: The MOPITT version 6 product: Algorithm enhancements and validation. *Atmos. Meas. Tech.*, **7**, 3623–3632, <https://doi.org/10.5194/amt-7-3623-2014>.

- , D. P. Edwards, G. L. Francis, J. C. Gille, S. Martínez-Alonso, H. M. Worden, and C. Sweeney, 2017: A climate-scale satellite record for carbon monoxide: The MOPITT version 7 product. *Atmos. Meas. Tech.*, **10**, 2533–2555, <https://doi.org/10.5194/amt-10-2533-2017>.
- , and Coauthors, 2019: Radiance-based retrieval bias mitigation for the MOPITT instrument: The version 8 product. *Atmos. Meas. Tech.*, **12**, 4561–4580, <https://doi.org/10.5194/amt-12-4561-2019>.
- Delaloye, R., and Coauthors, 2008: Recent interannual variations of rock glacier creep in the European Alps. *Proc. Ninth Int. Conf. on Permafrost*, Fairbanks, AK, University of Alaska Fairbanks, 343–348.
- , C. Lambiel, and I. Gärtner-Roer, 2010: Overview of rock glacier kinematics research in the Swiss Alps. *Geogr. Helv.*, **65**, 135–145, <https://doi.org/10.5194/gh-65-135-2010>.
- Deng, K., C. Azorin-Molina, S. Yang, C. Hu, G. Zhang, L. Minola, and D. Chen, 2022: Changes of Southern Hemisphere westerlies in the future warming climate. *Atmos. Res.*, **270**, 106040, <https://doi.org/10.1016/j.atmosres.2022.106040>.
- Dewitte, S., D. Crommelynck, and A. Joukof, 2004: Total solar irradiance observations from DIARAD/VIRGO. *J. Geophys. Res.*, **109**, A02102, <https://doi.org/10.1029/2002JA009694>.
- Dlugokencky, E. J., L. P. Steele, P. M. Lang, and K. A. Masarie, 1994: The growth rate and distribution of atmospheric methane. *J. Geophys. Res. Atmos.*, **99**(D8), 17 021–17 043, <https://doi.org/10.1029/94JD01245>.
- Domeisen, D. I. V., C. I. Garfinkel, and A. H. Butler, 2019: The teleconnection of El Niño Southern Oscillation to the stratosphere. *Rev. Geophys.*, **57**, 5–47, <https://doi.org/10.1029/2018RG000596>.
- Donat, M. G., L. V. Alexander, H. Yang, I. Durre, R. Vose, and J. Caesar, 2013: Global land-based datasets for monitoring climatic extremes. *Bull. Amer. Meteor. Soc.*, **94**, 997–1006, <https://doi.org/10.1175/BAMS-D-12-00109.1>.
- Dorigo, W., and Coauthors, 2017: ESA CCI soil moisture for improved Earth system understanding: State-of-the art and future directions. *Remote Sens. Environ.*, **203**, 185–215, <https://doi.org/10.1016/j.rse.2017.07.001>.
- , and Coauthors, 2021a: Closing the water cycle from observations across scales: Where do we stand? *Bull. Amer. Meteor. Soc.*, **102**, E1897–E1935, <https://doi.org/10.1175/BAMS-D-19-0316.1>.
- , L. Moesinger, R. van der Schalie, R. M. Zotta, T. Scanlon, and R. A. M. de Jeu, 2021b: Long-term monitoring of vegetation state through passive microwave satellites [in “State of the Climate in 2020”]. *Bull. Amer. Meteor. Soc.*, **102** (8), S110–S112, <https://doi.org/10.1175/BAMS-D-21-0098.1>.
- , R. Zotta, R. van der Schalie, W. Preimesberger, L. Moesinger, and R. A. M. de Jeu, 2022: Vegetation optical depth [in “State of the Climate in 2021”]. *Bull. Amer. Meteor. Soc.*, **103** (8), S108–S109, <https://doi.org/10.1175/BAMS-D-22-0092.1>.
- Dunn, R. J. H., 2019: HadISD version 3: Monthly updates. Hadley Centre Tech. Note 103, 10 pp., <http://www.metoffice.gov.uk/research/library-and-archive/publications/science/climate-science-technical-notes>.
- , and C. P. Morice, 2022: On the effect of reference periods on trends in percentile-based extreme temperature indices. *Environ. Res. Lett.*, **17**, 034026, <https://doi.org/10.1088/1748-9326/ac52c8>.
- , K. M. Willett, P. W. Thorne, E. V. Woolley, I. Durre, A. Dai, D. E. Parker, and R. S. Vose, 2012: HadISD: A quality-controlled global synoptic report database for selected variables at long-term stations from 1973–2011. *Climate Past*, **8**, 1649–1679, <https://doi.org/10.5194/cp-8-1649-2012>.
- , —, C. P. Morice, and D. E. Parker, 2014: Pairwise homogeneity assessment of HadISD. *Climate Past*, **10**, 1501–1522, <https://doi.org/10.5194/cp-10-1501-2014>.
- , —, D. E. Parker, and L. Mitchell, 2016: Expanding HadISD: Quality-controlled, sub-daily station data from 1931. *Geosci. Instrum. Methods Data Syst.*, **5**, 473–491, <https://doi.org/10.5194/gi-5-473-2016>.
- , and Coauthors, 2020: Development of an updated global land in situ-based data set of temperature and precipitation extremes: HadEX3. *J. Geophys. Res. Atmos.*, **125**, e2019JD032263, <https://doi.org/10.1029/2019JD032263>.
- , M. G. Donat, and L. V. Alexander, 2022a: Comparing extremes indices in recent observational and reanalysis products. *Front. Climate*, **4**, 989505, <https://doi.org/10.3389/fclim.2022.989505>.
- , C. Azorin-Molina, M. J. Menne, Z. Zeng, N. W. Casey, and C. Shen, 2022b: Reduction in reversal of global stilling arising from correction to encoding of calm periods. *Environ. Res. Commun.*, **4**, 061003, <https://doi.org/10.1088/2515-7620/ac770a>.
- ECMWF, 2022: Pakistan devastated by August floods. Copernicus Climate Change Service, accessed 24 January 2023, <https://climate.copernicus.eu/pakistan-devastated-august-floods>.
- Edwards, M., and A. Richardson, 2004: Impact of climate change on marine pelagic phenology and trophic mismatch. *Nature*, **430**, 881–884, <https://doi.org/10.1038/nature02808>.
- Ellis, H. T., and R. F. Pueschel, 1971: Solar radiation: Absence of air pollution trends at Mauna Loa. *Science*, **172**, 845–846, <https://doi.org/10.1126/science.172.3985.845>.
- Eriksen, H. Ø., L. Rouyet, T. R. Lauknes, I. Berthling, K. Isaksen, H. Hindberg, Y. Larsen, and G. D. Corner, 2018: Recent acceleration of a rock glacier complex, Ådjet, Norway, documented by 62 years of remote sensing observations. *Geophys. Res. Lett.*, **45**, 8314–8323, <https://doi.org/10.1029/2018GL077605>.
- Estilow, T. W., A. H. Young, and D. A. Robinson, 2015: A long-term Northern Hemisphere snow cover extent data record for climate studies and monitoring. *Earth Syst. Sci. Data*, **7**, 137–142, <https://doi.org/10.5194/essd-7-137-2015>.
- Etheridge, D. M., L. P. Steele, R. L. Langenfelds, R. J. Francey, J. M. Barnola, and V. I. Morgan, 1996: Natural and anthropogenic changes in atmospheric CO₂ over the last 1000 years from air in Antarctic ice and firn. *J. Geophys. Res.*, **101**, 4115–4128, <https://doi.org/10.1029/95JD03410>.
- Etzelmüller, B., and Coauthors, 2020: Twenty years of European mountain permafrost dynamics—The PACE legacy. *Environ. Res. Lett.*, **15**, 104070, <https://doi.org/10.1088/1748-9326/abae9d>.
- Eyring, V., and Coauthors, 2021: Human influence on the climate system. *Climate Change 2021: The Physical Science Basis*, V. Masson-Delmotte et al., Eds., Cambridge University Press, 423–552, <https://doi.org/10.1017/9781009157896.005>.
- Fan, J., and Coauthors, 2018: Substantial convection and precipitation enhancements by ultrafine aerosol particles. *Science*, **359**, 411–418, <https://doi.org/10.1126/science.aan8461>.
- FAO, 2022: Crop prospects and food situation. Quarterly Global Rep. 4, 46 pp., <https://www.fao.org/3/cc3233en/cc3233en.pdf>.

- Fasullo, J. T., J.-F. Lamarque, C. Hannay, N. Rosenbloom, S. Tilmes, P. DeRepentigny, A. Jahn, and C. Deser, 2022: Spurious late historical-era warming in CESM2 driven by prescribed biomass burning emissions. *Geophys. Res. Lett.*, **49**, e2021GL097420, <https://doi.org/10.1029/2021GL097420>.
- Feng, L., P. I. Palmer, S. Zhu, R. J. Parker, and Y. Liu, 2022: Tropical methane emissions explain large fraction of recent changes in global atmospheric methane growth rate. *Nat. Commun.*, **13**, 1378, <https://doi.org/10.1038/s41467-022-28989-z>.
- Fioletov, V. E., G. E. Bodeker, A. J. Miller, R. D. McPeters, and R. Stolarski, 2002: Global and zonal total ozone variations estimated from ground-based and satellite measurements: 1964–2000. *J. Geophys. Res.*, **107**, 4647, <https://doi.org/10.1029/2001JD001350>.
- , and Coauthors, 2008: The performance of the ground-based total ozone network assessed using satellite data. *J. Geophys. Res.*, **113**, D14313, <https://doi.org/10.1029/2008JD009809>.
- Fiore, A. M., and Coauthors, 2022: Understanding recent tropospheric ozone trends in the context of large internal variability: A new perspective from chemistry-climate model ensembles. *Environ. Res. Climate*, **1**, 025008, <https://doi.org/10.1088/2752-5295/ac9cc2>.
- Fogt, R. L., and G. J. Marshall, 2020: The Southern Annular Mode: Variability, trends, and climate impacts across the Southern Hemisphere. *Wiley Interdiscip. Rev.: Climate Change*, **11**, e652, <https://doi.org/10.1002/wcc.652>.
- Folland, C. K., J. Knight, H. W. Linderholm, D. Fereday, S. Ineson, and J. W. Hurrell, 2009: The summer North Atlantic Oscillation: Past, present and future. *J. Climate*, **22**, 1082–1103, <https://doi.org/10.1175/2008JCLI2459.1>.
- Foster, M. J., C. Phillips, A. K. Heidinger, E. E. Borbas, Y. Li, W. P. Menzel, A. Walther, and E. Weisz, 2023: PATMOS-x version 6.0: 40 years of merged AVHRR and HIRS global cloud data. *J. Climate*, **36**, 1143–1160, <https://doi.org/10.1175/JCLI-D-22-0147.1>.
- Forster, P. M. F., and K. P. Shine, 1999: Stratospheric water vapour changes as a possible contributor to observed stratospheric cooling. *Geophys. Res. Lett.*, **26**, 3309–3312, <https://doi.org/10.1029/1999GL010487>.
- , and Coauthors, 2021: The Earth's energy budget, climate feedbacks, and climate sensitivity. *Climate Change 2021: The Physical Science Basis*, V. Masson-Delmotte et al., Eds., Cambridge University Press, 923–1054, <https://doi.org/10.1017/9781009157896.009>.
- Frauenfelder, R., W. Haeblerli, and M. Hoelzle, 2003: Rock glacier occurrence and related terrain parameters in a study area of the Eastern Swiss Alps. *Permafrost: Proceedings of the 8th International Conference on Permafrost*, M. Phillips, S. M. Springman, and L. U. Arenson, Eds., A. A. Balkema, 253–258.
- Free, M., D. J. Seidel, J. K. Angel, J. Lanzante, I. Durre, and T. C. Peterson, 2005: Radiosonde Atmospheric Temperature Products for Assessing Climate (RATPAC): A new dataset of large-area anomaly time series. *J. Geophys. Res.*, **110**, D22101, <https://doi.org/10.1029/2005JD006169>.
- Freychet, N., S. F. B. Tett, Z. Yan, and Z. Li, 2020: Underestimated change of wet-bulb temperatures over East and South China. *Geophys. Res. Lett.*, **47**, e2019GL086140, <https://doi.org/10.1029/2019GL086140>.
- Friedlingstein, P., and Coauthors, 2022: Global carbon budget 2022. *Earth Syst. Sci. Data*, **14**, 4811–4900, <https://doi.org/10.5194/essd-14-4811-2022>.
- Friedrich, K., and Coauthors, 2018: Reservoir evaporation in the western United States: Current science, challenges, and future needs. *Bull. Amer. Meteor. Soc.*, **99**, 167–187, <https://doi.org/10.1175/BAMS-D-15-00224.1>.
- Frith, S. M., N. A. Kramarova, R. S. Stolarski, R. D. McPeters, P. K. Bhartia, and G. J. Labow, 2014: Recent changes in total column ozone based on the SBUV version 8.6 Merged Ozone Data Set. *J. Geophys. Res. Atmos.*, **119**, 9735–9751, <https://doi.org/10.1002/2014JD021889>.
- , R. S. Stolarski, N. A. Kramarova, and R. D. McPeters, 2017: Estimating uncertainties in the SBUV version 8.6 merged profile ozone data set. *Atmos. Chem. Phys.*, **17**, 14695–14707, <https://doi.org/10.5194/acp-17-14695-2017>.
- Füllekrug, M., E. Williams, C. Price, S. Goodman, R. Holzworth, K. Virts, and D. Buechler, 2022: Sidebar 2.1 lightning [in “State of the Climate in 2021”]. *Bull. Amer. Meteor. Soc.*, **103** (8), S79–S81, <https://doi.org/10.1175/BAMS-D-22-0092.1>.
- Funk, C., and Coauthors, 2015: The climate hazards infrared precipitation with stations—A new environmental record for monitoring extremes. *Sci. Data*, **2**, 150066, <https://doi.org/10.1038/sdata.2015.66>.
- Garane, K., and Coauthors, 2018: Quality assessment of the Ozone_cci Climate Research Data Package (release 2017) – Part 1: Ground-based validation of total ozone column data products. *Atmos. Meas. Tech.*, **11**, 1385–1402, <https://doi.org/10.5194/amt-11-1385-2018>.
- Garfinkel, C. I., and Coauthors, 2021: Influence of the El Niño–Southern Oscillation on entry stratospheric water vapor in coupled chemistry–ocean CCM1 and CMIP6 models. *Atmos. Chem. Phys.*, **21**, 3725–3740, <https://doi.org/10.5194/acp-21-3725-2021>.
- Garreaud, R. D., K. Clem, and J. V. Veloso, 2021: The South Pacific pressure trend dipole and the Southern Blob. *J. Climate*, **34**, 7661–7676, <https://doi.org/10.1175/JCLI-D-20-0886.1>.
- Gaudel, A., and Coauthors, 2018: Tropospheric Ozone Assessment Report: Present-day distribution and trends of tropospheric ozone relevant to climate and global atmospheric chemistry model evaluation. *Elem. Sci. Anthropocene*, **6**, 39, <https://doi.org/10.1525/elementa.291>.
- , and Coauthors, 2020: Aircraft observations since the 1990s reveal increases of tropospheric ozone at multiple locations across the Northern Hemisphere. *Sci. Adv.*, **6**, eaba8272, <https://doi.org/10.1126/sciadv.aba8272>.
- GCOS, 2016: The Global Observing System for Climate: Implementation needs. Tech. Rep. GCOS-200, World Meteorological Organization, 315 pp., https://library.wmo.int/doc_num.php?explnum_id=3417.
- , 2022a: The 2022 Global Climate Observing System (GCOS) implementation plan. GCOS-244, WMO, 98 pp., <https://gcos.wmo.int/en/publications/gcos-implementation-plan2022>.
- , 2022b: The 2022 GCOS ECVs requirements. GCOS-245, WMO, 244 pp., https://library.wmo.int/doc_num.php?explnum_id=11318.
- Gelaro, R., and Coauthors, 2017: The Modern-Era Retrospective Analysis for Research and Applications, version 2 (MERRA-2). *J. Climate*, **30**, 5419–5454, <https://doi.org/10.1175/JCLI-D-16-0758.1>.
- Getirana, A., S. Kumar, M. Giroto, and M. Rodell, 2017: Rivers and floodplains as key components of global terrestrial water storage variability. *Geophys. Res. Lett.*, **44**, 10359–10368, <https://doi.org/10.1002/2017GL074684>.

- Giglio, L., W. Schroeder, and C. O. Justice, 2016: The Collection 6 MODIS active fire detection algorithm and fire products. *Remote Sens. Environ.*, **178**, 31–41, <https://doi.org/10.1016/j.rse.2016.02.054>.
- GISTEMP Team, 2022: GISS Surface Temperature Analysis (GISTEMP), v4. NASA Goddard Institute for Space Studies, accessed 15 February 2022, <https://data.giss.nasa.gov/gistemp/>.
- , 2023: GISS Surface Temperature Analysis (GISTEMP), v4. NASA Goddard Institute for Space Studies, accessed 1 March 2023, <https://data.giss.nasa.gov/gistemp/>.
- Gleason, K. L., J. H. Lawrimore, D. H. Levinson, T. R. Karl, and D. J. Karoly, 2008: A revised U.S. Climate Extremes Index. *J. Climate*, **21**, 2124–2137, <https://doi.org/10.1175/2007JCLI1883.1>.
- Gobron, N., 2019: Terrestrial vegetation dynamics [in “State of the Climate in 2018”]. *Bull. Amer. Meteor. Soc.*, **100** (9), S63–S64, <https://doi.org/10.1175/2019BAMSStateoftheClimate.1>.
- , and M. Robustelli, 2013: Monitoring the state of the global terrestrial surfaces. *Proc. 2013 ESA Living Planet Symp.*, Edinburgh, United Kingdom, European Space Agency, JRC84937, <https://publications.jrc.ec.europa.eu/repository/handle/JRC84937>.
- , A. S. Belward, B. Pinty, and W. Knorr, 2010: Monitoring biosphere vegetation 1998–2009. *Geophys. Res. Lett.*, **37**, L15402, <https://doi.org/10.1029/2010GL043870>.
- Godin-Beekmann, S., and Coauthors, 2022: Updated trends of the stratospheric ozone vertical distribution in the 60°S–60°N latitude range based on the LOTUS regression model. *Atmos. Chem. Phys.*, **22**, 11 657–11 673, <https://doi.org/10.5194/acp-22-11657-2022>.
- Gonsamo, A., and Coauthors, 2021: Greening drylands despite warming consistent with carbon dioxide fertilization effect. *Global Change Biol.*, **27**, 3336–3349, <https://doi.org/10.1111/gcb.15658>.
- Goodman, S. J., and D. R. MacGorman, 1986: Cloud-to-ground lightning activity in mesoscale convective complexes. *Mon. Wea. Rev.*, **114**, 2320–2328, [https://doi.org/10.1175/1520-0493\(1986\)114<2320.CO;2](https://doi.org/10.1175/1520-0493(1986)114<2320.CO;2).
- , D. E. Buechler, K. Knupp, D. Driscoll, and E. E. McCaul Jr., 2000: The 1997–98 El Niño event and related wintertime lightning variations in the southeastern United States. *Geophys. Res. Lett.*, **27**, 541–544, <https://doi.org/10.1029/1999GL010808>.
- Granier, C., and Coauthors, 2011: Evolution of anthropogenic and biomass burning emissions of air pollutants at global and regional scales during the 1980–2010 period. *Climatic Change*, **109**, 163–190, <https://doi.org/10.1007/s10584-011-0154-1>.
- Grant, L., and Coauthors, 2021: Attribution of global lake systems change to anthropogenic forcing. *Nat. Geosci.*, **14**, 849–854, <https://doi.org/10.1038/s41561-021-00833-x>.
- Gruber, A., W. A. Dorigo, W. Crow, and W. Wagner, 2017: Triple collocation-based merging of satellite soil moisture retrievals. *IEEE Trans. Geosci. Remote Sens.*, **55**, 6780–6792, <https://doi.org/10.1109/TGRS.2017.2734070>.
- , T. Scanlon, R. van der Schalie, W. Wagner, and W. Dorigo, 2019: Evolution of the ESA CCI Soil Moisture climate data records and their underlying merging methodology. *Earth Syst. Sci. Data*, **11**, 717–739, <https://doi.org/10.5194/essd-11-717-2019>.
- Gulev, S. K., and Coauthors, 2021: Changing state of the climate system. *Climate Change 2021: The Physical Science Basis*, V. Masson-Delmotte et al., Eds., Cambridge University Press, 287–422, <https://doi.org/10.1017/9781009157896.004>.
- Guo, S., G. J. S. Bluth, W. I. Rose, I. M. Watson, and A. J. Prata, 2004: Re-evaluation of SO₂ release of the 15 June 1991 Pinatubo eruption using ultraviolet and infrared satellite sensors. *Geochem. Geophys. Geosyst.*, **5**, Q04001, <https://doi.org/10.1029/2003GC000654>.
- Haimberger, L., C. Tavalato, and S. Sperka, 2012: Homogenization of the global radiosonde temperature dataset through combined comparison with reanalysis background series and neighboring stations. *J. Climate*, **25**, 8108–8131, <https://doi.org/10.1175/JCLI-D-11-00668.1>.
- Hamid, E. Y., Z.-I. Kawasaki, and R. Mardiana, 2001: Impact of the 1997–98 El Niño events on lightning activity over Indonesia. *Geophys. Res. Lett.*, **28**, 147–150, <https://doi.org/10.1029/2000GL011374>.
- Hansen, J., R. Ruedy, M. Sato, and K. Lo, 2010: Global surface temperature change. *Rev. Geophys.*, **48**, RG4004, <https://doi.org/10.1029/2010RG000345>.
- Harris, I., T. J. Osborn, P. D. Jones, and D. H. Lister, 2020: Version 4 of the CRU TS monthly high-resolution gridded multivariate climate dataset. *Sci. Data*, **7**, 109, <https://doi.org/10.1038/s41597-020-0453-3>.
- Heath, M., 2022: Arid wheat fields and dead cows: A snapshot of Argentina’s worst drought in decades. Reuters, 9 December, www.reuters.com/business/environment/arid-wheat-fields-dead-cows-snapshot-argentinas-worst-drought-decades-2022-12-09/.
- Hersbach, H., and Coauthors, 2020: The ERA5 global reanalysis. *Quart. J. Roy. Meteor. Soc.*, **146**, 1999–2049, <https://doi.org/10.1002/qj.3803>.
- , and Coauthors, 2023: ERA5 monthly averaged data on pressure levels from 1940 to present. Copernicus Climate Change Service Climate Data Store, accessed 14 June 2023, <https://doi.org/10.24381/cds.6860a573>.
- Ho, S.-P., X. Zhou, Y.-H. Kuo, D. Hunt, and J.-H. Wang, 2010: Global evaluation of radiosonde water vapor systematic biases using GPS radio occultation from COSMIC and ECMWF analysis. *Remote Sens.*, **2**, 1320–1330, <https://doi.org/10.3390/rs2051320>.
- , and Coauthors, 2020a: The COSMIC/FORMOSAT-3 radio occultation mission after 12 years: Accomplishments, remaining challenges, and potential impacts of COSMIC-2. *Bull. Amer. Meteor. Sci.*, **101**, E1107–E1136, <https://doi.org/10.1175/BAMS-D-18-0290.1>.
- , and Coauthors, 2020b: Initial assessment of the COSMIC-2/FORMOSAT-7 neutral atmosphere data quality in NESDIS/STAR using in situ and satellite data. *Remote Sens.*, **12**, 4099, <https://doi.org/10.3390/rs12244099>.
- Hobday, A. J., and Coauthors, 2016: A hierarchical approach to defining marine heatwaves. *Prog. Oceanogr.*, **141**, 227–238, <https://doi.org/10.1016/j.pocean.2015.12.014>.
- , and Coauthors, 2018: Categorizing and naming marine heatwaves. *Oceanography*, **31**, 162–173, <https://doi.org/10.5670/oceanog.2018.205>.
- Hodnebrog, O., and Coauthors, 2020a: Updated global warming potentials and radiative efficiencies of halocarbons and other weak atmospheric absorbers. *Rev. Geophys.*, **58**, e2019RG000691, <https://doi.org/10.1029/2019RG000691>.
- , and Coauthors, 2020b: The effect of rapid adjustments to halocarbons and N₂O on radiative forcing. *npj Climate Atmos. Sci.*, **3**, 43, <https://doi.org/10.1038/s41612-020-00150-x>.
- Hofmann, D. J., and S. A. Montzka, 2009: Recovery of the ozone layer: The ozone depleting gas index. *Eos, Trans. Amer. Geophys. Union*, **90**, 1–2, <https://doi.org/10.1029/2009EO010001>.

- , J. H. Butler, E. J. Dlugokencky, J. W. Elkins, K. Masarie, S. A. Montzka, and P. Tans, 2006: The role of carbon dioxide in climate forcing from 1979 to 2004: Introduction of the annual greenhouse gas index. *Tellus*, **58B**, 614–619, <https://doi.org/10.1111/j.1600-0889.2006.00201.x>.
- Hrudya, P. H., H. Varikoden, and R. Vishnu, 2021: A review on the Indian summer monsoon rainfall, variability and its association with ENSO and IOD. *Meteor. Atmos. Phys.*, **133**, 1–14, <https://doi.org/10.1007/s00703-020-00734-5>.
- Huang, B., C. Liu, V. Banzon, E. Freeman, G. Graham, B. Hankins, T. Smith, and H.-M. Zhang, 2021: Improvements of the Daily Optimum Interpolation Sea Surface Temperature (DOISST) version 2.1. *J. Climate*, **34**, 2923–2939, <https://doi.org/10.1175/JCLI-D-20-0166.1>.
- Huang, C.-Y., W.-H. Teng, S.-P. Ho, and Y. H. Kuo, 2013: Global variation of COSMIC precipitable water over land: Comparisons with ground-based GPS measurements and NCEP reanalyses. *Geophys. Res. Lett.*, **40**, 5327–5331, <https://doi.org/10.1002/grl.50885>.
- Hugonnet, R., and Coauthors, 2021: Accelerated global glacier mass loss in the early twenty-first century. *Nature*, **592**, 726–731, <https://doi.org/10.1038/s41586-021-03436-z>.
- Hüser, I., B. Gehrke, and J. W. Kaiser, 2018: Methodology to correct biases in individual satellite FRP products. CAMS Rep. CAMS44-2016SC3-D44.3.3.1-2018-20187, ECMWF, <https://atmosphere.copernicus.eu/node/1029t>.
- Ingram, W., 2010: A very simple model for the water vapour feedback on climate change. *Quart. J. Roy. Meteor. Soc.*, **136**, 30–40, <https://doi.org/10.1002/qj.546>.
- Inness, A., and Coauthors, 2019: The CAMS reanalysis of atmospheric composition. *Atmos. Chem. Phys.*, **19**, 3515–3556, <https://doi.org/10.5194/acp-19-3515-2019>.
- Isaksen, K., J. Lutz, A. M. Sørensen, Ø. Godøy, L. Ferrighi, S. Eastwood, and S. Aaboe, 2022: Advances in operational permafrost monitoring on Svalbard and in Norway. *Environ. Res. Lett.*, **17**, 095012, <https://doi.org/10.1088/1748-9326/ac8e1c>.
- Irtubide, M., and Coauthors, 2020: An update of IPCC climate reference regions for subcontinental analysis of climate model data: Definition and aggregated datasets. *Earth Syst. Sci. Data*, **12**, 2959–2970, <https://doi.org/10.5194/essd-12-2959-2020>.
- Jenkins, S., C. Smith, M. Allen, and R. Grainger, 2023: Tonga eruption increases chance of temporary surface temperature anomaly above 1.5°C. *Nat. Climate Change*, **13**, 127–129, <https://doi.org/10.1038/s41558-022-01568-2>.
- John, V. O., G. Holl, R. P. Allan, S. A. Buehler, D. E. Parker, and B. J. Soden, 2011: Clear-sky biases in satellite infra-red estimates of upper tropospheric humidity and its trends. *J. Geophys. Res.*, **116**, D14108, <https://doi.org/10.1029/2010JD015355>.
- Junod, R. A., and J. R. Christy, 2020: A new compilation of globally gridded night-time marine air temperatures: The UAHN-MATV1 dataset. *Int. J. Climatol.*, **40**, 2609–2623, <https://doi.org/10.1002/joc.6354>.
- Kääb, A., T. Strozzi, T. Bolch, R. Caduff, H. Trefall, M. Stoffel, and A. Kokarev, 2021: Inventory and changes of rock glacier creep speeds in Ile Alatau and Kungöy Ala-Too, northern Tien Shan, since the 1950s. *Cryosphere*, **15**, 927–949, <https://doi.org/10.5194/tc-15-927-2021>.
- Kablick, G. P., D. R. Allen, M. D. Fromm, and G. E. Nedoluha, 2020: Australian pyroCb smoke generates synoptic-scale stratospheric anticyclones. *Geophys. Res. Lett.*, **47**, e2020GL088101, <https://doi.org/10.1029/2020GL088101>.
- Kainz, M. J., R. Ptacnik, S. Rasconi, and H. H. Hager, 2017: Irregular changes in lake surface water temperature and ice cover in subalpine Lake Lunz, Austria. *Inland Waters*, **7**, 27–33, <https://doi.org/10.1080/20442041.2017.1294332>.
- Kaiser, J. W., and Coauthors, 2012: Biomass burning emissions estimated with a global fire assimilation system based on observed fire radiative power. *Biogeosciences*, **9**, 527–554, <https://doi.org/10.5194/bg-9-527-2012>.
- Kaplan, A., 2011: Patterns and indices of climate variability [in “State of the Climate in 2010”]. *Bull. Amer. Meteor. Soc.*, **92** (6), S20–S25, <https://doi.org/10.1175/1520-0477-92.6.S1>.
- Kaplan Pastíriková, L., F. Hrbacek, T. Uxa, and K. Laska, 2023: Permafrost table temperature and active layer thickness variability on James Ross Island, Antarctic Peninsula, in 2004–2021. *Sci. Total Environ.*, **869**, 161690, <https://doi.org/10.1016/j.scitotenv.2023.161690>.
- Karpechko, A. Y., and A. C. Maycock, 2018: Stratospheric ozone changes and climate. Scientific Assessment of Ozone Depletion: 2018. Global Ozone Research and Monitoring Project Rep. 58, 5.1–5.50, <https://ozone.unep.org/sites/default/files/2019-05/SAP-2018-Assessment-report.pdf>.
- Keeling, C. D., and R. Revelle, 1985: Effects of El-Nino Southern Oscillation on the atmospheric content of carbon-dioxide. *Meteoritics*, **20**, 437–450.
- Kellerer-Pirklbauer, A., and V. Kaufmann, 2012: About the relationship between rock glacier velocity and climate parameters in central Austria. *Aust. J. Earth Sci.*, **105**, 94–112.
- , and Coauthors, 2018: Interannual variability of rock glacier flow velocities in the European Alps. *Fifth European Conf. on Permafrost*, Chamonix, France, Laboratoire EDYTEM, 615–616, <https://hal.archives-ouvertes.fr/hal-01816115/>.
- Kendon, M., M. McCarthy, S. Jevrejeva, A. Matthews, T. Sparks, and J. Garforth, 2022: State of the UK climate 2021. *Int. J. Climatol.*, **42** (S1), 1–80, <https://doi.org/10.1002/joc.7787>.
- Kennedy, J. J., N. A. Rayner, C. P. Atkinson, and R. E. Killick, 2019: An ensemble data set of sea surface temperature change from 1850: The Met Office Hadley Centre HadSST.4.0.0.0 data set. *J. Geophys. Res. Atmos.*, **124**, 7719–7763, <https://doi.org/10.1029/2018JD029867>.
- Kenner, R., M. Phillips, J. Beutel, M. Hiller, P. Limpach, E. Pointner, and M. Volken, 2017: Factors controlling velocity variations at short-term, seasonal and multiyear time scales, Ritigraben rock glacier, western Swiss Alps. *Permafrost Periglacial Processes*, **28**, 675–684, <https://doi.org/10.1002/ppp.1953>.
- Khandelwal, A., A. Karpatne, P. Ravirathinam, R. Ghosh, Z. Wei, H. A. Dugan, P. C. Hanson, and V. Kumar, 2022: RealSAT, a global dataset of reservoir and lake surface area variations. *Sci. Data*, **9**, 356, <https://doi.org/10.1038/s41597-022-01449-5>.
- Khaykin, S., and Coauthors, 2022: Global perturbation of stratospheric water and aerosol burden by Hunga eruption. *Commun. Earth Environ.*, **3**, 316, <https://doi.org/10.1038/s43247-022-00652-x>.
- Khazaei, B., and Coauthors, 2019: Climatic or regionally induced by humans? Tracing hydro-climatic and land-use changes to better understand the Lake Urmia tragedy. *J. Hydrol.*, **569**, 203–217, <https://doi.org/10.1016/j.jhydrol.2018.12.004>.
- Kobayashi, S., and Coauthors, 2015: The JRA-55 reanalysis: General specifications and basic characteristics. *J. Meteor. Soc. Japan*, **93**, 5–48, <https://doi.org/10.2151/jmsj.2015-001>.

- Konapala, G., A. K. Mishra, Y. Wada, and M. E. Mann, 2020: Climate change will affect global water availability through compounding changes in seasonal precipitation and evaporation. *Nat. Commun.*, **11**, 3044, <https://doi.org/10.1038/s41467-020-16757-w>.
- Konings, A. G., Y. Yu, L. Xu, Y. Yang, D. S. Schimel, and S. S. Saatchi, 2017: Active microwave observations of diurnal and seasonal variations of canopy water content across the humid African tropical forests. *Geophys. Res. Lett.*, **44**, 2290–2299, <https://doi.org/10.1002/2016GL072388>.
- Kopp, G., and J. L. Lean, 2011: A new, lower value of total solar irradiance: Evidence and climate significance. *Geophys. Res. Lett.*, **38**, L01706, <https://doi.org/10.1029/2010GL045777>.
- Kraemer, B. M., A. Seimon, R. Adrian, and P. B. McIntyre, 2020: Worldwide lake level trends and responses to background climate variation. *Hydrol. Earth Syst. Sci.*, **24**, 2593–2608, <https://doi.org/10.5194/hess-2019-470>.
- Kratz, D. P., P. W. Stackhouse Jr., S. K. Gupta, A. C. Wilber, P. Sawaengphokhai, and G. R. McGarragh, 2014: The Fast Longwave and Shortwave Flux (FLASHFlux) data product: Single-scanner footprint fluxes. *J. Appl. Meteor. Climatol.*, **53**, 1059–1079, <https://doi.org/10.1175/JAMC-D-13-061.1>.
- Kubota, T., T. Saito, and K. Nishida, 2022: Global fast-traveling tsunamis driven by atmospheric Lamb waves on the 2022 Tonga eruption. *Science*, **377**, 91–94, <https://doi.org/10.1126/science.abo4364>.
- Labitzke, K., and M. P. McCormick, 1992: Stratospheric temperature increases due to Pinatubo aerosols. *Geophys. Res. Lett.*, **19**, 207–210, <https://doi.org/10.1029/91GL02940>.
- Lan, X., and Coauthors, 2019: Long-term measurements show little evidence for large increases in total US methane emissions over the past decade. *Geophys. Res. Lett.*, **46**, 4991–4999, <https://doi.org/10.1029/2018GL081731>.
- , and Coauthors, 2021: Improved constraints on global methane emissions and sinks using $\delta^{13}\text{C}-\text{CH}_4$. *Global Biogeochem. Cycles*, **35**, e2021GB007000, <https://doi.org/10.1029/2021GB007000>.
- Landerer, F. W., and S. C. Swenson, 2012: Accuracy of scaled GRACE terrestrial water storage estimates. *Water Resour. Res.*, **48**, W04531, <https://doi.org/10.1029/2011WR011453>.
- , and Coauthors, 2020: Extending the global mass change data record: GRACE Follow-On instrument and science data performance. *Geophys. Res. Lett.*, **47**, e2020GL088306, <https://doi.org/10.1029/2020GL088306>.
- Laughner, J. L., and Coauthors, 2021: Societal shifts due to COVID-19 reveal large-scale complexities and feedbacks between atmospheric chemistry and climate change. *Proc. Natl. Acad. Sci. USA*, **118**, e2109481118, <https://doi.org/10.1073/pnas.2109481118>.
- Lee, H.-T., and NOAA CDR Program, 2018: NOAA Climate Data Record (CDR) of Monthly Outgoing Longwave Radiation (OLR), version 2.7. NOAA National Centers for Environmental Information, accessed 5 January 2023, <https://doi.org/10.7289/V5W37TKD>.
- Legras, B., and Coauthors, 2022: The evolution and dynamics of the Hunga Tonga–Hunga Ha’apai sulfate aerosol plume in the stratosphere. *Atmos. Chem. Phys.*, **22**, 14957–14970, <https://doi.org/10.5194/acp-22-14957-2022>.
- Lenssen, N. J. L., G. A. Schmidt, J. E. Hansen, M. J. Menne, A. Persin, R. Ruedy, and D. Zyss, 2019: Improvements in the GISTEMP uncertainty model. *J. Geophys. Res. Atmos.*, **124**, 6307–6326, <https://doi.org/10.1029/2018JD029522>.
- Levy, R. C., S. Mattoo, L. A. Munchak, L. A. Remer, A. M. Sayer, F. Patadia, and N. C. Hsu, 2013: The Collection 6 MODIS aerosol products over land and ocean. *Atmos. Meas. Tech.*, **6**, 2989–3034, <https://doi.org/10.5194/amt-6-2989-2013>.
- Li, M., and Coauthors, 2017: Anthropogenic emission inventories in China: A review. *Natl. Sci. Rev.*, **4**, 834–866, <https://doi.org/10.1093/nsr/nwx150>.
- Li, Z., Z. W. Yan, Y. N. Zhu, N. Freychet, and S. Tett, 2020: Homogenized daily relative humidity series in China during 1960–2017. *Adv. Atmos. Sci.*, **37**, 318–327, <https://doi.org/10.1007/s00376-020-9180-0>.
- Liu, Ya., A. Guha, R. Said, E. Williams, J. Lapiere, M. Stock, and S. Heckman, 2020: Aerosol effects on lightning characteristics: A comparison of polluted and clean regimes. *Geophys. Res. Lett.*, **47**, e2019GL086825, <https://doi.org/10.1029/2019GL086825>.
- Liu, Y., and Coauthors, 2022: Increases in China’s wind energy production from the recovery of winds since 2012. *Environ. Res. Lett.*, **17**, 114035, <https://doi.org/10.1088/1748-9326/ac9cf4>.
- Lo, Y. T. E., and Coauthors, 2023: Optimal heat stress metric for modelling heat-related mortality varies from country to country. *Int. J. Climatol.*, **43**, 1–16, <https://doi.org/10.1002/joc.8160>.
- Loeb, N. G., B. A. Wielicki, D. R. Doelling, G. L. Smith, D. F. Keyes, S. Kato, N. Manalo-Smith, and T. Wong, 2009: Toward optimal closure of the Earth’s top-of-atmosphere radiation budget. *J. Climate*, **22**, 748–766, <https://doi.org/10.1175/2008JCLI2637.1>.
- , S. Kato, W. Su, T. Wong, F. Rose, D. R. Doelling, and J. Norris, 2012: Advances in understanding top-of-atmosphere radiation variability from satellite observations. *Surv. Geophys.*, **33**, 359–385, <https://doi.org/10.1007/s10712-012-9175-1>.
- , and Coauthors, 2018: Clouds and the Earth’s Radiant Energy System (CERES) Energy Balanced and Filled (EBAF) Top-of-Atmosphere (TOA) edition-4.0 data product. *J. Climate*, **31**, 895–918, <https://doi.org/10.1175/JCLI-D-17-0208.1>.
- MacCallum, S. N., and C. J. Merchant, 2012: Surface water temperature observations of large lakes by optimal estimation. *Can. J. Remote Sens.*, **38**, 25–45, <https://doi.org/10.5589/m12-010>.
- MacFarling Meure, C., D. Etheridge, C. Trudinger, P. Steele, R. Langenfelds, T. van Ommen, A. Smith, and J. Elkins, 2006: Law Dome CO₂, CH₄ and N₂O ice core records extended to 2000 years BP. *Geophys. Res. Lett.*, **33**, L14810, <https://doi.org/10.1029/2006GL026152>.
- Magnin, F., P. Deline, L. Raveland, J. Noetzi, and P. Pogliotti, 2015: Thermal characteristics of permafrost in the steep alpine rock walls of the Aiguille du Midi (Mont Blanc Massif, 3842 m a.s.l.). *Cryosphere*, **9**, 109–121, <https://doi.org/10.5194/tc-9-109-2015>.
- Mahowald, N. M., R. Scanza, J. Brahney, C. L. Goodale, P. G. Hess, J. K. Moore, and J. Neff, 2017: Aerosol deposition impacts on land and ocean carbon cycles. *Curr. Climate Change Rep.*, **3**, 16–31, <https://doi.org/10.1007/s40641-017-0056-z>.
- Marchant, R., C. Mumbi, S. Behera, and T. Yamagata, 2007: The Indian Ocean dipole – The unsung driver of climatic variability in East Africa. *Afr. J. Ecol.*, **45**, 4–16, <https://doi.org/10.1111/j.1365-2028.2006.00707.x>.
- Marshall, G. J., 2003: Trends in the Southern Annular Mode from observations and reanalyses. *J. Climate*, **16**, 4134–4143, [https://doi.org/10.1175/1520-0442\(2003\)016<0413>2.CO;2](https://doi.org/10.1175/1520-0442(2003)016<0413>2.CO;2).
- Martens, B., and Coauthors, 2017: GLEAM v3: Satellite-based land evaporation and root-zone soil moisture. *Geosci. Model Dev.*, **10**, 1903–1925, <https://doi.org/10.5194/gmd-10-1903-2017>.

- , W. Waegeman, W. A. Dorigo, N. E. C. Verhoest, and D. G. Miralles, 2018: Terrestrial evaporation response to modes of climate variability. *npj Climate Atmos. Sci.*, **1**, 43, <https://doi.org/10.1038/s41612-018-0053-5>.
- Matoza, R. S., and Coauthors, 2022: Atmospheric waves and global seismoacoustic observations of the January 2022 Hunga eruption, Tonga. *Science*, **377**, 95–100, <https://doi.org/10.1126/science.abo7063>.
- McKittrick, R., and J. Christy, 2020: Pervasive warming bias in CMIP6 tropospheric layers. *Earth Space Sci.*, **7**, e2020EA001281, <https://doi.org/10.1029/2020EA001281>.
- McVicar, T. R., and Coauthors, 2012: Global review and synthesis of trends in observed terrestrial near-surface wind speeds: Implications for evaporation. *J. Hydrol.*, **416–417**, 182–205, <https://doi.org/10.1016/j.jhydrol.2011.10.024>.
- Mears, C. A., and F. J. Wentz, 2016: Sensitivity of satellite-derived tropospheric temperature trends to the diurnal cycle adjustment. *J. Climate*, **29**, 3629–3646, <https://doi.org/10.1175/JCLI-D-15-0744.1>.
- , D. K. Smith, L. Ricciardulli, J. Wang, H. Huelsing, and F. J. Wentz, 2018: Construction and uncertainty estimation of a satellite-derived total precipitable water data record over the world's oceans. *Earth Space Sci.*, **5**, 197–210, <https://doi.org/10.1002/2018EA000363>.
- , J. P. Nicolas, O. Bock, S. P. Ho, and X. Zhou, 2022: Total column water vapor [in “State of the Climate in 2021”]. *Bull. Amer. Meteor. Soc.*, **103** (8), 552–554, <https://doi.org/10.1175/BAMS-D-22-0092.1>.
- Meesters, A. G. C. A., R. A. M. De Jeu, and M. Owe, 2005: Analytical derivation of the vegetation optical depth from the microwave polarization difference index. *IEEE Trans. Geosci. Remote Sens.*, **2**, 121–123, <https://doi.org/10.1109/LGRS.2005.843983>.
- Menne, M. J., I. Durre, R. S. Vose, B. E. Gleason, and T. G. Houston, 2012a: An overview of the Global Historical Climatology Network-Daily database. *J. Atmos. Oceanic Technol.*, **29**, 897–910, <https://doi.org/10.1175/JTECH-D-11-00103.1>.
- , and Coauthors, 2012b: Global Historical Climatology Network—Daily (GHCN-Daily), version 3.24. NOAA National Climatic Data Center, accessed 24 July 2023, <https://doi.org/10.7289/V5D21VHZ>.
- Menzel, A., Y. Yuan, M. Matiu, T. H. Sparks, H. Scheifinger, R. Gehrig, and N. Estrella, 2020: Climate change fingerprints in recent European plant phenology. *Global Change Biol.*, **26**, 2599–2612, <https://doi.org/10.1111/gcb.15000>.
- Messenger, M. L., B. Lehner, G. Grill, I. Nedeva, and O. Schmitt, 2016: Estimating the volume and age of water stored in global lakes using a geo-statistical approach. *Nat. Commun.*, **7**, 13603, <https://doi.org/10.1038/ncomms13603>.
- MeteoSwiss, 2023: Klimabulletin Jahr 2022. MeteoSwiss, 13 pp., www.meteoschweiz.admin.ch/service-und-publikationen/publikationen/berichte-und-bulletins/2022/klimabulletin-jahr-2022.html.
- Meyer, M. F., S. G. Labou, A. N. Cramer, M. R. Brouil, and B. T. Luff, 2020: The global lake area, climate, and population dataset. *Sci. Data*, **7**, 174, <https://doi.org/10.1038/s41597-020-0517-4>.
- Michel, S. E., J. R. Clark, B. H. Vaughn, M. Crotwell, M. Madronich, E. Moglia, D. Neff, and J. Mund, 2022: Stable isotopic composition of atmospheric methane (^{13}C) from the NOAA GML Carbon Cycle Cooperative Global Air Sampling Network, 1998–2021. University of Colorado, Institute of Arctic and Alpine Research (INSTAAR), accessed 15 December 2022, <https://doi.org/10.15138/9p89-1x02>.
- Millán, L., and Coauthors, 2022: The Hunga Tonga-Hunga Ha’apai hydration of the stratosphere. *Geophys. Res. Lett.*, **49**, e2022GL099381, <https://doi.org/10.1029/2022GL099381>.
- Miller, B. R., and Coauthors, 2010: HFC-23 (CHF₃) emission trend response to HCFC-22 (CHClF₂) production and recent HFC-23 emission abatement measures. *Atmos. Chem. Phys.*, **10**, 7875–7890, <https://doi.org/10.5194/acp-10-7875-2010>.
- Minola, L., H. Reese, H. W. Lai, C. Azorin-Molina, J. A. Guijarro, S. W. Son, and D. Chen, 2022: Wind stilling-reversal across Sweden: The impact of land-use and large-scale atmospheric circulation changes. *Int. J. Climatol.*, **42**, 1049–1071, <https://doi.org/10.1002/joc.7289>.
- Miralles, D. G., T. R. H. Holmes, R. A. M. De Jeu, J. H. Gash, A. G. C. A. Meesters, and A. J. Dolman, 2011: Global land-surface evaporation estimated from satellite-based observations. *Hydrol. Earth Syst. Sci.*, **15**, 453–469, <https://doi.org/10.5194/hess-15-453-2011>.
- , and Coauthors, 2014: El Niño–La Niña cycle and recent trends in continental evaporation. *Nat. Climate Change*, **4**, 122–126, <https://doi.org/10.1038/nclimate2068>.
- Mishra, M. K., L. Hoffmann, and P. K. Thapliyal, 2022: Investigations on the global spread of the Hunga Tonga-Hunga Ha’apai volcanic eruption using space-based observations and Lagrangian transport simulations. *Atmosphere*, **13**, 2055, <https://doi.org/10.3390/atmos13122055>.
- Mitchell, L., E. Brook, J. E. Lee, C. Buizert, and T. Sowers, 2013: Constraints on the late Holocene anthropogenic contribution to the atmospheric methane budget. *Science*, **342**, 964–966, <https://doi.org/10.1126/science.1238920>.
- Mo, K. C., J. K. E. Schemm, and S. H. Yoo, 2009: Influence of ENSO and the Atlantic multidecadal oscillation on drought over the United States. *J. Climate*, **22**, 5962–5982, <https://doi.org/10.1175/2009JCLI2966.1>.
- Moesinger, L., W. Dorigo, R. de Jeu, R. van der Schalie, T. Scanlon, I. Teubner, and M. Forkel, 2020: The global long-term microwave Vegetation Optical Depth Climate Archive (VODCA). *Earth Syst. Sci. Data*, **12**, 177–196, <https://doi.org/10.5194/essd-12-177-2020>.
- Montzka, S. A., J. H. Butler, R. C. Myers, T. M. Thompson, T. H. Swanson, A. D. Clarke, L. T. Lock, and J. W. Elkins, 1996: Decline in the tropospheric abundance of halogen from halocarbons: Implications for stratospheric ozone depletion. *Science*, **272**, 1318–1322, <https://doi.org/10.1126/science.272.5266.1318>.
- , and Coauthors, 2018: An unexpected and persistent increase in global emissions of ozone-depleting CFC-11. *Nature*, **557**, 413–417, <https://doi.org/10.1038/s41586-018-0106-2>.
- , and Coauthors, 2021: A decline in global CFC-11 emissions during 2018–2019. *Nature*, **590**, 428–432, <https://doi.org/10.1038/s41586-021-03260-5>.
- Morice, C. P., and Coauthors, 2021: An updated assessment of near-surface temperature change from 1850: The HadCRUT5 data set. *J. Geophys. Res. Atmos.*, **126**, e2019JD032361, <https://doi.org/10.1029/2019JD032361>.
- Moron, V., and G. Plaut, 2003: The impact of El Niño–Southern Oscillation upon weather regimes over Europe and the North Atlantic during boreal winter. *Int. J. Climatol.*, **23**, 363–379, <https://doi.org/10.1002/joc.890>.
- Mote, P. W., and Coauthors, 1996: An atmospheric tape recorder: The imprint of tropical tropopause temperatures on stratospheric water vapor. *J. Geophys. Res.*, **101**, 3989–4006, <https://doi.org/10.1029/95JD03422>.

- Mühle, J., and Coauthors, 2010: Perfluorocarbons in the global atmosphere: Tetrafluoromethane, hexafluoroethane, and octafluoropropane. *Atmos. Chem. Phys.*, **10**, 5145–5164, <https://doi.org/10.5194/acp-10-5145-2010>.
- , and Coauthors, 2019: Perfluorocyclobutane (PFC-318, $c\text{-C}_4\text{F}_8$) in the global atmosphere. *Atmos. Chem. Phys.*, **19**, 10335–10359, <https://doi.org/10.5194/acp-19-10335-2019>.
- Myhre, G., and Coauthors, 2013: Anthropogenic and natural radiative forcing. *Climate Change 2013: The Physical Science Basis*, T. F. Stocker et al., Eds., Cambridge University Press, 659–740.
- Naumann, G., and Coauthors, 2021: The 2019–2021 extreme drought episode in La Plata Basin. EUR 30833 EN, Publications Office of the European Union, 44 pp., <https://doi.org/10.2760/773>.
- NCEI, 2023: Annual 2022 Global Climate Report. Accessed 8 February 2023, <https://www.ncei.noaa.gov/access/monitoring/monthly-report/global/202213>.
- Newman, P. A., J. S. Daniel, D. W. Waugh, and E. R. Nash, 2007: A new formulation of equivalent effective stratospheric chlorine (EESC). *Atmos. Chem. Phys.*, **7**, 4537–4552, <https://doi.org/10.5194/acp-7-4537-2007>.
- Nicholson, S. E., 2017: Climate and climatic variability of rainfall over eastern Africa. *Rev. Geophys.*, **55**, 590–635, <https://doi.org/10.1002/2016RG000544>.
- NIWA, 2022: “Exceptional” August atmospheric river sets record. NIWA, <https://niwa.co.nz/news/exceptional-august-atmospheric-river-sets-record>.
- NOAA/NCEI, 2023: Monthly global climate report for annual 2022. Accessed 24 January 2023, <https://www.ncei.noaa.gov/access/monitoring/monthly-report/global/202213>.
- Noetzli, J., and Coauthors, 2021: Best practice for measuring permafrost temperature in boreholes based on the experience in the Swiss Alps. *Front. Earth Sci.*, **9**, 607875, <https://doi.org/10.3389/feart.2021.607875>.
- , H. H. Christiansen, P. Deline, M. Gugliemin, K. Isaksen, S. Smith, L. Zhao, and D. A. Streletskiy, 2022: Permafrost temperature and active layer thickness [in “State of the Climate in 2021”]. *Bull. Amer. Meteor. Soc.*, **103** (8), S41–S43, <https://doi.org/10.1175/BAMS-D-22-0092.1>.
- OCHA, 2022: South Africa: Floods and landslides – Apr 2022. ReliefWeb, accessed 9 February 2023, <https://reliefweb.int/disaster/fl-2022-000201-zaf>.
- Oh, Y., and Coauthors, 2022: Improved global wetland carbon isotopic signatures support post-2006 microbial methane emission increase. *Commun. Earth Environ.*, **3**, 159, <https://doi.org/10.1038/s43247-022-00488-5>.
- O’Keefe, J., 2021: Phenology of woody species at Harvard Forest since 1990. Harvard Forest Data Archive: HF003, accessed 25 July 2023, <https://harvardforest1.fas.harvard.edu/exist/apps/datasets/showData.html?id=HF003>.
- Orimoloye, I. R., J. A. Belle, Y. M. Orimoloye, A. O. Olusola, and O. O. Ololade, 2022: Drought: A common environmental disaster. *Atmosphere*, **13**, 111, <https://doi.org/10.3390/atmos13010111>.
- Osborn, T. J., P. D. Jones, D. H. Lister, C. P. Morice, I. R. Simpson, J. P. Winn, E. Hogan, and I. C. Harris, 2021: Land surface air temperature variations across the globe updated to 2019: The CRUTEM5 dataset. *J. Geophys. Res. Atmos.*, **126**, e2019JD032352, <https://doi.org/10.1029/2019JD032352>.
- Osprey, S. M., N. Butchart, J. R. Knight, A. A. Scaife, K. Hamilton, J. A. Anstey, V. Schenzinger, and C. Zhang, 2016: An unexpected disruption of the atmospheric quasi-biennial oscillation. *Science*, **353**, 1424–1427, <https://doi.org/10.1126/science.aah4156>.
- Otto, F. E. L., and Coauthors, 2022: Climate change likely increased extreme monsoon rainfall, flooding highly vulnerable communities in Pakistan. World Weather Attribution, 36 pp., <https://www.worldweatherattribution.org/wp-content/uploads/Pakistan-floods-scientific-report.pdf>.
- Park, H., and Coauthors, 2023: Continuous increase in East Asia HFC-23 emissions inferred from high-frequency atmospheric observations from 2008 to 2019. *EGU Sphere*, <https://doi.org/10.5194/egusphere-2023-6>.
- Park, S., and Coauthors, 2021: A decline in emissions of CFC-11 and related chemicals from eastern China. *Nature*, **590**, 433–437, <https://doi.org/10.1038/s41586-021-03277-w>.
- Park, T., and Coauthors, 2016: Changes in growing season duration and productivity of northern vegetation inferred from long-term remote sensing data. *Environ. Res. Lett.*, **11**, 084001, <https://doi.org/10.1088/1748-9326/11/8/084001>.
- Parsons, L. A., Y. J. Masuda, T. Kroeger, D. Shindell, N. H. Wolff, and J. T. Spector, 2022: Global labor loss due to humid heat exposure underestimated for outdoor workers. *Environ. Res. Lett.*, **17**, 014050, <https://doi.org/10.1088/1748-9326/ac3dae>.
- Pekel, J.-F., A. Cottam, N. Gorelick, and A. S. Belward, 2016: High-resolution mapping of global surface water and its long-term changes. *Nature*, **540**, 418–422, <https://doi.org/10.1038/nature20584>.
- Pellet, C., and Coauthors, 2022: Rock glacier velocity [in “State of the Climate in 2021”]. *Bull. Amer. Meteor. Soc.*, **103** (8), S43–S45, <https://doi.org/10.1175/BAMS-D-22-0092.1>.
- Pelto, M., M. Dryak, J. Pelto, T. Matthews, and L. B. Perry, 2022: Contribution of glacier runoff during heat waves in the Nooksack River Basin USA. *Water*, **14**, 1145, <https://doi.org/10.3390/w14071145>.
- Peng, S., and Coauthors, 2022: Wetland emission and atmospheric sink changes explain methane growth in 2020. *Nature*, **612**, 477–482, <https://doi.org/10.1038/s41586-022-05447-w>.
- Pepin, N., and Coauthors, 2015: Elevation-dependent warming in mountain regions of the world. *Nat. Climate Change*, **5**, 424–430, <https://doi.org/10.1038/nclimate2563>.
- PERMOS, 2022: Swiss Permafrost Bulletin 2021. J. Noetzli and C. Pellet, Eds., Swiss Permafrost Monitoring Network, 22 pp., <https://doi.org/10.13093/permos-bull-2022>.
- Phillips, C., and M. J. Foster, 2022: Cloudiness [in “State of the Climate in 2021”]. *Bull. Amer. Meteor. Soc.*, **103** (8), S31–S33, <https://doi.org/10.1175/BAMS-D-22-0092.1>.
- Pielmeier, C., B. Zweifel, F. Techel, C. Marty, and T. Stucki, 2023: *Schnee und Lawinen in den Schweizer Alpen. Hydrologisches Jahr 2021/22*. WSL Berichte, Vol. 128, WSL-Institut für Schnee- und Lawinenforschung SLF, 72 pp., <https://doi.org/10.55419/wsl:32462>.
- Pierrehumbert, R. T., 2014: Short-lived climate pollution. *Annu. Rev. Earth Planet. Sci.*, **42**, 341–379, <https://doi.org/10.1146/annurev-earth-060313-054843>.
- Pinty, B., and Coauthors, 2011: Exploiting the MODIS albedos with the Two-stream Inversion Package (JRC-TIP): 2. Fractions of transmitted and absorbed fluxes in the vegetation and soil layers. *J. Geophys. Res.*, **116**, D09106, <https://doi.org/10.1029/2010JD015373>.
- Pisano, M. F., G. D’Amico, N. Ramos, N. Pommarés, and E. Fucks, 2020: Factors that control the seasonal dynamics of the shallow lakes in the Pampean region, Buenos Aires, Argentina. *J. South Amer. Earth Sci.*, **98**, 102468, <https://doi.org/10.1016/j.jsames.2019.102468>.

- Platnick, S., and Coauthors, 2015: MODIS atmosphere L3 monthly product. NASA MODIS Adaptive Processing System, Goddard Space Flight Center, accessed 11 February 2022, https://doi.org/10.5067/MODIS/MYD08_M3.061.
- PMDCDPC, 2022: Pakistan monsoon 2022 rainfall report. Pakistan Meteorological Department-CDPC, 3 pp., https://www.pmd.gov.pk/cdpc/Monsoon_2022_update/Pakistan_Monsoon_2022_Rainfall_Update.pdf.
- PMDNWFC, 2022: Monthly weather report August 2022. National Weather Forecasting Center Islamabad, Pakistan Meteorological Department, 23 pp., <https://nwfc.pmd.gov.pk/new/assets/monthly-weather-reports/1664253472.pdf>.
- Po-Chedley, S., T. J. Thorsen, and Q. Fu, 2015: Removing diurnal cycle contamination in satellite-derived tropospheric temperatures: Understanding tropical tropospheric trend discrepancies. *J. Climate*, **28**, 2274–2290, <https://doi.org/10.1175/JCLI-D-13-00767.1>.
- , B. D. Santer, S. Fueglistaler, M. D. Zelinka, P. J. Cameron-Smith, J. Painter, and Q. Fu, 2021: Natural variability contributes to model-satellite differences in tropical tropospheric warming. *Proc. Natl. Acad. Sci. USA*, **118**, e2020962118, <https://doi.org/10.1073/pnas.2020962118>.
- , J. T. Fasullo, N. Siler, E. A. Barnes, Z. M. Labe, C. J. W. Bonfils, and B. D. Santer, 2022: Internal variability and forcing influence model-satellite differences in the rate of tropical tropospheric warming. *Proc. Natl. Acad. Sci. USA*, **119**, e2209431119, <https://doi.org/10.1073/pnas.2209431119>.
- Pogliotti, P., M. Guglielmin, E. Cremonese, U. M. di Cella, G. Filippa, C. Pellet, and C. Hauck, 2015: Warming permafrost and active layer variability at Cime Bianche, western European Alps. *Cryosphere*, **9**, 647–661, <https://doi.org/10.5194/tc-9-647-2015>.
- Poli, P., and N. M. Shapiro, 2022: Rapid characterization of large volcanic eruptions: Measuring the impulse of the Hunga Tonga Ha'apai explosion from teleseismic waves. *Geophys. Res. Lett.*, **49**, e2022GL098123, <https://doi.org/10.1029/2022GL098123>.
- Popp, T., and Coauthors, 2016: Development, production and evaluation of aerosol climate data records from European satellite observations (Aerosol_cci). *Remote Sens.*, **8**, 421, <https://doi.org/10.3390/rs8050421>.
- Prather, M. J., C. D. Holmes, and J. Hsu, 2012: Reactive greenhouse gas scenarios: Systematic exploration of uncertainties and the role of atmospheric chemistry. *Geophys. Res. Lett.*, **39**, L09803, <https://doi.org/10.1029/2012GL051440>.
- Proud, S. R., A. T. Prata, and S. Schmauß, 2022: The January 2022 eruption of Hunga Tonga-Hunga Ha'apai volcano reached the mesosphere. *Science*, **378**, 554–557, <https://doi.org/10.1126/science.abo4076>.
- Quaas, J., and Coauthors, 2022: Robust evidence for reversal of the trend in aerosol effective climate forcing. *Atmos. Chem. Phys.*, **22**, 12 221–12 239, <https://doi.org/10.5194/acp-22-12221-2022>.
- Rajeevan, M., K. L. Srivastava, Z. Lareef, and J. Revadekar, 2011: South Asia [in "State of the Climate in 2010"]. *Bull. Amer. Meteor. Soc.*, **92** (6), S217–S219, <https://doi.org/10.1175/1520-0477-92.6.S1>.
- Ramon, J., L. Lledó, V. Torralba, A. Soret, and F. J. Doblas-Reyes, 2019: What global reanalysis best represents near-surface winds? *Quart. J. Roy. Meteor. Soc.*, **145**, 3236–3251, <https://doi.org/10.1002/qj.3616>.
- Randel, W. J., and J. B. Cobb, 1994: Coherent variations of monthly mean total ozone and lower stratospheric temperature. *J. Geophys. Res.*, **99**, 5433–5447, <https://doi.org/10.1029/93JD03454>.
- , F. Wu, S. J. Oltmans, K. Rosenlof, and G. E. Nedoluha, 2004: Interannual changes of stratospheric water vapor and correlations with tropical tropopause temperatures. *J. Atmos. Sci.*, **61**, 2133–2148, [https://doi.org/10.1175/1520-0469\(2004\)0612.0.CO;2](https://doi.org/10.1175/1520-0469(2004)0612.0.CO;2).
- Randel, W. J., B. R. Johnston, J. J. Braun, S. Sokolovskiy, H. Vömel, A. Podglajen, and B. Legras, 2023: Stratospheric water vapor from the Hunga Tonga–Hunga Ha'apai volcanic eruption deduced from COSMIC-2 radio occultation. *Remote Sens.*, **15**, 2167, <https://doi.org/10.3390/rs15082167>.
- Ravishankara, A. R., J. S. Daniel, and R. W. Portmann, 2009: Nitrous oxide (N₂O): The dominant ozone-depleting substance emitted in the 21st century. *Science*, **326**, 123–125, <https://doi.org/10.1126/science.1176985>.
- Ray, E. A., F. L. Moore, J. W. Elkins, K. H. Rosenlof, J. C. Laube, T. Röckmann, D. R. Marsh, and A. E. Andrews, 2017: Quantification of the SF₆ lifetime based on mesospheric loss measured in the stratospheric polar vortex. *J. Geophys. Res. Atmos.*, **122**, 4626–4638, <https://doi.org/10.1002/2016JD026198>.
- Rayner, N. A., D. E. Parker, E. B. Horton, C. K. Folland, L. V. Alexander, D. P. Rowell, E. C. Kent, and A. Kaplan, 2003: Global analyses of sea surface temperature, sea ice, and night marine air temperature since the late nineteenth century. *J. Geophys. Res.*, **108**, 4407, <https://doi.org/10.1029/2002JD002670>.
- Reichstein, M., and Coauthors, 2013: Climate extremes and the carbon cycle. *Nature*, **500**, 287–295, <https://doi.org/10.1038/nature12350>.
- Rémy, S., N. Bellouin, Z. Kipling, M. Ades, A. Benedetti, and O. Boucher, 2021: Aerosols [in "State of the Climate in 2021"]. *Soc.*, **102** (8), S11–S42, <https://doi.org/10.1175/BAMS-D-22-0092.1>.
- RGIK, 2022a: Rock glacier velocity as an associated parameter of ECV permafrost: Baseline concepts (version 3.1). IPA Action Group Rock Glacier Inventories and Kinematics, 12 pp., https://bigweb.unifr.ch/Science/Geosciences/Geomorphology/Pub/Website/IPA/CurrentVersion/Current_RockGlacierVelocity.pdf.
- , 2022b: Towards standard guidelines for inventorying rock glaciers: Baseline concepts (version 4.2.2). IPA Action Group Rock Glacier Inventories and Kinematics, 13 pp., https://bigweb.unifr.ch/Science/Geosciences/Geomorphology/Pub/Website/IPA/CurrentVersion/Current_Baseline_Concepts_Inventorying_Rock_Glaciers.pdf.
- Ricciardulli, L., and F. J. Wentz, 2015: A scatterometer geophysical model function for climate-quality winds: QuikSCAT Ku-2011. *J. Atmos. Oceanic Technol.*, **32**, 1829–1846, <https://doi.org/10.1175/JTECH-D-15-0008.1>.
- , and A. Manaster, 2021: Intercalibration of ASCAT scatterometer winds from MetOp-A, -B, and -C, for a stable climate data record. *Remote Sens.*, **13**, 3678, <https://doi.org/10.3390/rs13183678>.
- Richardson, A. D., 2019: Tracking seasonal rhythms of plants in diverse ecosystems with digital camera imagery. *New Phytol.*, **222**, 1742–1750, <https://doi.org/10.1111/nph.15591>.
- , and J. O'Keefe, 2009: Phenological differences between understory and overstory. *Phenology of Ecosystem Processes*, A. Noormets, Ed., Springer, 87–117.
- Rieger, L. A., W. J. Randel, A. E. Bourassa, and S. Solomon, 2021: Stratospheric temperature and ozone anomalies associated with the 2020 Australian New Year fires. *Geophys. Res. Lett.*, **48**, e2021GL095898, <https://doi.org/10.1029/2021GL095898>.

- Rigby, M., and Coauthors, 2019: Increase in CFC-11 emissions from eastern China based on atmospheric observations. *Nature*, **569**, 546–550, <https://doi.org/10.1038/s41586-019-1193-4>.
- Rodell, M., and D. Wiese, 2022: Groundwater and terrestrial water storage [in “State of the Climate in 2021”]. *Bull. Amer. Meteor. Soc.*, **103** (8), 563–564, <https://doi.org/10.1175/BAMS-D-22-0092.1>.
- Roderick, M. L., L. D. Rotstayn, G. D. Farquhar, and M. T. Hobbins, 2007: On the attribution of changing pan evaporation. *Geophys. Res. Lett.*, **34**, L17403, <https://doi.org/10.1029/2007GL031166>.
- Rohde, R. A., and Z. Hausfather, 2020: The Berkeley Earth land/ocean temperature record. *Earth Syst. Sci. Data*, **12**, 3469–3479, <https://doi.org/10.5194/essd-12-3469-2020>.
- Rosemartin, A. H., and Coauthors, 2014: Organizing phenological data resources to inform natural resource conservation. *Biol. Conserv.*, **173**, 90–97, <https://doi.org/10.1016/j.biocon.2013.07.003>.
- Rosenfeld, D., and W. L. Woodley, 2003: Closing the 50-year circle: From cloud seeding to space and back to climate change through precipitation physics. *Cloud Systems, Hurricanes, and the Tropical Rainfall Measuring Mission (TRMM)*, Meteor. Monogr., No. 51, Amer. Meteor. Soc., 59–80.
- , U. Lohmann, G. B. Raga, C. D. O’Dowd, M. Kulmala, S. Fuzzi, A. Reissell, and M. O. Andreae, 2008: Flood or drought: How do aerosols affect precipitation? *Science*, **321**, 1309–1313, <https://doi.org/10.1126/science.1160606>.
- Saji, N. H., B. N. Goswami, P. N. Vinayachandran, and T. Yamagata, 1999: A dipole mode in the tropical Indian Ocean. *Nature*, **401**, 360–363, <https://doi.org/10.1038/43854>.
- Sanap, S. D., 2021: Global and regional variations in aerosol loading during COVID-19 imposed lockdown. *Atmos. Environ.*, **246**, 118132, <https://doi.org/10.1016/j.atmosenv.2020.118132>.
- Santer, B. D., and Coauthors, 2008: Consistency of modelled and observed temperature trends in the tropical troposphere. *Int. J. Climatol.*, **28**, 1703–1722, <https://doi.org/10.1002/joc.1756>.
- , and Coauthors, 2021: Using climate model simulations to constrain observations. *J. Climate*, **34**, 6281–6301, <https://doi.org/10.1175/JCLI-D-20-0768.1>.
- Santos, E. B., E. D. de Freitas, S. A. A. Raífe, T. Fujita, A. P. Rudke, L. D. Martins, R. A. F. de Souza, and J. A. Martin, 2021: Spatio-temporal variability of wet and drought events in the Paraná River basin—Brazil and its association with the El Niño–Southern Oscillation phenomenon. *Int. J. Climatol.*, **41**, 4879–4897, <https://doi.org/10.1002/joc.7104>.
- Sátori, G., E. Williams, and I. Lempferger, 2009b: Variability of global lightning activity on the ENSO time scale. *Atmos. Res.*, **91**, 500–507, <https://doi.org/10.1016/j.atmosres.2008.06.014>.
- SAWS, 2022: Media release: Extreme rainfall and widespread flooding overnight: KwaZulu-Natal and parts of Eastern Cape. South African Weather Service, 12 April, accessed 14 February 2023, https://www.weathersa.co.za/Documents/Corporate/Medrel12April2022_12042022142120.pdf.
- Scafetta, N., 2023: CMIP6 GCM ensemble members versus global surface temperatures. *Climate Dyn.*, **60**, 3091–3120, <https://doi.org/10.1007/s00382-022-06493-w>.
- Schaaf, C. B., and Coauthors, 2002: First operational BRDF, albedo nadir reflectance products from MODIS. *Remote Sens. Environ.*, **83**, 135–148, [https://doi.org/10.1016/S0034-4257\(02\)00091-3](https://doi.org/10.1016/S0034-4257(02)00091-3).
- Schoeberl, M. R., Y. Wang, R. Ueyama, G. Taha, E. Jensen, and W. Yu, 2022: Analysis and impact of the Hunga Tonga-Hunga Ha’apai stratospheric water vapor plume. *Geophys. Res. Lett.*, **49**, e2022GL100248, <https://doi.org/10.1029/2022GL100248>.
- Schwartz, M. J., and Coauthors, 2020: Australian New Year’s PyroCb impact on stratospheric composition. *Geophys. Res. Lett.*, **47**, e2020GL090831, <https://doi.org/10.1029/2020GL090831>.
- Seyednasrollah, B., A. M. Young, K. Hufkens, T. Milliman, M. A. Friedl, S. Frolking, and A. D. Richardson, 2019: Publisher correction: Tracking vegetation phenology across diverse biomes using version 2.0 of the PhenoCam Dataset. *Sci. Data*, **6**, 261, <https://doi.org/10.1038/s41597-019-0270-8>.
- Shao, X., S.-P. Ho, X. Jing, X. Zhou, Y. Chen, T.-C. Liu, B. Zhang, and J. Dong, 2023: Characterizing the tropospheric water vapor variation using COSMIC radio occultation and ECMWF reanalysis data. *Atmos. Chem. Phys. Discuss.*, <https://doi.org/10.5194/acp-2022-660>.
- Sharma, S., and R. I. Woolway, 2021: Lake ice [in “State of the Climate in 2020”]. *Bull. Amer. Meteor. Soc.*, **102** (8), S48–S51, <https://doi.org/10.1175/BAMS-D-21-0098.1>.
- , J. J. Magnuson, R. D. Batt, L. Winslow, J. Korhonen, and Y. Aono, 2016: Direct observations of ice seasonality reveal changes in climate over the past 5–7 centuries. *Sci. Rep.*, **6**, 25061, <https://doi.org/10.1038/srep25061>.
- , and Coauthors, 2019: Widespread loss of lake ice around the Northern Hemisphere in a warming world. *Nat. Climate Change*, **9**, 3, <https://doi.org/10.1038/s41558-018-0393-5>.
- , K. Blagrove, A. Filazzola, M. A. Imrit, and H.-J. Hendricks Franssen, 2021: Forecasting the permanent loss of lake ice within the 21st century. *Geophys. Res. Lett.*, **48**, e2020GL091108, <https://doi.org/10.1029/2020GL091108>.
- , and Coauthors, 2022: Lake ice [in “State of the Climate in 2021”]. *Bull. Amer. Meteor. Soc.*, **103** (8), S47–S49, <https://doi.org/10.1175/BAMS-D-22-0092.1>.
- Shaw, T., G. Ulloa, D. Fariás-Barahona, R. Fernandez, J. Lattus, and J. McPhee, 2021: Glacier albedo reduction and drought effects in the extratropical Andes, 1986–2020. *J. Glaciol.*, **67**, 158–169, <https://doi.org/10.1017/jog.2020.102>.
- Shi, L., and J. J. Bates, 2011: Three decades of intersatellite-calibrated high-resolution infrared radiation sounder upper tropospheric water vapor. *J. Geophys. Res.*, **116**, D04108, <https://doi.org/10.1029/2010JD014847>.
- Sindelarova, K., and Coauthors, 2014: Global data set of biogenic VOC emissions calculated by the MEGAN model over the last 30 years. *Atmos. Chem. Phys.*, **14**, 9317–9341, <https://doi.org/10.5194/acp-14-9317-2014>.
- Sioris, C. E., A. Malo, C. A. McLinden, and R. D’Amours, 2016: Direct injection of water vapor into the stratosphere by volcanic eruptions. *Geophys. Res. Lett.*, **43**, 7694–7700, <https://doi.org/10.1002/2016GL069918>.
- Skeie, R., and Coauthors, 2020: Historical total ozone radiative forcing derived from CMIP6 simulations. *npj Climate Atmos. Sci.*, **3**, 32, <https://doi.org/10.1038/s41612-020-00131-0>.
- Smiljanic, I., M. Higgins, D. Melfi, and I. A. Abdulsalam, 2022: Monsoon floods in Pakistan. EUMETSAT, 13 September, accessed 23 January 2023, <https://www.eumetsat.int/monsoon-floods-pakistan>.
- Smith, A., N. Lott, and R. Vose, 2011: The integrated surface database: Recent developments and partnerships. *Bull. Amer. Meteor. Soc.*, **92**, 704–708, <https://doi.org/10.1175/2011BAMS3015.1>.

- Smith, S. L., H. B. O'Neill, K. Isaksen, J. Noetzi, and V. E. Romanovsky, 2022: The changing thermal state of permafrost. *Nat. Rev. Earth Environ.*, **3**, 14, <https://doi.org/10.1038/s43017-021-00240-1>.
- Soden, B. J., D. L. Jackson, V. Ramaswamy, M. D. Schwarzkopf, and X. Huang, 2005: The radiative signature of upper tropospheric moistening. *Science*, **310**, 841–844, <https://doi.org/10.1126/science.1115602>.
- Sofieva, V. F., and Coauthors, 2021: Measurement report: Regional trends of stratospheric ozone evaluated using the Merged GRidded Dataset of Ozone Profiles (MEGRIDOP). *Atmos. Chem. Phys.*, **21**, 6707–6720, <https://doi.org/10.5194/acp-21-6707-2021>.
- Solomon, S., K. Stone, P. Yu, D. M. Murphy, D. Kinnison, A. R. Ravishankara, and P. Wang, 2023: Chlorine activation and enhanced ozone depletion induced by wildfire aerosol. *Nature*, **615**, 259–264, <https://doi.org/10.1038/s41586-022-05683-0>.
- Song, X.-P., M. C. Hansen, S. V. Stehman, P. V. Potapov, A. Tyukavina, E. F. Vermote, and J. R. Townshend, 2018: Global land change from 1982 to 2016. *Nature*, **560**, 639–643, <https://doi.org/10.1038/s41586-018-0411-9>.
- Soulard, N., and H. Lin, 2017: The spring relationship between the Pacific-North American pattern and the North Atlantic Oscillation. *Climate Dyn.*, **48**, 619–629, <https://doi.org/10.1007/s00382-016-3098-3>.
- SPARC/I03C/GAW, 2019: SPARC/I03C/GAW report on long-term ozone trends and uncertainties in the stratosphere. I. Petropavlovskikh et al., Eds., SPARC Rep. 9, WCRP-17/2018, GAW Rep. 241, 99 pp., <https://doi.org/10.17874/f899e57a20b>.
- Spencer, R. W., J. R. Christy, and W. D. Braswell, 2017: UAH version 6 global satellite temperature products: Methodology and results. *Asia-Pac. J. Atmos. Sci.*, **53**, 121–130, <https://doi.org/10.1007/s13143-017-0010-y>.
- Stackhouse, P. W., T. Wong, D. P. Kratz, P. Sawaengphokhai, A. C. Wiber, S. K. Gupta, and N. G. Loeb, 2016: Earth radiation budget at top-of-atmosphere [in “State of the Climate in 2015”]. *Bull. Amer. Meteor. Soc.*, **97** (8), S41–S43, <https://doi.org/10.1175/2016BAMSStateoftheClimate.1>.
- Stanley, K. M., and Coauthors, 2020: Increase in global emissions of HFC-23 despite near-total expected reductions. *Nat. Commun.*, **11**, 397, <https://doi.org/10.1038/s41467-019-13899-4>.
- Staub, B., C. Lambiel, and R. Delaloye, 2016: Rock glacier creep as a thermally-driven phenomenon: A decade of inter-annual observation from the Swiss Alps. *XI Int. Conf. on Permafrost*, Potsdam, Germany, Alfred Wegener Institute Helmholtz Center for Polar and Marine Research, 96–97, <https://doi.org/10.2312/GFZ.LIS.2016.001>.
- Steinbrecht, W., and Coauthors, 2017: An update on ozone profile trends for the period 2000 to 2016. *Atmos. Chem. Phys.*, **17**, 10675–10690, <https://doi.org/10.5194/acp-17-10675-2017>.
- Stolarski, R. S., A. R. Douglass, L. D. Oman, and D. W. Waugh, 2015: Impact of future nitrous oxide and carbon dioxide emissions on the stratospheric ozone layer. *Environ. Res. Lett.*, **10**, 034011, <https://doi.org/10.1088/1748-9326/10/3/034011>.
- Strahan, S. E., and Coauthors, 2022: Unexpected repartitioning of stratospheric inorganic chlorine after the 2020 Australian wildfires. *Geophys. Res. Lett.*, **49**, e2022GL098290, <https://doi.org/10.1029/2022GL098290>.
- Streletskiy, D., J. Noetzi, S. L. Smith, G. Vieira, P. Schoeneich, F. Hrbacek, and A. M. Irrgang, 2021: Strategy and implementation plan for the Global Terrestrial Network for Permafrost (GTN-P) 2021–2024. International Permafrost Association, 44 pp., <https://doi.org/10.5281/ZENODO.6075468>.
- Stroeve, J., J. E. Box, Z. Wang, C. Schaaf, and A. Barrett, 2013: Re-evaluation of MODIS MCD43 Greenland albedo accuracy and trends. *Remote Sens. Environ.*, **138**, 199–214, <https://doi.org/10.1016/j.rse.2013.07.023>.
- Stull, R., 2011: Wet-bulb temperature from relative humidity and air temperature. *J. Appl. Meteor. Climatol.*, **50**, 2267–2269, <https://doi.org/10.1175/JAMC-D-11-0143.1>.
- Susskind, J., G. Molnar, L. Iredell, and N. G. Loeb, 2012: Interannual variability of outgoing longwave radiation as observed by AIRS and CERES. *J. Geophys. Res.*, **117**, D23107, <https://doi.org/10.1029/2012JD017997>.
- Szopa, S., and Coauthors, 2021: Short-lived climate forcers. *Climate Change 2021: The Physical Science Basis*, V. Masson-Delmotte et al., Eds., Cambridge University Press, 817–922, <https://doi.org/10.1017/9781009157896.008>.
- Taha, G., R. Loughman, P. R. Colarco, T. Zhu, L. W. Thomason, and G. Jaross, 2022: Tracking the 2022 Hunga Tonga-Hunga Ha’apai aerosol cloud in the upper and middle stratosphere using space-based observations. *Geophys. Res. Lett.*, **49**, e2022GL100091, <https://doi.org/10.1029/2022GL100091>.
- Tapley, B. D., S. Bettadpur, J. C. Ries, P. F. Thompson, and M. M. Watkins, 2004: GRACE measurements of mass variability in the Earth system. *Science*, **305**, 503–505, <https://doi.org/10.1126/science.1099192>.
- Tarasick, D. W., and Coauthors, 2019: Tropospheric ozone assessment report: Tropospheric ozone from 1877 to 2016, observed levels, trends and uncertainties. *Elementa*, **7**, 39, <https://doi.org/10.1525/elementa.376>.
- Teng, W.-H., C.-Y. Huang, S.-P. Ho, Y.-H. Kuo, and X.-J. Zhou, 2013: Characteristics of global precipitable water in ENSO events revealed by COSMIC measurements. *J. Geophys. Res. Atmos.*, **118**, 8411–8425, <https://doi.org/10.1002/jgrd.50371>.
- Teubner, I. E., and Coauthors, 2019: A carbon sink-driven approach to estimate gross primary production from microwave satellite observations. *Remote Sens. Environ.*, **229**, 100–113, <https://doi.org/10.1016/j.rse.2019.04.022>.
- Thibert, E., and X. Bodin, 2022: Changes in surface velocities over four decades on the Laurichard rock glacier (French Alps). *Permafrost Periglacial Processes*, **33**, 323–335, <https://doi.org/10.1002/ppp.2159>.
- Thompson, A. M., R. M. Stauffer, K. Wargan, J. C. Witte, D. E. Kolonig, and J. R. Ziemke, 2021: Regional and seasonal trends in tropical ozone from SHADOZ profiles: Reference for models and satellite products. , **126**, e2021JD034691, <https://doi.org/10.1029/2021JD034691>.
- Thompson, R. L., and Coauthors, 2019: Acceleration of global N₂O emissions seen from two decades of atmospheric inversion. *Nat. Climate Change*, **9**, 993–998, <https://doi.org/10.1038/s41558-019-0613-7>.
- Thornton, J. A., K. S. Virts, R. H. Holzworth, and T. P. Mitchell, 2017: Lightning enhancement over major shipping lanes. *Geophys. Res. Lett.*, **44**, 9102–9111, <https://doi.org/10.1002/2017GL074982>.
- Toffolon, M., S. Piccolroaz, and E. Calamita, 2020: On the use of averaged indicators to assess lakes’ thermal response to changes in climatic conditions. *Environ. Res. Lett.*, **15**, 034060, <https://doi.org/10.1088/1748-9326/ab763e>.
- Toreti, A., and Coauthors, 2022: Drought in China September 2022. GDO Analytical Rep. EUR 31245 EN, JRC130850, 33 pp., <https://doi.org/10.2760/377056>.

- Torralla, V., F. J. Doblas-Reyes, and N. Gonzalez-Reviriegol, 2017: Uncertainty in recent near-surface wind speed trends: A global reanalysis intercomparison. *Environ. Res. Lett.*, **12**, 114019, <https://doi.org/10.1088/1748-9326/aa8a58>.
- United Nations Environment Programme, 2021: Global methane assessment: Benefits and costs of mitigating methane emissions. United Nations Environment Programme and Climate and Clean Air Coalition Rep., 172 pp., <https://www.unep.org/resources/report/global-methane-assessment-benefits-and-costs-mitigating-methane-emissions>.
- Utrabo-Carazo, E., C. Azorin-Molina, E. Serrano-Navarro, E. Aguilar, M. Brunet, and J. A. Guijarro, 2022: Wind stilling ceased in the Iberian Peninsula since the 2000s, 1961–2019. *Atmos. Res.*, **272**, 106153, <https://doi.org/10.1016/j.atmosres.2022.106153>.
- van der A, R. J., Allaart, M. A. F., and Eskes, H. J., 2015: Extended and refined multi sensor reanalysis of total ozone for the period 1970–2012. *J. Geophys. Res.*, **120**, 3021–3035, <https://doi.org/10.5194/amt-8-3021-2015>.
- Vanderkelen, I., N. P. M. Van Lipzig, and W. Thiery, 2018: Modelling the water balance of Lake Victoria (East Africa)-Part 2: Future projections. *Hydrol. Earth Syst. Sci.*, **22**, 5527–5549, <https://doi.org/10.5194/hess-22-5527-2018>.
- van der Schalie, R., and Coauthors, 2017: The merging of radiative transfer-based surface soil moisture data from SMOS and AMSR-E. *Remote Sens. Environ.*, **189**, 180–193, <https://doi.org/10.1016/j.rse.2016.11.026>.
- , and Coauthors, 2022: Soil moisture [in “State of the Climate in 2021”]. *Bull. Amer. Meteor. Soc.*, **103** (8), 564–566, <https://doi.org/10.1175/BAMS-D-22-0092.1>.
- van der Schrier, G., J. Barichivich, K. R. Briffa, and P. D. Jones, 2013: A scPDSI-based global dataset of dry and wet spells for 1901–2009. *J. Geophys. Res. Atmos.*, **118**, 4025–4048, <https://doi.org/10.1002/jgrd.50355>.
- van der Werf, G. R., and Coauthors, 2017: Global fire emissions estimates during 1997–2016. *Earth Syst. Sci. Data*, **9**, 697–720, <https://doi.org/10.5194/essd-9-697-2017>.
- Vargin, P. N., A. V. Koval, and V. V. Guryanov, 2022: Arctic stratosphere dynamical processes in the winter 2021–2022. *Atmosphere*, **13**, 1550, <https://doi.org/10.3390/atmos13101550>.
- Vecellio, D. J., S. T. Wolf, R. M. Cottle, and W. M. Kenney, 2022: Evaluating the 35°C wet-bulb temperature adaptability threshold for young, healthy subjects (PSU HEAT Project). *J. Appl. Physiol.*, **132**, 340–345, <https://doi.org/10.1152/jappphysiol.00738.2021>.
- Velasco, I., and J. M. Fritsch, 1987: Mesoscale convective complexes in the Americas. *J. Geophys. Res.*, **92**, 9591–9613, <https://doi.org/10.1029/JD092iD08p09591>.
- Virts, K., T. Lang, D. Buechler, and P. Bitzer, 2023: Bayesian analysis of the detection performance of the lightning imaging sensors. *11th Conf. on the Meteorological Application of Lightning Data*, Denver, CO, Amer. Meteor. Soc., 12 pp., https://ntrs.nasa.gov/api/citations/20220019219/downloads/2023_AMS_LIS_absde_final.pdf.
- Vivero, S., X. Bodin, D. Farías-Barahona, S. MacDonell, N. Schaffer, B. A. Robson, and C. Lambiel, 2021: Combination of aerial, satellite, and UAV photogrammetry for quantifying rock glacier kinematics in the dry Andes of Chile (30°S) since the 1950s. *Front. Remote Sens.*, **2**, 784015, <https://doi.org/10.3389/frsen.2021.784015>.
- Vömel, H., S. Evan, and M. Tully, 2022: Water vapor injection into the stratosphere by Hunga Tonga-Hunga Ha’apai. *Science*, **377**, 1444–1447, <https://doi.org/10.1126/science.abq2299>.
- Vose, R. S., and Coauthors, 2021: Implementing full spatial coverage in NOAA’s global temperature analysis. *Geophys. Res. Lett.*, **48**, e2020GL090873, <https://doi.org/10.1029/2020GL090873>.
- Vreugdenhil, M., S. Hahn, T. Melzer, B. Bauer-Marschallinger, C. Reimer, W. Dorigo, and W. Wagner, 2017: Assessing vegetation dynamics over mainland Australia with Metop ASCAT. *IEEE J. Sel. Top. Appl. Earth Obs. Remote Sens.*, **10**, 2240–2248, <https://doi.org/10.1109/JSTARS.2016.2618838>.
- Wang, H., and Coauthors, 2022: Global tropospheric ozone trends, attributions, and radiative impacts in 1995–2017: An integrated analysis using aircraft (IAGOS) observations, ozonesonde, and multi-decadal chemical model simulations. *Atmos. Chem. Phys.*, **22**, 13 753–13 782, <https://doi.org/10.5194/acp-22-13753-2022>.
- Wang, Q., Z. Li, J. Guo, C. Zhao, and M. Cribb, 2018: The climate impact of aerosols on lightning: Is it detectable from long-term aerosol and meteorological data? *Atmos. Chem. Phys.*, **18**, 12 797–12 816, <https://doi.org/10.5194/acp-18-12797-2018>.
- Wang, X., and Coauthors, 2022: Stratospheric climate anomalies and ozone loss caused by the Hunga Tonga volcanic eruption. ESS Open Archive, <https://essopenarchive.org/doi/full/10.1002/essoar.10512922.1>.
- Wang, Z., and Coauthors, 2021: Incorrect Asian aerosols affecting the attribution and projection of regional climate change in CMIP6 models. *npj Climate Atmos. Sci.*, **4**, 2, <https://doi.org/10.1038/s41612-020-00159-2>.
- Weatherhead, E. C., and Coauthors, 1998: Factors affecting the detection of trends: Statistical considerations and applications to environmental data. *J. Geophys. Res.*, **103**, 17 149–17 161, <https://doi.org/10.1029/98JD00995>.
- Weber, M., and Coauthors, 2022: Global total ozone recovery trends attributed to ozone-depleting substance (ODS) changes derived from five merged ozone datasets. *Atmos. Chem. Phys.*, **22**, 6843–6859, <https://doi.org/10.5194/acp-22-6843-2022>.
- Wells, N., S. Goddard, and M. J. Hayes, 2004: A self-calibrating Palmer drought severity index. *J. Climate*, **17**, 2335–2351, [https://doi.org/10.1175/1520-0442\(2004\)0172.0.CO;2](https://doi.org/10.1175/1520-0442(2004)0172.0.CO;2).
- Wentz, F. J., 1997: A well calibrated ocean algorithm for Special Sensor Microwave/Imager. *J. Geophys. Res.*, **102**, 8703–8718, <https://doi.org/10.1029/96JC01751>.
- , 2015: A 17-year climate record of environmental parameters derived from the Tropical Rainfall Measuring Mission (TRMM) microwave imager. *J. Climate*, **28**, 6882–6902, <https://doi.org/10.1175/JCLI-D-15-0155.1>.
- , L. Ricciardulli, K. Hilburn, and C. Mears, 2007: How much more rain will global warming bring? *Science*, **317**, 233–235, <https://doi.org/10.1126/science.1140746>.
- WGMS, 2021: Global Glacier Change Bulletin No. 4 (2018-2019). M. Zemp et al., Eds., ISC(WDS)/IUGG(IACS)/UNEP/UNESCO/WMO, World Glacier Monitoring Service, 278 pp., <https://doi.org/10.5904/wgms-fog-2021-05>.
- Wielicki, B. A., B. R. Barkstrom, E. F. Harrison, R. B. Lee III, G. L. Smith, and J. E. Cooper, 1996: Clouds and the Earth’s Radiant Energy System (CERES): An Earth observing system experiment. *Bull. Amer. Meteor. Soc.*, **77**, 853–868, [https://doi.org/10.1175/1520-0477\(1996\)0772.0.CO;2](https://doi.org/10.1175/1520-0477(1996)0772.0.CO;2).
- , and Coauthors, 1998: Clouds and the Earth’s Radiant Energy System (CERES): Algorithm overview. *IEEE Trans. Geosci. Remote Sens.*, **36**, 1127–1141, <https://doi.org/10.1109/36.701020>.
- Wiese, D. N., F. W. Landerer, and M. M. Watkins, 2016: Quantifying and reducing leakage errors in the JPL RL05M GRACE mascon solution. *Water Resour. Res.*, **52**, 7490–7502, <https://doi.org/10.1002/2016WR019344>.

- Wild, B., I. Teubner, L. Moesinger, R.-M. Zotta, M. Forkel, R. van der Schalie, S. Sitch, and W. Dorigo, 2022: VODCA2GPP—A new, global, long-term (1988–2020) gross primary production dataset from microwave remote sensing. *Earth Syst. Sci. Data*, **14**, 1063–1085, <https://doi.org/10.5194/essd-14-1063-2022>.
- Willett, K., 2023a: HadISDH.extremes Part 1: A gridded wet bulb temperature extremes index product for climate monitoring. *Adv. Atmos. Sci.*, <http://www.iapjournals.ac.cn/aas/en/article/doi/10.1007/s00376-023-2347-8>, in press.
- , 2023b: HadISDH.extremes Part 2: Exploring humid heat extremes using wet bulb temperature indices. *Adv. Atmos. Sci.*, <http://www.iapjournals.ac.cn/aas/en/article/doi/10.1007/s00376-023-2348-7>, in press..
- , C. N. Williams Jr., R. J. H. Dunn, P. W. Thorne, S. Bell, M. de Podesta, P. D. Jones, and D. E. Parker, 2013: HadISDH: An updated land surface specific humidity product for climate monitoring. *Climate Past*, **9**, 657–677, <https://doi.org/10.5194/cp-9-657-2013>.
- , R. J. H. Dunn, P. W. Thorne, S. Bell, M. de Podesta, D. E. Parker, P. D. Jones, and C. N. Williams Jr., 2014: HadISDH land surface multi-variable humidity and temperature record for climate monitoring. *Climate Past*, **10**, 1983–2006, <https://doi.org/10.5194/cp-10-1983-2014>.
- Williams, E. R., 1992: The Schumann resonance: A global tropical thermometer. *Science*, **256**, 1184–1187, <https://doi.org/10.1126/science.256.5060.1184>.
- , 2020: Lightning and climate change. *Fundamentals and Modelling*, Vol. 1, *Lightning Interaction with Power Systems*, A. Piantini, Ed., CRC Press, 1–46, https://doi.org/10.1049/PB-P0172F_ch1.
- , A. Guha, R. Boldi, H. Christian, and D. Buechler, 2019: Global lightning activity and the hiatus in global warming. *J. Atmos. Sol.-Terr. Phys.*, **189**, 27–34, <https://doi.org/10.1016/j.jastp.2019.03.011>.
- , and Coauthors, 2020: Evolution of global lightning in the transition from cold to warm phase preceding two super El Niño events. *J. Geophys. Res. Atmos.*, **126**, e2020JD033526, <https://doi.org/10.1029/2020JD033526>.
- WMO, 2018: Scientific assessment of ozone depletion, 2018. Global Ozone Research and Monitoring Project Rep. 58, 588 pp., <https://csl.noaa.gov/assessments/ozone/2018>.
- , 2022: Scientific assessment of ozone depletion: 2022. GAW Rep. 278, 509 pp., <https://ozone.unep.org/sites/default/files/2023-02/Scientific-Assessment-of-Ozone-Depletion-2022.pdf>.
- Wohland, J., N.-E. Omrani, D. Witthaut, and N.-S. Keenlyside, 2019: Inconsistent wind speed trends in current twentieth century reanalyses. *J. Geophys. Res. Atmos.*, **124**, 1931–1940, <https://doi.org/10.1029/2018JD030083>.
- Wolter, K., and M. S. Timlin, 1998: Measuring the strength of ENSO events – How does 1997/98 rank? *Weather*, **53**, 315–324, <https://doi.org/10.1002/j.1477-8696.1998.tb06408.x>.
- Woolway, R. I., and C. J. Merchant, 2018: Intralake heterogeneity of thermal responses to climate change: A study of large Northern Hemisphere lakes. *J. Geophys. Res. Atmos.*, **123**, 3087–3098, <https://doi.org/10.1002/2017JD027661>.
- , B. M. Kraemer, J. D. Lenters, C. J. Merchant, C. M. O'Reilly, and S. Sharma, 2020: Global lake responses to climate change. *Nat. Rev. Earth Environ.*, **1**, 388–403, <https://doi.org/10.1038/s43017-020-0067-5>.
- Worden, J. R., A. A. Bloom, S. Pandey, Z. Jiang, H. M. Worden, T. W. Walker, S. Houweling, and T. Röckmann, 2017: Reduced biomass burning emissions reconcile conflicting estimates of the post-2006 atmospheric methane budget. *Nat. Commun.*, **8**, 2227, <https://doi.org/10.1038/s41467-017-02246-0>.
- Yeh, and Coauthors, 2018: ENSO atmospheric teleconnections and their response to greenhouse gas forcing. *Rev. Geophys.*, **56**, 185–206, <https://doi.org/10.1002/2017RG000568>.
- Yook, S., D. W. J. Thompson, and S. Solomon, 2022: Climate impacts and potential drivers of the unprecedented Antarctic ozone holes of 2020 and 2021. *Geophys. Res. Lett.*, **49**, e2022GL098064, <https://doi.org/10.1029/2022GL098064>.
- Yosef, Y., E. Aguilar, and P. Alpert, 2021: Is it possible to fit extreme climate change indices together seamlessly in the era of accelerated warming? *Int. J. Climatol.*, **41**, E952–E963, <https://doi.org/10.1002/joc.6740>.
- Yoshida, S., T. Morimoto, T. Ushio, and Z. Kawasaki, 2007: ENSO and convective activities in Southeast Asia and western Pacific. *Geophys. Res. Lett.*, **34**, L21806, <https://doi.org/10.1029/2007GL030758>.
- Yu, B., X. Zhang, G. Li, and W. Yu, 2022: Interhemispheric asymmetry of climate change projections of boreal winter surface winds in CanESM5 large ensemble simulations. *Climatic Change*, **170**, 23, <https://doi.org/10.1007/s10584-022-03313-2>.
- Zeng, Z., and Coauthors, 2019: A reversal in global terrestrial stilling and its implications for wind energy production. *Nat. Climate Change*, **9**, 979–985, <https://doi.org/10.1038/s41558-019-0622-6>.
- Zhang, G., W. Luo, W. Chen, and G. Zheng, 2019: A robust but variable lake expansion on the Tibetan Plateau. *Sci. Bull.*, **64**, 1306–1309, <https://doi.org/10.1016/j.scib.2019.07.018>.
- Zhang, G. F., and Coauthors 2021: Uneven warming likely contributed to declining near-surface wind speeds in northern China between 1961 and 2016. *J. Geophys. Res. Atmos.*, **126**, e2020JD033637, <https://doi.org/10.1029/2020JD033637>.
- Zhang, R., H. Wang, Q. Fu, P. J. Rasch, and X. Wang, 2019: Unraveling driving forces explaining significant reduction in satellite-inferred Arctic surface albedo since the 1980s. *Proc. Natl. Acad. Sci. USA*, **116**, 23 947–23 953, <https://doi.org/10.1073/pnas.1915258116>.
- Zhang, X., L. Alexander, G. C. Hegerl, P. Jones, A. K. Tank, T. C. Peterson, B. Trewin, and F. W. Zwiers, 2011: Indices for monitoring changes in extremes based on daily temperature and precipitation data. *Wiley Interdiscip. Rev.: Climate Change*, **2**, 851–870, <https://doi.org/10.1002/wcc.147>.
- Zhang, Y., and Coauthors, 2016: Multi-decadal trends in global terrestrial evapotranspiration and its components. *Sci. Rep.*, **5**, 19124, <https://doi.org/10.1038/srep19124>.
- Zhao, G., Y. Li, L. Zhou, and H. Gao, 2022: Evaporative water loss of 1.42 million global lakes. *Nat. Commun.*, **13**, 3686, <https://doi.org/10.1038/s41467-022-31125-6>.
- Zhao, L., and Coauthors, 2020: Changing climate and the permafrost environment on the Qinghai–Tibet (Xizang) Plateau. *Permafrost Periglacial Processes*, **31**, 396–405, <https://doi.org/10.1002/ppp.2056>.
- Zheng, B., and Coauthors, 2019: Global atmospheric carbon monoxide budget 2000–2017 inferred from multi-species atmospheric inversions. *Earth Syst. Sci. Data*, **11**, 1411–1436, <https://doi.org/10.5194/essd-11-1411-2019>.
- , and Coauthors, 2023: Record-high CO₂ emissions from boreal fires in 2021. *Science*, **379**, 912–917, <https://doi.org/10.1126/science.ade0805>.

- Zhu, Y., and Coauthors, 2022: Perturbations in stratospheric aerosol evolution due to the water rich plume of the 2022 Hunga-Tonga eruption. *Commun. Earth Environ*, **3**, 248, <https://doi.org/10.1038/s43247-022-00580-w>.
- Ziemke, J. R., and Coauthors, 2019: Trends in global tropospheric ozone inferred from a composite record of TOMS/OMI/MLS/OMPS satellite measurements and the MERRA-2 GMI simulation. *Atmos. Chem. Phys.*, **19**, 3257–3269, <https://doi.org/10.5194/acp-19-3257-2019>.
- Ziese, M., A. Rauthe-Schöch, A. Becker, P. Finger, E. Rustemeier, S. Hänsel, U. Schneider, 2022: GPCC full data daily version 2022 at 1.0°: Daily land-surface precipitation from rain-gauges built on GTS-based and historic data. DWD, accessed 24 July 2023, https://doi.org/10.5676/DWD_GPCC/FD_D_V2022_100.
- Zipser, E. J., C. Liu, D. J. Cecil, S. W. Nesbitt, and D. P. Yorty, 2006: Where are the most intense thunderstorms on Earth? *Bull. Amer. Meteor. Soc.*, **87**, 1057–1071, <https://doi.org/10.1175/BAMS-87-8-1057>.
- Zou, C.-Z., H. Xu, X. Hao, and Q. Fu, 2021: Post-millennium atmospheric temperature trends observed from satellites in stable orbits. *J. Geophys. Res.*, **48**, e2021GL093291, <https://doi.org/10.1029/2021GL093291>.
- , —, —, and Q. Liu, 2023: Mid-tropospheric layer temperature record derived from satellite microwave sounder observations with backward merging approach. *J. Geophys. Res. Atmos.*, **128**, e2022JD037472, <https://doi.org/10.1029/2022JD037472>.